THE EAST PACIFIC RISE CRUSTAL THICKNESS, MOHO TRANSITION ZONE CHARACTER AND OFF-AXIS MAGMA LENS MELT CONTENT FROM 9°37.5'N TO 9°57'N: RESULTS FROM THREE-DIMENSIONAL MULTICHANNEL SEISMIC DATA ANALYSIS

by

Omid Aghaei

Submitted in partial fulfilment of the requirements
for the degree of Doctor of Philosophy

at

Dalhousie University
Halifax, Nova Scotia
November 2013

Happily dedicated to my wife, Sara, with appreciation and love

TABLE OF CONTENTS

LIST OF TABLES

LIST OF FIGURES

ABSTRACT

This thesis discusses the results from the first multi-source and multi-streamer three-dimensional multichannel seismic experiment conducted over a mid-ocean ridge environment. Prestack time migration was applied to the dataset resulting in the most detailed reflection images of a spreading center and its flanks to date. The key products from this work are maps of crustal velocities, crustal thickness, and Moho transition zone (MTZ) reflection character for a section of the fast-spreading East Pacific Rise (EPR) from 9°37.5'N to 9°57'N, excluding the area from 9°40'N to 9°42'N where no data were collected. Moho reflections were imaged within ~92% of the study area. The derived average crustal thickness and average crustal velocity for the investigated ~880 km^2 area are 5920±320 m and 6320±290 m/s, respectively. The average crustal thickness varies little from Pacific to Cocos plate suggesting mostly uniform crustal production in the last ~180 Ka.

Detailed analysis of the crustal thickness and MTZ reflection character shows that the third-order segmentation is governed by melt extraction processes within the uppermost mantle while the fourth-order ridge segmentation arises from mid- to upper-crustal processes. This analysis also suggests that both the mechanism of lower-crustal accretion and the volume of melt delivered to the crust vary along the investigated section of the EPR. More efficient mantle melt extraction is inferred at latitudes from 9°42'N to 9°51.5'N, with greater proportion of the lower crust accreted from the AML than for the rest of the study area. Larger volume of melt is delivered to the crust from 9°37.5'N to 9°40'N than to the investigated crust further north. At some locations, the Moho reflections are for the first time unambiguously imaged below the AML away from any ridge discontinuity suggesting that the Moho is formed at zero age at least at some sections of the spreading centers. The first study of the melt content of mid-crustal off-axis magma lenses (OAML), done using amplitude variation with offset technique calibrated for a magmatic plumbing system, shows that these magma bodies contain 0 to 20% melt. This suggests that OAMLs likely contribute little to the overall crustal formation.

LIST OF ABBREVIATIONS AND SYMBOLS USED

AML	Axial magma lens
AST	Axial summit trough
AVO	Amplitude variation with offset
bsf	below seafloor
CIG	Common image gather
CMP	Common midpoint
EPR	East Pacific Rise
ESP	Expanding spread profile
GPS	Global positioning system
LIFT	Leading Intelligent Filter Technology
LVZ	low-velocity zone
MAR	Mid-Atlantic Ridge
MBA	Mantle Bouguer anomaly
MCS	Multichannel seismic
MLVZ	Mantle low-velocity zone
MOR	Mid-ocean ridge
MTZ	Moho transition zone
MVA	Migration velocity analysis
NMO	Normal moveout
OAML	Off-axis magma lens
OBS	Ocean-bottom seismometer
OSC	Overlapping spreading center

PreSTM	Prestack time migration
RMO	Residual moveout
RMS	root-mean-squares
S/N	signal-to-noise
TWTT	Two-way traveltime
Vp	Compressional wave velocity
Vs	Shear wave velocity
Vrms	Root-mean-square velocity
t_0	Normal-incidence two-way traveltime
ρ	Density
θ	Angle of incidence
φ	Migration aperture

ACKNOWLEDGEMENTS

This dissertation would not have been possible without the guidance, support and expertise of several people whom I would like to express my deepest appreciation here.

First and foremost, I wish to express my sincere thanks to my supervisor Mladen R. Nedimović for his continuous mentorship, support, and encouragement over the last six years. He understood the difficulties, was supportive, and was optimistic for getting the solutions. Thank you Mladen for your patience, understanding, and support during my PhD study.

Special thanks to my committee members, Keith Louden, Matthew Salisbury, and Pablo Canales, for their encouragement towards the end of my dissertation. Thank you for reading my dissertation, discussing the problems, and providing important insights into this work.

I was on board of the cruise MGL0812 for collecting these data used in this dissertation. I am thankful to the chief scientists of this cruise, John Mutter, Suzanne Carbotte, Pablo Canales, Mladen Nedimović, and all my friends in this cruise, Helene Carton, Min Xu, Milena Marjanović, and Kori Newman, for sharing their knowledge with me during this cruise.

I would like to thank Caryl Michaelson-Rotermund for her feedbacks on my manuscripts and John Thibodeau for assisting with the technical issues in the lab.

Many thanks to the external examiner, Andy Calvert, for reviewing this dissertation, his comments, and questions.

CHAPTER 1 INTRODUCTION

1.1 Oceanic Crust

The oceanic crust covers nearly 60% of the Earth's surface and is continuously accreted along the global mid-ocean ridges (MORs) by a complex combination of magmatic, tectonic and hydrothermal processes. However, we do not have a thorough understanding of the oceanic crust accretion processes. The MOR plate boundaries provide an important window into understanding the dynamics of crustal formation and the kinematics of plate tectonics that are of fundamental importance in marine Earth sciences.

Marine seismology has been the primary source of our knowledge about the structure of the oceanic crust at MORs. Based on the compilation of seismic refraction data, mostly from two-ship experiments, it was shown by *Raitt* [1963] that the seismic structure of the oceanic crust is simple comprising two igneous layers, layer 2 and layer 3. The layer 2 was further subdivided into upper part 2A and lower part 2B based on the compilation of sonobouy refraction data [*Houtz and Ewing,* 1976]. This early view of the oceanic crust as a small number of homogenous layers was replaced by structural models obtained from synthetic modeling of ocean bottom seismograms recorded by ocean bottom seismometers (OBSs) [e.g., *Spudich and Orcutt,* 1980]. In these models, layer 2 is a region in which velocity increases rapidly with depth, in particular in the lower part of layer 2A, and layer 3 is a region of more gradual velocity increase with depth [e.g., *Kennett and Orcutt*, 1976]. Comparisons with ophiolites and laboratory measurements on dredged rocks and drill core samples have been used to interpret the seismic velocity structure of the oceanic crust in terms of crustal lithology [e.g., *Fox et al.,* 1973; *Christensen and Salisbury* 1975, *Spudich and Orcutt*, 1980]. A generalized view of the

oceanic crust has emerged from these comparisons. In this view, the extrusive sequence and the underlying sheeted dike complex of an ophiolite collectively make up the upper oceanic crust and correspond to layers 2A and 2B, respectively. Layer 2A with P-wave velocities <~2.5 km/s is associated with basaltic pillow lavas, and layer 2B with seismic P-wave velocities of ~5.5-6 km/s corresponds with some or the entire sheeted dike complex. The likely petrology of layer 3 with P-wave velocity 6.3-7.2 km/s is similar to values measured for gabbroic rock samples [*Christensen and Salisbury* 1975, *Houtz*, 1976; *Karson,* 1998]. The Mohorovičić Discontinuity (Moho) lies at the base of the seismic layer 3 and, in most cases, represents a rapid increase from lower crustal velocities to upper mantle velocities.

1.2 Crustal Accretion

In the early 1970s, to explain the seismic structure of the crust a large steady-state molten body or a "magma chamber" with cross sectional width of ~8 km at the base of the crust below MORs was suggested in which melt accumulates and undergoes differentiation prior to eruption [*Cann,* 1974]. This model was appealing in that it could provide a relatively simple explanation for the stratigraphy of the oceanic crust inferred from seismic studies and ophiolite complexes. In this model, intrusion and eruption from the chamber can produce extrusive pillow lavas and dikes of the upper crust, freezing of the margins of the chamber can form a middle layer of isotropic gabbro, and a thick, basal unit of layered gabbro and ultramafics can accumulate at the bottom of the chamber [*Sinton and Detrick*, 1992].

The search for such a large axial magma chamber (AMC) at the East Pacific Rise (EPR) between 8º30'N and 10ºN using 2D multichannel seismic (MCS) reflection profiling and

OBS refraction work resulted in discovery of an axial low velocity zone (LVZ) and a bright mid-crustal seismic reflector beneath the ridge axis which was interpreted as the roof of an AMC [*Orcutt et al.,* 1975; *Herron et al.,* 1978; 1980] (Figure 1.1). This important discovery initiated about two decades of intensive research that has seen many seismic experiments including seismic reflection, refraction and tomography conducted along, across and adjacent to the EPR ridge axis between 16°N and 20°S.

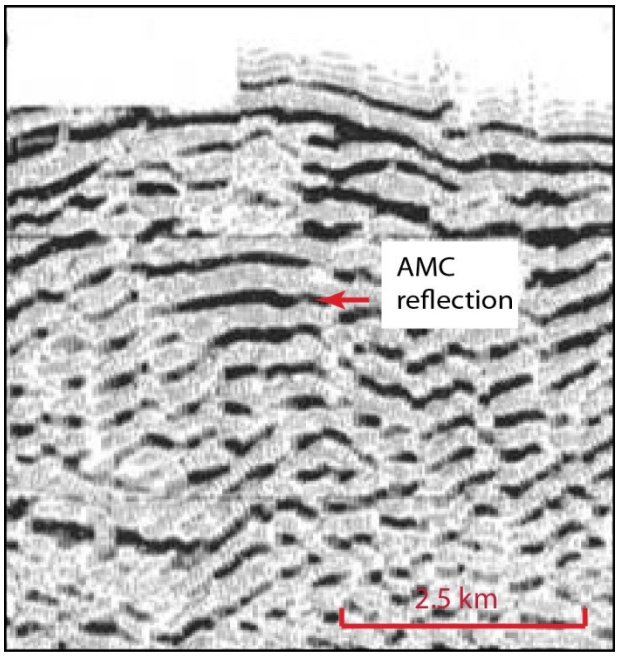

Figure 1.1 One of the first MCS reflection images across the EPR showing an event interpreted as the axial melt lens (AML). Adapted from *Heron et al.* [1980].

These studies have significantly improved our knowledge of the structure of the oceanic crust at a MOR environment. For example, the results from an extensive 2D MCS study along and across the EPR between 9° N and 13°30'N, where the Cocos and Pacific tectonic plates spread apart at half spreading rate of 56 mm/yr [*Carbotte and Macdonald*, 1992], show that instead of a large AMC, a thin (<50 m), 0.25-4-km-wide, upper-crust axial magma lens (AML) is located beneath the seafloor at a depth of 1.4-1.75 km

[*Detrick et al*., 1987, *Kent et al.,* 1993]. Seismic tomography experiments at 9°30'N show that this AML is underlain by a broad (5-7 km), partially molten region, characterized by low seismic velocity [*Toomey et al.,* 1990; *Vera et al.,* 1990] and high attenuation [*Wilcock et al.,* 1995] (Figure 1.2). These investigations resulted in a fundamental shift away from the traditional view of large mid-ocean magma chambers as they showed that a thin, narrow AML overlays a thicker, wider crystal mush zone at fast-spreading ridges.

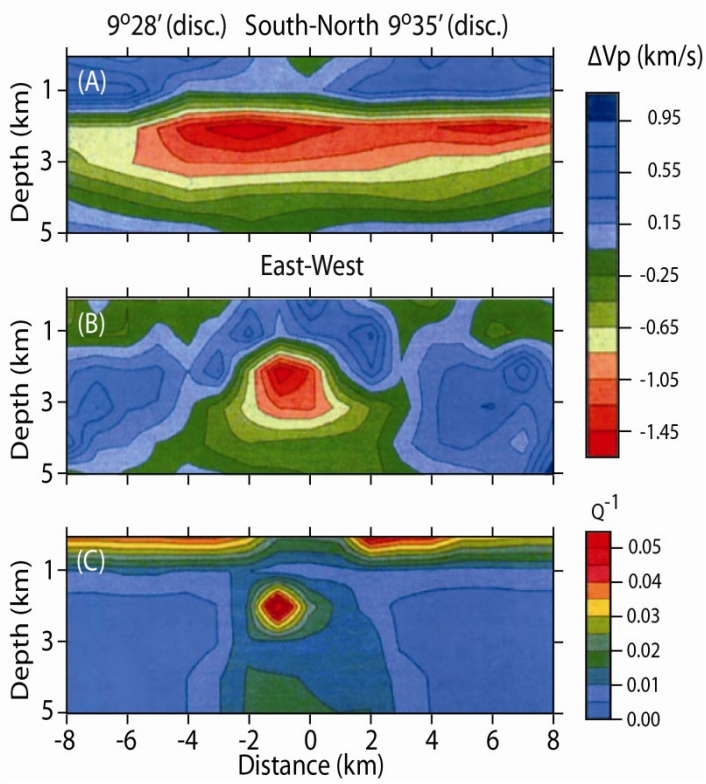

Figure 1.2 P-wave velocity perturbation and seismic attenuation (Q^{-1}) structures computed from seismic tomographic imaging of the EPR axial structure at 9°30'N where two fourth-order ridge discontinuities (disc.) occur at about -6 and 4 km from the ridge axis [*Toomey et al.,* 1990, *Wilcock et al.,* 1991]. (a) Along-axis P-wave velocity perturbation ~1 km west of the ridge axis. (b) Across-axis velocity perturbation ~2 km south of the 9°32'N. The colors represent departures from the initial velocity model; positive differences are faster than average, negative slower than average; 0.2 km/s contour interval. (c) Across-axis seismic attenuation (Q^{-1}). The largest velocity anomaly is <2 km wide, and it is <1-1.5 km thick. The model shows the region of high attenuation in the mid-crust that extends to lower crust. Adapted from *Solomon and Toomey,* [1992].

During the same two decades, intermediate-spreading ridges such as Juan de Fuca (half spreading rate 30 mm/yr; [*Riddihough,* 1984]) and slow-spreading ridges such as Mid-Atlantic Ridge (half spreading rate 10 mm/yr; *Kong et al.,* [1992]) were detailed using seismic experiments [e.g., *Morton et al.,* 1987; *Rohr et al*., 1988; *Purdy and Detrick,* 1986; *Louden et al.,* 1986]. Seismic reflection profiles across the Endeavor segment of the northern Juan de Fuca ridge have revealed an ~1-km-wide bright reflector at 2-3 km depth below the seafloor [*Rohr et al.,* 1988] that is substantially deeper than the AML mapped at EPR. In the slow-spreading Mid-Atlantic Ridge (MAR), geophysical evidence for a steady-state mid crustal AML similar to the EPR was not found [e.g., *Purdy and Detrick*, 1986; *Detrick et al.,* 1990]. However, *Calvert* [1995] published images of a small AML on a 2D MCS reflection profile collected along the MAR in one of the most magmatically robust and hydrothermally active areas of this ridge (south of the Kane Fracture zone at 23°15'N) suggesting that, perhaps, not all of the MAR is void of an AML.

Based on the presence of an AML and on the basis of structural studies of ophiolites, new numerical crustal accretion models were tested. The obtained results indicated that the lower oceanic crust can be formed by partial crystallization of the AML followed by ductile flow downward from this melt lens [e.g., *Phipps Morgan and Chen* 1993; *Henstock et al.,* 1993; *Chen and Phipps Morgan*, 1996]. This model is known as the gabbro-glacier model (Figure 1.3a). At about the same time, *Shouten and Denham* [1995] suggested a dual-sill model of accretion. In this model the lower crust accretes from two melt lenses, one at the dike/gabbro transition and the other at Moho (Figure 1.3b). The appearance of an alternative model was not surprising because field studies of ophiolites

were suggesting that the accretion process is likely more complex than what the gabbro-glacier model suggests. For example, *Boudier et al.* [1996] observed striking structural and petrological differences between the lower layered unit and upper foliated gabbros in the Oman ophiolite and questioned the gabbro-glacier model of crustal accretion. Furthermore, *Kelemen et al*. [1997] showed that the lower, layered gabbros were compositionally identical to gabbro sills in the Moho transition zone (MTZ). However, the dual-sill model did not appear sufficiently robust because it requires crystallization of about 50% of the crustal mass at the base of the crust, where heat removal by conduction and hydrothermal convection may not be efficient [*Kelemen and Aharanov*, 1998]. Thus, various research groups proposed emplacement of sills near the Moho and within the lower crust, as well as just below the dike/gabbro transition. These observations and hypotheses, together with the results of chemical modeling [*Kelemen and Aharanov*, 1998] led to the sheeted sills model of crustal formation, in which the lower crust forms by crystallization in sills at a variety of depths, from the dike/gabbro transition to the base of the crust (Figure 1.3c). During the last decade, a hybrid model of crustal accretion has also been proposed [e.g., *Maclennan et al.,* 2004] in which the lower third of the lower crust is crystallized in situ, and the top third of the lower crust is made via the gabbro glacier model. The middle third forms in a transition between these two mechanisms. Geophysical evidence for some form of the sheeted sills model has recently been provided by seafloor compliance measurements [*Crawford and Webb*, 2002], wide-angle OBS tomography [*Dunn et al.,* 2001], and MCS reflection imaging [*Nedimović et al.,* 2005; *Canales et al.,* 2009]. These observations provide critical support for the

hypothesis that the crust is accreted from multiple magma bodies, and that the volcanic systems on spreading centers have a complex plumbing system.

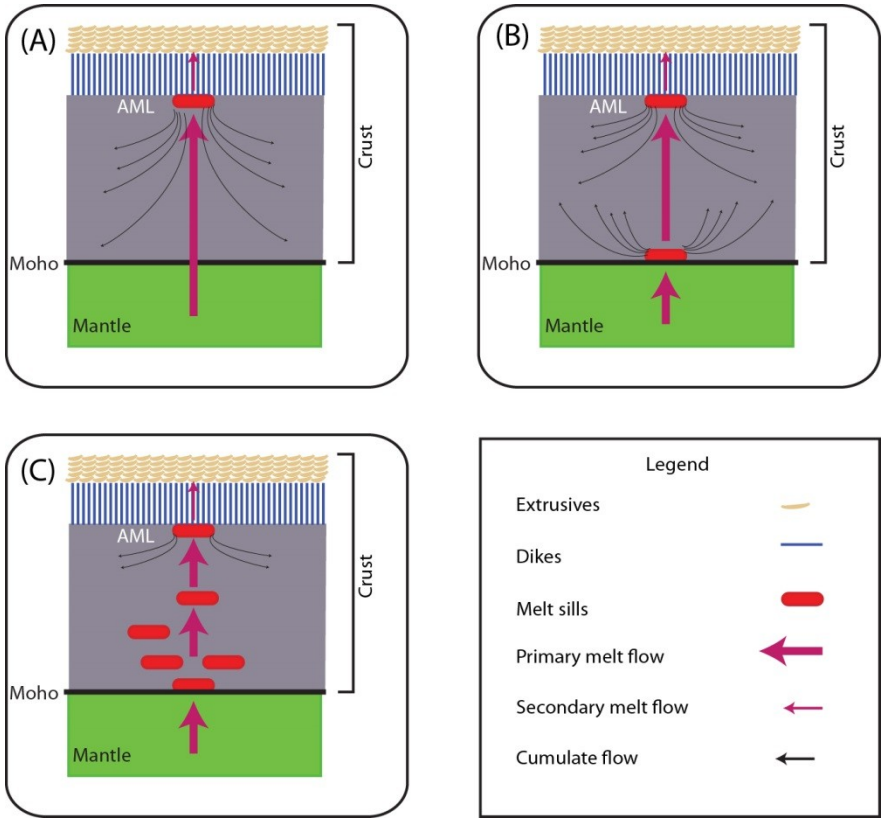

Figure 1.3 Schematic crustal accretion models. a) Gabbro-galcier model [e.g., *Nicolas et al*., 1988] where the lower crust is formed by gravitational settling of cumulates from the AML. b) Dual-sill model of crustal accretion [e.g., *Schouten and Denham*, 1995] in which the crust is formed by a combination of crystallization at AML and MTZ. Flow of largely crystalline "mush" from the two sills forms the gabbroic lower crust. c) Sheet-like model of crystallization [e.g., *Kelemen et al.* 1997]. In this model, most or even all of the lower crust is formed in situ. Modified from *Durant* [2011].

The size and internal properties (e.g., amount of melt) of the AML has been the subject of several investigations [e.g., *Vera et al.,* 1990; *Husseneder et al.,* 1996*; Collier and Singh*, 1997; *Canales et al.,* 2006; *Xu*, 2012]. These studies shows that the AML is thin (<100

m) [*Husseneder et al.,* 1996], and it contains a variable amount of melt along the ridge axis. Qualitative assessment of the melt content of the AML has been performed at a regional scale by analysis of 2D partial-offset stacks [e.g., *Singh et al.,* 1998; *Xu*, 2012]. This method, applied to the swath 3D MCS data collected along the axis between 9°30'N and 10°'N at the EPR, showed that the AML is partitioned into what appear to be melt and mush zones.

From applying 1D waveform inversion to high-resolution swath 3D at the EPR between 9°30'N and 10°N, *Xu* [2012] showed that the AML is ~16-40 m thick at these two locations. The measured P- and S-wave velocity at ~9°42'N, and 9°49'N were attributed to the presence of 95-100%, and ~40-45%, respectively [*Xu*, 2012] when compared with theoretically computed Hashin-Shtrikman bounds [*Hashin and Shtrikman*, 1963] that are the upper and lower bounds for the effective elastic moduli of a multiphase material.

1.3 Crustal Thickness

The average thickness of the oceanic crust away from anomalous regions is 6.0±1.6 km for all spreading rates [e.g., *Raitt,* 1963]. Compilations of more recent and more detailed seismic measurements and rare earth element inversions show that the crust formed at slow-spreading ridges (half spreading rate <20 mm/yr) displays much greater in-situ thickness variability than the crust formed at the fast-spreading ridges (half spreading rate >30 mm/yr) [*White et al.,* 1992]. For example, the results from a seismic refraction study along ~100 km of the median valley of the MAR [*Purdy and Detrick*, 1986] show that the crust is thickest in the segment center (~7 km), and it is thinnest (~3 km) at the segment ends. On the other hand, at the well-studied portion of the fast spreading EPR from 8°50'N to 9°50'N the crustal thickness measured from interpreting Moho reflection

times observed on 2D MCS profiles varies by 2.6 km [*Barth and Mutter*, 1996]. These seismic constraints on the oceanic crustal thickness are mostly formed by analysis of wide-angle OBS and near-offset MCS data, in particular from the information that Moho reflections and crustal/mantle refractions contain. The accuracy of the seismic measurements of crustal thickness is high because the transition from the crust to the uppermost mantle, the Moho Discontinuity or the MTZ, is in most cases relatively sharp, occurring within only a few 10s to a few 100s of meters [e.g., *Boudier and Nicolas*, 1995; *Jousselin and Nicolas*, 2000].

The long-wavelength (>50 km) variations in seismically measured thickness of the crust formed at the MAR are consistent with the gravity measurements [e.g., *Purdy and Detrick*, 1986; *Morris and Detrick*, 1991] performed along this spreading center suggesting that the bulk of the crustal thickness variations seem to be linked to the melt extraction processes occurring within the axial accretionary zone. Along-axis gravity profiles at the MAR show large gradients of mantle Bouguer anomaly (MBA) [e.g., *Lin et al.,* 1990].

By contrast, at the fast-spreading EPR the MBA has relatively small variations [e.g., *Madsen et al.,* 1990]. Based on these observations, *Lin and Phipps Morgan* [1992] proposed that the melt extraction processes occurring in the upper mantle are plume-like (3D) beneath a slow spreading ridge but more sheet-like (2D) beneath a fast spreading ridge. This 3D pattern of mantle upwelling at slow-spreading ridges requires enhanced melting at the center of each ridge segment and less melting at ends resulting in the observed pattern of crustal thickness variations at the slow-spreading ridges.

The results from a recent wide-angle OBS study at fast-spreading EPR (8°30'N-10°N) show along-axis crustal thickness variations of 2-2.7 km with the thinnest crust (5.3 km) at one segment end and the thickest crust (7.3-7.8 km) at about the segment center [*Canales et al.,* 2003]. From this study, *Canales et al.* [2003] showed 1) that the suggested sheet-like pattern of mantle upwelling that results in uniform crustal thickness at fast-spreading ridges is unlikely, and 2) the crustal thickness measurements are a valid proxy for magmatic segmentation at fast-spreading ridges at least for the first- and second-order ridge segments.

Imaging the Moho reflection in the axial region of the spreading ridges, however, is challenging even at the fast spreading centers that are characterized by smooth topography [e.g., *Herron et al.*, 1980; *Detrick et la.*, 1987; *Kent et al.,* 1994; *Barth and Mutter*, 1996]. So far only one study [*Singh et al.,* 2006] claims to have imaged the Moho reflection below the ridge axis, across the EPR on the eastern limb of the 9°03'N overlapping spreading center (OSC) (Figure 1.4). But the interpreted Moho reflection in this environment could be associated with ridge propagation over a pre-existing Moho [*Singh et al.,* 2006]. As a result, the crustal thickness of the axial accretionary zone, which is important in that it provides insight into the thermomechanical processes of MORs [e.g., *Buck and Su*, 1989], is not well constrained.

There is a growing body of evidence showing that the crustal accretion at MORs is not limited to the axial neovolcanic zone. These studies include: a) anomalously young basalt samples identified at ~4 km away from the axial zone at 9°31'N, and between 9°48'N and 9°52'N [*Goldstein et al*., 1998; *Sims et al.,* 2003]; b) formation of near-axis seamounts 5 to 15 km from the ridge axis at fast spreading ridges [e.g., *Shen et al.,* 1993];

c) detection of anomalously low S-wave velocities in the lower crust at ~10 km off axis at 9°48'N [*Crawford and Webb*, 2002] and in the MTZ at ~22 km off axis at 12°50'N [*Garmany*, 1989]; d) identification of an off-axis P-wave LVZ at ~20 km from the ridge axis at ~9°20'N [*Durant et al.,* 2009]; e) discovery of a network of crustal off-axis magma lenses (OAMLs) between ~9°37'N and 9°57'N [*Canales et al.,* 2012].

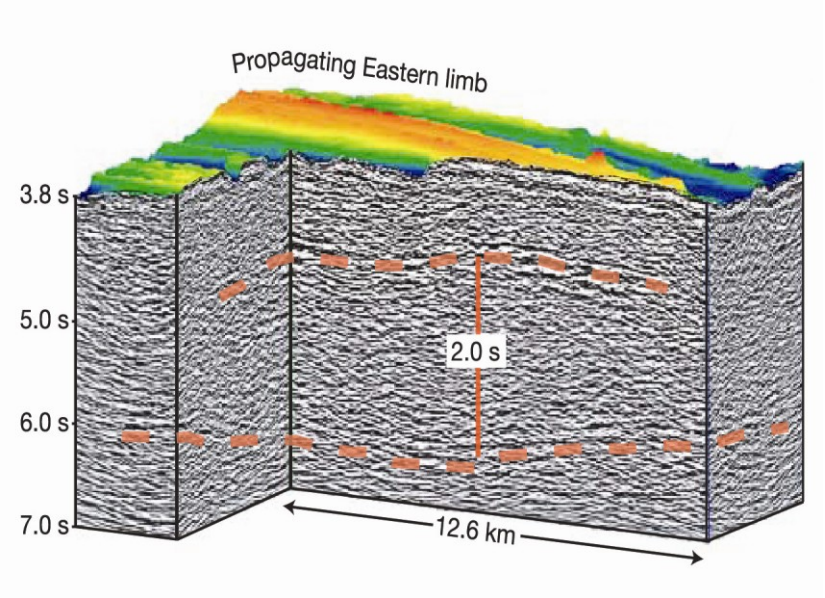

Figure 1.4 Images of Moho below the AML on the eastern limb of the OSC at 9°03'N from the ARAD psudo-3D survey described by *Singh et al.* [2006].

The source of the off-axis magmatism is not yet fully understood. Melt accumulation at the base of a thermal boundary and its ascent to the ridge flanks through a leaky permeability barrier [*Sohn and Sims*, 2005], or rapid magmatic ascent directly from the mantle to the upper crust through high permeability channels [*Katz and Weatherly*, 2012] are some of the suggested origins for the off-axis magmatism.

1.4 Ridge Segmentation

After the advent of high-resolution multibeam swath mapping systems in the mid 80's, it became apparent that the spreading centers between transform faults are segmented by additional types of non-rigid discontinuities [*Macdonald et al.,* 1988]. Crustal thickness variations were used to explain the source and origin of this segmentation of the spreading centers [e.g., *Lin et al*., 1990].

The high resolution images of the EPR between 5°N and 25°N resulting from the use of SeaMarc II and Sea Beam sonar systems show that the plate boundary in this area is segmented at a variety of temporal and spatial scales [e.g., *Macdonald et al.,* 1988]. Fine-scale (average spacing of 8 km) analysis of the seafloor lava compositions between 5°30'N to 14°30'N at the EPR by *Langmuir et al.* [1986] show that this portion of the EPR is also petrologically segmented at spatial scales much smaller than the known large-scale segmentation that occurs at OSCs and transform faults. The combined result of the *Macdonald et al*. [1988; 1991] and *Langmuir et al.* [1986] studies was a new hierarchy of physical segmentation of MORs. On fast-spreading ridges, first-order discontinuities (transform faults) persist for $>5x10^6$ years, partition the ridge axis at intervals of 600±300 km, and offset the ridge axis by >30 km. Second-order discontinuities are OSCs that partition the ridge axis on the scale of 140±90 km, persist of the order of $0.5\text{-}5x10^6$ years and offset the ridge axis by 2-30 km. Third-order discontinuities are small OSCs, 50±30 km in length, offset the ridge axis by 0.5-2 km, and last for $10^4\text{-}10^5$ years. The finest-scale (14±8 km) segmentation of the ridge axis is represented by small (<1 km) non-overlapping bends or changes in strike (1°-5°) of the

axial summit trough (AST) that last for 10^2-10^4 years and are known as deviation from axial linearity (deval). The first- and second-order discontinuities result in what is often referred to as large-scale segmentation and the third- and fourth-order discontinuities result in small-scale segmentation of MORs.

Langmuir et al. [1986] proposed that the source of petrologic segmentation at various spatial scales may reflect different scales of melt supply from different depth levels of the upwelling mantle. *Macdonald et al.* [1988] proposed that first-order segmentation reflects astenospheric upwelling, with the second- and third-order segmentations manifesting melt segregation events. Unlike *Langmuir et al.* [1986], who suggested mantle-level processes as the origin of fourth-order segmentation, *Macdonald et al.* [1988] suggested that pinching and swelling of the AMLs cause fourth-order segmentation. From major and minor analysis of glass samples at the EPR between 13°N and 23°N, *Sinton et al.* [1991] drew similar conclusions to *Langmuir et al.* [1986] and *Macdonald et al.* [1988], namely that the identified second- and third-order segment boundaries correspond to processes occurring in the mantle. However, *Sinton et al.* [1991] suggest that not all the fourth-order segment boundaries are also geochemical boundaries. Some of the fourth-order discontinuities mark termination of fissure eruptions indicating upper crustal origin [*Sinton et al.,* 1991]. The results from probing a second-order EPR segment from 9°09'-54'N using the near-bottom ARGO imaging system showed that the along-strike axial hydrothermal activity in this area correlates well with the fourth-order tectonic segmentation [*Haymon et al.,* 1991]. This led these investigators to propose that the origin of the fourth-order segmentation is also within the upper crust and is related to diking processes.

More recent high-resolution shipboard multibeam data collected over third-order tectonic segments at the southern EPR from 18°30'S to 17°15'S [*White et al.,* 2000], and across the northern EPR from 9°08'N to 10°N [*White et al.,* 2002] established a distinction between third- and fourth-order segments. More pillowed flows and lava domes were found near the third-order segment ends, and more sheet flows were found in third-order segment centers. This suggests that effusion rate is highest in third-order segment centers and lowest at segment ends, which is consistent with the idea that third-order segments are individual volcanic segments controlled by the AML [*White et al.,* 2002]. Fourth-order segments did not show the consistent middle-to-end reduction in effusion rate and were suggested to be controlled by diking in the upper crust similar to *Sinton et al.*'s [1991] and *Haymon et al.*'s [1991] interpretations.

Controlled source seismic studies of the crust and upper mantle were employed to image ridge structures at depth and try to resolve the ambiguity of the origin of small-scale segmentation. Vertical injection of mantle melt into the crust near the fourth-order segment center was postulated by *Toomey et al.* [1991] based on the results of a seismic tomography study conducted over a fourth-order segment in the EPR between 9°28'N and 9°35'N. The P-wave velocities of the middle to uppercrust in this study showed relatively lower velocity at the segments ends compared with the segment center [*Toomey et al.,* 1990] (Figure 1.2). Using the same dataset of *Toomey et al.* [1990], tomographic images of the lower crust and upper mantle between the 9°28'N and 9°35'N fourth-order discontinuities were provided by *Dunn et al.*[2000]. The results from this study showed that along-axis variation in velocity structure of the lower crust and upper mantle correlates with the morphologic segmentation. In this view, the origin of the fourth-order

segmentation is related to the dynamics of melt generation and transport from the mantle rather than to the tectonic activity. Additionally, a causal relationship between third-order segmentation and variations in mantle melt delivery was inferred based on the results of a more recent tomographic study that directly imaged the upper mantle between 9°N and 10°N. These results show correlation between the location of third-order segments and mantle LVZs [*Toomey et al.,* 2007].

However, the results of an extensive 2D MCS experiment between 15°30'N to 16°40'N were interpreted to show that there is linkage between fourth-order tectonic segmentation and upper crustal magma plumbing system [*Carbotte et al.,* 2000], which is similar to the inference made by *Macdonald et al.* [1988]. The AML reflector in this latitude range was segmented at a scale comparable with fourth-order discontinuities [*Carbotte et al.,* 2000]. The casual relationship between mid-crustal magma reservoir and small-scale segmentation at the EPR was further tested by analysis of high-resolution seismic images of the AML from the Siqueiros to Clipperton Transforms using modern swath 3D MCS data [*Carbotte et al.,* 2013]. This study showed that the crustal magma body is partitioned into segments 5-15 km long coinciding with the fourth-order ridge segmentation. This confirms the linkage between fourth-order tectonic segmentation and upper crustal magma plumbing system suggested by *Carbotte et al.* [2000]. Disruption of the magma lens was also observed by *Carbotte et al.* [2013] study at third-order segment boundaries.

1.5 Objectives

The seismic investigations conducted along and across the global MOR have significantly increased our knowledge of the processes of crustal and lithospheric formation and evolution at MORs. In particular, the 2D MCS studies at the best-studied

portion of the global MOR between 9°N to 10°N of the EPR (Figure 1.5) have detailed the structure of the shallow crust and the midcrustal magma reservoirs beneath the EPR. Still poorly understood, however, is the structure of the magmatic system within the lowermost crust and the uppermost mantle. Consequently, the nature of mantle melting, melt extraction and its delivery to the crust are not yet thoroughly understood.

While first- and second-order ridge segments have been carefully investigated and are thought to be well understood [*Macdonald et al.,* 1984, 1988], the nature and origin of small-scale, third- and fourth-order ridge segmentation are still largely debated.

The Moho reflection is not imaged in the vicinity (~±3 km) of the ridge axis. As a result, the age of Moho formation, and the distance from the axis at which the crust reached its full thickness are not yet known.

The geometry and the physical properties of the AML have been the subject of several studies. However, the melt content of the OAMLs, their contribution to formation of the lower crust, and their connectivity to the AML are not known.

Based on the above unknowns, the questions that are aimed to be answered in this dissertation are as follows:

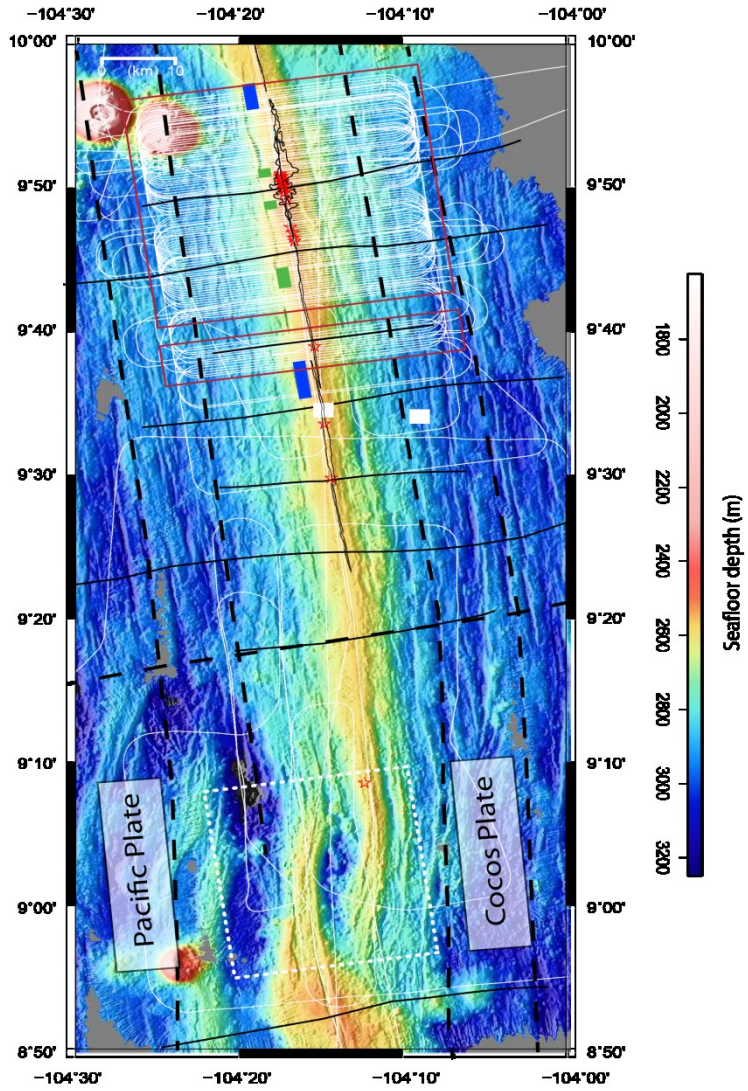

Figure 1.5 Ship track for cruise MGL0812 is shown with thin white lines superimposed over the EPR bathymetry (color background) data collected during the MGL0812 survey (EM120 gridded at 50 m). The data from the area outlined with red square were used in this study for 3D processing. The blue and green filled rectangles show the third- and fourth-order discontinuity zones in the study area, respectively [*White et al.*, 2006; *Carbotte et al.,* 2013]. The location of selected earlier seismic experiments conducted in the area is also shown: psudo-3D MCS reflection (dotted square [*Kent et al.,* 2000]), 2D MCS reflection (solid line [*Detrick et al.*, 1987]); the UNDERSHOOT wide-angel seismic experiment (dashed lines [*Toomey et al.,* 1998]), midpoint location of ESP-5 (on the ridge axis) and ESP-1 (~10 km off-axis) (white squares [*Vera et al.,* 1990]). Hydrothermal vent locations shown with red stars are from *Haymon et al.* [1991]. Axial summit trough (AST) shown with thin black line is as interpreted by *Soule et al.* [2007]. Extent of 2005-2006 eruption shown with black polygon is from *Soule et al.* [2009].

1. What is the mode of crustal accretion in the study area and does it vary spatially? While most researchers today agree that the ridge magmatic systems are complex and that the lower oceanic crust is formed from multiple magma bodies, what the contribution of various magma bodies is to lower crustal accretion and how it changes in space and time remain open questions. Geophysical fingerprints of crustal accretion modes may be established by detailing the local crustal thickness, AML geometry, and MTZ character and linking them with the local style of crustal accretion predicted by modeling and/or suggested by geochemical studies;
2. Can detailed crustal thickness and MTZ character measurements be used to infer small-scale segmentation at fast-spreading ridges? The body of work on ridge segmentation summarized in Section 1.4 indicates that the origin and nature of small-scale, third- and fourth-order ridge segmentation is still not fully understood. As such, the location and order of some of the mall-scale ridge discontinuities remains challenging to determine and is debated. Detailed mapping of MTZ character and crustal thickness at a scale and resolution comparable to small-scale segmentation may provide complementary information on the processes that govern small-scale segmentation. Moreover, it may help delineate location and order of these segments discontinuities;
3. What is the age of Moho formation and are the crustal thickness and MTZ seismic signature symmetric or asymmetric across the ridge axis? The Moho formation age, an important parameter for understanding crustal accretion, is not known. Moho reflection is generally not imaged in the immediate vicinity of the ridge

axis (~±3 km) but it is not understood if this is a) due to the Moho not being formed at the same time as much of the crust or b) because the imaging methodology used so far for academic investigations of the ridges is inadequate for imaging in areas of large lateral velocity variations and high signal attenuation. Crustal accretion is thought to be symmetric and any asymmetricity of the crustal thickness and MTZ character on the two ridge flanks may indicate variations in early crustal and MTZ evolution;

4. What is the melt content of the OAMLs, what is their contribution to the overall crustal thickness, and are the mid-crustal AML and OAMLs connected? Computing the melt content of the OAMLs and the fraction of the crustal thickness produced from the OAMLs may help constrain the volume of melt extracted from the mantle in the off-axis region and shed light on the dynamics of off-axis magmatism that is largely debated. It is generally agreed that the sources of on- and off-axis magmatism are largely separated. However, the most likely way to conclusively determine the spatial relationship between the mid-crustal AML and the OAMLs is through detailed 3D MCS imaging, as carried out for this thesis work.

Based on the above questions, the objectives of this Ph.D thesis are:

1. Investigate the average crustal velocity and crustal thickness along and across the ridge axis and their relationship to ridge segmentation, melt lens distribution, style of crustal accretion, crustal age, bathymetry, and magmatism;

2. Detail the MTZ reflection character along and across the ridge axis and its relationship to ridge segmentation, melt lens distribution, style of crustal accretion, crustal age, bathymetry, and magmatism;
3. Examine the melt content of OAMLs and their spatial relationship with the AML.

1.6 Methodology

To achieve the objectives listed above, I have analyzed the 3D MCS data collected in 2008 onboard *R/V Marcus G. Langseth* during cruise MGL0812 carried out over the EPR from 9°37.5' to 9°57'N (Figure 1.5); The acquired dataset is a result of the first high-resolution multi-source and multi-streamer 3D MCS experiment conducted over a MOR environment [*Mutter et al.,* 2009]. Covering an area of almost 1000 km^2 and summing up to ~5 TB of data, this dataset is massive from the perspective of pure academic research. For data analysis, I applied the following methods to the data:

1. Standard 3D Kirchhoff poststack that is detailed in Appendix A and in section 2.3,
2. State-of the-art 3D Kirchhoff prestack migration processing that is explained in Appendix B and section 3.3,
3. The AVO analysis of the OAMLs that is explained in Appendix C and section 4.3.

1.7 Dissertation Outline

The remainder of this Ph.D. thesis consists of chapters 2 to 5 and appendices A to C. *Chapter 2* is entitled "Crustal thickness and Moho character from poststack-migrated 3D MCS data collected over the fast-spreading EPR from 9°42'N to 9°57'N". In this chapter I present the results of the MCS data analysis of the larger, northern 3D box. These

results provide a window into the 3D architecture of the young oceanic crust at a fast-spreading MOR at a scale and resolution that was not previously possible. The interpretation, centered on detailing the crustal thickness and the MTZ reflection character and establishing linkages with small-scale ridge segmentation and style of crustal accretion, provides, within the reference frame of existing geophysical, geochemical, and morphological data, a new perspective on these MOR processes. For producing the post-stack migrated 3D reflection volume, I applied the processing sequence detailed in appendix A. I then picked the igneous basement and Moho reflection, interpolated in 3D existing OBS velocity profiles, computed the local crustal thickness, and examined the Moho reflection character to map the type of the MTZ. This chapter is in preparation for submission to the *Geochemistry, Geophysics, Geosystems.*

Chapter 3 is entitled "The East Pacific Rise crust and Moho transition zone from 9°37.5'N to 9°57'N: Results from prestack time migration of 3D MCS data". Here I present and interpret the results of applying 3D Kirchhoff prestack time migration (PreSTM) to the full 3D MCS dataset that includes both the northern and the southern 3D volume. This is the first time a 3D PreSTM has been applied to a MOR dataset. This time consuming and computationally demanding process has yielded the most comprehensive reflection images and average crustal velocity for this intensely investigated portion of the EPR and MOR environment in general. Improved and extended detailed information on the crustal thickness and MTZ character is presented for ~880 km^2 of the EPR between 9°37.5'N to 9°57'N, excluding a 3.3-km-wide gap from 9°40'N to 9°42'N. The results of this chapter shed new light on the on-going debate of the Moho formation age, and provide additional information on segmentation and crustal accretion hypothesized in

Chapter 2. This chapter is in preparation for submission to the *Geochemistry, Geophysics, Geosystems*.

Chapter 4 is entitled "AVO characterization of two large mid-crustal OAMLs at the EPR from 9º37.5'N to 9º54'N". In this chapter I present the results of applying the AVO crossplot technique to determine the melt content of off-axis magma bodies quantitatively using the Hashin-Shtrikman bounds. A background trend is required to interpret the results of AVO crossplotting in the framework suggested by *Castagna et al.* [1998]. I show that using the Hashin-Shtrikman bounds and the recent results for the amount of melt determined for the AML from 1D waveform inversions [*Xu*, 2012], a background trend can be estimated. The qualitative melt assessment of *Marjanović* [2013] for the AML is examined in the new interpretation framework and the amount of melt at the OAMLs is compared with the one at the AML. Also examined in this chapter is the spatial relationship between the OAMLs and the AML.

Chapter 5, entitled "Conclusions and future work", concludes the dissertation with a summary of all research contributions presented in chapters 2, 3 and 4, and provides a list of recommendations for future work directions.

Appendix A, entitled "Three-dimensional (3D) seismic data acquisition and processing " details the acquisition parameters for the MGL0812 survey, 3D geometry definition for processing the data, prestack data processing, and poststack migration and image conditioning.

Appendix B, entitled "3D Kirchhoff prestack time migration", summarizes the kinematics of the Kirchhoff 3D PreSTM applied to the 3D MCS data, and explains the processing steps applied to the common image gathers (CIGs) that are the products of migration.

Appendix C, entitled “Overview of AVO theory” provides the theoretical background for the AVO equations and details the crossplot technique.

CHAPTER 2 CRUSTAL THICKNESS AND MOHO CHARACTER FROM POSTSTACK-MIGRATED 3D MCS DATA COLLECTED OVER THE FAST-SPREADING EAST PACIFIC RISE FROM 9˚42'N TO 9˚57'N

This chapter has been submitted for publication to Geochemistry, Geophysics, Geosystems journal and is presently under review.

Omid Aghaei is the principal researcher and the corresponding author of the article. He conducted the research as part of his PhD. Thus, while he received supervision and guidance from his supervisor Dr. Mladen R. Nedimović, he carried out the work, wrote the article, and communicated with the editor of the journal. Minor grammatical and content changes have been made to integrate the article within this dissertation.

2.1 Abstract

We computed crustal thickness (5740±270 m) and mapped Moho reflection character using 3D multichannel seismic data covering 658 km2 of the fast-spreading East Pacific Rise (EPR) from 9˚42'-9˚57'N. Moho reflections are imaged within ~87% of the study area. The average crustal thickness for study area quadrants varies little suggesting uniform crustal production in the last ~180 Ka. However, individual crustal thickness measurements differ by as much as 1.75 km indicating that mantle upwelling is not 2D. Third-order, but not fourth-order ridge discontinuities are associated with changes in the Moho reflection character and/or near-axis crustal thickness. This suggests that the third-order segmentation is governed by melt distribution processes within the uppermost mantle while the fourth-order ridge segmentation arises from mid- to upper-crustal processes. In this light, we assign fourth-order ridge discontinuity status to the debated ridge segment boundary at ~9˚44.8'N and third-order status at ~9˚51.5'N to the ridge segment boundary that was previously interpreted as a fourth-order discontinuity at 9˚51.5'N or 9˚53'N. The new seismic results also suggest that the mechanism of lower-crustal accretion varies along the investigated section of the EPR but that the volume of

melt delivered to the crust is mostly uniform. More efficient mantle melt extraction is inferred within the southern half of our survey area with greater proportion of the lower crust accreted from the AML than that for the northern half. This south-to-north variation in the crustal accretion style may be caused by interaction between the melt sources for the ridge and the Lamont seamounts.

2.2 Introduction

The structure of the oceanic crust formed along the global mid-ocean ridge (MOR) system is simple compared with the continental crust [e.g., *Raitt* 1956]. However, the nature of mantle melting, melt extraction, and melt delivery to the crust has been a subject of considerable research over the past three decades and is still investigated. To address the outstanding questions related to crustal accretion, a number of controlled source seismic experiments have been conducted along and across the East Pacific Rise (EPR) from the mid-1970s to mid-1990s [e.g., *Orcutt et al.,* 1975*; Herron et al.,* 1980; *Detrick et al.,* 1987*; Kent et al.,* 1993]. These studies imaged a mid-crustal reflection that was interpreted to originate from a thin magma sill (<50 m) here referred to as the axial magma lens (AML). The AML is detected beneath much of the ridge axis and sits atop the roof of a broader low-velocity volume (5-10 km wide) extending to the base of the crust and into the uppermost mantle [e.g., *Vera et al.,* 1990*; Dunn et al.,* 2000]. The discovery of the AML led to the development of the gabbro-glacier models for crustal formation at fast spreading ridges [e.g., *Phipps Morgan and Chen* 1993; *Henstock et al.,* 1993*; Chen and Phipps Morgan,* 1996; *Quick and Delinger*, 1993]. In these models, magma is fed directly from the mantle to the AML where partial crystallization occurs. The upper crust is formed by dike injection and lava extrusion, while the lower crust is

formed by downward flow of the crystalline residue due to gravitational forces. More recent ophiolite studies [e.g., *Boudier et al.,* 1996] suggest that magma can also accumulate on-axis at lower-crust levels and within the Moho transition zone (MTZ) leading to the dual-sill, multiple magma lens and hybrid crustal accretion hypotheses [e.g., *Shouten and Denham,* 1995; *Kelemen et al.,* 1997; *Maclennan et al.,* 2004]. In these models, which are supported by tomography, seafloor compliance, and multichannel seismic (MCS) studies [e.g., *Dunn and Toomey* 1997*; Crawford et al.,* 2002*; Nedimović et al.,* 2005*; Canales et al.,* 2009], gabbro crystallization also occurs within the lower crust and a substantial amount of the lower crust is formed in-situ.

The MOR system is partitioned into distinct morphological segments over a variety of spatial and temporal scales [e.g., *Macdonald et al., 1988*]. First- and second-order (large scale) ridge segments, bounded by transform faults and overlapping spreading centers (OSCs) respectively, have been carefully investigated and are thought to be well understood [e.g., *Macdonald et al.,* 1984, 1988; *Langmuir et al.* 1986]. First-order segments extend for 600±300 km and persist for $>5\times10^6$ years. Second-order segments extend for 140±90 km and persist for $0.5\text{-}5\times10^6$ years. However, the nature and origin of small-scale, third- (50±30 km) and fourth-order (14±8 km) ridge segments, which are proposed to last for $10^4\text{-}10^5$ and $10^2\text{-}10^4$ years respectively [e.g., *Macdonald*, 1998], is still largely debated. *Langmuir et al.* [1986], based on a study of lava compositions, and *Macdonald et al.* [1988], based on high-resolution multibeam swath mapping and acoustic imaging, drew similar conclusions about the source of the third-order ridge segmentation ascribing it to melt extraction processes in the upwelling mantle. However, the two studies disagree about the origin of fourth-order ridge segmentation. Unlike

Langmuir et al. [1986] who suggested mantle-level processes as the origin of fourth-order segmentation, *Macdonald et al.* [1988] suggested that pinching and swelling of the AMLs causes fourth-order segmentation. From major and minor analysis of glass samples, *Sinton et al.* [1991] drew similar conclusions to *Langmuir et al.* [1986] and *Macdonald et al.* [1988] that the third-order segment boundaries correspond to processes occurring in the mantle. However, *Sinton et al.* [1991] suggest that some of the fourth-order segment boundaries are not geochemical boundaries but mark termination of fissure eruptions indicating upper crustal origin. Like *Sinton et al.* [1991] but based on the study of along-strike axial hydrothermal activity, *Haymon et al.* [1991] propose that the origin of the fourth-order segmentation is within the upper crust and related to diking processes. Results from more recent high-resolution shipboard multibeam studies by *White et al.* [2002] suggest that the third-order segmentation is controlled by the AML while the fourth-order segmentation seems to be controlled by diking in the upper crust, as proposed by *Sinton et al.* [1991] and *Haymon et al.* [1991].

Controlled source seismic studies of the crust and upper mantle were employed to image ridge structures at depth and address the ambiguity of the origin of small-scale segmentation. Results from tomography studies done by *Dunn et al.* [2000] and *Toomey et al.* [2007] indicate that the origin of both third- and fourth-order segmentation is related to the dynamics of melt generation and transport from the mantle rather than to the tectonic activity, in agreement with *Langmuir et al.* [1986]. However, from interpretation of 2D MCS data, *Carbotte et al.* [2000] show that there is linkage between fourth-order tectonic segmentation and upper crustal magma plumbing system [*Carbotte et al.,* 2000], which is similar to the inference made by *Macdonald et al.* [1988]. The

causal relationship between mid-crustal magma reservoir and small-scale segmentation was further tested by analysis of high-resolution reflection images of the AML from Siqueiros to Clipperton Transform using modern swath 3D MCS data [*Carbotte et al.,* 2013]. This study showed that the crustal magma body is partitioned into segments 5-15 km long coinciding with the fourth-order ridge segmentation further confirming the linkage between fourth-order tectonic segmentation and upper crustal magma plumbing system.

Here we hypothesize that MTZ character and crustal thickness reflect the style of crustal accretion, and that the mode of accretion can vary along axis possibly from one small-scale ridge segment to another. All of the multiple magma body accretion models call for magma sills within the MTZ suggesting a thicker and more complex crust-mantle transition than that associated with the gabbro-glacier model. If the melt extraction processes in the upwelling mantle are at the origin of the small-scale ridge segmentation, as proposed by most authors for the third-order and by some for the fourth-order segmentation, then it is possible that the variations in the melt delivery between adjacent segments are also reflected in variations in the MTZ character and crustal thickness. To test this, we carry out a detailed analysis of the crustal thickness and the MTZ character along the EPR from 9˚42'N to 9˚57'N. For this analysis, we use state-of-the-art 3D MCS dataset acquired in summer 2008 on *R/V Langseth* and covering 658 km^2 [*Mutter et al.,* 2009]. This is the first full, multi-source and multi-streamer 3D MCS dataset collected over a MOR environment. Examination of the formed high-resolution 3D reflection cube provides new constraints and insights on the crustal thickness, fine-scale ridge segmentation, and style of crustal accretion along this section of the EPR.

2.3 Study Area

Located in the Pacific Ocean about 900 km southwest of Mexico, the study area covers the fast-spreading EPR (11 cm/yr full rate [*Carbotte and Macdonald,* 1992]) between 9˚42'N and 9˚57'N (Figure 2.1). In the east-west direction, the survey extends on both ridge flanks out to about 10 km away from the ridge axis, or to crustal ages of ~180 Ka as the spreading rate did not change during the last ~0.73 Ma [*Carbotte and Macdonald,* 1992].

The study area represents a part of the second order EPR segment that is bounded to the south by the OSC at ~9˚03'N and to the north by the Clipperton transform fault at ~10˚10'N [*Macdonald et al.,* 1984, 1992], which are second and first order ridge discontinuities respectively. Within the study area, a third order discontinuity is identified extending from 9°56'-9°58'N [e.g., *White et al.,* 2006], as well as a number of smaller discontinuities including one at 9°43'-9°45'N that has been variously interpreted as a third- or fourth-order offset [*White et al.,* 2002; 2006]. Other fourth-order discontinuities have been identified at ~9°49'N and ~9°51.5'N [*Haymon et* al., 1991; *White et al.,* 2002; 2006*; Haymon and White,* 2004; *Carbotte et al.,* 2013]. *White et al.* [2006] provide an alternative location of the fourth-order discontinuity centered at 9˚51.5'N at 9˚53'N (Figure 2.1).

An axial mid-crustal magma lens is identified along the whole length of the EPR from the OSC at 9˚03'N to the Clipperton transform, suggesting that the whole area is an active magmatic system [e.g., *Kent et al.,* 1993]. Nevertheless, a third-order discontinuity at 9˚37'N [*Smith et al.,* 2001], just south of the study area, appears to mark a magmatic and hydrothermal boundary.

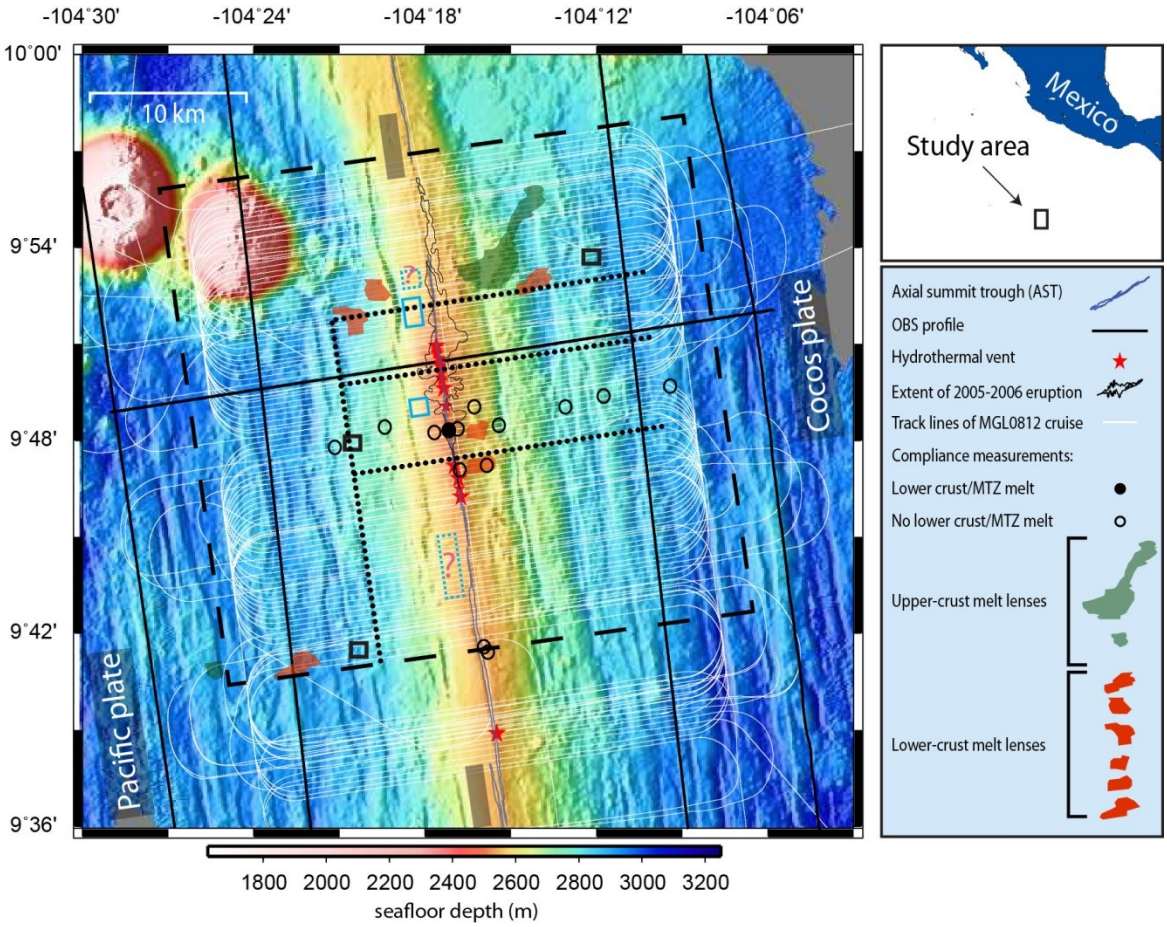

Figure 2.1 Ship track for cruise MGL0812 is shown using thin white lines superimposed over the EPR bathymetry (color background) between 9˚36'N and 10˚N latitude. Dashed box outlines the extent of the area of 3D MCS coverage analyzed for this study. Three open black squares show the location of the CMP supergathers presented in Figure 2.3. Dotted lines show the surface trace of in-lines and cross-lines from the 3D migrated stack presented in Figure 2.4. Solid lines are OBS profiles are from the 1997 UNDERSHOOT experiment [*Toomey et al.,* 1997]. Hydrothermal vent locations are from *Haymon et al.* [1991] and the Marine Geoscience Data System. Axial summit trough (AST) is as interpreted by *Soule et al.* [2007]. Extent of 2005-2006 eruption is from *Soule et al.* [2009]. Compliance measurements (circles) are from *Crawford and Webb* [2002]. Third-order segment boundaries are shown with filled gray rectangles; fourth-order segment boundaries are shown with open blue rectangles; debated third- and fourth-order segment boundaries are shown with dashed blue rectangles. Locations of discontinuities are from *Haymon et al.* [1991], *White et al.* [2002; 2006], and *Carbotte et al.* [2013]. Off-axis magma lens locations are from this study.

Based on studies performed on lava chemistry, lava age and volcanic morphology, it is suggested that the ridge north of this discontinuity has recently been more magmatically robust than its southern counterpart [*Smith et al.,* 2001]. This section of the EPR north of

9˚37’N is characterized by a broad axial cross-sectional area, shallower ridge axis, numerous hydrothermal vents and the presence of a mid-crustal axial magma body, all of which are indicative of high magma budget [*Scheirer and Macdonald,* 1993*; Macdonald et al.,* 1984*; Haymon et al.,* 1991*; Detrick et al.,* 1987]. Seafloor volcanic eruptions of 1991 [*Haymon et al.,* 1993] and 2005-2006 [*Tolstoy et al.,* 2006] at 9˚50’N further suggest increased magma volume/presence in this region of the EPR where the hottest magma erupts coincident with the shallowest region along the ridge axis which is located between 9˚48’N and 9˚50’N [*Batiza and Niu,* 1992].

2D MCS experiments conducted from the early 1980s to the mid 1990s [*Herron et al.,* 1980; *Detrick et al.,* 1987; *Harding et al.,* 1993; *Kent et al.,* 1993] over the EPR between 9˚N and 10˚N resulted in images of a narrow mid-crustal AML (about 0.5 to 1.2 km wide and 10-50 m thick [e.g., *Kent et al.* 1993]) that resides 1.4-1.9 km below the seafloor. Extreme values of 0.25 and 4 km for the width of AML are found outside our 3D box, at ~9˚35’N and ~9˚18’N respectively [*Kent et al.,* 1993]. Moho transition zone melt accumulations have been identified from compliance measurements (Figure 2.1) at 9˚48’N [*Crawford and Webb,* 2002]. Intra-crustal off-axis magma lenses (OAMLs) have also been reported in our study area (Figure 2.1) [*Canales et al.,* 2012] using a subset of the 3D MCS data analyzed for this work. The investigators interpret intra-crustal reflection events as indicative of partially molten OAMLs based on both MCS and ocean bottom seismometer (OBS) data. The MCS data show reversed polarity for the OAML events, just as they do for the mid-crustal AMLs, indicating a negative impedance contrast. The OBS data show high attenuation of seismic arrivals that travelled through the crust where OAMLs occur. The OAMLs described by *Canales et al.* [2012] and

found in the upper crust from 9˚52.5'N to 9˚56'N are located 5.5 km to 7 km east of the ridge axis at depth of 2.1 to 2.3 km below seafloor (bsf). A deeper OAML, found in the same area at 4.2 km below the igneous basement, has also been described by *Canales et al.* [2012].

Velocity and thickness of seismic layer 2A, the shallowest part of the igneous oceanic crust, have been determined in the study area and surrounding regions by the same 2D MCS data used to study the AML and crust in general [e.g., *Harding et al.,* 1993], but also from near-bottom refraction data [e.g., *Christeson et al.,* 1992], OBS tomography [e.g., *Toomey et al.,* 1990; *Tian et al.,* 2000; *Sohn et al.,* 2004], and expanding spread profile (ESP) refraction studies [*Vera et al.,* 1990]. Based on the 1D models derived from on-axis ESP experiments from 9˚32'N to 9˚35'N, the P-wave velocity of the uppermost (100-200 m) crust is low (<2.5 km/s) and increases rapidly to ~5 km/s at ~500 m below the seafloor [*Vera et al.,* 1990]. The 2D MCS data from 9˚40'N to 9˚50'N show that the thickness of layer 2A varies from ~250 m at the ridge axis to >500 m at places away from the ridge axis [*Harding et al.,* 1993]. Based on this MCS study, the average layer 2A thickness in our study area and up to a distance of 10 km away from the axis is ~460 m. The asymmetric cross-axis velocity of layer 2A, with the velocities on the western flank slower than on the eastern flank, is observed at 9˚50'N from OBS data [*Tian et al.,* 2000]. An OBS refraction experiment conducted at 9˚50'N using near-bottom source [*Sohn et al.,* 2004] further constrains the fine-scale seismic structure of layer 2A. This low-velocity layer (P- and S-wave velocity of 2.20 km/s and 0.42 km/s, respectively), made of extremely porous lava and basalt breccia, has a thickness that increases systematically

from ~20 m on the rise axis to ~120 m at a distance of ~1.5 km to the east and ~0.5 km to the west of the ridge axis.

2D MCS data collected over young oceanic crust contain a prominent reflection event at about 2 s two-way traveltime (TWTT) below the seafloor that is interpreted as the Moho reflection event [e.g., *Stoffa et al.,* 1980*; Herron et al.,* 1980*; Barth and Mutter,* 1996]. Seismic modeling of this event shows that the Moho is not a single discontinuity but rather a transition zone (MTZ) with both positive velocity gradients and varying thicknesses [*Vera et al.,* 1990]. Seismic profiling carried out along the EPR at 14˚S shows that, where the Moho reflection response is imaged, the seismic character of Moho varies from impulsive, shingled, to diffusive [*Kent et al.,* 1994]. This spatial and temporal variability of the Moho reflection response was interpreted to be caused by a heterogeneous interface between the crust and the mantle. A similar pattern for the Moho reflection response was identified within the 8˚50'N to 9˚50'N EPR area [*Barth and Mutter*, 1996].

The thickness of the igneous crust for the 8˚50'N to 9˚50'N area has been computed by *Barth and Mutter* [1996] using 2D MCS data and for the area between Clipperton and Siqueiros transform faults by *Canales et al.* [2003] using OBS data. The computed thickness based on reflection profiles about 3.5 km apart and a few 1D ESP velocity models of *Vera et al.* [1990] was mostly done for crust up to ~300 Ka old. The results show that the crustal thickness variation for the 8˚50'N to 9˚50'N latitude range is ~2.6 km, with the thinnest crust at 5-5.5 km between ~9˚40'N and 9˚50'N and the thickest crust 7-7.3 km immediately north of the OSC between 9˚15'N and 9˚20'N. The crust gradually thickens to the south between these two locations, and then thins south of

9˚15'N-9˚20'N to ~6.5 km at 8˚50'N. The majority of this crustal thickness variation was attributed to layer 3.

The crustal thickness between 8˚15'N and 10˚10'N (Siqueiros and Clipperton transform faults respectively), computed by simultaneous inversion of OBS refraction and wide-angle Moho reflection arrivals [*Canales et al.,* 2003], is based on four ridge-parallel profiles evenly distributed on each side of the ridge axis and two ridge-perpendicular velocity profiles. Two of the ridge-parallel profiles are located on ~150 Ka old crust and the other two velocity profiles are located on ~300 Ka old crust. The ridge-perpendicular velocity profiles at ~8˚35'N and ~9˚15'N are ~75 km apart. The computed mean crustal thickness between the Siqueiros and Clipperton fracture zones is 6.7-6.8 km. The crust thickens away from the Siqueiros and Clipperton transforms, to the north and south respectively, reaching maximum thickness of 7.3-7.8 km north of the 9˚03'N OSC at 9˚15'N, about midway between the transforms. This excludes measurements over seamounts where the crust can be anomalously thick. The thinnest crust (5.3 km) is found within the Siqueiros transform. From 9˚15'N to 9˚50'N, the OBS results show a smaller crustal thickness variation (1.3-1.8 km) in comparison to the crustal thickness variation for this same area computed from 2D MCS data (2.3 km) [*Barth and Mutter*, 1996]. For the study area investigated in this work, the mean crustal thickness to crustal age of 300 Ka is ~5.5 km based on the 2D MCS results [*Barth and Mutter,* 1996] and to crustal age of 225 Ka is ~6.8 km based on the OBS data [*Canales et al.,* 2003].

2.4 Data

2.4.1 Data Acquisition

In summer of 2008 we conducted a 3D MCS survey over the EPR between 9˚35.6'N and 9˚57'N onboard R/V Marcus Langseth during expedition MGL0812. Two areas of 3D coverage separated by a 3.3 km gap were acquired. The larger, northern area (~714 km2) that is investigated in this study is located between 9˚42'N and 9˚57'N (Figure 2.1). This area is covered with 94 primary, 11 infill and 10 reshoot sail lines. Sail lines are 24 km long, separated by 300 m, and have an azimuth of 82˚ from North. Four 6-km-long hydrophone streamers separated by 150 m were towed at a depth of 10 m along sail lines. Each streamer was composed of 468 receiver-array groups spaced every 12.5 m, for a total recording of 1872 channels per shot. Recording time was 10240 ms and sample rate was 2 ms. Two seismic sources, each comprised of two linear arrays of nine airguns with a total volume of 3300 in3 were towed at a depth of 7.5 m. The two sources were fired in an alternating (flip-flop) mode every 37.5 m resulting in eight CMP profiles per sail line. These CMP lines are separated by 37.5 m. The total number of shots fired in the northern area is 73,737 and total number of data traces recorded is 138,053,664. Shot and receiver positions were determined with a 1 and <3 m horizontal accuracy respectively, through analysis of global positioning system (GPS), acoustic transponder, and streamer compass information.

The geometry of the survey yields CMP bins that are 37.5 m wide and 6.25 m long in cross-ridge-axis and along-ridge-axis directions, respectively. To achieve full nominal fold of 40 traces per CMP bin for the central 16 km-wide area about the ridge axis (~451 km2), sail lines included 4 km run-in and run-out. Nevertheless, fold distribution deviated

from the nominal value due to streamer feathering, survey gaps caused by marine life, and technical shutdowns. The average feathering was ±5˚ requiring minimal infill. Gaps in the survey due to marine life and technical shutdown were minimized with reshoot lines. Additional details on data acquisition are given in Mutter et al. [2009].

2.4.2 Data Analysis

The survey geometry is developed by using shot and receiver locations to compute true source-receiver offsets and midpoint positions for all seismic data traces. The data traces are then assigned to nominal 37.5x6.25 m CMP bins. The prestack processing sequence applied to the data starts with bandpass filtering (1-6-200-220 Hz) and frequency spectrum balancing, both 1D processes, and continues with 2D filtering of shot gathers. Both filters are used to remove ambient and low frequency cable-tow noise. The frequency spectrum balancing is applied only to the low frequency range from 0 to 14 Hz to remove a spike with peak frequency between 4 and 6 Hz.

For 2D filtering, we evaluated the effectiveness of available algorithms by first computing a synthetic shot gather in the frequency domain using a finite-difference solution of the acoustic wave equation [*Pratt et al.,* 1990]. A P-wave velocity and density model for the EPR is required for this process. We used a 1D hybrid velocity model that includes a) a velocity-depth variation from seafloor to AML from the ESP5 velocity function of Vera et al. [1990]; b) a linear velocity gradient layer to model layer 3 starting from 5.5 km/s just below the AML and increasing to 6.5 km/s at the Moho; c) a step velocity function of 8 km/s to model mantle. This velocity model resulted in both AML and Moho reflections, which allowed us to test the effectiveness of available 2D filters at different traveltimes and signal-to-noise (S/N) ratios. A minimum phase Keuper wavelet

with a bandwidth from 0 to 50 Hz was used as the source function in this test. Pure ambient and streamer noise recorded during the data acquisition was added to the modeled shot gather to simulate a typical shot gather for the survey.

Test results on this shot gather show that the LIFT method [*Choo et al.,* 2004], simplified so as not to include the signal-add-back step, removes noise efficiently without taking out signal. Because much of the dominant low-frequency cable noise is in 0 to 15 Hz range, the shot gathers were divided before filtering into low- and high-frequency bands, that is 1 to 10-15 Hz and 15-20 to 220 Hz respectively, with an intermediate band represented by the difference between the original data and the low and high frequency bands. In the simplified LIFT sequence, a frequency-wavenumber (FK) filter is applied to the low frequency band of the data to suppress ambient and streamer noise followed by applying a 2D median filter to all frequency ranges to suppress amplitude spikes. All frequency bands are combined after 2D filtering to form the filtered shot gathers (Figure 2.2). Offset-dependent spherical divergence correction to compensate for geometrical spreading, surface-consistent amplitude balancing to normalize abnormally high/low shot and channel amplitudes, and trace editing follow in the processing sequence. After noise cleanup and amplitude normalization are completed, Moho reflection is in most cases still challenging to identify on individual CMP bin gathers so they need to be combined into CMP bin supergathers. Although visible on many and strong on some CMP supergathers (Figure 2.3), the Moho reflection on prestack gathers is not strong enough and continuous enough for a systematic normal moveout (NMO) velocity analysis. Therefore, three 3D velocity models were developed for stacking the data by hanging existing 1D velocity functions from the seafloor.

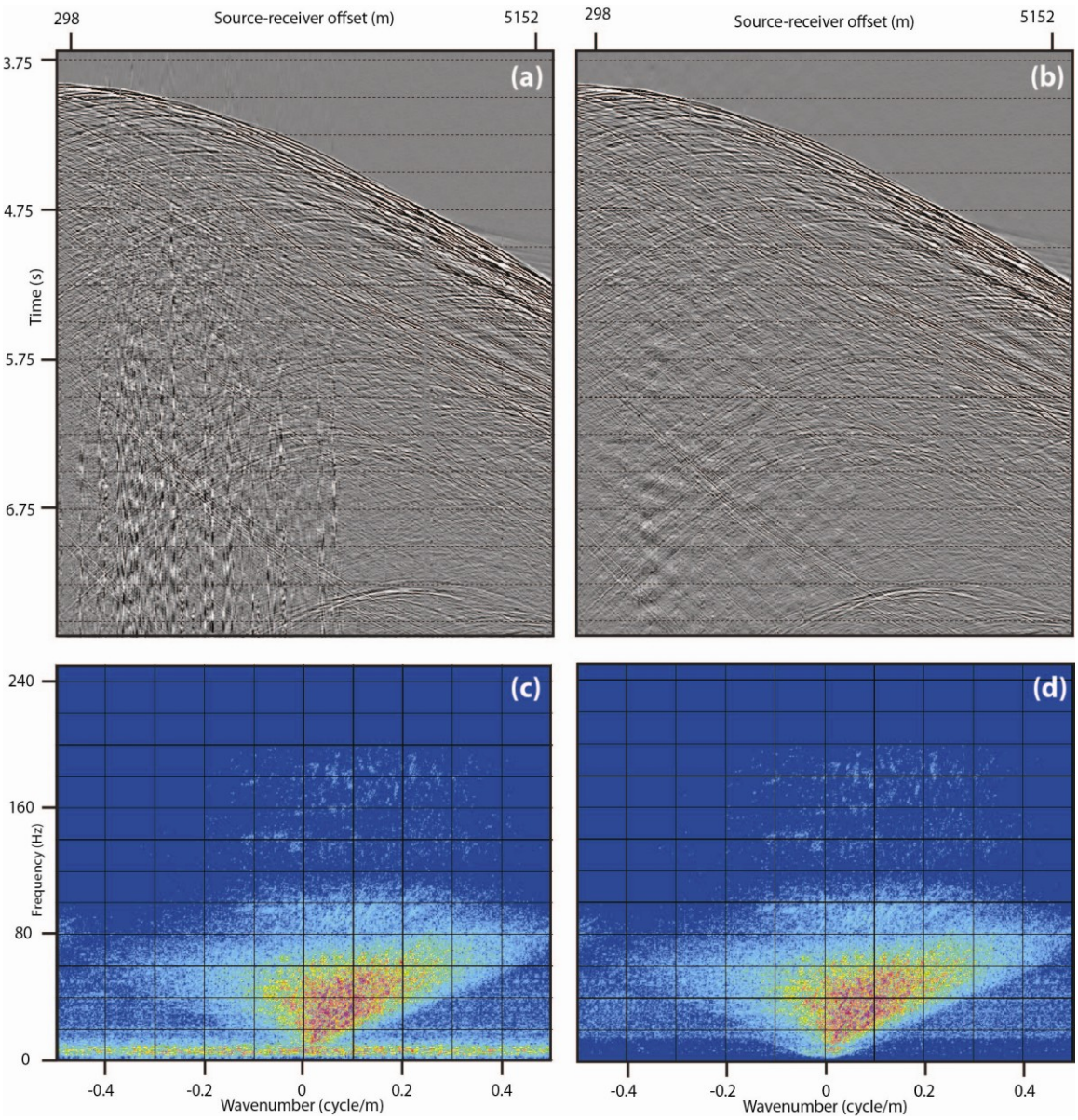

Figure 2.2 Noise suppression on shot gathers by application of simplified LIFT method. Top: shot gather before (a) and after LIFT (b). Bottom: frequency-wavenumber spectrum (c) and (d) corresponding to (a) and (b), respectively. Level of streamer and ambient noise is high as this shot is recorded when turning onto a sail line.

The stack volumes produced in this way are based on the ESP5 function [*Vera et al.,* 1990] determined from axial data, the ESP1 function [*Vera et al.*, 1990] determined using data collected ~10 km off the axis, and cross-axis OBS velocity profile at 9˚50'N [*Canales et al.,* 2012]. Common midpoint bin gathers were then NMO corrected,

stretched far offset arrivals were muted, and these gathers were summed to form stacked 3D image volumes. The maximum offset used in CMP bin gathers for stacking the AML event was ~2.7 km and the maximum offset range that resulted in the best overall image for Moho event was 4.5 km. Stacking the full offset range of CMP bin gathers (~6 km) at Moho level led to poorer images of the Moho reflection at some locations likely because the velocity models did not fully flatten this event. The 3D stack volume produced using the ESP1 velocity function provided the best overall image of all structures, including the AML, despite the velocities being extracted from off-axis data.

Poststack processing included a seafloor multiple mute to reduce migration noise followed by 3D Kirchhoff poststack time migration. The 3D migration velocity model was produced by hanging from the seafloor the 1D ESP1 velocity function of *Vera et al.* [1990] and converting it to RMS velocity. Time-variant bandpass filtering and time-variant balancing were applied to the migrated stack volume (Figure 2.4). For imaging the layer 2A/2B boundary, the prestack processing is identical up to the velocity analysis. Normal moveout velocities that flatten the retrograde part of 2A refraction are then chosen and the data are again stacked using 1600-3550 m offset range. Stacking velocity for layer 2A gradually increased from 1580 m/s on the ridge axis to some 100 m/s higher stacking velocity on the ridge flanks, at the outer edge of the 3D volume. The layer 2A 3D stack volume was migrated in the in-line and cross-line direction and unwanted parts of the new image volume were zeroed to extract only the layer 2A event.

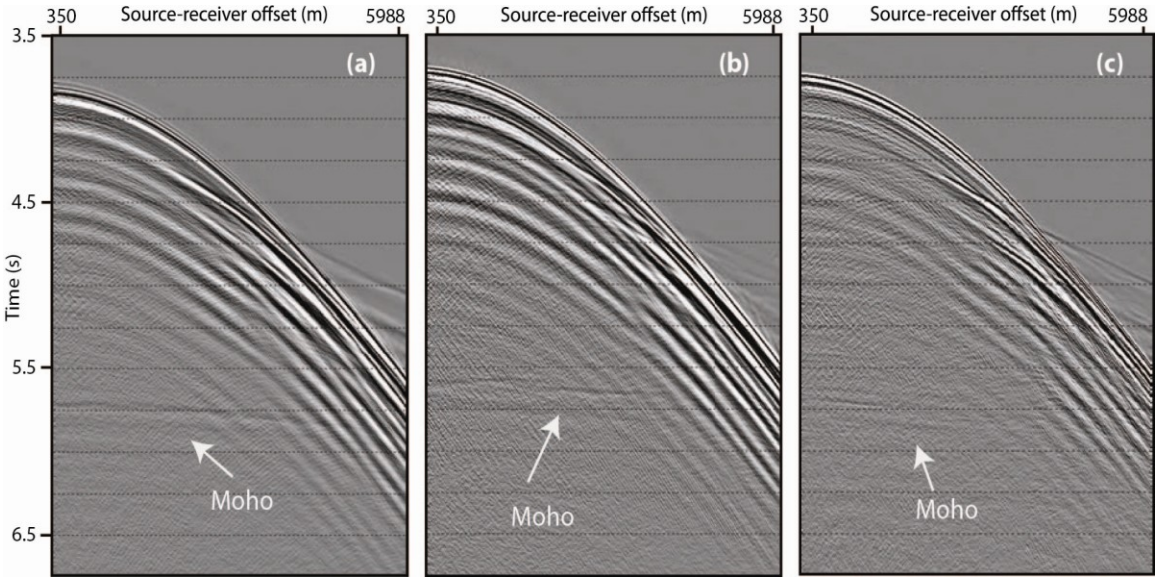

Figure 2.3 Variations in the Moho reflection strength and character on CMP bin supergathers: (a) Strong impulsive Moho; (b) Moderate strength impulsive Moho; (c) Moderate strength diffusive Moho. CMP supergathers for the impulsive Moho were constructed ~7 km from the ridge axis on the Pacific Plate at (a) 9˚42'N and (b) 9˚48'N. CMP supergather for the diffusive Moho was constructed at ~10 km on the Cocos Plate at ~9˚54'N. Note that the Moho reflection strength and character are defined on the migrated stack volume and that the shingled Moho has the same appearance on CMP supergathers as the impulsive Moho. Where the Moho reflection is weak in the stacked volume, it is not visible on CMP supergathers. For creating CMP supergathers at impulsive and shingled Moho areas, CMP bin data around the target gather and common to 40 inlines and 200 crosslines were combined. This means that CMP bin data from 1250x1500 m area were presented as one large gather. Number of crosslines used at diffusive area was reduced to 50 because of the more rapid spatial variation of the reflection response of a diffusive Moho that results in negative interference and cancelation of the signal.

2.5 Results

The primary result of this work is a 714 km^2 3D migrated stack volume of the EPR between 9˚42'N and 9˚57'N, of which some 658 km^2 are considered to have satisfactory S/N ratio for interpretation because of the sufficiently high CMP bin fold and even offset distribution. This 3D image volume allows for detailed mapping of the seafloor and MTZ reflections (Figure 2.4), which are needed for the study of the MTZ character and crustal thickness presented here. To facilitate the discussion, we also pick the layer 2A/2B boundary and map on- and off-axis magma lenses. However, detailed analysis of the AML, OAMLs and layer 2A are beyond the scope of this work.

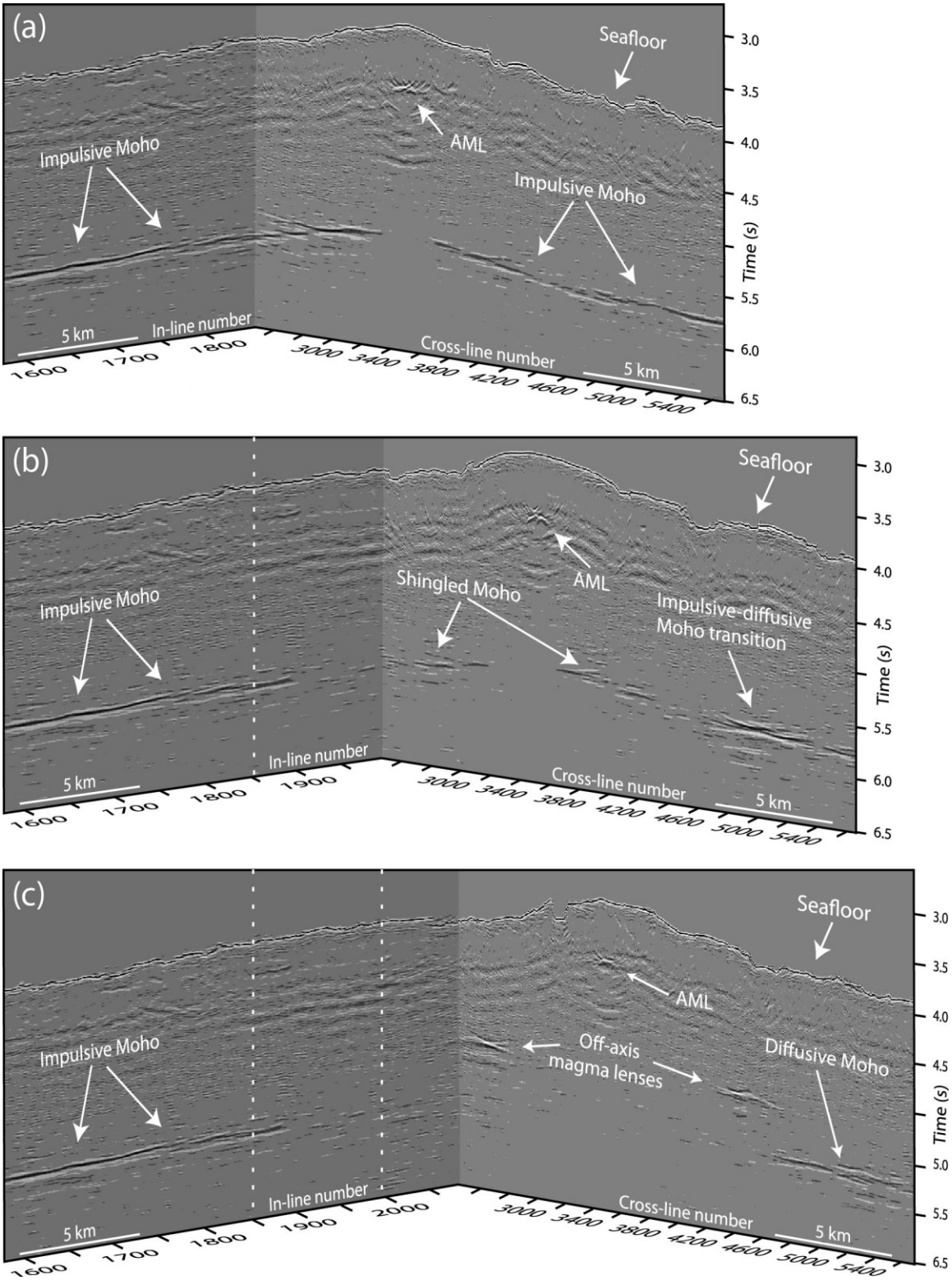

Figure 2.4 Seismic images from the 3D migrated stack volume showing reflection responses from the seafloor, AML, OAMLs and Moho. Also visible in the first second of crustal TWTT and at

lower amplitudes are low frequency (~5 Hz) reverberations most likely representing the residual bubble pulse. All three images feature the same cross-line (2500) and a different in-line which, from south to north, are: (a) 1850; (b) 1990; (c) 2090. Note the remarkable clarity of the Moho and other recorded reflections, as well as the variation in the Moho reflection response from impulsive in the south to diffusive in the north. In-lines are 37.5 m separated CMP lines in the sail line (~ENE) direction. Cross-lines, separated 6.25 m, are perpendicular to the in-lines.

2.5.1 Moho Reflection Response

Moho transition zone reflections are imaged in about 87% of the study area. Where the Moho reflection response is imageable, its strength and character vary spatially both on CMP bin supergathers (Figure 2.3) and migrated stack images (Figures 2.4 and 2.5). In terms of the Moho reflection response amplitude, we differentiate in a qualitative way between strong, moderate, weak, and absent Moho. This amplitude differentiation of the Moho reflection response was designed on and applies to the 3D migrated stack (Figures 2.4 and 2.5), but does not apply to the CMP bin supergathers (see Figure 2.3 caption for more details). In terms of the Moho reflection response character, we differentiate similar to *Kent et al.* [1994] between impulsive, shingled, and diffusive.

Thin MTZs are thought to generate the impulsive and shingled Moho reflection responses [*Brocher et al.,* 1985; *Collins et al.,* 1986; *Nedimović et al.,* 2005]. Both the impulsive and shingled Moho types are single-phase reflection responses. The difference is that the impulsive Moho response is continuous and shingled Moho response is broken in smaller sections that are vertically offset and can overlap. Where the single-phase Moho is composed of overlapping segments that resemble roof shingling (e.g., Figure 2.5), overlap between individual segments can be as large as 500-1000 m.

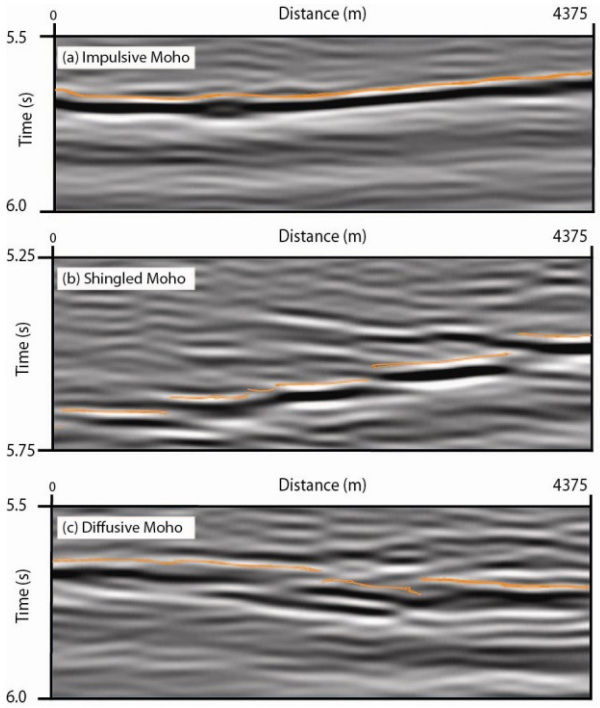

Figure 2.5 Zoom on the types of Moho reflection responses in the study area: (a) Impulsive; (b) shingled; (c) diffusive. Orange lines show the Moho reflection arrival picks.

This overlap does not represent real structure but rather a migration artifact caused by using true velocities for migration, which at these depths are high and can cause lateral smearing. Images produced using reduced migration velocities do not exhibit lateral smearing. This result was anticipated. Although it is generally agreed that normal faults at fast-spreading ridges are confined to the shallow crust [e.g., *Macdonald,* 1998], we would not expect overlaps in reflections from the same horizon even if these extensional faults extended to Moho. Thick MTZs are believed to generate the diffusive Moho type [*Brocher et al.,* 1985; *Collins et al.,* 1986; *Nedimović et al.,* 2005], which is characterized by a multi-phase reflection response.

The MTZ reflection strength and character, identified visually and assigned manually to each trace, including pick uncertainty are summarized for the whole study area in Figure

2.6. Strong Moho reflections are imaged within 39%, moderate within 25%, and weak within 23% of the study area (Figure 2.6a). Spatial distribution of on- and off-axis magma lenses is closely associated with the regions where no Moho reflections can be recognized, which cover some 7% of the study area. The challenge of imaging structures below or in the vicinity of magma lenses has long been known with only one study claiming to have imaged Moho reflections beneath the ridge axis [e.g., *Singh et al.,* 2006]. Areas with magma strongly attenuate and disperse seismic energy to the point that it still remains unclear at which age the reflection Moho forms. In *Kent et al.* [1994] and *Barth and Mutter* [1996] studies of the EPR, Moho was imaged within 1-2 km from the AML edge. With standard processing sequence applied, Moho reflections were not imaged anywhere below the ridge axis. However, our results show that the distance from the ridge axis at which the Moho reflections become weak and disappear varies with latitude. From ~9˚42'N to ~9˚48.5'N and from ~9˚53'N to ~9˚57'N the Moho reflection is imaged until about 450 m from the ridge axis. The Moho reflection gap beneath the ridge axis increases to ~1050 m from ~9˚48.5'N to ~9˚50'N and to 2400 m from ~9˚50'N to ~9˚52.5'N on the Pacific plate and 1250 m on the Cocos plate. For ~1 km along-axis distance north of ~9˚52.5'N, Moho reflections cannot be imaged on the Cocos plate until ~5 km away from the axis. The last two areas described, covering from ~9˚50'N to ~9˚53'N, show asymmetry between the opposing flanks in terms of the distance from the ridge axis at which Moho reflections become imageable. The only region away from the ridge axis where Moho reflections are not imaged lies between ~9˚50'N to ~9˚56'N, where most and where largest off-axis melt lenses are concentrated (Figure 2.6a).

Impulsive MTZ reflection response is imaged within 41%, shingled within 29%, and diffusive within 17% of the study area (Figure 2.6b). The map in Figure 2.6b was formed by, for the purpose of this study, assuming that if the Moho reflection response is single-phase and continuous for ≥2 km, the Moho type is impulsive. If the Moho reflection response is single-phase and segmented by vertical offsets into sections ≤2 km long, the Moho type is shingled. All multiphase MTZ reflection responses are representative of the diffusive Moho type. Figure 2.6c shows the uncertainty in Moho reflection picks. More than half of the area where Moho reflections are imaged (46% of the study area) has picks of low uncertainty, with smaller portions represented with medium and high uncertainty (24% and 17% of the study area, respectively). We assign 16, 66 and 116 ms picking error for zones of low-, mid- and high-uncertainty. Substantial portion of the high uncertainty picks are from the edges of the picked area, where migration can produce lateral smearing of the Moho reflection signal.

From ~9˚42'N to ~9˚48'N on the Pacific Plate, Moho reflection response appears as an impulsive single-phase event that dips away from the ridge axis. Reflection strength and S/N ratio are high and the Moho reflection is easy to identify. The Moho reflection is continuous in segments >3 km with small (<150 m) disruptions between them. Moho reflection picks have a low uncertainty in this latitude range.

From ~9˚48'N to ~9˚56'N on the Pacific plate, Moho reflection character is at marked difference with the same at southern latitudes on this plate. From ~9˚48'N to ~9˚50'N, Moho reflection changes from a continuous, single-phase event to vertically offset and overlapping discontinuous event with segments ≤2 km long, which we interpret as shingled Moho.

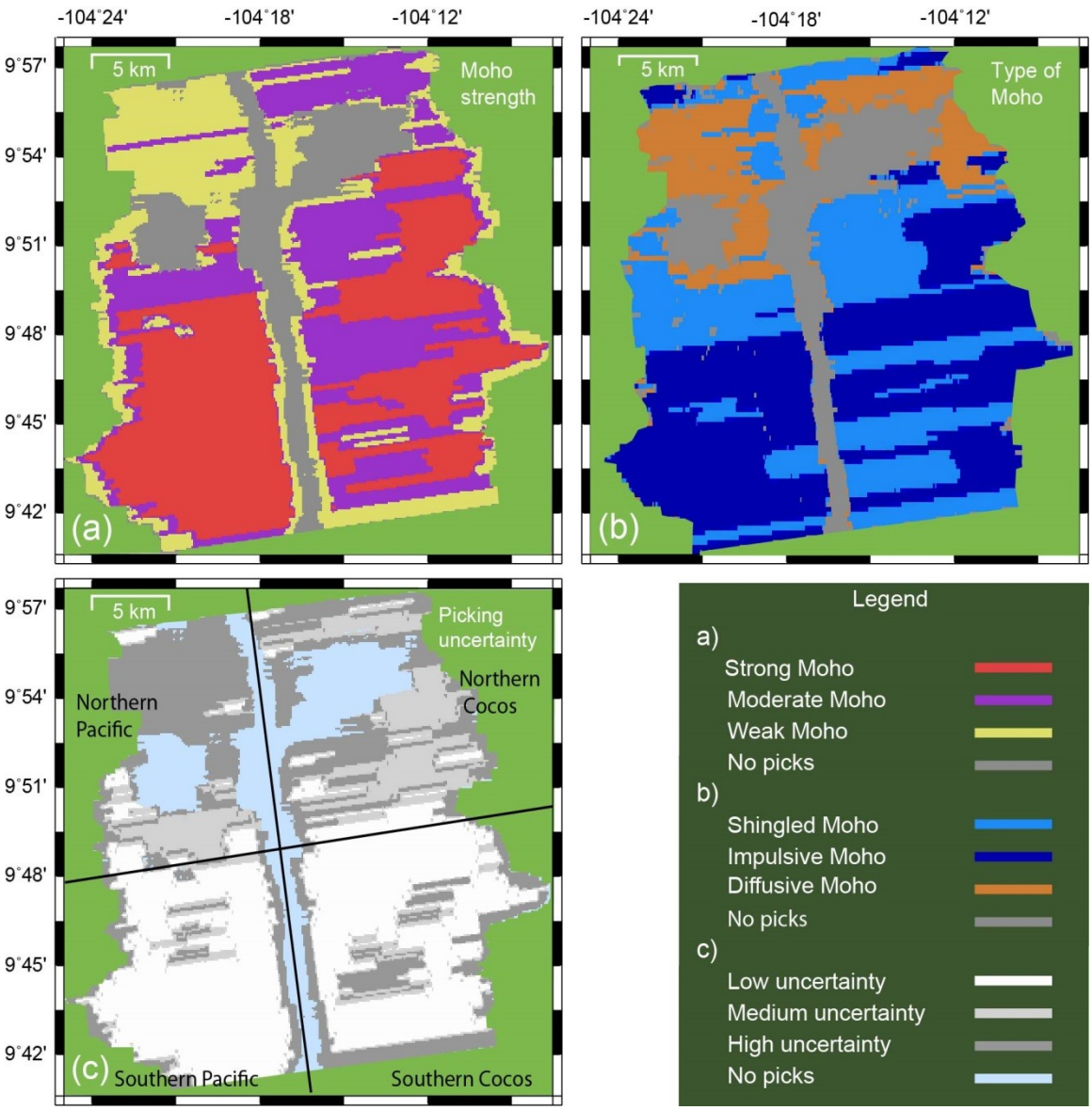

Figure 2.6 MTZ reflection response maps showing: (a) Moho reflection strength; (b) Moho reflection type; (c) pick uncertainty. These maps were formed by analysis of in-lines and cross-lines extracted from the 3D migrated stack volume at every 300 m and 150 m, respectively. Thin black crossing lines in (c) divide the study area into northern Cocos, northern Pacific, southern Pacific, and southern Cocos quadrants.

At some locations, because of lower S/N ratio and overlapping segments, Moho picks are of higher (moderate) uncertainty. Further north on the Pacific plate (~9˚50'N to ~9˚56'N), seismic character of the Moho response changes from a single-phase event to a

multi-phase event, and the reflection strength weakens. The Moho reflection response is also disrupted at intervals sometimes ≤1 km. This area is characterized by the highest pick uncertainty. The area from ~9˚56'N to ~9˚57'N, at the northern edge of the 3D box, appears to be transitional with the Moho reflection response returning to mostly shingled and impulsive. However, the reflection strength and S/N ratio are variable and pick uncertainty is mostly high.

Moho reflection amplitudes are weaker and more variable across the ridge axis on the Cocos plate. The Moho reflection response alternates between shingled and impulsive from ~9˚42'N to ~9˚52'N, with the shingled Moho occurring closer to the ridge axis at ~9˚42'N to ~9˚43.5'N and from ~9˚50'N to ~9˚52'N, and the impulsive Moho appearing some 6 km away from the axis. Where shingled, Moho reflection strength is mostly lower and picking uncertainty mostly higher. From ~9˚52 to 9˚55'N Moho reflections are in large part not traceable, and where they are the MTZ reflection response is diffuse. From ~9˚55'N to 9˚57'N, Moho seismic character changes back from diffusive to impulsive.

2.5.2 Crustal Thickness

Figure 2.7 shows maps of (a) Moho reflection TWTT, (b) seafloor to Moho reflection TWTT or crustal TWTT, (c) velocity at 6 km depth below the seafloor, and (d) crustal thickness. A minimum curvature method was used for creating the gridded maps.

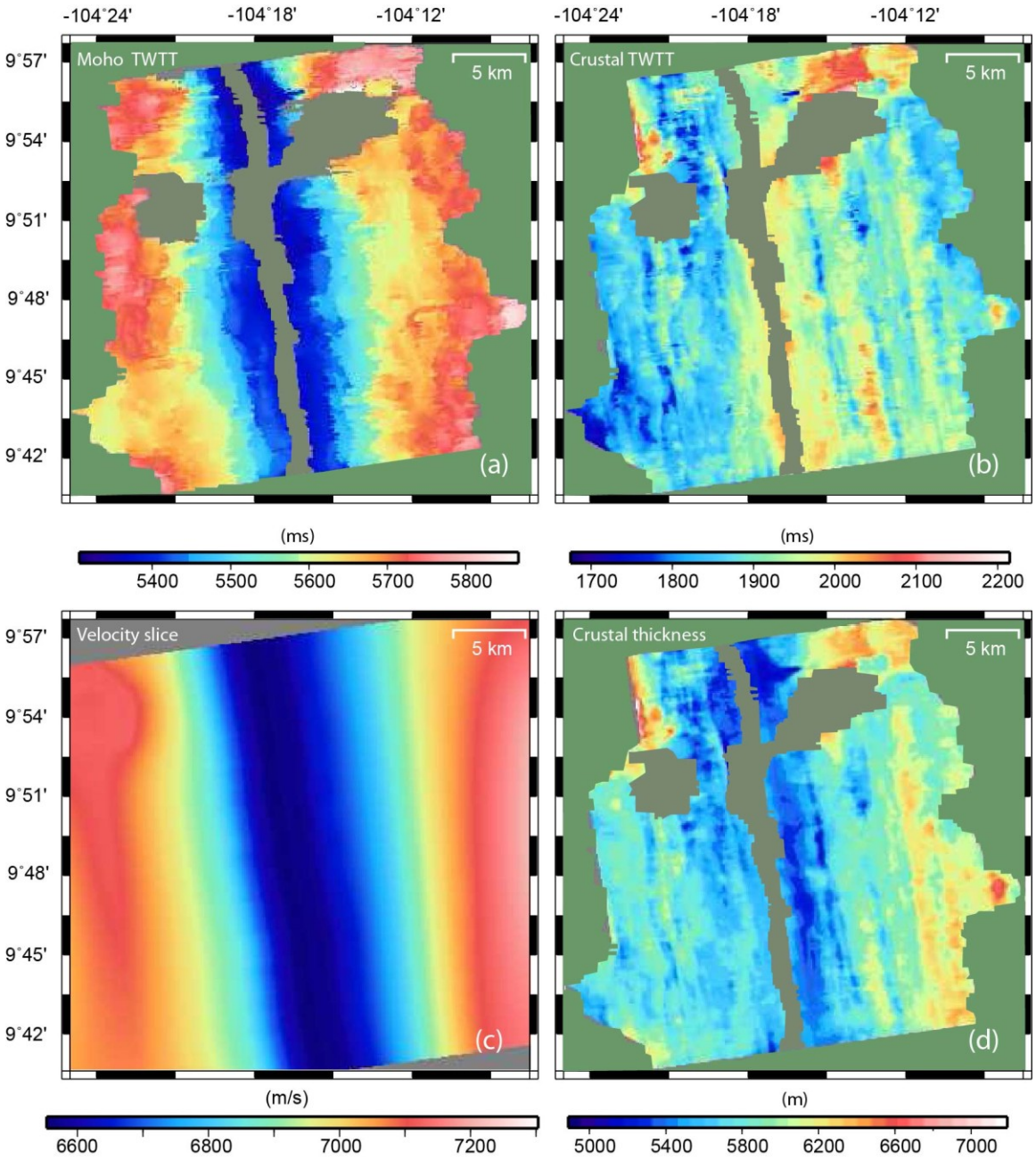

Figure 2.7 Crustal thickness variation in the study area: (a) Moho reflection TWTT map; (b) Crustal TWTT map; (c) velocity at 6 km depth below the seafloor; (d) Crustal thickness after converting smoothed TWTT values to depth using the velocity model shown in (c) and developed from the OBS profiles (Figure 2.1). These maps were formed by interpolating and extrapolating the picked Moho reflection response information for up to 700 m and 350 m between and away from the data points, respectively.

These maps cover some 87% of the study area, which corresponds to the percentage of the area where the MTZ reflections are imaged. Moho TWTTs were picked manually in great detail, on every other in-line (every 75 m) of the 3D migrated stack volume. The first negative break of the energy reflected from the Moho was chosen for picking. Because the airgun array produces a minimum phase wavelet and the marine MCS acquisition equipment is calibrated so that the first arriving energy on the records has negative amplitudes, this picking increases the true crustal TWTTs by ~18 ms, which is equivalent to the delay from the onset of arriving energy to the first negative peak. To reduce this picking-related increase in crustal TWTTs, the first negative break for the seafloor reflection arrival was also picked introducing a similar delay of ~5 ms. The magnitude of the two delays is different because of the different frequency spectrums of the signal at the top of the igneous basement and at the MTZ (i.e., dominant signal frequencies of ~50 Hz and ~14 Hz, respectively). When subtracted, the two delays yield 13 ms difference, or ~41 m assuming average crustal velocity of 6250 m/s. This systematic error in measured crustal TWTTs was removed.

Figure 2.7b shows that the largest variation of crustal TWTTs is in the across-axis direction, along the flow lines, and that the smallest variation of TWTTs is in the axis-parallel direction, along the isochrones, forming what appears to look as striping in the along axis direction. A smoothed crustal TWTT map was produced by removing the short wavelength components of the spectrum (≤250 m) from the seafloor TWTT map before subtracting this map from the Moho TWTT map, which lacks the corresponding short wavelengths. For smoothing we used a locally weighted polynomial regression filter in a 425 m wide and 225 m long window across- and along-axis, respectively. After the

smoothing, the crustal TWTT map still exhibits the same general features with maximum TWTT variation in the across-axis direction of ~200 ms/km and ~100 ms/km in the direction parallel to the ridge axis.

Figure 2.8a and Tables 2.1 and 2.2 show results of statistical and error analyses of crustal TWTT data presented in Figure 2.7b. The statistical and error analyses were carried out for the whole study area, excluding an anomalous 750-m-wide stripe region close to the Lamont seamount (upper left corner in Figure 2.7), as well as for each of the two flanks, and for the study area divided (shown in Figure 2.6c) into northern and southern Pacific and Cocos plate quadrants. Figure 2.8a shows box plots of crustal TWTT. Each box plot shows the first, second (median) and third quartile. For each box plot 99.3% of data coverage is considered and the maximum and minimum whisker length is $\pm 2.7\sigma$, which is commonly used for defining outliers. The data without outliers for both plates (99.3% of all crustal TWTTs) fall within a 330 ms time window, with half of the TWTTs (between 25^{th} and 75^{th} percentiles) falling within a 90 ms window (Table 2.2). The mean crustal TWTT varies from 1.86 s on the Pacific plate to 1.91 s on the Cocos plate, with the mean crustal TWTT of 1.89 s for the entire study area (Table 2.1). Computed standard deviation and average propagated error vary little (40-60 ms) for all plate quadrants and their combinations. When combined, the northern and southern quadrants show the same mean TWTT of 1.89 s.

Crustal thickness (Figure 2.7d) was computed by depth converting the smoothed Moho TWTT. The 2D crustal velocities used for depth conversion were developed by *Canales et al.* [2003; 2012] by simultaneous traveltime tomographic inversion of refraction and wide-angle Moho reflection arrivals recorded on four axis-parallel and one axis-

perpendicular OBS profiles (Figure 2.1) acquired as part of the Undershoot Seismic Experiment [*Toomey et al.,* 1998]. The across-axis velocity profile approximately coincides with in-line 2003 of the 3D survey. To constrain the velocity along the axis before interpolation, we used the 6-km-wide segment from the across axis velocity profile. This 6-km-wide velocity profile segment was centered at the ridge axis and projected along the axis every 150 m. The 3D velocity volume was then constructed by interpolating velocity values at known locations, the 6-km-wide strip along the ridge axis and four axis-parallel velocity profiles found at greater distance from the axis, using the minimum curvature method.

Table 2.1 Computed crustal TWTT range and mean with associated standard deviation and average propagated error for the investigated section of the EPR, Pacific and Cocos plates, and various parts of the study area.

Plate section	Range (ms)	Mean value (ms)	Standard deviation (ms)	Average propagated error (ms)
Southern Cocos	1770-2040	1910	40	40
Northeren Cocos	1770-2100	1910	60	50
Southern Pacific	1700-2010	1860	50	40
Northern Pacific	1720-2200	1860	60	60
Southern Cocos & Pacific	1700-2040	1890	50	40
Northern Cocos & Pacific	1720-2200	1890	70	50
Pacific	1700-2200	1860	50	50
Cocos	1770-2100	1910	50	40
Cocos and Pacific	1700-2200	1890	60	40

Table 2.2 Summary of additional statistical parameters on crustal TWTTs for the investigated section of the EPR, Pacific and Cocos plates, and various parts of the study area.

Plate section	25th percentile (ms)	75th percentile (ms)	75%-25% interval (ms)	Median (ms)	Lower adjacent (ms)	Upper adjacent (ms)	Upper-to-lower adjacent interval (ms)
Southern Cocos	1880	1940	60	1910	1780	2030	250
Northeren Cocos	1870	1960	90	1910	1730	2090	360
Southern Pacific	1820	1890	70	1850	1730	1990	260
Northern Pacific	1820	1890	70	1860	1720	1990	270
Southern Cocos & Pacific	1850	1930	80	1890	1730	2040	310
Northern Cocos & Pacific	1840	1930	90	1880	1720	2060	340
Pacific	1820	1890	70	1850	1730	1990	260
Cocos	1880	1950	70	1910	1790	2040	250
Cocos and Pacific	1840	1930	90	1890	1720	2050	330

Figure 2.8b and Tables 2.3 and 2.4 show results of statistical and error analyses of computed crustal thickness values presented in Figure 2.7d. The statistical and error analyses were carried out for the whole study area and its components as described for crustal TWTTs.

Figure 2.8b shows box plots of computed crustal thickness. The computed crustal thickness values without outliers for both plates (99.3% of all crustal thickness values) fall within a 1480 m window, with half of the crustal thickness values (between 25th and 75th percentiles) falling within a 360 m window (Table 2.4). The mean crustal thickness

varies from 5660 m on the Pacific plate to 5800 m on the Cocos plate, with the mean crustal thickness of 5740 m for the entire study area (Table 2.3). Computed standard deviation and average propagated error for all plate quadrants and their combinations vary from 130 to 310 m and from 220 to 370 m, respectively.

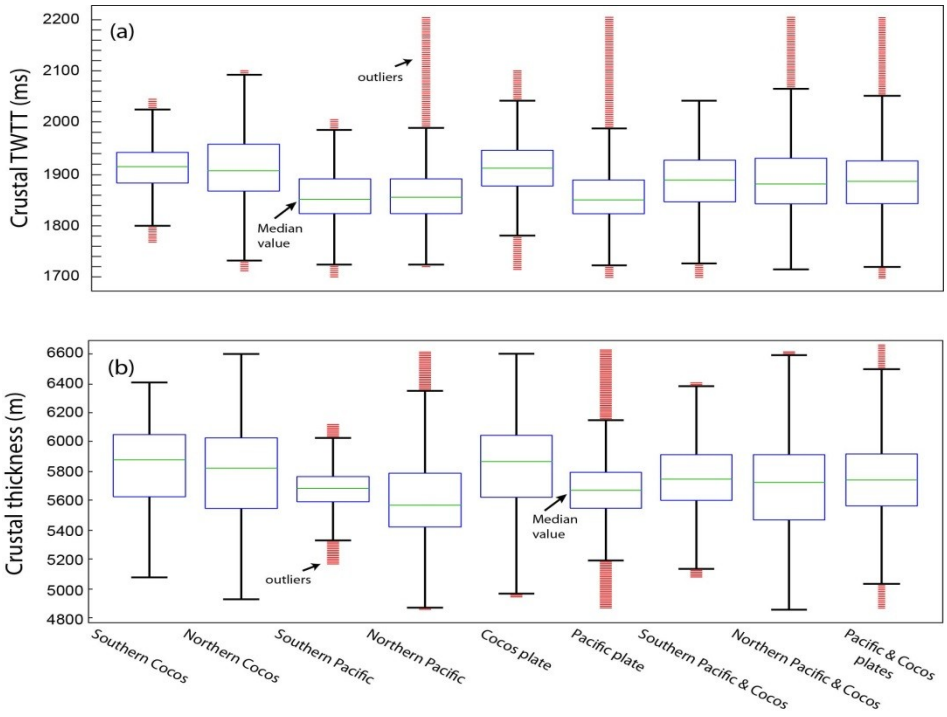

Figure 2.8 Box plots of crustal TWTT (a), and crustal thickness (b) for plate quadrants shown in Figure 2.6c, combination of them, and the entire study area. On each box, the central green line marks the median value and the upper and lower edges of the blue box are 25th and 75th percentiles, respectively. The whisker length of 1.5 corresponds to ± 2.7σ extending to the adjacent values that are the most extreme data values that are not outliers. The results of box plot in (a) and (b) are summarized in Table 2.2, and 2.3, respectively. Crustal thickness is most variable on northern Cocos plate and it is least variable on the southern Cocos plate. The median crustal thickness on the northern Pacific plate is 260 m smaller than the median crustal thickness on the northern Cocos plate. The difference in median crustal thickness between southern Pacific plate and southern Cocos plate is 180 m where the southern Cocos plate is thicker and the median crustal thickness on the Pacific plate is 190 m smaller than this value on the Cocos plate.

For error analysis we use the assigned 16, 66 and 116 ms picking error for zones of low-, mid- and high-uncertainty in determining Moho reflection arrival time (see Figure 2.6c), respectively, and for seafloor picks we assign 8 ms error. The error for the OBS-derived

velocity models [*Canales et al.,* 2012] is 200 m/s, and average crustal velocity used 6250 m/s [*Canales et al.,* 2003]. The calculated crustal thickness errors vary from 190 m to 450 m with mean value of 270 m (Table 2.3). Error values of 150-250 m, 250-350 m and 350-450 m in crustal thickness cover 50%, 26% and 11% of the imaged area, respectively.

Table 2.3 Computed crustal thickness range and mean with associated standard deviation and average propagated error for the investigated section of the EPR, Pacific and Cocos plates, and various parts of the study area.

Plate section	Range (m)	Mean value (m)	Standard deviation (m)	Average propagated error (m)
Southern Cocos	5080-6400	5830	280	220
Northeren Cocos	4940-6600	5790	310	300
Southern Pacific	5170-6120	5680	130	220
Northern Pacific	4804-6610	5620	260	370
Southern Cocos & Pacific	5080-6400	5760	240	220
Northern Cocos & Pacific	4860-6610	5710	300	330
Pacific	4860-6610	5660	190	290
Cocos	4940-6600	5800	290	260
Cocos and Pacific	4860-6610	5740	260	270

2.5.3 Layer 2A Thickness

The layer 2A was picked manually and automatically [*Carton et al.*, 2010]. For depth conversion, a layer 2A velocity model symmetric around the ridge axis was applied. The velocity for depth conversion of layer 2A was developed by analyzing CMP supergathers along in-line 1476 [*Han et al.,* 2010] using JDseis software that permits modeling gradient velocity layers [*Nedimović et al.,* 2008]. The layer 2A thickness varies from 107 to 517 m with average thickness of 230 m.

Table 2.4 Summary of additional statistical parameters on crustal thickness for the investigated section of the EPR, Pacific and Cocos plates, and various parts of the study area.

Plate section	25th percentile (m)	75th percentile (m)	%75-%25 interval (m)	Median (m)	Lower adjacent (m)	Upper adjacent (m)	Upper-to-lower adjacent interval (m)
Southern Cocos	5630	6050	420	5880	5080	6400	1320
Northeren Cocos	5550	6020	470	5830	4940	6600	1660
Southern Pacific	5600	5770	170	5700	5330	6030	700
Northern Pacific	5420	5800	380	5570	4880	6350	1470
Southern Cocos & Pacific	5600	5900	300	5750	5100	6400	1300
Northern Cocos & Pacific	5500	5900	400	5700	4800	6600	1800
Pacific	5540	5780	240	5670	5180	6130	950
Cocos	5600	6000	400	5860	4970	6600	1630
Cocos and Pacific	5560	5920	360	5740	5020	6500	1480

2.5.4 Intra-crustal Magma Lenses

On- and off-axis intra-crustal reflections with wavelet polarity reversed relative to the polarity of the seafloor event (e.g., Figure 2.4) are interpreted as partially molten magma sills. Spatial distribution of these magma sills is shown in Figures 2.1, 2.9, 2.10 and 2.11. The AML reflection persists throughout the entire section with variable width (Figures 2.9, 2.10, 2.11) [*Carton et al.,* 2010]. The width of the AML reflector is ~1 km from 9˚42'N to 9˚50'N, it decreases to ~500-700 m at 9˚50'N, and it is widest (~2 km) at 9˚51'N. From 9˚51'N to 9˚57'N, the AML width is ~1 km.

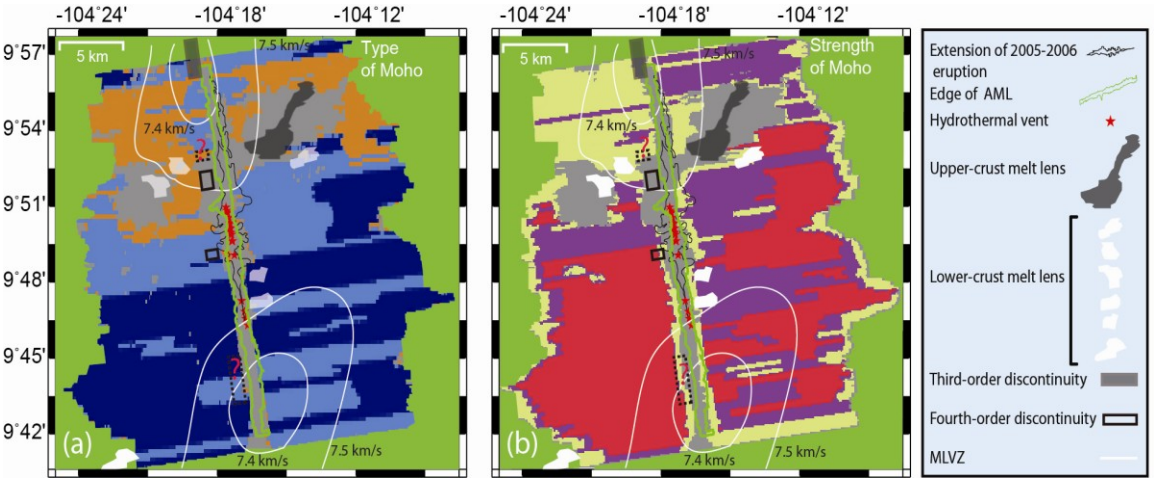

Figure 2.9 MTZ reflection character (a) and reflection strength (b) from this work, and their spatial relationship with magmatic segmentation, hydrothermal activity and mantle low velocity zones (MLVZs). Black dotted rectangles with red question marks are locations of disputed discontinuities. Location of MLVZs is from *Toomey et al.* [2007]. Edge of the AML is from *Carton et al.* [2010]. Color scale is the same as Figure 2.6. Source of other information same as in Figure 2.1.

The upper-crust magma lenses to the east of the ridge axis from 9˚52.5'N to 9˚56'N are located 0.7 to 0.8 s TWTT below seafloor (bsf) with the shallower ones closer to the ridge axis. A deeper OAML is present at ~7.5 km east of the ridge axis in the lower crust at ~1.35 s TWTT bsf. These OAMLs were reported by *Canales et al.* [2012]. The lenses to the west of the ridge axis from 9˚51'N to 9˚52'N are lower crustal magma lenses and are located ~5 km and ~3.5 km from the rise axis at 1.22 and 1.75 s bsf, respectively. Two lower-crust magma lenses are also found at 9˚48'N. These lenses are located ~1.5 km from the ridge axis at 1.8 s bsf, are ~1.2 km apart, and are ~120 ms above Moho. The lower-crust magma lens at 9˚41'N that appears at 1.64 s bsf is ~10 km from the ridge axis, and the small upper-crust magma lens at 9˚41'N is about 1 s bsf and ~16 km from the ridge axis.

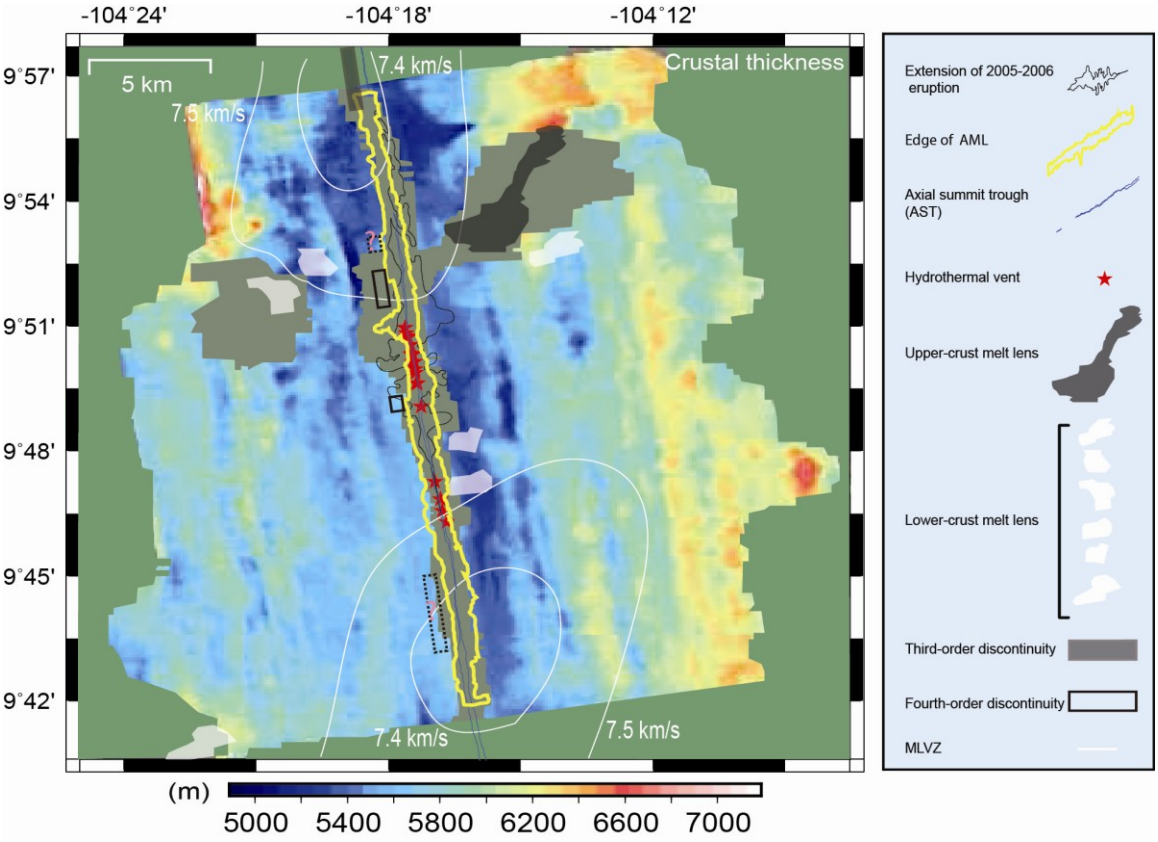

Figure 2.10 Crustal thickness from Figure 2.7d is shown together with the location of magmatic segmentation, hydrothermal activity, MLVZs, OAMLs, AML, AST and extent of 2005-2006 volcanic eruption. Black dotted rectangles with red question marks are locations of disputed discontinuities. Source of information is same as in Figures 2.1 and 2.9.

2.6 Discussion

We focus the discussion of our results on three primary topics: crustal thickness variation, ridge segmentation, and style of crustal accretion.

2.6.1 Crustal Thickness

Average crustal thickness in the study area (5740 m), on each plate (Pacific 5660 m, Cocos 5800 m), and for each of the four subareas varies only within the estimated errors (Figure 2.8b, Tables 2.3 and 2.4), suggesting an overall uniform crustal production for the last 180 Ka. Furthermore, the small estimated differences in crustal thickness between the two plates could arise from errors in the velocity models used for depth conversion. The

average P-wave velocities used for depth conversion on the Pacific plate are ~3% lower than the P-wave velocities on the Cocos plate. If the velocities on both ridge flanks were the same, then the measured average crustal thickness on the Pacific and Cocos plates would differ by only 30 m or 0.5%. Uncertainties in the velocity models used for depth conversion are large (325 m/s) due to the sparseness of the 2D OBS profiles used to form the 3D interval velocity model for depth conversion, and are about twice that of the difference in the average velocity between the two flanks.

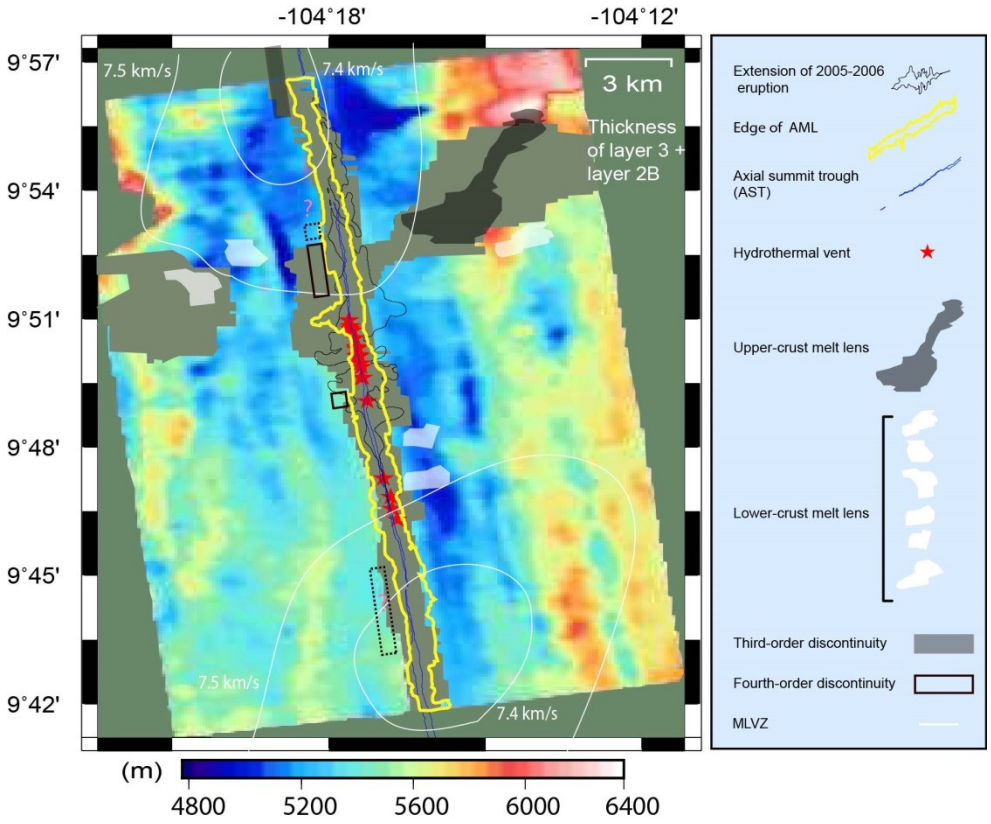

Figure 2.11 Crustal thickness from Figure 2.7d after removing layer 2A is shown together with the location of magmatic segmentation, hydrothermal activity, MLVZs, OAMLs, AML, AST and extent of 2005-6 volcanic eruption. Black dotted rectangles with red question marks are locations of disputed discontinuities. Source of information is same as in Figures 2.1 and 2.9.

Individual thickness measurements, however, can differ significantly beyond the error bounds, with the thinnest (4860 m) and thickest (6610 m) crust measured giving a crustal thickness range of 1.75 km. This value falls within the range of crustal thickness variation (1.3-1.8 km) for the second-order EPR segment between 9˚15'N and 9˚50'N derived from the wide angle OBS study of *Canales et al.* [2003], and it is about 70% of the crustal thickness variation (~2.3 km) in the same latitude range derived from the MCS study of *Barth and Mutter* [1996]. For the latitude range coincident with our 3D survey, the crustal thickness derived from the wide angle OBS study of *Canales et al.* [2003] shows variation of ~1 km. The MCS study of *Barth and Mutter* [1996] is coincident with only the southern half of our 3D survey area (9˚42'N to 9˚50'N). Within this area, their MCS derived crustal thickness shows a variation of ~1.5 km. However, the *Canales et al.* [2003] and *Barth and Mutter* [1996] studies cover a much larger surface area even within the latitude range coincident with our 3D survey because they extend to older crust. Therefore, the results of this study indicate that the variation in thickness of normal oceanic crust formed at fast spreading centers is, perhaps, even greater than that observed with earlier studies of *Barth and Mutter* [1996] and *Canales et al.* [2003], and can occur over areas comparable in size to small-scale ridge segmentation.

Taken together, the *Barth and Mutter* [1996], *Canales et al.* [2003] and this study all consistently show that the crust produced at the fast spreading EPR varies in thickness less than the crust found along an individual segment of a slow spreading center where this variation is ~4 km [e.g., *Tolstoy et al.,* 1993]. Nevertheless, the crustal thickness variation observed at the EPR is significant considering that the mantle upwelling at fast spreading centers is thought to be 2D or sheet-like [e.g., *Lin and Phipps Morgan*, 1992]

and that crustal thickness is therefore expected to be uniform. This is unlike at the slow spreading centers where the mantle upwelling is thought to be 3D with large variations in crustal thickness predicted [e.g., *Forsyth et al.,* 1992].

The average crustal thickness of 5740±270 m from the results of detailed 3D MCS reflection imaging carried out in this work is about 5% greater than the average crustal thickness of ~5.5 km estimated for our study area by *Barth and Mutter* [1996] and based on 2D MCS profiles spaced some 3 km apart. Despite the difference in thickness, the two results agree within the error limits. The average crustal thickness of ~6.8 km for the same area and based on the wide-angle OBS results of *Canales et al.* [2003] is significantly larger than the same based on the interpretation of the reflection data. This is not surprising because reflection and refraction estimates of crustal thickness are likely to differ if the transition from lower crustal to mantle velocities is through a thick MTZ, as opposed to a single step in velocity. Indeed, crustal thickness estimates based on reflection imaging are calculated down to the top of the MTZ based on the onset in TWTT of the Moho reflection, whereas refraction studies constrain the entire gradient region associated with the MTZ and thus can provide thickness values down to the base of this gradient zone. The advantage of using both methods is that they provide complementary information about the subsurface and in this particular case tell us that the average thickness of the MTZ in the study area is about 1 km. Earlier estimates of the MTZ thickness from ESP data on-axis and 10 km off-axis axis at ~9°35'N are 0.5 and 1.7 km, respectively [*Vera et al.,* 1990]. Our 1 km average MTZ thickness is consistent with these earlier results.

To investigate the effect of layer 2A on crustal thickness variations within our study area, we calculated its thickness and removed it from the total crustal thickness (Figure 2.11). Statistical analysis for the combined layer 2B and 3 thickness is summarized in Table 2.5. The propagated error is updated considering an 80 m uncertainty for layer 2A thickness [*Nedimović et al.,* 2008]. The results show that in our study area the variations in the layer 2A thickness have only a minor impact on the variations in the total crustal thickness and do not impact the conclusions reached.

We could not compute crustal thickness for the areas where the AML and the main grouping of OAMLs occur because the Moho reflection was not imaged there (Figures 2.9, 2.10, 2.11). The three likely reasons for not imaging Moho reflections in these areas are: a) Moho is not yet formed below the AML at zero or near zero crustal age; b) Moho is overprinted by the ascending melt at major OAML locations; c) standard reflection imaging methodology used in this study is not adequate for imaging the Moho beneath the AML and OAMLs, which are characterized by large lateral velocity variations and high seismic attenuation [e.g., *Dunn et al.,* 2000; *Wilcock et al.,* 1996; *Canales et al.,* 2012].

Excluding the area in the vicinity of the Lamont seamount on the Pacific plate, which for most part is not taken into account for crustal thickness computations in this work because of its anomalous nature, the thickest crust in the study area is found at ~9°56'N on the Cocos plate, some 5 km east from the ridge axis and south of the WatchStander seamounts [*Scheirer and Macdonald*, 1995]. This locally thick crust could be due to significant crustal underplating associated with seamount magmatism. The only minor seafloor expression of constructional off-axis volcanism directly above this thick crust

may indicate that the OAMLs in this area contribute mainly to accretion of the lower crust.

2.6.2 Ridge Segmentation

Existing models of ridge segmentation for our study area (e.g. Figures 2.11 and 2.12a) are based on the surface expression of the EPR, geochemical investigations, tomographic inversions, and the results from MCS reflection imaging of the AML [e.g., *Langmuir et al.*, 1986; *Macdonald et al.,* 1988, 1992; *Haymon et al.,* 1991; 2004; *White et al.*, 2002, 2006; *Toomey et al.*, 2007; *Carbotte et al.,* 2013]. Information on the MTZ character and crustal thickness derived in this work has provides a complementary, mantle melt delivery related view into the ridge segmentation. The thickness of the oceanic crust is a measure of the volume of melt extracted from the underlying mantle and has been used to study magmatic segmentation along MORs [e.g., *Forsyth,* 1992]. The thickness of the MTZ is a measure of the volume of gabbro melt within the uppermost mantle and has been associated with mantle diapirism [e.g., *Nicolas et al.,* 1996], thus also providing information on the distribution and delivery of magma along the ridge axis.

To evaluate our hypothesis, we first compute average crustal thickness for the near axial region (Figure 2.12a). The average crustal thickness was computed on crust from 0.5 to 3.0 km away from the ridge axis (or crust ~10-55 Ka old) to characterize the effect of present and recent segmentation processes on crustal thickness [e.g., *Dunn et al.,* 2000]. To remove the potential bias from variations in Layer 2A thickness, which varies along the axis in the study area [*Tian et al.,* 2000; *Sohn et al.,* 2004], the crustal thickness is shown with and without layer 2A (Figure 2.12a). We then calibrate our approach through search for crustal thickness and MTZ character fingerprints of third- and fourth-order

segment discontinuities. This is done by analyzing variations in both of these parameters (Figures 2.9 and 2.12a) along the undisputed segment boundaries of the most recent models for our study area [e.g., *White et al.*, 2002, 2006; *Haymon et al.,* 2004; *Carbotte et al.,* 2013]. Finally, by using the inferred crustal thickness and MTZ character signatures of the undisputed third- and fourth-order segment discontinuities, we re-evaluate the disputed discontinuities and evaluate other changes in crustal thickness and MTZ character along the ridge axis.

Table 2.5 Computed crustal thickness range and mean after removing layer 2A with associated standard deviation and average propagated error for the investigated section of the EPR, Pacific and Cocos plates, and various parts of the study area.

Zone	Range (m)	Mean value (m)	Standard deviation (m)	Average propagation error
Southern Cocos	4910-5975	5450	220	230
Northeren Cocos	4690-6380	5450	300	310
Southern Pacific	5110-5790	5420	100	230
Northern Pacific	4660-6093	5300	200	380
Southern Cocos & Pacific	4910-5975	5430	170	230
Northern Cocos & Pacific	4660-6380	5370	270	340
Pacific	4660-6093	5370	160	300
Cocos	4690-6380	5450	250	270
Cocos and Pacific	4660-6380	5410	220	280

The undisputed third-order discontinuity identified within our study area and centered at 9˚56’-9˚58’N [*White et al.*, 2002; 2006] appears to be associated with a major change in both the MTZ character and crustal thickness (Figure 2.12a). Both the MTZ and crust are

inferred to thin from ~9˚56'N to 9˚57'N, where our 3D reflection cube ends, supporting earlier interpretations of a third-order boundary in this area between segments that do behave as independent magmatic units with a unique mantle melt source. The undisputed fourth-order discontinuity at 9˚49'N is found in an area mostly characterized by shingled reflection Moho (Figure 2.12a), a variation of an impulsive reflection Moho. Both impulsive and shingled Moho reflection types are indicative of a thin MTZ. The lack of variation in the Moho reflection combined with little change in crustal thickness observed in this area suggest a boundary between segments that do not behave as independent magmatic units with a unique mantle melt source. Therefore, our MTZ character and crustal thickness data appear to support the suggestion that the third-order segment-scale variations in in magma supply are related to mantle melt extraction processes occurring near the Moho, whereas smaller-scale fourth-order segmentation arises from the processes related to the crustal magma system [*Langmuir et al.,* 1986; *Macdonald et al.,* 1988; *Toomey and Hooft*, 2008].

The debated third- or fourth-order discontinuity at 9˚44.8'N (Figure 2.12a), also described as an atypical segment boundary or a boundary that is at its developing stage [*White et al.,* 2002], is located in an area that is practically void of variations in the MTZ character and crustal thickness. This leads us to believe that this ridge boundary is indeed a fourth-order discontinuity. The fourth-order segment boundary with a debated location at 9˚51.5'N [*White et al.*, 2002] or 9˚53'N [*White et al.*, 2006] falls within a zone of major change in both the MTZ character and crustal thickness (Figure 2.12a).

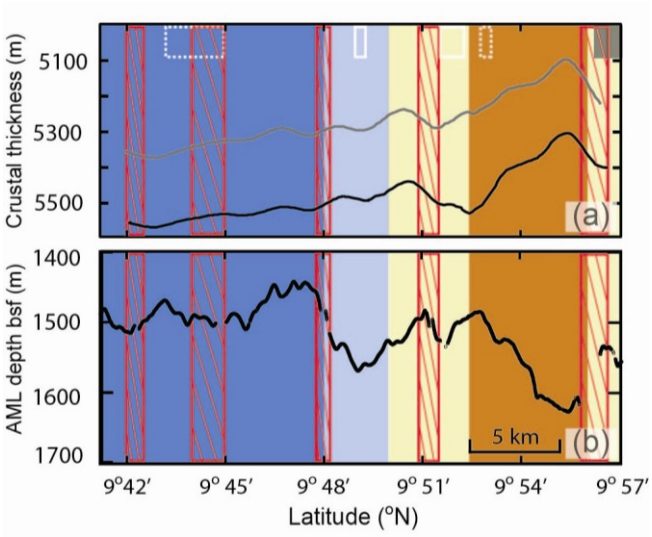

Figure 2.12 Relationship between the MTZ character (background; see Figure 2.6 for color code) and: (a) MCS derived crustal thickness with (black line) and without (gray line) layer 2A; (b) AML depth bsf. The MCS crustal thickness in (a) is average crustal thickness for the area near the ridge axis (0.5 to 3.0 km or crust ~10-55 Ka old). The AML depth bsf is from *Carbotte et al.* [2013]. The background color indicates the dominant MTZ type on both flanks as a function of latitude. Transitional areas, where no particular MTZ type dominates, are shown in yellow White rectangles are fourth-order and filled grey rectangles are third-order segment discontinuities [*White et al.,* 2002; 2006; *Haymon and White*, 2004; *Carbotte et al.,* 2013]. Dotted white rectangles show the location of disputed small-scale segment discontinuities. Red rectangles are AML disruption zones from *Carbotte et al.* [2013].

Considering that the third-order ridge discontinuity at 9˚56'N-9˚58'N is associated with a transitional area similar to that found at 9˚50'N-9˚52.5'N, we suggest that this is not a fourth-order but rather a third-order segment boundary with its central part positioned at 9°51-51.5'N, where a discontinuity in the AML is identified by *Carbotte et al.* [2013].

2.6.3 Crustal Accretion Style

Lower crustal accretion models from multiple magma bodies [e.g., *Shouten and Denham,* 1995; *Kelemen et al.,* 1997; *Maclennan et al.,* 2004] imply a larger volume of gabbro melt embedded in the uppermost mantle rocks than the gabbro-glacier model and thus are characterized by a thicker MTZ [e.g., *Rabinowicz et al.,* 1987; *Nicolas et al.,* 1995;

Kelemen and Aharonov, 1998]. Because seismic modeling of ophiolites [e.g., *Collins et al.,* 1986; *Brocher et al.,* 1985] shows that thin and thick MTZs have a distinctly different reflection signature, single-phase and multi-phase response respectively, seismic reflection images that capture the MTZ character appear to have the potential to be used to infer the lower crustal accretion style of the imaged oceanic crust. This seems true for crust both on- and off-axis because a portion of the gabbro melt embedded in thick MTZs cools and solidifies in-situ leaving evidence about the deep melt distribution at the time the crust was formed [e.g., *Nedimović et al.,* 2005]. Field studies of ophiolites further suggest that thick MTZs are associated with mantle diapirs [*Nicolas et al.,* 1996] and produce thinner oceanic crust [*Reuber et al.,* 1991]. Using these studies as a framework, we interpret the primary results from our extensive 3D reflection imaging, maps of the MTZ character and crustal thickness (Figures 2.6, 2.7, 2.9, 2.10, 2.11 and 2.12a), in terms of the accretion style within the study area.

The overall character of the MTZ on both plates (Figure 2.12, color shading) is impulsive from ~9˚42'N to 9˚48'N, indicating a sharp transition from the crust to mantle. The MTZ becomes mostly shingled from 9˚48'N to 9˚50'N, where it changes into transitional from 9˚50'N to 9˚52.4'N. A diffuse Moho reflection response and hence a thick MTZ is preponderant from 9˚52.4'N to 9˚56'N, after which it becomes transitional until the northern edge of the survey at 9˚57'N. In parallel with these changes in MTZ character, the average crustal thickness for the youngest crust (calculated for crust ~10-55 Ka old; Figure 2.12a) gradually decreases from 9˚42'N to ~9˚51.5'N and more rapidly from 9˚51.5'N to 9˚56'N, reaching a minimum at ~9˚55.5'N. This is consistent with studies of the Bay of Island and Oman ophiolite complexes that document high degrees of lateral

variation in the internal structure of the crust and MTZ in these paleo-ridge environments [*Karson et al.,* 1984; *Brocher et al.,* 1985; *Benn et al.,* 1988].

From the spatial variations in MTZ character, we infer that the style of crustal accretion varies in the study area with more efficient extraction of mantle melts to the crust in the southern part of our survey (9˚42'N to 9˚49.5'N) and perhaps more of the crust formed from the AML. Measured crustal thickness variation is small, at the limit of what we can resolve, suggesting that the mantle melt supply does not vary significantly for our study area. The northern half of the survey area (9˚49.5'N to 9˚57'N) is also associated with greater off-axis magmatism as inferred from the imaged OAML distribution (e.g., Figure 2.10) and deeper AML (Figure 2.12b), which may be related to less focused upper mantle magma delivery to the axis and therefore its broader distribution within the MTZ.

From a study of major element and volatile concentrations in olivine-hosted melt inclusions from lavas sampled at 9˚50'N, *Wanless and Shaw* [2012] infer that magma crystallization occurs over a wide range of depths. Over 50% of crystallization appears to occur at depths consistent with crystallization within the AML whereas >25% of crystallization takes place in the lower crust or mantle. These results contrast with samples from 12°48'N where *Wanless and Shaw* [2012] infer that practically all crystallization occurred at shallow depths in the crust. The nature of the MTZ in these two areas differs. In the 9°50'N region, where significant crystallization at lower crustal/upper mantle depths is inferred, the MTZ is transitional, thin on the Cocos plate and thick on the Pacific plate. In contrast, an impulsive Moho reflection event is observed in 2D seismic reflection data available from 12˚48'N [*Barth and Mutter*, 1996]. These observations are consistent with the inference that the thicker/diffuse MTZ is

associated with more of a multiple magma sill mode of accretion. While these results are suggestive, clearly the data are sparse and further melt-inclusion studies would be needed to evaluate the linkages between MTZ character and crystallization depths, for example within the thin MTZ (e.g., 9˚45'N) and a thick MTZ (e.g., 9˚54'N) regions in our study area.

Compliance measurements within or near our study area have been made at 9˚48'N, 9˚47'N and 9˚41'N (Figure 2.1) [*Crawford and Webb*, 2002]. Melt in the lower crust and/or MTZ was inferred only for the on-axis area at 9˚48'N. While directly beneath this region the seismic imaging indicates a thin MTZ in the near-axis crust, this measurement is close to the transition to a thick MTZ at 9˚50'N. The off-axis compliance measurement at 9˚47'N showing no lower crustal/MTZ melt was taken in the area where we identify an OAML in the lower crust. However, the identified OAML is very small and characterized by weak signal to noise ratio suggesting small amounts of melt that may be below the sensitivity threshold of the compliance method. Future compliance measurements at 9˚45'N and 9˚54'N would be particularly useful for further correlation tests with the seismic reflection imaging results.

Thermodynamic modeling of melt migration across a section of the northern EPR that includes our study area [*Durant*, 2011] suggests that axis-centered mantle melt delivery is associated with a gabbro-glacier mode of crustal accretion, where the majority of the lower crust is formed from subsiding cumulates originating from the AML [e.g., *Henstock et al.,* 1993*; Phipps Morgan and Chen,* 1993], while off-axis mantle melt delivery is associated with multiple magma body modes of lower-crustal accretion [e.g., *Maclennan et al.*, 2004]. There are two bulls-eye shaped mantle low-velocity zones

(MLVZs), generally interpreted to indicate higher melt concentrations, within our study area (e.g., Figures 2.10 and 2.11) [*Toomey et al*., 2007]. One coincides with our survey from 9˚42'N to 9˚47'N and the other from 9˚52'N to 9˚57'N. While the northern MLVZ shows a slight degree of skewness with its center shifted somewhat toward the Pacific plate, both MLVZs are mostly centered beneath the ridge axis suggesting similar axis-centered mantle melt delivery and therefore mode of crustal accretion at both locations. However, we infer a major difference in the MTZ thickness between the two MLVZs and infer that the style of crustal accretion likely differs between the two locations. The location of the northern MLVZ corresponds with our zone of inferred thick MTZ and thinner crust, while the southern MLVZ corresponds with the thin MTZ and thicker crust. Interestingly, the region between the two MLVZ corresponds with our transitional MTZ (e.g., Figures 2.11 and 2.12).

It is unclear as to what is the cause for the apparent south to north variation in the mantle melt delivery and the corresponding change in the crustal accretion style within our study area as interpreted from the presented MTZ character and crustal thickness information. However, the presence of most recently formed Lamont seamount at the very NW corner of our 3D box, concentration of the OAMLs around 9˚53'N where the current Lamont seamounts axis of alignment projects to the EPR, slight skewness of the northern MLVZ toward the Pacific plate, deeper AML, as well as the thick MTZ and thinner crust in this area suggest that the local mantle melt delivery to the crust becomes increasingly defocused from south to north. This variation in the mantle melt delivery to the crust appears to induce a change in the crustal accretion style, both of which may possibly be caused by an interaction between ridge and seamount melt sources.

2.7 Conclusions

Analysis of the first dense, multi-source and multi-streamer 3D MCS dataset collected over a MOR has yielded the first detailed maps of the oceanic MTZ character and crustal thickness. The data were collected along the EPR between 9˚42'N and 9˚57'N. The MTZ reflections were imaged, and therefore crustal thickness determined, within ~87% of the study area, with 41% of the total area characterized with impulsive, 29% with shingled, and 17% with diffusive MTZ reflections. Examination of ~658 km^2 of the produced 3D reflection cube gives new insights into the (1) crustal thickness, (2) ridge segmentation and, (3) style of crustal accretion across this section of the EPR.

(1) The computed average crustal thickness of 5740±270 m is about 5% greater than the average crustal thickness of ~5.5 km/s estimated for the study area by an earlier MCS study [*Barth and Mutter*, 1996]. The average crustal thickness for the study area of ~6.8 km based on the wide-angle OBS data remains significantly greater than what is obtained from the MCS data. The difference in the average crustal thickness of ~1 km is caused by inherent differences in the way crustal thickness is estimated using MCS and OBS data, where the former estimates do not include the MTZ and the latter do. The average crustal thickness computed in this work varies little from Pacific to Cocos plate, as well as between the investigated study area quadrants suggesting uniform crustal production in the last 180 Ka. However, the individual crustal thickness measurements can vary by as much as 1.75 km. This shows that the variation in thickness of normal oceanic crust formed at a fast spreading center and covering an area comparable in size to small-scale ridge segments is significant, which suggests that mantle upwelling at fast spreading centers is not likely to be 2D as has been proposed.

(2) Key observations pertaining to ridge segmentation that emerge from the analysis of the MTZ character and near-axis crustal thickness are: (a) The third-order ridge discontinuity at 9˚56-58'N evident in the seafloor morphology of the axial zone, geochemical investigations, tomographic inversions, and MCS reflection imaging of the AML appears to be associated with a change in the MTZ character and crustal thickness; (b) These changes occur over an area 3-4 km long indicating that third-order discontinuities are not point locations, in agreement with other recent ridge segmentation studies; (c) Fourth-order ridge discontinuities appear to show no correlation with variations in the MTZ character and/or crustal thickness. In general, this suggests that the third-order segmentation is governed by melt distribution within the uppermost mantle while the fourth-order ridge segmentation arises from mid- to upper-crustal processes. In this light, the controversial third- and fourth- order segment discontinuities along the investigated section of the northern EPR were reinterpreted. The debated third- or fourth-order ridge segment boundary at 9˚44.8'N is assigned a fourth-order status. The ridge segment boundary with contested location at 9˚51.5'N or 9˚53'N that was previously interpreted as a fourth-order discontinuity is assigned a third-order discontinuity status centered at 9˚51-51.5'N.

(3) We infer variations in the accretion style within our study area (a) based on the main results from our extensive 3D reflection imaging, maps of the MTZ character and crustal thickness, and (b) in the context of the existing knowledge gathered from ophiolite and controlled source seismic studies. The MTZ character maps suggest more efficient mantle melt extraction within the southern half of our survey area (9˚42'N to 9˚49.5'N) with greater proportion of the lower crust accreted from the AML than that for the northern

half (9˚49.5’N to 9˚57’N), where mantle melt delivery to the axis seems less focused and crustal accretion more closely follows the multiple magma body model. The crustal thickness of the near-axial region is only slightly smaller across the northern half of the survey area which is characterized with thick and transitional MTZ, indicating little variation in the mantle melt supply within the study area and supporting the inferred less efficient melt delivery for the northern area. It remains unclear as to what is the cause for the apparent south to north variation in the style but not volume of the mantle to crust melt delivery and the inferred corresponding change in the crustal accretion style. However, the most likely culprit is the melt source interaction between the ridge and the Lamont seamounts.

2.8 References

Barth, G. A., and J. C. Mutter, (1996), Variability in oceanic crustal thickness and structure: Multichannel seismic reflection results from the northern East Pacific Rise, *J. Geophys. Res.*, 101, 17951–17975, doi: 10.1029/96JB00814.

Batiza, R., and Y. Niu (1992), Petrology and magma chamber processes at the East Pacific Rise -9˚30'N, *J. Geophys. Res.,* 97, 6779–6797.

Benn, K., A. Nicolas, and I. Reuber (1988), Mantle-crust transition zone and origin of wehrlitic magmas: evidence from the Oman ophiolite, *Tectonophysics,* 151, 75-85.

Boudier, F., A. Nicolas, and B. Ildefonse (1996), Magma chambers in the Oman ophiolite: Fed from the top and the bottom, *Earth Planet. Sci. Lett*., 144, 239–250.

Brocher, T. A., J. A. Karson, and J. A. Collins (1985), Seismic stratigraphy of the oceanic Moho based on ophiolite models: *Geology*, 13, 62–65.

Canales, J. P., R. S. Detrick, D. R. Toomey, and W. S. D. Wilcock (2003), Segment scale variations in the crustal structure of 150-300 kyr old fast-spreading oceanic crust (East Pacific Rise, 8°15'N–10°5'N) from wide-angle seismic refraction profiles, *Geophys. J. Int., 152*(3), 766–794, doi:10.1046/j.1365-246X.2003.01885.x.

Canales, J. P., M. R. Nedimović, G. M. Kent, S. M. Carbotte, and R. S. Detrick (2009), Seismic reflection images of a near-axis melt sill within the lower crust at the Juan de Fuca ridge, *Nature*, 460, 89–93, doi:10.1038/nature08095.

Canales, J. P., H. Carton, S. M. Carbotte, J. C. Mutter, M. R. Nedimović, M. Xu, O. Aghaei, M. Marjanović, and K. Newman (2012), Network of off-axis melt bodies at the East Pacific Rise. *Nat. Geosci*., 5, 279–283, http://dx.doi.org/10.1038/ NGEO1377.

Carbotte, S., and K. Macdonald (1992), East Pacific Rise 8°–10°30'N: Evolution of ridge segments and discontinuities from SeaMARC II and three-dimensional magnetic studies, *J. Geophys. Res.,* 97, 6959–6982, doi: 10.1029/91JB03065.

Carbotte, S., G. Ponce-Correa, and A. Solomon (2000), Evaluation of morphological indicators of magma supply and segmentation from a seismic reflection study of the EPR 15˚30– 17˚N, *J. Geophys. Res*., 105, 2737–2759.

Carbotte, S. M., M. Marjanović, H. Carton, J.C. Mutter, J.P. Canales, M.R. Nedimović, S. Han, and M.R. Perfit (2013). Fine-scale segmentation of the crustal magma reservior beneath the East Pacific Rise, *Nat. Geosci., in press*.

Carton, H. D., S. M. Carbotte, J. C. Mutter, J. P. Canales, M. R. Nedimović, O. Aghaei, M. Marjanović, and K. R. Newman (2010), Three-dimensional seismic reflection images of axial melt lens and seismic layer 2A between 9°42'N and 9°57_N on the East Pacific Rise, Abstract OS21C-1514, *Presented at 2010 Fall Meeting, AGU*, San Francisco, California.

Christeson, G. L., G. M. Purdy, and G. J. Fryer (1992), Structure of young upper crust at the East Pacific Rise near $9^0$30'N, *Geophys. Res. Lett*., 19, 1045–1048.

Choo, J., Downton J, and Dewar J, (2004), Lift: a new and practical approach to noise and multiple attenuation, *First Break*, 22, 39–44.

Chen, Y. J., and J. Phipps Morgan (1996), The effects of spreading rate, the magma budget, and the geometry of magma emplacement on the axial heat flux at mid-ocean ridges, *J. Geophys. Res*, 101, 11475–11482.

Collins, J. A., T. M. Brocher, and J. A. Karson (1986), Two-dimensional seismic reflection modeling of the inferred crust-mantle transition in the Bay of Islands Ophiolite, *J. Geophys. Res.,* 91, 12520–12538.

Crawford, W. C., and S. C. Webb (2002), Variations in the distribution of magma in the lower crust and at the Moho beneath the East Pacific Rise at 9°–10°N, *Earth Planet. Sci. Lett*., 203, 117–130, doi:10.1016/S0012-821X(02)00831-2.

Detrick, R. S., P. Buhl, E. Vera, J. Mutter, J. Orcutt, J. Madsen, and T. Brocher (1987), Multi-channel seismic imaging of a crustal magma chamber along the East Pacific Rise, *Nature, 326*, 35–41.

Dunn, R. A., and Toomey, D. R (1997), Seismological evidence for three-dimensional melt migration beneath the East Pacific Rise, *Nature* 388, 259–262.

Dunn, R. A., D.R. Toomey, and S.C. Solomon (2000), Three-dimensional seismic structure and physical properties of the crust and shallow mantle beneath the East Pacific Rise at 9°30′N, *J. Geophys. Res.*, 105, p. 23,537–23,555, doi: 10.1029/2000JB900210

Durant, D. T. (2011), Effects of the off-axis melt supply at fast-spreading mid-ocean ridges: a study of the 9˚-10˚N region of the East Pacific Rise, Ph.D. thesis, Dep. of Geol. Sciences., Univ. of Oregon, Eugene, Oregon, USA.

Forsyth, D. W., (1992), Geophysical constraints on mantle flow and melt migration beneath mid-ocean ridges, in *Mantle Flow and Melt Generation at Mid-ocean Ridges*, *Geophys. Monogr. Ser*., Vol. 71, pp. 1–65, edited by Phipps Morgan, J., et al., AGU, Washington, DC.

Goss, A. R., M. R. Perfit, W. I. Ridley, K. H. Rubin, G. D. Kamenov, S. A. Soule, A. T. Fundis, and D. J. Fornari (2010), Geochemistry of lavas from the 2005–2006 eruption at the East Pacific Rise, 9°46'N-9°56'N: Implications for ridge crest plumbing and decadal changes in magma chamber compositions, *Geochem. Geophys. Geosyst*., 11, Q05T09, doi:10.1029/2009GC002977.

Han, S., H. D. Carton, S. M. Carbotte, J. C. Mutter, J. Canales, and M. R. Nedimović (2011), 3D Seismic Reflection Images of an off-axis melt lens and its associated upper crust around 9° 39'N, East Pacific Rise. Abstract OS22A-02 *presented at 2011 Fall Meeting, AGU*, San Francisco, Calif., 5-9 Dec.

Harding, A. J., G. M. Kent, and J. A. Orcutt (1993), A multichannel seismic investigation of upper crustal structure at 9˚N on the East Pacific Rise: Implications for crustal accretion, *J. Geophys. Res*., 98, 13925–13944.

Haymon, R. M., D. J. Fornari, M. H. Edwards, S. M. Carbotte, D. Wright, and K. C. Macdonald (1991), Hydrothermal vent distribution along the East Pacific Rise crest (9˚9'–54'N) and its relationship to magmatic and tectonic processes on fast spreading mid-ocean ridges, *Earth Planet. Sci. Lett., 104*, 513–534, doi:10.1016/0012-821X(91)90226-8.

Haymon, R. M., D. J. Fornari, K. L. Von Damm, M. D. Lilley, M. R. Perfit, J. M. Edmond, W. C. Shanks, III, R. A. Lutz, J. M. Grebmeier, S. Carbotte, D. Wright, E. McLaughlin, M. Smith, N. Beedle, and E. Olson (1993), Volcanic eruption of the mid-ocean ridge along the East Pacific Rise crest at 9˚45'–52'N: Direct submersible observations of seafloor phenomena associated with an eruption event in April, 1991, *Earth Planet. Sci. Lett., 119*, 85–101, doi:10.1016/0012-821X(93) 90008-W.

Haymon, R. M., and S. M. White (2004), Fine-scale segmentation of volcanic/hydrothermal systems along fast-spreading ridge crests, *Earth Planet. Sci. Lett., 226*, 367–382, doi:10.1016/j.epsl.2004.08.002.

Henstock, T. J., A. W. Woods, and R. S. White (1993), The accretion of oceanic crust by episodic sill intrusion, *J. Geophys. Res*., 98, 4143–4161.

Herron, T. J., P. L. Stoffa, and P. Buhl (1980), Magma chamber and mantle reflections - East Pacific Rise, *Geophys. Res. Lett*., 7, 989–992.

Karson, J. A., J. A. Collins, and J. F. Casey (1984), Geologic and seismic velocity structure of the crust/mantle transition in the Bay of Islands ophiolite complex, *J. Geophys. Res*., 89, 6126–6138, doi:10.1029/JB089iB07p06126.

Kent, G. M., A. J. Harding, and J. A. Orcutt (1993), Distribution of magma beneath the East Pacific Rise between the Clipperton transform and the 9˚17'N deval from forward modeling of common depth point data, *J. Geophys. Res*., 98, 13,945–13,969.

Kent, G. M., A. J. Harding, J. A. Orcutt, R. S. Detrick, J. C. Mutter, and P. Buhl (1994), Uniform accretion of oceanic crust south of the Garrett transform at 14˚15'S on the East Pacific Rise, *J. Geophys. Res.*, 99 , 9097-9116,doi:10.1029/93JB02872.

Kelemen, P. B., K. Koga, and N. Shimizu (1997), Geochemistry of gabbro sills in the crust-mantle transition zone of the Oman ophiolite: Implications for the origin of the oceanic lower crust, *Earth Planet. Sci. Lett*., 146, 475–488.

Kelemen P. B., and E. Aharonov (1998), Periodic formation of magma fractures and generation of layered gabbros in the lower crust beneath oceanic spreading ridges, in *Faulting and Magmatism at Mid-Ocean Ridges, Geophys. Monogr. Ser*., vol. 106, edited by W.R Buck et al., pp 267–289. AGU, Washington, D.C.

Langmuir, C. H., J. F. Bender, and R. Batiza (1986), Petrological and tectonic segmentation of the East Pacific Rise, 5˚30'N– 14˚30'N, *Nature*, 322, 422–429.

Macdonald, K. C., J. C. Sempere, and P. J. Fox (1984), East Pacific Rise from Siqueiros to Orozco fracture zones: Along strike continuity of axial neovolcanic zone and structure and evolution of overlapping spreading centers, *J. Geophys. Res*., 89, 6049–6069.

Macdonald, K. C., P. J. Fox, L. J. Perram, M. F. Eisen, R. M. Haymon, S. P. Miller, S. M. Carbotte, M.-H. Cormier, and A. N. Shor (1988), A new view of the mid-ocean ridge from the behavior of ridge axis discontinuities, *Nature,* 335, 217–225, doi:10.1038/335217a0.

Macdonald, K. C., P. J. Fox, S. P. Miller, S. M. Carbotte, M. H. Edwards, M. F. Eisen, D. J. Fornari, L. J. Perram, R. Pockalny, R. M. Haymon, D. S. Scheirer, S. Tighe, C. Weiland, D. Wilson (1992), The East Pacific Rise and its flanks 8°–18°N: History of segmentation, propagation and spreading direction based on SeaMARC II and SeaBeam studies, *Mar. Geophys. Res*., 14, 299–344.

Macdonald, K. C (1998), Periodic formation of magma fractures and generation of layered gabbros in the lower crust beneath oceanic spreading ridges, in *Faulting and Magmatism at Mid-Ocean Ridges, Geophys. Monogr. Ser*., vol. 106, edited by W.R Buck et al., pp 27–58. AGU, Washington, D.C.

Maclennan, J., T. Hulme, and S. C. Singh (2004), Thermal models of oceanic crustal accretion: linking geophysical, geological and petrological observations, *Geochem. Geophys. Geosyst.* 5, Q02F25, doi:10.1029/2003GC000605.

Magde, L. S., D. W. Sparks, and R. S. Detrick (1997), The relationship between buoyant mantle flow, melt migration, and gravity bull's eyes at the Mid-Atlantic Ridge between 33°N and 35°N, *Earth Planet. Sci. Lett.*, 148, 59–67.

Mutter, J. C., S. M. Carbotte, M. R. Nedimović, J. P. Canales, and H. Carton (2009), Seismic imaging in three dimensions on the East Pacific Rise. *Eos Trans. AGU,* 90, 374–375, http://dx.doi.org/10.1029/2009EO420002.

Nedimović, M. R., S. M. Carbotte, A. J. Harding, R. S. Detrick, J. P. Canales, J. B. Diebold, G. M. Kent, M. Tischer, and J. M. Babcock (2005), Frozen magma lenses below the oceanic crust, *Nature*, 436, 1149–1152, doi:10.1038/nature03944.

Nedimović, M. R., S. M. Carbotte, J. B. Diebold, A. J. Harding, J. P. Canales, and G. M. Kent (2008), Upper crustal evolution along the Juan de Fuca Ridge flanks. *Geochem. Geophys. Geosyst.,* 9, Q09006, http:// dx.doi.org/10.1029/2008GC002085.

Nicolas, A. and F. Boudier (1995), Mapping oceanic ridge segments in Oman ophiolites, *J. Geophys. Res.,* 100, 6179–6197.

Nicolas, A., F. Boudier, and B. Ildefonse (1996), Variable crustal thickness in the Oman Ophiolite: Implication for oceanic crust, *J. Geophys. Res*., 101, 17941–17950.

Orcutt, J., N. Kennett, L. Dorman, and W. Prothero (1975), A low-velocity zone underlying a fast-spreading ridge crest, *Nature*, 256, 475–476.

Phipps Morgan, J., and Y. Chen (1993), The genesis of oceanic crust, magma injection, hydrothermal circulation and crustal flow, *J. Geophys. Res*., 98, 6283–6297.

Pratt, R. G., and Worthington, M. H. (1990), Inverse theory applied to multi-source cross-hole tomography. Part I: Acoustic wave-equation method, *Geophysical Prospecting*, 38: 287-310.

Quick, J. E., and R. P. Delinger (1993), Ductile deformation and the origin of layered gabbro in ophiolites, *J. Geophys. Res*., 98, 14015-14027.

Rabinowicz, M., A. Nicolas, and J. Vigneresse (1984), A rolling mill effect in the asthenosphere beneath oceanic spreading centers, *Earth Planet. Sci. Lett*., 67, 97–108, doi:10.1016/0012-821X(84)90042-6.

Raitt, R.W. (1956), Seismic-refraction studies of the Pacific Ocean Basin, *Bull. Geol. Soc. Am.*, 67, 1623–1640.

Reuber, I., P. Nehlig, and T. Juteau (1991), Axial segmentation at a fossil oceanic spreading centre in the Haylayn block (Semail nappe, Oman): Off-axis mantle diapir and advancing ridge tip, *J. Geodyn*., 13, 253–278.

Scheirer, D. S., and K. C. Macdonald (1993), Variation in cross-sectional area of the axial ridge along the East Pacific Rise: Evidence for the magmatic budget of a fast-spreading center, *J. Geophys. Res.*, 98, 7871–7885, doi:10.1029/ 93JB00015.

Schouten, H., and C. Denham (1995), Virtual ocean crust, *Eos Trans. AGU*, 76, Spring meet. Suppl., 84.

Singh, S. C., A. J. Harding, G. M. Kent, M. C. Sinha, V. Combier, S. Bazin, C. H. Tong, J. W. Pye, P. J., Barton, R.W. Hobbs, R. S. White, and J. A. Orcutt (2006), Seismic reflection images of the Moho underlying melt sills at the East Pacific Rise, *Nature,* 442, 287–290.

Sinton, J. M., S. M. Smaglik, J. J. Mahoney, and K. C. Macdonald (1991). Magmatic processes at superfast spreading mid-ocean ridges: glass compositional variations along the East Pacific Rise 13°-23°S, *J. Geophys. Res*. 96, 6133–6155.

Sinton, J. M., and R. S. Detrick (1992), Mid-ocean ridge magma chambers, *J. Geophys. Res.*, 97, 197-216.

Smith, M. C., M. R. Perfit, D. J. Fornari, W. I. Ridley, M. E. Edwards, G. Kurras, and K. L. Von Damm (2001), Magmatic processes and segmentation at a fast spreading mid-ocean ridge: Detailed investigation of an axial discontinuity on the East Pacific Rise crest at 9°37'N, *Geochem. Geophys. Geosyst., 2*, 1040, doi:10.1029/2000GC000134.

Sohn, R. A., S. C. Webb, and J. A. Hildebrand (2004), Fine-scale seismic structure of the shallow volcanic crust on the East Pacific Rise at 9o50'N, *J. Geophys. Res.,* 109, B12104, doi:10.1029/2004JB003152.

Soule, S. A., D. J. Fornari, M. R. Perfit, and K. Rubin (2007), New insights into mid-ocean ridge volcanic processes from the 2005–2006 eruption of the East Pacific Rise, 9°46'N– 9°56'N, *Geology, 35*, 1079–1082, doi:10.1130/G23924A.1.

Soule, S. A., Escartín, J. and D. J. Fornari (2009), A record of eruption and intrusion at a fast spreading ridge axis: Axial summit trough of the East Pacific Rise 9-10°N. *Geochem. Geophys. Geosyst.* 10, Q10T07.

Stoffa, P. L., P. Buhl, T. J. Herron, J. K. Kan, and W. J. Ludwig (1980), Mantle reflections from beneath the crestal zone of the East Pacific Rise from multi-channel seismic data, *Mar. Geol*., 35, 83–97.

Tian, T., S. D. Wilcock, D. R. Toomey, and R. S. Detrick (2000), Seismic heterogeneity in the upper crust near the 1991 eruption site on the East Pacific Rise, 9˚50'N, *Geophys. Res. Lett*., 27, 2369–2372, doi:10.1029/1999GL011191.

Tolstoy, M., J. P. Cowen, E. T. Baker, D. J. Fornari, K. H. Rubin, T. M. Shank, F. Waldhauser, D. R. Bohnenstiehl, D. W. Forsyth, R. C. Holmes, B. Love, M. R. Perfit, R. T. Weekly, S. A. Soule, B. Glazer (2006), A sea-floor spreading event captured by seismometers, *Science*, 314, 1920–1922, doi:10.1126/ science.1133950.

Toomey, D. R., G. M. Purdy, S. C. Solomon, and W. S. D. Wilcock (1990), The three-dimensional seismic velocity structure of the East Pacific Rise near latitude 9!300N, *Nature,* 347, 639–645, doi:10.1038/347639a0.

Toomey, D.R., W.S.D Wilcock, R.S. Detrick, and R. A. Dunn (1998) Mapping melt and matrix flow in the uppermost mantle: preliminary results from undershooting the EPR, *EOS, Trans. AGU*, 79, Fall Meet. Suppl., F805.

Toomey, D. R., Jousselin, D., Dunn, R. A., Wilcock, W. S. D. and Detrick, R. S, (2007), Skew of mantle upwelling beneath the East Pacific Rise governs segmentation. *Nature* 446, 409–414.

Toomey, D. R., and E. E. E Hooft (2008), Mantle upwelling, magmatic differentiation, and the meaning of axial depth at fast-spreading ridges, *Geology* 36 (9), 679–682.

Vera, E. E., J. C. Mutter, P. Buhl, J. A. Orcutt, A. J. Harding, M. E. Kappus, R. S. Detrick, and T. M. Brocher (1990), The structure of 0- to 0.2-m.y.-old oceanic crust at 9°N on the East Pacific Rise from expanded spread profiles, *J. Geophys. Res., 95*, 15529–15556.

Wanless, V. D., and A. M. Shaw (2012), Lower crustal crystallization and melt evolution at mid-ocean ridges, *Nat. Geosci*., 5, 651–655, doi:10.1038/ngeo1552.

White, S. M., R. M. Haymon, D. J. Fornari, M. R. Perfit, and K. C. Macdonald (2002), Correlation between volcanic and tectonic segmentation of fast-spreading ridges: Evidence from volcanic structures and lava flow morphology on the East Pacific Rise at 9˚–10˚N, *J. Geophys. Res.,* 107, 2173, doi: 10.1029/2001JB000571.

White, S. M., R. M. Haymon, and S. Carbotte (2006), A new view of ridge segmentation and near-axis volcanism at the East Pacific Rise, 8˚–12˚N, from EM300 multibeam bathymetry, *Geochem. Geophys. Geosyst*., 7, Q12O05, doi:10.1029/2006GC001407.

CHAPTER 3 THE EAST PACIFIC RISE CRUST AND MOHO TRANSITION ZONE FROM 9˚37.5'N TO 9˚57'N: RESULTS FROM PRESTACK TIME MIGRATION OF 3D MCS DATA

3.1 Introduction

The globally detected Mohorovičić discontinuity or "Moho" has been widely used to explain processes related to formation, deformation and destruction of the lithosphere. However, there are still fundamental questions regarding the age of Moho formation, its structure, origin, and physical properties. The answer to some of these questions could be found by detailing the Moho structure at a mid-ocean ridge (MOR) environment where the nature of the Moho has not been influenced by geologic processes over long periods of geologic times. The first high-resolution multi-source, multi-streamer 3D multichannel seismic (MCS) data over a MOR environment [*Mutter et al.,* 2009; *Aghaei et al.*, 2013, submitted] are used in this chapter to address some of the questions regarding Moho formation. For this purpose, I have applied for the first time state-of-the-art 3D prestack time migration (PreSTM) to this 3D MCS dataset.

The first images a mid-crustal seismic reflector and the Moho reflection event were provided more than three decades ago at the fast-spreading East Pacific Rise (EPR) between 9°N and 10°N on three MCS reflection profiles [*Heron et al*., 1978; 1980]. This ground-breaking discovery initiated three decades of intensive research that has seen many seismic experiments including seismic reflection, refraction and tomography conducted along, across and adjacent to the EPR ridge axis between 16°N and 20°S. With a single exception [*Kent et al.,* 2000], the MCS reflection experiments have aimed for broad coverage of the EPR with widely-spaced (~3.5 km) 2D MCS profiles, mainly

motivated by the objective of examining the geometry of the mid-crustal seismic reflector known as the axial magma lens (AML), its physical properties and its role in formation of the crust [e.g., *Kent et al*., 1987; *Collier and Singh*, 1997]. As a result, the size, shape, and internal properties of this elongated AML are well constrained. During the same time period, the lower oceanic crust was the subject of several investigations [e.g., *Orcutt et al.,* 1975; *Stoffa et al.,* 1980; *Toomey et al.,* 1990; *Kent et al*., 1994; *Dunn et al.,* 2000; *Singh et al.,* 2005]. What has emerged from these studies is evidence for the presence of an axial low-velocity (LVZ) that extends from 1-2 km below seafloor (bsf) to the base of the crust. The LVZ is flatter and narrower (~2 km) at its top and is wider (5-7 km) at the base of the crust. The Moho reflection identified in the late 1970s [*Herron et al.,* 1978] is generally not imaged in the immediate vicinity of the ridge axis (~±3 km) [*Kent et al*., 1994; *Barth and Mutter*, 1996] possibly because it is not formed at the same time as much of the crust or because the imaging methodology used so far for academic investigations of the ridges is inadequate for imaging in areas of large lateral velocity variations and high signal attenuation.

Measurements of the crustal thickness puts important constraints on the amount of melt extracted from the mantle, and it has been widely used to explain thermo-mechanical models of MORs, ridge axis discontinuities, and mantle upwelling patterns [e.g., *Buck and Su,* 1989; *Lin and Phipps Morgan*, 1992; *Forsyth*, 1992]. A compilation of the seismically measured crustal thickness shows that crust formed at slow-spreading ridges (half spreading rate <20 mm/yr) displays much greater in-situ thickness variability than crust formed at fast-spreading ridges (half spreading rate >30 mm/yr) [*White et al.,* 1992]. To explain this spreading-rate dependence of crustal thickness variations, two models of

mantle upwelling beneath spreading centers were suggested. A two-dimensional or sheet-like pattern of mantle upwelling and melt migration has been suggested for fast-spreading centers as opposed to a three-dimensional or plume-like pattern of mantle upwelling at slow-spreading MORs [e.g., *Lin and Phipps Morgan*, 1992; *Magde and Sparks*, 1997]. However, the results of a wide-angle ocean-bottom seismometer (OBS) study at the fast-spreading EPR from 8°30'N to 10°N [*Canales et al.,* 2003] show along-axis crustal thickness variations of ~2.7 km in this first-order ridge segment. In addition, the results from the only 3D MCS study at the EPR from 9°42'N to 9°57'N that covers part of a third-order ridge segment [*Aghaei et al.,* 2013, submitted] show that the crustal thickness varies by as much as ~1.8 km in this area. These studies combined, show that the proposed 2D pattern of mantle upwelling and melt migration at fast-spreading MORs is too simplistic, and that the detailed relationship between crustal production and the pattern of mantle melt delivery at fast-spreading rates is still unknown.

The available velocity models of the crust for the well-studied EPR (from 9°N to 10°N) include five 1D velocity functions derived from ESP refraction experiments [*Vera et al.,* 1990], four ridge-parallel and a single ridge-perpendicular OBS velocity profiles [*Canales et al.,* 2003; 2012], and a 3D velocity model from tomography imaging centred at 9°30'N [*Dunn et al.,* 2000]. No 3D seismic velocity model of the crust for this magmatically robust portion of the EPR has yet been provided from a systematic analysis of the MCS reflection data. This is a key piece of information that can be used to compute the crustal thickness in a scale and resolution comparable with seafloor hydrothermal and volcanic activity.

In this chapter, results are provided of a detailed analysis of the crustal thickness, average crustal velocity, and the Moho transition zone (MTZ) character along the EPR from 9˚37.5'N to 9˚57'N, excluding a 3.3-km-wide gap from 9°40'N to 9°42'N. In this analysis, for the first time a state-of-the-art 3D PreSTM was applied to the 3MCS dataset acquired in the summer of 2008 on *R/V Langseth* and covering ~875 km^2 [*Mutter et al.,* 2009], and a systematic migration velocity analysis (MVA) was performed using the common image gathers (CIGs). This is the first dense, multi-source and multi-streamer 3D MCS dataset collected over a MOR environment. Examination of the produced 3D reflection cube provides new constraints and insights on the age of Moho formation, crustal thickness, and average velocity of the crust along this section of the EPR.

Applying PreSTM to this dataset is advantageous over applying prestack depth migration (PreSDM) because a) PreSDM is more sensitive to velocity errors compared to PreSTM, b) unlike PreSDM, the root-mean-square (RMS) velocity can be estimated directly through MVA in PreSTM, and c) the 2D dynamic raytracing used in PreSDM is more computation-intensive compared to the 1D raytracing used in PreSTM [*Biondi*, 2007]. The lateral velocity variations are handled accurately in PreSDM since the interval velocity is used for tracing rays from the diffraction point at the subsurface to surface locations ensuring that the diffraction curve at every location is computed accurately. In PreSTM, on the other hand, the estimated RMS velocity on a point-to-point basis facilitates 1D raytracing and lateral velocity variations are not handled as precisely as it is handled in PreSDM.

3.2 Study Area

The first multi-source and multi-streamer 3D MCS data (MGL0812) covering a ridge magmatic-hydrothermal system were collected in summer 2008 along a 37-km-long section of the fast-spreading EPR between 9˚37.5'N and 9˚57'N [*Mutter et al.,* 2009] (Figure 3.1). The survey extends on both ridge flanks out to ~10 km away from the ridge axis, or to ~180 Ka-old crust as the spreading rate (11 cm/yr full rate) did not change during the last ~0.73 Ma [*Carbotte and Macdonald,* 1992]. The investigated area represents part of a second order EPR segment. This segment is confined at its northern end by the Clipperton transform fault (10˚10'N), where the axis is offset by ~85 km, and at its southern end by the ~9˚03'N OSC, where the spreading centers are offset by a shorter distance of 8 km [*Macdonald and Fox*, 1983*; Macdonald et al.,* 1988]. The investigated portion of the EPR has been subjected to numerous geologic, geomorphic, geophysical, geochemical and hydrothermal surveys and probably is the most investigated section of the global MOR system.

Three third-order ridge discontinuities centred at about 9˚57'N, 9˚51.5'N and 9˚37'N divide the investigated area into two third-order ridge segments [*Haymon et al.,* 1991*; Smith et al.,* 2001; *Haymon and White,* 2004; *White et al.,* 2006; *Carbotte et al.,* 2013; *Aghaei et al.,* 2013, submitted]. The northern third-order segment is almost completely covered and the southern one mostly covered by the 3D MCS survey (Figure 3.1).

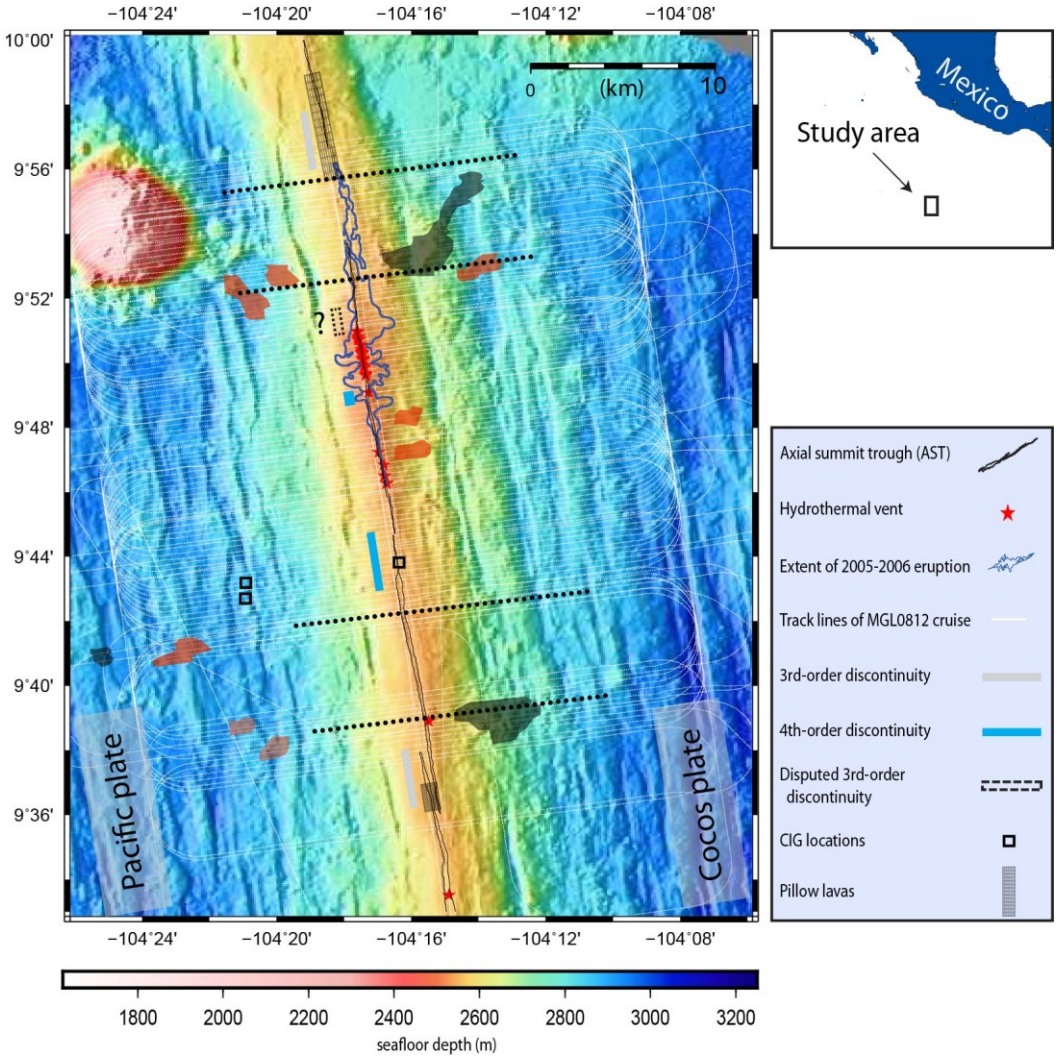

Figure 3.1 Ship track for cruise MGL0812 is shown using thin white lines superimposed over the EPR bathymetry (color background) between 9˚35'N and 10˚N latitude. Three black squares show the location of the CIGs presented in Figures 3.3 and 3.4. Dotted lines show the surface trace of in-lines from the 3D migrated stack presented in Figure 3.6a, b, c, d. Lower- and upper-crust off-axis magma lens (OAML) location are shown with filled black and red polygons, respectively. Locations and extent of pillow lavas are from *White et al.* [2002] and locations of third-order discontinuities are from *White et al.* [2006], *Carbotte et al.* [2013], and *Aghaei et al.* [2013, submitted]. Hydrothermal vent locations are from *Haymon et al.* [1991] and the Marine Geoscience Data System. Axial summit trough (AST) is as interpreted by *Soule et al.* [2007]. Extent of 2005-2006 eruption is from *Soule et al.* [2009].

The third-order ridge segment boundaries appear as transition zones rather than discontinuities, with the one at 9˚56'-58'N characterized by axial lava pillow domes extending from 9˚55.7'-9˚59'N [*White et al.*, 2002], the one at ~9˚51.5'N characterized

by ridge-axis rotation occurring between 9˚51.5'-9˚53'N [*Haymon et al.,* 1991], and the one at 9˚37'N characterized by a ~3 km-long overlap (~9˚36'-39'N) between the eastern and western axial summit trough (AST) that are offset in a right-lateral sense by ~0.45 km [*White et al.*, 2006]. The southern third-order segment hosts two fourth-order ridge discontinuities centred at about 9˚49'N and 9˚44.8'N [*Haymon et al.,* 1991*; Haymon and White,* 2004] that partition the southern third-order segment into three fourth-order segments (Figure 3.1). The fourth-order discontinuity centred at 9˚44.8'N and the third-order discontinuity at 9˚51.5'N were also interpreted in earlier publications as third- and fourth-order discontinuities, respectively. However, recent detailed information on the Moho transition zone character and crustal thickness from deep seismic imaging [*Aghaei et al.,* 2013, submitted] support the interpretation presented here.

A diverse series of seismic experiments conducted along and across the EPR axis constrain regional seismic structure of the young oceanic crust in the study area and its vicinity. To a varying degree of detail, the width and thickness of the mid-crustal AML, distribution and size of the off-axis magma lenses (OAMLs), layer 2A structure, and velocity and thickness of the crust have been determined.

A bright and almost continuous reflection originating from the mid-crustal AML and interpreted to mark the top of an axial magma chamber (AMC) characterized by a low velocity zone has been identified by the conducted 2D MCS experiments [e.g., *Herron et al.,* 1980; *Detrick et al.,* 1987; *Harding et al.,* 1993; *Kent et al.,* 1993]. In the study area, this bright reflection is visible along the axis and lies at an average depth of 1.48 km bsf [*Detrick et al.,* 1987; *Kent et al.,* 1993]. The width of AML measured along three 2D MCS profiles across the axis in the study area increases from 0.5 km at 9˚50'N to 0.7 km

at 9˚40'N. Extreme values of 0.25 and 4 km for the width of the AML within this second order ridge segment fall outside the study area at ~9˚35'N and ~9˚18'N, respectively [*Kent et al.,* 1993]. Thickness of the mid-crustal AML has been constrained by applying waveform inversion to the same 2D MCS data used for estimating the width of the AML. These results show that the AML is ~30 m thick at 9˚40'N [*Collier and Singh,* 1997]. On axis ESP data collected at 9˚35'N show that the AML at that location consists of fully molten material with P- and S-wave velocities of ~3 km/s and 0 km/s, respectively [*Vera et al.,* 1990]. Preliminary processing of the northern box of the 3D MCS data analyzed for this work [*Carton et al.,* 2010] indicates that the AML persists from 9˚42'N to 9˚57'N with variable width. The width of the AML reflection holds steady at ~1 km from 9˚42'-9˚50'N and 9˚51'-9˚57'N, with some variation from 0.5-2 km only from 9˚50'N to 9˚51'N. Intra-crustal OAMLs of variable shape and surface area have been identified within our study area (Figure 3.1) [*Canales et al.,* 2012; *Aghaei et al.,* 2013, submitted] using the 3D MCS data analyzed in this work. These OAMLs are found from ~1.5 km to ~16 km away from the ridge axis, at depths from >2 km to <5 km bsf. Melt accumulations at the MTZ have also been identified from seafloor compliance measurements on- and off-axis at 9˚48'N [*Crawford and Webb,* 2002].

Seismic velocity structure and thickness of the uppermost oceanic crust (layer 2A) in the study area and surrounding region have been determined from 2D MCS data [e.g., *Harding et al.,* 1993], ESP investigations [*Vera et al.,* 1990], and tomography experiments [*Toomey et al.,* 1991; *Tian et al.,* 2000; *Sohn et al.,* 2004]. The thickness of layer 2A varies from as low as ~100 m at some sections of the ridge axis to as high as ~500 m for some areas on the ridge flanks. Despite the significant difference between the

two layer 2A thickness extremes, layer 2A thickness on the flanks is not highly variable and does not have a major impact on local crustal thickness variation [*Aghaei et al.,*2013, submitted].

Reflections interpreted to originate from the MTZ are visible at about 2 s TWTT bsf on the early 2D MCS profiles [*Herron et al.,* 1980; *Stoffa et al*., 1980; *Detrick et al.,* 1987; *Barth and Mutter*, 1996]. Reflection Moho on these sections is not imaged beneath the AML but can generally be traced starting at 2-3 km away from the rise axis [e.g., *Detrick et al.,* 1987]. Detailed analysis of the MTZ reflection response in the study area has recently been carried out using a migrated stack of the northern 3D MCS box (Figure 3.1) [*Aghaei et al.,* 2013, submitted]. At its extremes, MTZ reflections imaged nearest to the rise axis can be observed beginning as close as ~0.45 km and as far as ~5 km away from the axis. The character of the MTZ reflection response varies from a sharp single-phase event to a diffusive multi-phase event [*Barth and Mutter*, 1996; *Aghaei et al.,* 2013, submitted].

Singh et al. [2006] imaged the Moho beneath the ridge crest on the eastern propagating limb of the OSC at 9°03'N using the pseudo-3D MCS data of the ARAD experiment [*Kent et al.,* 2000]. It is not yet clear if the imaged Moho by *Singh et al.* [2006] was formed at zero time, or that it is associated with ridge propagation over a pre-existing Moho. Except for the *Singh et al.* [2006] study, no observations of Moho directly beneath the ridge crest have yet been reported.

The thickness of the igneous crust for the 8˚50'N to 9˚50'N area has been computed by *Barth and Mutter* [1996] using 2D MCS migrated stacks, for the area between the Clipperton (8˚15'N) and Siqueiros (10˚10'N) transform faults by *Canales et al.* [2003]

using 2D OBS tomographic results, at 9˚35'N by *Vera et al.* [1990] from traveltime modeling of 1D ESP data, and between 9˚42'N and 9˚57'N by *Aghaei et al.* [2013, submitted] using a 3D MCS migrated stack and OBS velocities from *Canales et al.* [2003, 2012]. The computed thickness based on reflection profiles about 3.5 km apart was mostly done for crust up to ~300 Ka old. The results show that the crustal thickness variation for the 8˚50'N to 9˚50'N latitude range is ~2.6 km, with the thinnest crust at 5-5.5 km between ~9˚40'N and 9˚50'N and the thickest crust at 7-7.3 km between 9˚15'N and 9˚20'N. The crust gradually thickens toward the south between these two locations, and then thins south of 9˚15'N-9˚20'N to ~6.5 km at 8˚50'N. The majority of this crustal thickness variation was attributed to layer 3. Analysis of the ESP data centered at 180 Ka-old Cocos plate at ~9°33'N yields 6.8 km thick crust that is underlain by a 1.4 km thick MTZ.

The crustal thickness computed by simultaneous inversion of 2D OBS refraction and wide-angle Moho reflection arrivals [*Canales et al.,* 2003, 2012] is based on four ridge-parallel profiles evenly distributed on each side of the ridge axis and three ridge-perpendicular velocity profiles. Two of the ridge-parallel profiles are located on ~150 Ka-old crust and the other two velocity profiles are located on ~300 Ka-old crust, some 10 and 20 km away from the rise axis, respectively. The ridge-perpendicular velocity profiles at about 8˚35'N, 9˚15'N and 9˚50'N are about 75 km and 65 km apart from each other, respectively. The computed mean crustal thickness between the Siqueiros and Clipperton fracture zones is 6.7-6.8 km. The crust thickens away from the Siqueiros and Clipperton transforms, to the north and south respectively, reaching a maximum

thickness of 7.3-7.8 km north of the 9˚03'N OSC at 9˚15'N. The thinnest crust (5.3 km) is found within the Siqueiros transform.

For the study area investigated in this work, the mean crustal thickness from zero to crustal age of 300 Ka is ~5.75 km based on the 2D MCS results [*Barth and Mutter,* 1996], from zero to 225 Ka is ~6.8 km based on the 2D OBS data [*Canales et al.,* 2003], and from zero to ~180 Ka is ~5.75 km based on the 3D MCS migrated stack volume located between 9˚42'N and 9˚57'N [*Chapter 2*, *Aghaei et al.,* 2013, submitted].

3.3 Data

3.3.1 Data Acquisition

To collect the 3D MCS data, four 6-km-long hydrophone arrays (streamers), each consisting of 468 groups of hydrophones with group spacing of 12.5 m, were towed at a depth of 10 m. Separation between streamers was 150 m so that the total separation between outermost streamers was 450 m. Recording time was 10240 ms and sample rate was 2 ms. Two seismic sources, each comprised of two linear arrays of nine airguns with a total volume of 3300 in^3 were towed at a depth of 7.5 m. The two sources were fired in an alternating (flip-flop) mode every 37.5 m resulting in eight CMP profiles per sail line separated by 37.5 m. Sail lines were 300 m apart and were run in a successive racetrack loop pattern with each loop having a breath of about 6300 m. Sail lines 24 km long provide 16 km of full-fold coverage immediately across the ridge axis.

The four streamers and two airgun sources were navigated with a combination of Global Positioning System (GPS), acoustic transponders and 20 streamer compasses along each streamer to provide shot and receivers position accuracy of 1 and <3 m, respectively. The

streamer compasses used for controlling depth of each streamer have accuracy better than 1 m.

The geometry of the survey yields CMP bins that are 37.5 m wide and 6.25 m long in the cross-ridge-axis and along-ridge-axis directions, respectively. To achieve full nominal fold of 40 traces per CMP bin for the central 16 km-wide area about the ridge axis, sail lines included 4 km run-in and run-out. Nevertheless, fold distribution deviated from the nominal value due to streamer feathering, survey gaps caused by marine life, and technical shutdowns. The average feathering was ±5˚ requiring minimal infill. Gaps in the survey due to marine life and technical shutdown were closed with reshoot lines. *Mutter et al.* [2009] detailed data acquisition and the operational experience of this 3D seismic data acquisition project.

Two areas of 3D coverage separated by a 3.3 km gap were acquired. The larger, northern area (~714 km^2) is located between 9˚42'N and 9˚57'N (Figure 3.1). This area is covered with 94 primary (collected along the designed survey grid), 11 infill (collected in between primaries due to high streamer feathering) and 10 reshoot sail lines (recollected along the planned grid due to either technical problems or data gaps associated with marine mammal observing). The smaller area of 3D coverage (~100 km^2; 9˚37.5'N to 9˚40'N; Figure 3.1) includes 14 sail lines that are separated from the larger 3D area by 3.3 km.

In all, data from the whole area of full 3D coverage consisting of 108 sail lines with a total ship-track length of 3709.95 km were analyzed. Each of the sail lines forms eight CMP profiles resulting in total CMP line acquisition of 29679.6 km. There are 97,304 shot gathers, 182,153,088 sources-receive pairs and a total of 932,623,810,560 data

samples, which at 4 bytes per sample adds up to some 3.7 TB of data including trace headers.

3.3.2 Data Analysis

The 3D MCS data were 3D Kirchhoff PreSTM to produce a reflection image volume for interpretation. The average seismic velocity structure of the crust in the study area, an important by-product of the PreSTM process, was estimated by the migration velocity analysis (MVA) method where 3D Kirchhoff PreSTM is used for performing residual velocity analysis [*Stork*, 1992]. Prestack data processing steps applied to prepare the 3D MCS data for PreSTM are detailed by *Aghaei et al.* [2013, submitted]. The main components of the data preparation include construction of 37.5x6.25 m common midpoint (CMP) bin geometry, 1D bandpass filtering, 2D filtering using the LIFT approach [*Choo et al.,* 2004] simplified so as not to include a signal-add-back step, offset-dependent spherical divergence correction, surface-consistent amplitude balancing and trace editing.

Several passes of 3D PreSTM, each of which requires significant computational resources, are often necessary to converge to an acceptable velocity model. The most CPU and RAM demanding components of the Kirchhoff PreSTM are ray tracing, which is required to build summation surfaces, and the summation of these surfaces, which is required to form CIGs. The CPU time and RAM required for these two processes are proportional to the dimensions and nominal fold of the survey, size of migration aperture, dimensions of migration output grid, and output CIG fold [*Biondi,* 2007]. Considering that the required computational power and time can be quite large, quick convergence to

the optimum 3D PreSTM parameters through tests on a small section of the dataset is highly desired.

The starting minimum migration aperture suggested is twice the size of the Fresnel zone [*Sun and Bancroft*, 2001]. Assuming 5.5 s for the Moho reflection TWTT, a dominant frequency of 15 Hz and an RMS velocity of 4 km/s at the Moho level, the minimum migration aperture increases from ~2400 m at near-offset to 2470 m at far-offset. The migration aperture for the first pass of 3D PreSTM was chosen to be 3500 m in both the in-line and cross-line directions with hopes that including more data with a larger aperture will result in better imaging of the Moho reflection response, which is generally of low S/N ratio within single data traces. The initial velocity used for performing PreSTM is an average interval velocity from seafloor to Moho of 6250 m/s computed from the ESP1 velocity function of *Vera et al.* [1990] measured about 10 km off-axis. This interval velocity was converted to root-mean-square (RMS) velocity and hung from the seafloor (Figure 3.2).

The output CIGs of the first pass of 3D PreSTM were calculated at grid points that are 150 m apart across the ridge axis and 300 m apart along the ridge axis. Spacing of 50 m was chosen for the CIG seismic traces in order to have sufficient continuity of the Moho reflection response for performing residual velocity analysis. The near and far source-receiver offset in the CIGs is similar to what is found in the CMP bin gathers, 100 m and 6000 m respectively. A sample CIG is shown in Figure 3.3a. Where present, the Moho and melt lens reflection responses in CIGs are masked by water reverberations that were removed by a second pass of LIFT [*Choo et al.,* 2004].

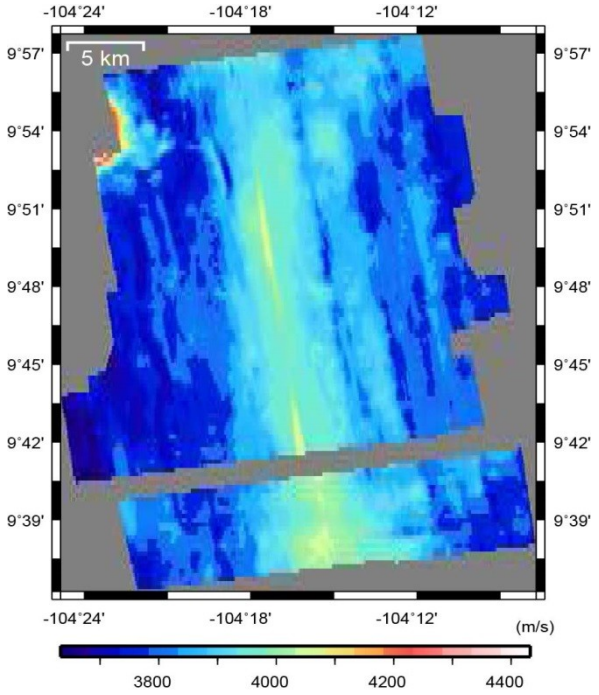

Figure 3.2 The initial root-mean-square (RMS) velocity model used for running the first pass of 3D Kirchhoff PreSTM. The 1D interval velocity of 6250 m/s hung from the seafloor is the average velocity of ESP1 of *Vera et al.* [1990].

For LIFT, the CIG data were first divided into low-frequency (0–8-15 Hz) and high-frequency (15-22–200-220 Hz) bands. A residual mid-frequency (8-15–15-22 Hz) range was obtained by subtracting the low and high frequency components from the full spectrum. An FX filter was applied to the low frequency band followed by a median filter applied to data in all frequency bands. The result of applying the second pass of LIFT to a sample CIG is depicted in Figure 3.3b.

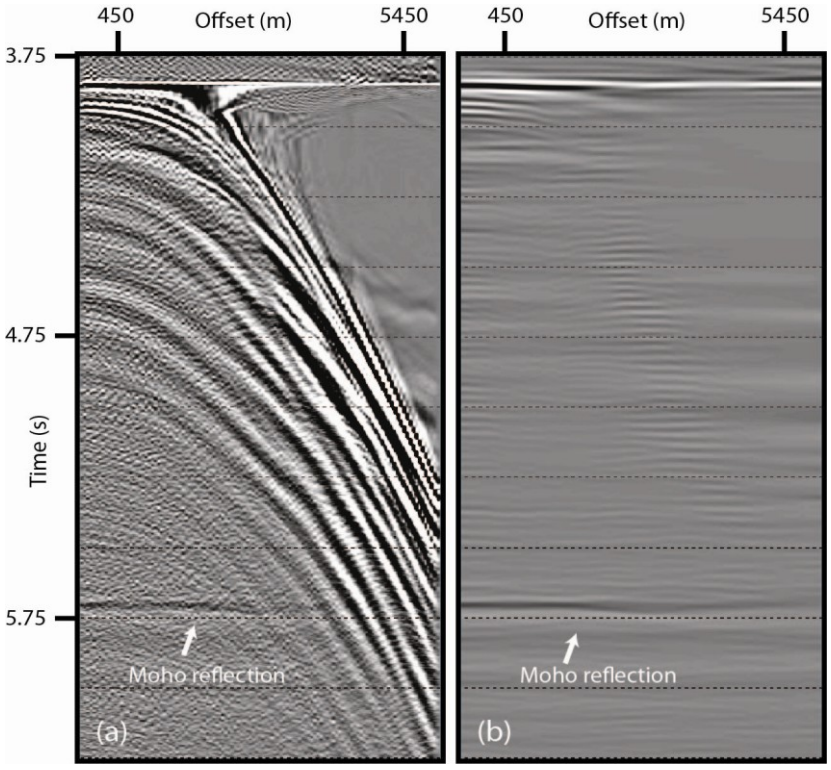

Figure 3.3 Noise suppression on a sample common image gather (CIG) by application of LIFT method. The CIG before (a) and after LIFT (b).

The coherency of reflection arrivals on CIGs after migration is used to find the optimum migration velocity for each reflection event. If the velocity used for migration is correct, reflections for each event are flat along the offset axis of the CIGs. The measured departure from flatness of a reflection event in the CIGs is called residual moveout (RMO), and it is used to update the initial RMS velocity model [*Biondi,* 2007]. Two CIGs before and after RMO, and their corresponding velocity spectra, are shown in Figure 3.4. The CIG corresponding to CMP bin 1214412 is located at the crossing of in-line 1672 and cross-line 2224, ~10 km west of the ridge axis on the Pacific plate (Figure 3.4a-c). The CIG corresponding to CMP bin 1215756 is located at the crossing of cross-line 3568 and the same in-line 1672, right over the ridge axis (Figure 3.4d-f). Flattening

of the AML and Moho reflection events of the CIGs 1214412 and 1215756 required RMO velocities of 200 m/s and 420 m/s, respectively.

The obtained RMO velocity volume is shown in Figure 3.5a. In general, significant modification of the initial crustal RMS velocities, and therefore the interval velocities, ranging to more than several hundred m/s were required in order to flatten the reflection events within the CIGs. The RMO velocity volume from Figure 3.5a was smoothed (Figure 3.5b) and used to update the initial RMS velocity model. After computing the new RMS velocity model (Figure 3.5c), a second pass of 3D PreSTM was run. An aperture of 2500 m in both the in-line and cross-line directions was selected for the second pass of PreSTM instead of the larger original aperture of 3500 m because it resulted in better focusing of the signal. The chosen output grid locations are 6.25 m apart in the cross-axis direction and 300 m apart in the along-axis direction. Much finer spacing along the in-lines, equivalent to the CMP bin spacing, is needed to adequately image the structures that exhibit greater structural complexity in the ridge-perpendicular direction.

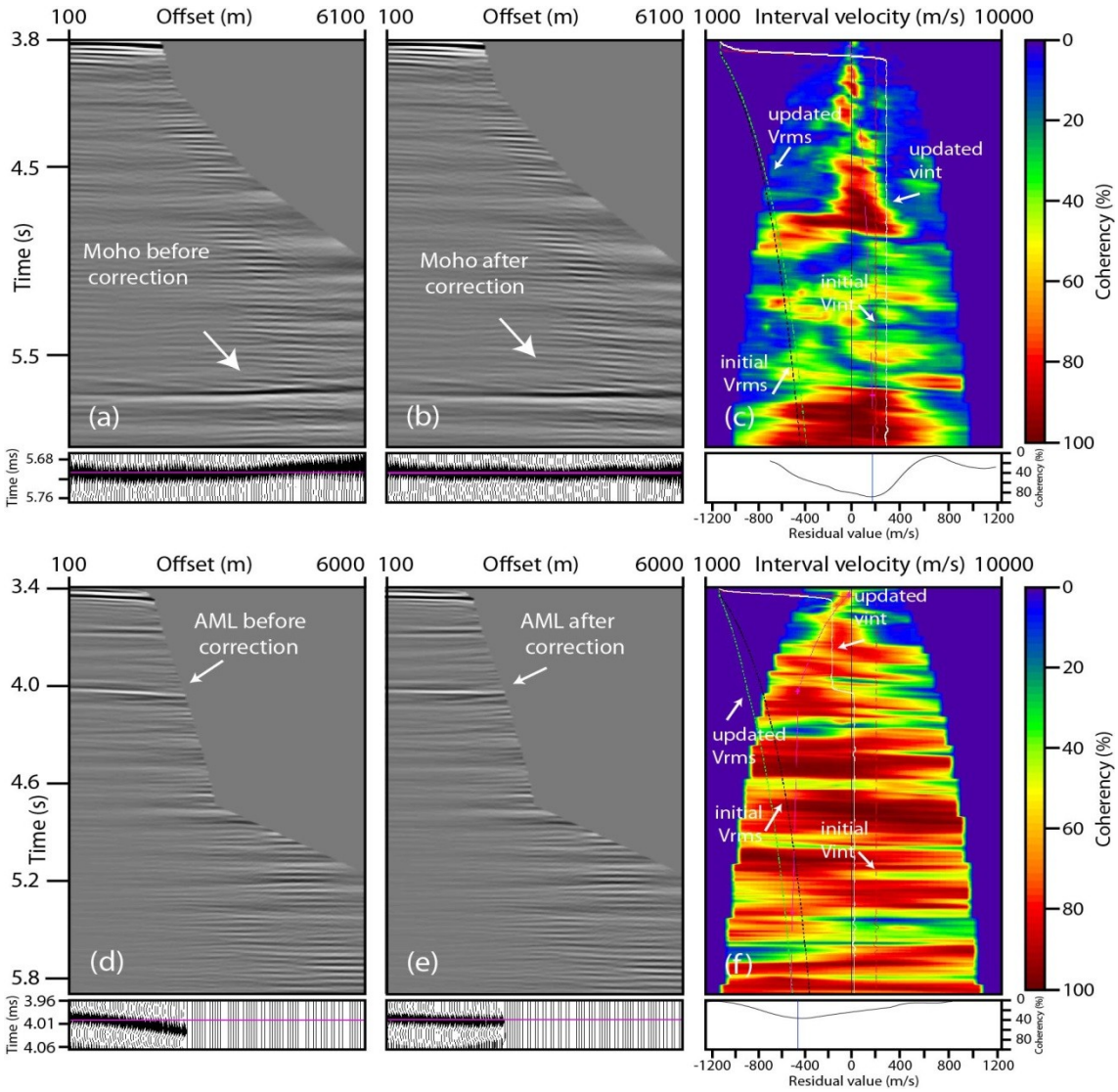

Figure 3.4 Two sample CIG and their corresponding velocity spectra used for performing MVA. a) CIG where Moho reflection event is over corrected because of too slow velocity. b) CIG of (a) after flattening the Moho reflection event by increasing the RMS velocity. c) Velocity spectrum of (a) where the initial interval velocity is shown with red line and the initial RMS velocity is shown in balck dashed line. The updated interval velocity is shown in white and the updated RMS velocity is shown in green dashed line. The small boxes below (a) and (b) show the zoomed Moho before and after picking, respectively. After increasing the RMS velocity by ~200 m/s, the Moho event flattens. The small box below (c) shows the coherency of the picked event. The location of this CIG is shown in Figure 3.1 with the upper black square that is ~10 km off-axis. d) CIG where the AML reflection is under corrected because of too high velocity. e) CIG of (d) after flattening the AML reflection by decreasing the initial RMS velocity by ~420 m/s. f) Velocity spectrum of (d) where the initial interval velocity is shown with red line and the initial RMS velocity is shown in black dashed line. The updated interval velocity is shown in white line and the updated RMS velocity is shown in green dashed line. From left to right, the small boxes

below (d) and (e) show zoomed AML before and after picking the residual RMS velocity, respectively. The small box below (f) shows the coherency of the picked event.

A smaller migration aperture and a coarser grid in the cross-line direction reduced the computation time far more than fine-grid spacing in the in-line direction. The data trace spacing for constructing a CIG for the second pass of migration was 100 m and the PreSTM was carried out in two stages, first for the near-offset (100-3000 m) data and then for the far-offset (3100-6000 m) data. The near-offset and far-offset CIGs were merged to build the full-offset CIGs. The computations for full PreSTM took ~18 days using 20 dual quad-core Xeon computation nodes (160 processors) with 3 GHz clock speed and 16 GB of RAM each (320 GB RAM in total).

Reverberations in CIGs were removed by LIFT, as described for the RMO velocity analysis, and far-offset stretch mute. The gathers were then summed to form the migrated image volume. Post migration processing included time-variant bandpass filtering (1-6–10-120 Hz for the top 100 ms TWTT through the igneous crust and 1-6–20-30 Hz for all the later TWTTs), time-variant scaling, and frequency spectrum balancing followed by FX deconvolution. A sample image from the created 3D PreSTM volume is shown in Figure 3.6 where the seafloor, AML, OAML and MTZ reflection events are identified.

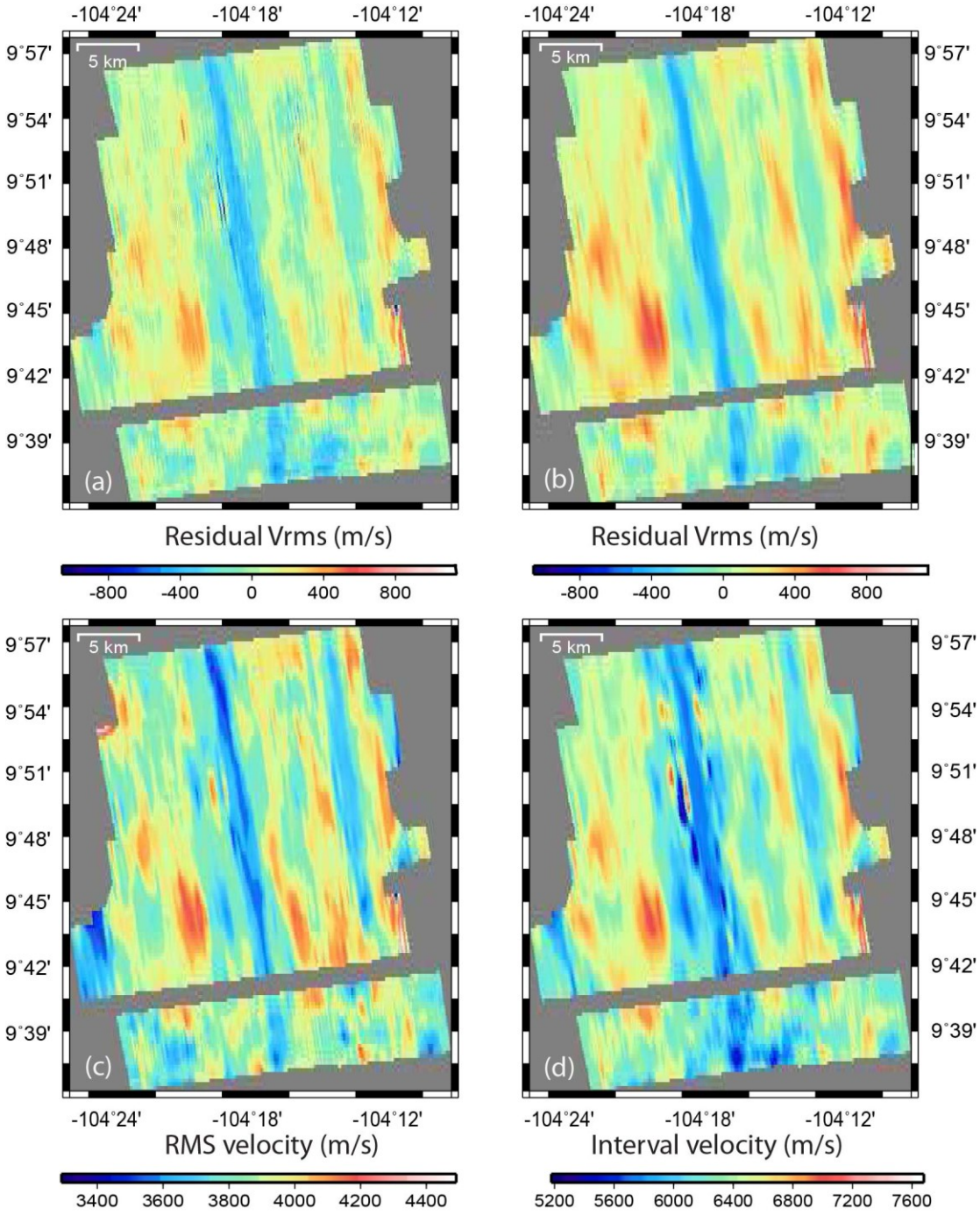

Figure 3.5 Interval velocity in the study area: a) The result of picking residual RMS velocity before and b) after smoothing. c) The updated initial RMS velocity of Figure 3.2, and d) the updated interval velocity. For flattening the Moho reflection event, we picked the residual RMS velocity every 300 m in the in-line direction and for flattening AML, the picking interval is 150 m in the in-line direction. I used the minimum curvature method for building the gridded maps.

3.4 Results

The primary results in this chapter are based on 874 km^2 of prestack migrated volume for the area between 9˚37'N and 9˚57' of the EPR, excluding a ~3.3-km-wide gap between ~9˚40'N and 9˚42'N. For this same area, a detailed velocity structure of the crust and images of Moho reflection are provided. The prestack migrated volume provides an area of ~728 km^2 with sufficiently high S/N ratio for interpretation. The 3D imaged volume facilitates detailed mapping of the seafloor and MTZ reflections that are required for computing the crustal thickness using the 3D average velocity model obtained through MVA. The MTZ is characterized and on- and off-axis magma lenses are mapped using this 3D image volume.

3.4.1 Seismic Velocity Structure of the Crust

The residual RMS velocities were determined using the MVA method. These residual RMS velocity values were used to update the initial velocity of the crust. The grid points for picking the residual RMS velocity were chosen 600 m apart in the along-axis direction and 300 m apart in the across-axis direction. The residual RMS velocity of the AML was determined at smaller grid interval of 150 m in the across-axis direction. Figure 3.5 shows (a) the gridded map of the measured residual RMS velocity, (b) the smoothed version of (a), (c) the updated initial RMS velocity of Figure 3.2 constructed by adding the results from (b), and (d) the corresponding interval velocity of (c). The minimum curvature method was used for producing the gridded maps.

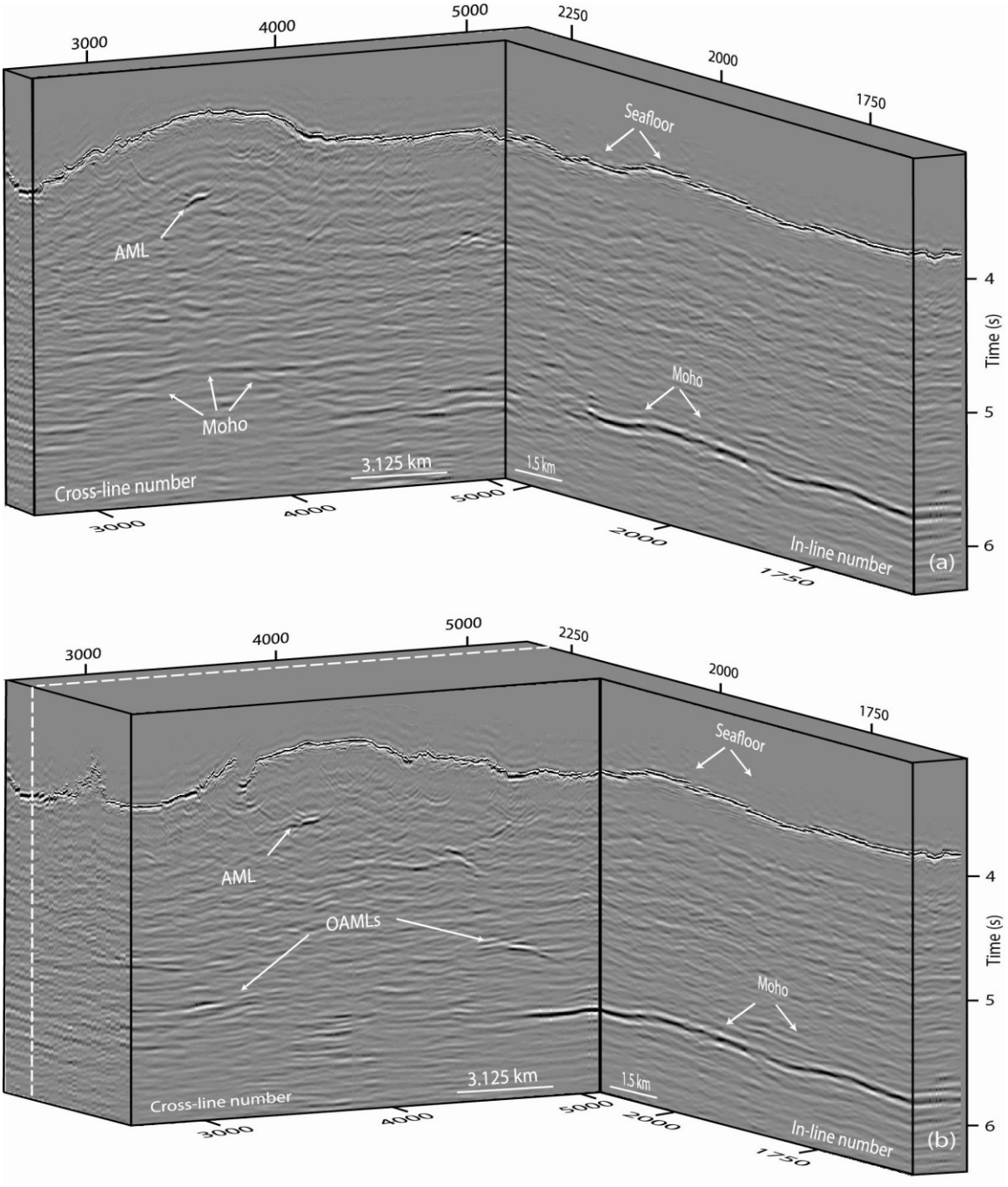
3000
4000
5000
2250
2000
1750
Seafloor
AML
Moho
Moho
3.125 km
1.5 km
Cross-line number
In-line number
(a)
Time (s)
4
5
6
3000
4000
5000
2250
2000
1750
Seafloor
AML
OAMLs
Moho
3.125 km
1.5 km
Cross-line number
In-line number
(b)
Time (s)
4
5
6

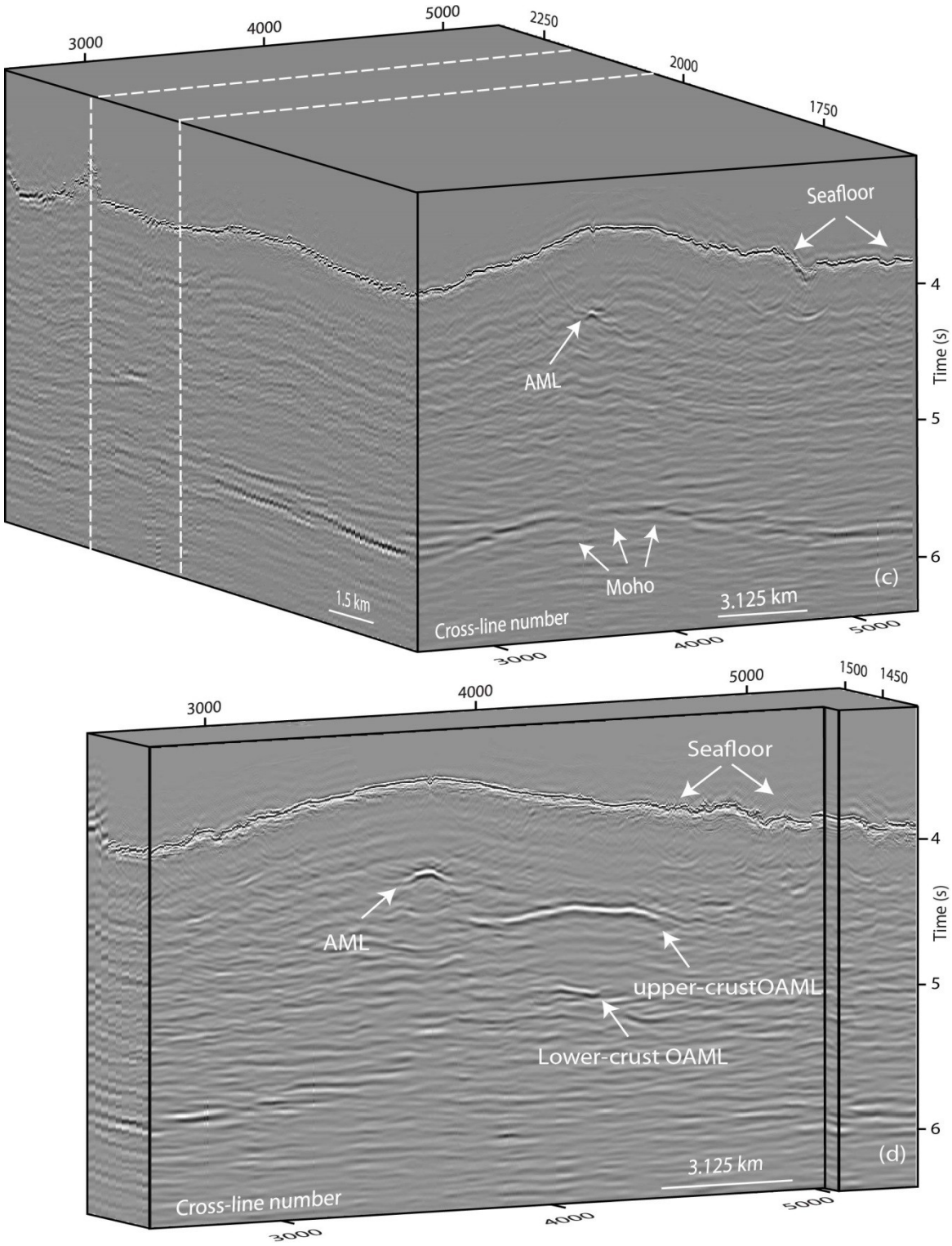

Figure 3.6 Seismic images from the 3D PreSTM volume showing reflection responses from the seafloor, AML, OAMLs and Moho. The in-lines from north to south are: (a) 2272; (b) 2052; (c) 1592 and (d) 1425. Note the remarkable clarity of the Moho and other recorded reflections, as well as the variation in the Moho reflection response from south to north.

The residual RMS velocity values show the largest variations along the across-axis lines and form axis-parallel zones of negative and positive residual RMS velocity (Figure 3.5a, b). From 9˚42'N to 9˚50'N, the axial zone of negative residual RMS velocity extends ~5 km from the ridge axis to the ridge flank on the Pacific plate. On the Cocos plate, this zone extends ~2 km from the ridge axis to the ridge flank in the same latitude range (Figure 3.5b). From 9˚50'N to 9˚57'N, the axial zone of negative residual RMS extends ~3 km from the ridge axis to the ridge flanks on the Cocos and Pacific plates.

Two axis-parallel zones of negative residual RMS velocity are located off axis on the Cocos plate (Figure 3.5b). The first negative zone at ~4.2 km away from the axis widens from 9˚53'N to 9˚56'N where OAMLs are located and connects to the second negative stripe that is ~8.7 km away from the axis.

The residual RMS velocity (Figure 3.5a) was smoothed using a locally weighted polynomial regression filter that was 300 m wide and 275 m long across- and along-axis, respectively (Figure 3.5b). Statistical analysis of the residual RMS values of Figure 3.5b is summarized in Table 3.1.

The residual RMS velocity value for the study area varies from -487 m/s to 656 m/s with mean value of 16 m/s. On the Cocos plate, the residual RMS velocity values vary from -466 m/s to 656 m/s with mean value of 7 m/s, and it changes from -487 m/s to 424 m/s on the Pacific plate where the mean value is 26 m/s.

Table 3.1 The residual RMS values range for the Cocos and Pacific plate, and for various sections of the study area with mean and standard deviations. See Figure 3.7a for plate section locations.

Plate section	Range (m/s)	Mean Value (m/s)	Standard deviation (m/s)
Southern Cocos	-466-323	-33	160
Central Cocos	-420-650	32	190
Northern Cocos	-430-380	5	160
Southern Pacific	-487-368	-10	140
Central Pacific	-430-420	50	190
Northern Pacific	-426-290	12	150
Southern Cocos & Pacific	-490-370	-22	150
Central Cocos & Pacific	-430-656	41	190
Northern Cocos& Pacific	-430-378	5	160
Pacific	-487-424	26	170
Cocos	-466-656	7	170
Cocos and Pacific	-487-656	16	170

The result of adding the smoothed residual RMS velocity (Figure 3.5b) to the initial RMS velocity of Figure 3.2 is shown in Figure 3.5c. Large across-axis RMS velocity variations and axis-parallel zones of high and low RMS velocity are observed in this figure. The RMS velocity of Figure 3.5c was converted to interval velocity (Figure 3.5d) using Dix equations [*Dix,* 1955]. These velocity values represent the average interval velocity of the crust. The same pattern of large across-axis velocity variation forming axis-parallel zones of high and low velocities similar to Figure 3.5c is observed in the interval velocity of Figure 3.5d. The results of average velocity of the crust are summarized in Table 3.2.

The interval velocity for the study area varies from 5150 to 7620 m/s with an average value of 6320 m/s. The average velocity of the Pacific plate (6320 m/s) is ~20 m/s faster than the average velocity of the Cocos plate.

Table 3.2 The interval velocity range and mean with associated standard deviation and average propagated error for the investigated section of the EPR, Pacific and Cocos plates, and various parts of the study area.

Plate section	Range (m/s)	Mean Value (m/s)	Standard deviation (m/s)	Standard error (m/s)
Southern Cocos	5590-6670	6180	250	190
Central Cocos	5360-7620	6310	300	160
Northern Cocos	5380-6970	6300	270	160
Southern Pacific	5150-7550	6320	260	190
Central Pacific	5190-7000	6330	320	160
Northern Pacific	5150-7550	6320	260	190
Southern Cocos & Pacific	5590-6820	6200	250	190
Central Cocos & Pacific	5150-7550	6315	270	160
Northern Cocos& Pacific	5190-7620	6320	310	190
Pacific	5150-7550	6320	300	160
Cocos	5350-7620	6300	290	160
Cocos and Pacific	5150-7620	6320	290	170

3.4.2 Moho Reflection

Reflections from the MTZ are observed in about 92% of the study area. Where Moho is identified, its seismic phase and continuity varies spatially within the 3D image volume (Figure 3.6). There are variations in the Moho reflection response which are differentiated between impulsive, shingled, and diffusive characteristics [*Kent et al.,* 1994]. Impulsive and shingled Moho are single-phase events that are associated with a thin MTZ [e.g., *Brocher et al.,* 1985; *Nedimović et al.,* 2005]. The difference in their seismic response is that an impulsive Moho is laterally continuous, whereas a shingled Moho response is broken into smaller sections that are vertically offset. A thick MTZ generates diffusive Moho reflection responses [e.g., *Brocher et al.,* 1985; *Nedimović et al.,* 2005] characterized by a multi-phase seismic response similar to the results from seismic modeling of Bay of Island ophiolites [e.g., *Brocher et al.,* 1985].

The MTZ reflection response was found to be 37% impulsive, 35% shingled, and 28% diffusive where Moho reflections were imaged (Figure 3.7b). If the Moho reflection response is single-phase and continuous for ≥2 km, the Moho type is characterized as impulsive. If the Moho reflection response is single-phase and segmented by vertical offsets into sections ≤2 km long, the Moho type is shingled. Figure 3.7a shows the uncertainty in Moho reflection picks. About 50% of the area where Moho reflections are imaged have high uncertainty in picking with 116 ms of picking error, ~35% of the area have low uncertainty with 16 ms of picking error and the smallest area (~15%) has medium uncertainty in picking with 66 ms of picking error.

In the southern Cocos and Pacific plates (from ~9˚38'N to ~9˚40'N), the Moho reflection response is dominantly multi-phase, the S/N ratio is relatively low and picking the Moho reflections has high uncertainty (Figure 3.7).

In the central Pacific plate (from ~9˚42'N to ~9˚48'N), the Moho reflection response appears as an impulsive single-phase event that dips away from the ridge axis. The Moho reflections are easy to identify and the S/N ratio is high (Figure 3.7). The Moho reflection is continuous in segments >3 km with small (<150 m) disruptions between them. Picking Moho reflection has low uncertainty in this latitude range (Figure 3.7a).

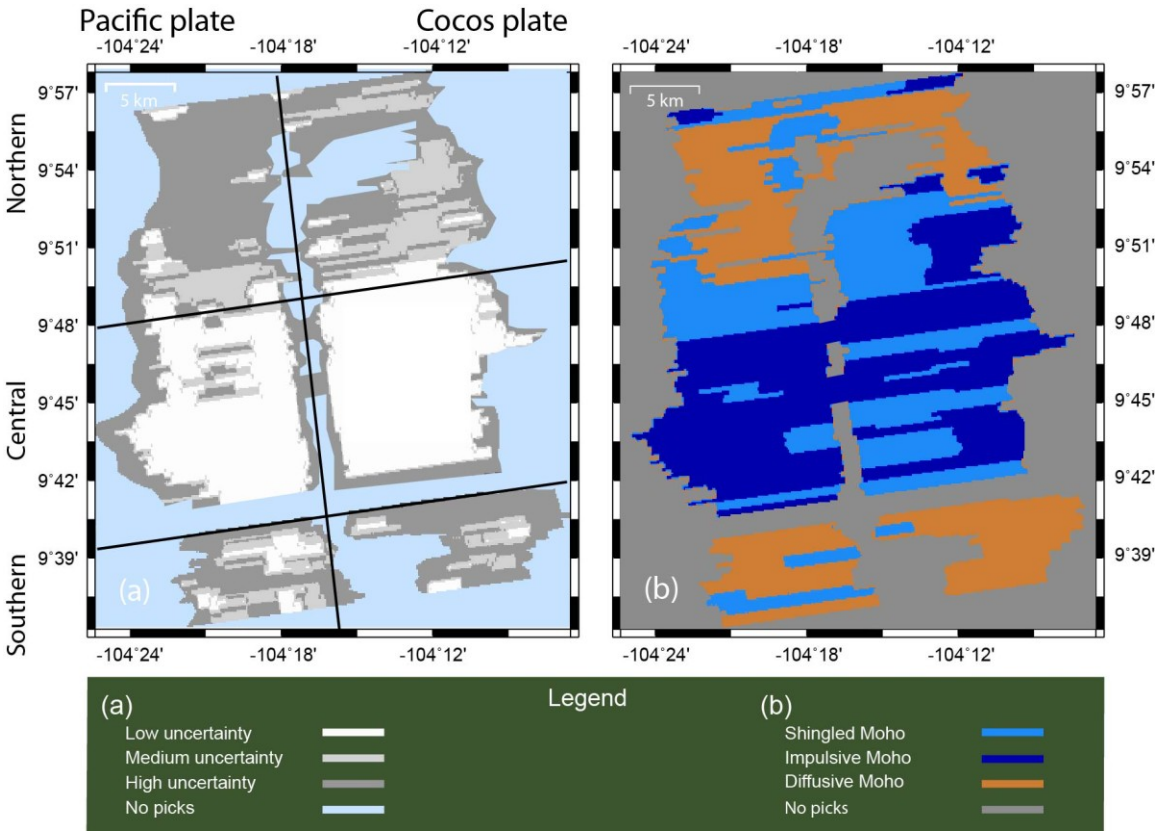

Figure 3.7 Moho transition zone reflection response maps showing: (a) pick uncertainty; (b) Moho reflection type. These maps were formed by analysis of in-lines and cross-lines extracted from the 3D migrated stack volume at every 600 m and 150 m, respectively. Thin black crossing lines in (c) divide the study area into northern, southern, and central sections.

For the northern Pacific plate (from ~9˚48'N to ~9˚56'N), the Moho reflection character is markedly different to that at southern latitudes on this plate. From ~9˚48'N to ~9˚50'N, the Moho reflection changes from a continuous, single-phase event to vertically offset events with segments ≤2 km long, which are interpreted as shingled Moho. At some locations, because of lower S/N ratio and overlapping segments, Moho picks are of higher (moderate) uncertainty. Further north on the Pacific plate (~9˚50'N to ~9˚56'N), the seismic character of the Moho response changes from a single-phase event to a multi-phase event, and the reflection strength weakens. The Moho reflection response is also

disrupted at intervals sometimes >1 km. In this area, where the MTZ is thick, picking uncertainty is highest. The area from ~9˚56'N to ~9˚57'N, at the northern edge of the 3D box, appears to be transitional with the Moho reflection response returning to mostly shingled and impulsive. However, the reflection strength and S/N ratio are variable and pick uncertainty is mostly high.

Moho reflections are identified occasionally below the AML. From south to north, the Moho appears below the AML at ~9˚38.5'N, ~9˚45'N, ~9˚50'N, and ~9˚54.5'N. Sample profiles where the Moho reflections are identified below the AML along in-lines 2272 and 1592 are shown in Figures 3.6a, c.

Areas where Moho is not visible occur on the Cocos and Pacific plates, and below the AML. From ~9˚38'N to ~9°39'N, and from ~9°39'N to ~9°40'N on the Cocos plate, the Moho is not imaged to ~5 km, and ~7 km distance from the ridge axis, respectively (Figure 3.8a). From 9˚40.5'N to 9˚49.5'N on the Cocos and Pacific plates, the Moho can be identified to ~450 m from the edges of the AML and at some locations it extends below the AML. From 9˚49.5'N to ~9˚52'N on the Pacific plate, there are ~1- to 2-km-wide gaps in the Moho reflections at ~5 km distance away from the ridge axis. From ~9˚52'N to ~9˚55'N on the Cocos plate, the Moho disappears from ~1 km to ~7 km distance from the ridge axis. On this plate, Moho is not imaged in a ~1-km-wide area at ~9˚55.5'N.

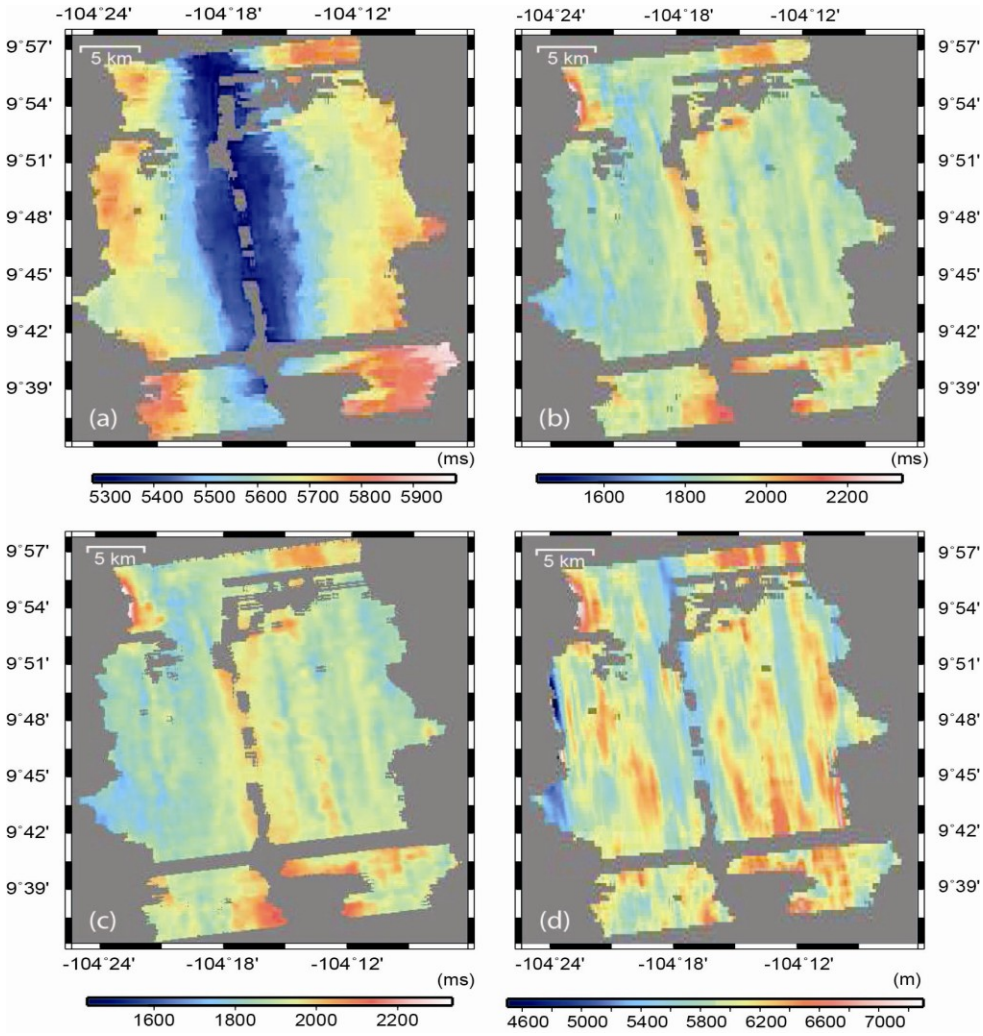

Figure 3.8 Crustal thickness variation in the study area: (a) Moho reflection TWTT map; (b) Crustal TWTT map before and (c) after smoothing; (d) Crustal thickness after converting the TWTT values to depth using the updated interval velocity volume. These maps were formed by interpolating and extrapolating the picked Moho reflection response information for up to 700 m and 350 m between and away from the data points, respectively.

3.4.3 Crustal Thickness

After running the second pass of 3D PreSTM using the updated velocity model of Figure 3.5c and creating the migrated volume from the CIGs detailed in section 3.2, the first negative break of the energy reflected from the seafloor, Moho, AML and OAMLs were picked manually on every 8 in-lines (300 m) on the migrated volume. The gridded

surfaces created from the manual picks using the minimum curvature method are shown in the opaque seismic volume of Figure 3.9 for the northern area.

Figure 3.8 shows (a) the Moho reflection TWTT, (b,c) crustal TWTT (TWTT from seafloor to Moho), and (d) crustal thickness. The minimum curvature method was used for creating the gridded maps. Because of the difference between the onset of the arriving energy and the first negative pick, picking-related adjustments are introduced to the crustal TWTT. The delay at the seafloor is ~5 ms where the dominant frequency is ~50 Hz and it is ~18 ms at Moho level where the dominant frequency is 14 Hz. To remove this error, ~13 ms is subtracted from the crustal TWTT values which is equal to 41 m, assuming an average velocity of 6320 m/s for the crust.

Figure 3.8b shows that the crustal TWTT variations in the cross-axis direction, along the flow-lines, are more pronounced than the crustal TWTT variations along the isochrones in the along-axis direction. The crustal TWTT variations in the cross-axis direction on the Cocos plate form a stripped pattern in the along-axis direction. Excluding the area in the vicinity of Lamont seamount, the largest crustal TWTT in the axial zone is observed in the area between ~9˚37.5'N and ~9˚41'N.

A locally weighted polynomial regression filter (600 m wide across the axis and 250 m long along the axis) was applied to Figure 3.8b with results shown in Figure 3.8c. After smoothing the crustal TWTT, both maps (Figures 3.8b and 3.8c) show a distinct pattern where largest crustal TWTT variations are across-axis.

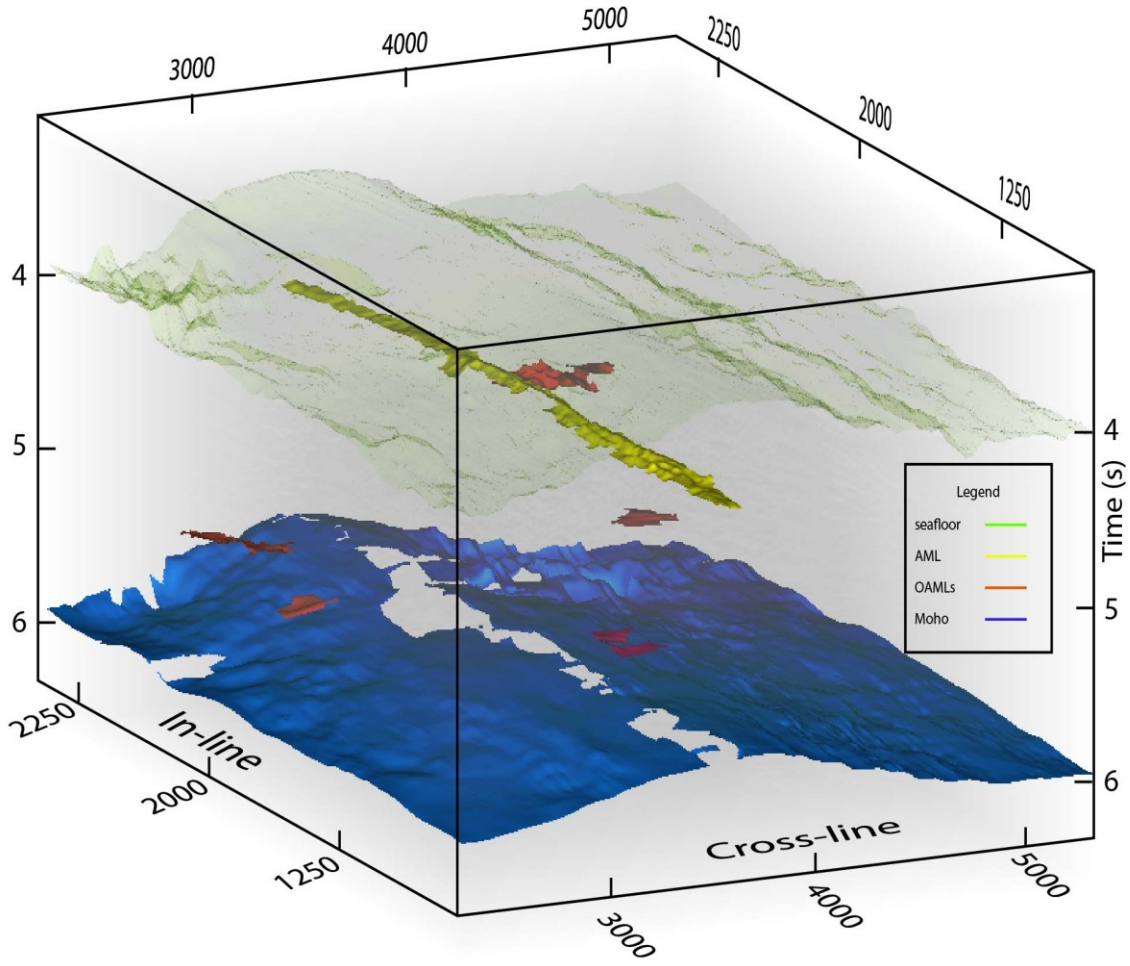

Figure 3.9 Opaque 3D PreSTM seismic volume of the northern box where the surfaces created from picking Moho, OAMLs, AML and seafloor are shown. Minimum curvature method was used for building the surfaces. Moho surface was smoothed by using a locally weighted polynomial regression filter.

In Figure 3.7a, the study area is divided into southern, central and northern Cocos and Pacific plates. The statistical and error analysis for crustal TWTT (Table 3.3) was performed for the areas shown in Figure 7a, their combination, each ridge flank and the whole study area. The 750-m-wide circular stripe close to the Lamont seamount is excluded for statistical and error analysis. The mean crustal TWTT for the Cocos plate is 1.9 s, decreases to 1.86 s on the Pacific plate, and averages 1.88 s for the whole study

area (Table 3.3). The central- and northern-Pacific display the minimum mean crustal TWTT, 1.85 s, and the maximum crustal TWTT, 1.95 s, is displayed by the southern-Cocos. Standard deviation varies from 50 to 70 ms and the average propagated error varies from 47 to 55 ms with an average value of 52 ms for the entire area.

Table 3.3 Computed crustal TWTT range and mean with associated standard deviation and average propagated error for the investigated section of the EPR, Pacific and Cocos plates, and various parts of the study area.

Plate section	Range (s)	Mean Value (s)	Standard deviation (s)	Standard error (ms)
Southern Cocos	1.75-2.17	1.95	70	55
Central Cocos	1.7-2.02	1.9	50	47
Northern Cocos	1.65-2.25	1.9	70	50
Southern Pacific	1.76-2.15	1.93	70	55
Central Pacific	1.65-2.02	1.85	70	47
Northern Pacific	1.62-2.11	1.85	60	55
Southern Cocos & Pacific	1.75-2.17	1.94	70	55
Central Cocos & Pacific	1.61-2.25	1.88	70	47
Northern Cocos& Pacific	1.61-2.25	1.87	70	55
Pacific	1.61-2.14	1.86	70	50
Cocos	1.65-2.25	1.9	60	50
Cocos and Pacific	1.61-2.25	1.88	70	52

The crustal thickness (Figure 3.8d) is computed by depth converting the smoothed Moho TWTT using the 3D velocity model developed from performing the MVA analysis detailed in section 3.3.1.

Results of statistical and error analysis for the computed crustal thickness shown in Figure 3.8d are summarized in Table 3.4. Statistical and error analysis was performed for the whole study area and sub-areas as described for crustal TWTTs. The crustal thickness decreases from 5970 m on the Cocos plate to 5850 m on the Pacific plate, with a mean

crustal thickness of 5920 m for the whole study area (Table 3.4). The northern Pacific section has the thinnest average crustal thickness of 5790 m and the average crustal thickness is highest on the southern Cocos plate (6070 m). The combination of southern Cocos and Pacific plates has a mean crustal thickness of 6030 m.

Table 3.4 Computed crustal thickness range and mean with associated standard deviation and average propagated error for the investigated section of the EPR, Pacific and Cocos plates, and various parts of the study area.

Plate section	Range (m)	Mean Value (m)	Standard deviation (m)	Standard error (m)
Southern Cocos	5420-7000	6070	250	350
Central Cocos	5040-7200	5980	290	300
Northern Cocos	5030-7100	5900	290	300
Southern Pacific	5280-7200	5980	200	350
Central Pacific	4560-7600	5850	290	300
Northern Pacific	3960-6600	5790	290	350
Southern Cocos & Pacific	5280-7000	6030	240	350
Central Cocos & Pacific	4560-7600	5840	300	300
Northern Cocos& Pacific	3960-7100	5860	300	350
Pacific	3960-7600	5850	280	300
Cocos	5030-7120	5970	290	300
Cocos and Pacific	3960-7600	5920	290	320

For error analysis I assign 16, 66 and 116 ms picking errors for zones of low-, mid- and high-uncertainty in determining Moho reflection arrival times (see Figure 3.7a), respectively, and for picking seafloor I assign an 8 ms error. The error for the velocity models is 280 m/s, and the average crustal velocity used for calculating systematic error is 6320 m/s (Table 3.1). The calculated crustal thickness errors vary from 260 m to ~500 m with a mean value of 320 m (Table 3.4). Error values of 250-350 m, 350-450 m and 450-550 m in crustal thickness cover 14%, 82% and 4% of the study area, respectively.

3.5 Discussion

In the following sections, I discuss the results to explain: (1) the age of oceanic Moho formation; (2) the source and origin of the off-axis LVZs; (3) the reason of different crustal thickness estimates from the MVA and OBS velocity models; (4) the source of different average crustal thickness from reflection and wide-angle OBS studies in the study area; (5) the crustal style of accretion; and (6) the source of third-order ridge segmentation.

3.5.1 Moho Formation at Zero-age Crust

It is not yet clear why the Moho is not visible below the AML. This could be due to either a) the pervious imaging methodology is not adequate for the ridge environment, or b) the Moho is not formed at the same time as much of the crust. These possibilities are discussed below.

The results from 1D waveform modeling by *Xu* [2012] show that the AML at ~9°43'N contains 95-100% melt and it includes 40-45% melt at ~9°49'N. The P-wave attenuation factors for the upper crust at these two locations are significantly different. At ~9°43'N, the P-wave attenuation of the upper crust is five times greater than the same at ~9°49'N [*Xu*, 2012]. Given that the Moho is not identified below the AML at 9°43'N (Figures 3.8, 3.10) where the upper crust seismic attenuation is high, and that clear images of Moho are obtained at 9°49'N, where the upper crustal seismic attenuation is relatively low, it is concluded that higher attenuation of the seismic P-wave at the upper crust at 9°43'N could be the main reason for Moho not being imaged below the AML at this location.

The Moho is not identified below the AML at ~9°42'-45'N, 9°46.5'N, 9°48'N, and 9°51'-52'N (Figure 3.8). These areas coincide roughly with melt-rich AML zones along the ridge axis at ~9°42'-9°44'N, 9°47'N-9°48'N, and 9°51'N-9°52. These melt-rich areas are inferred from the analysis of P- and S-wave partial stacking, and they contain 90-100% melt [*Xu*, 2012]. The P-wave attenuation of the upper crust at these locations is not known except at 9°43'N. Since the estimated amount of melt for the AML at these locations is similar to the AML melt content at 9°43'N, and the Moho is invisible below them (Figure 3.8a), it is concluded that the P-wave energy is highly attenuated in the upper crust for these areas. The reason for lateral changes in upper crust attenuation is not clear and it is beyond the scope of this work. However, lower attenuation could be caused by more efficient heat removal from the upper crust since the attenuation quality factor is strongly dependent on the temperature [*Kampfmann and Berckhemer*, 1985].

In a ridge environment where the velocity changes laterally [e.g., *Canales et al.,* 2012], and the seismic energy is attenuated significantly [e.g., *Wilcock et al.,* 1996], improved processing sequences and high quality data can have a profound effect on imaging the Moho reflection. From the seismic images of Moho below the AML (Figure 3.8b) and the occurrence of high attenuation zones in the upper crust, it seems that the Moho reflection is invisible below the AML where the P-wave is highly attenuated in the upper crust. This implies that the Moho is a feature which forms contemporaneously with the oceanic crust [*Stoffa et al.,* 1980] and its disappearance below the AML on seismic sections is because of the seismic energy being highly attenuated and not because of the absence of Moho.

3.5.2 Explaining the On- and Off-axis LVZs

In the velocity maps (Figures 3.5d, 3.10c), two LVZ are identified. One of the LVZs is observed in the axial area, and the other is at ~10 km east of the ridge axis (Figure 3.10c). While the source of the axial LVZ is known [e.g., *Dunn et al.,* 2000], the origin of the off-axis LVZ is not clear. In this section, the source of the off-axis LVZ is explained and the axial LVZ obtained from the MVA method is compared with the results from tomographic imaging.

In the axial area, the Moho reflections in the CIGs were flattened by decreasing the initial velocity. This formed the axial strip of negative residual RMS velocity (Figures 3.5b, c, 3.10c) known as the axial LVZ [e.g., *Canales et al.,* 2012]. The axial LVZ obtained from MVA in the study area is ~6 km wide and has an average velocity of ~6 km/s. Below the AML in this area, no Moho reflection is visible on the CIGs and finding the optimum velocity was not possible. Thus, an average velocity of 5.5 km/s was assigned to the areas where velocity could not be defined. This is the average velocity of the ESP-5 velocity function for the lower crust measured at the ridge axis [*Vera et al.,* 1990] at 9°34'N. The cross-axis width of the LVZ (~6 km) is comparable to that at 9°30'N (5-6 km) attained from seismic tomography [e.g., *Dunn et al.,* 2000]. However, the average velocity of ~6 km/s for the LVZ in the study area is ~8% higher than the 5.5 km/s velocity value reported by *Dunn et al.* [2000] for the LVZ at 9°30'N.

The source of an 8% difference in the estimated velocity comes from the method of measuring the velocity for the LVZ. The tomographic imaging provides 2D seismic velocity structure using reflection and refraction seismic phases whereas the MVA method provides an average velocity value.

Local zones of anomalously low S-wave velocities beneath the ridge axis of the EPR were found from compliance measurements at 9°48'N, 9°33'N and 9°03'N that were attributed to the presence of a mush zone in the lower crust [*Crawford and Webb*, 2002]. The lower-crust mush zone includes a minimum amount of 2.5% melt probably in connected films or tubes or in flattened sills [*Crawford and Webb*, 2002]. Two separate lower crust magma lenses are detected in the axial zone at ~9°48'N (Figure 3.10).

In addition to the axial LVZ, an off-axis LVZ at ~10 km from the ridge axis on the Cocos plate is detected in the study area (Figures 3.5d, 3.10c). The possibility that the LVZ is real conflicts with the results of a small aperture tomography experiment at 9˚50'N [*Tian et al.,* 2000], which shows that the average velocity of the upper 1.5 km of the crust decreases by ~0.4 km/s from ~7 km to ~10 km east of the ridge axis on the Cocos plate. For producing the observed off-axis LVZ in the crust, a velocity decrease of ~1.3 km/s in the upper 1.5 km of the crust is required, but this is not supported by the latter tomography experiment.

The second possibility for explaining the off-axis LVZ is the limitations of 3D PreSTM. For building the traveltime tables used in diffraction summation of Kirchhoff PreSTM, 1D raytracing is used where the velocity is assumed to be laterally constant. When the velocity model varies laterally or the seafloor changes abruptly, 1D raytracing fails in computing the geometry of diffraction hyperbola properly. Abrupt topography changes introduce traveltime delays at far offsets which result in reduced moveout velocities [*Kent et al.,* 1993]. The Moho reflections on CIGs appear as undercorrected events as a result of abrupt topography change and as a result the initial velocity needs to be reduced

for flattening the Moho reflection. These reduced RMS velocities produced a strip of off-axis LVZ in the interval velocity map (Figure 3.5d, 3.10c).

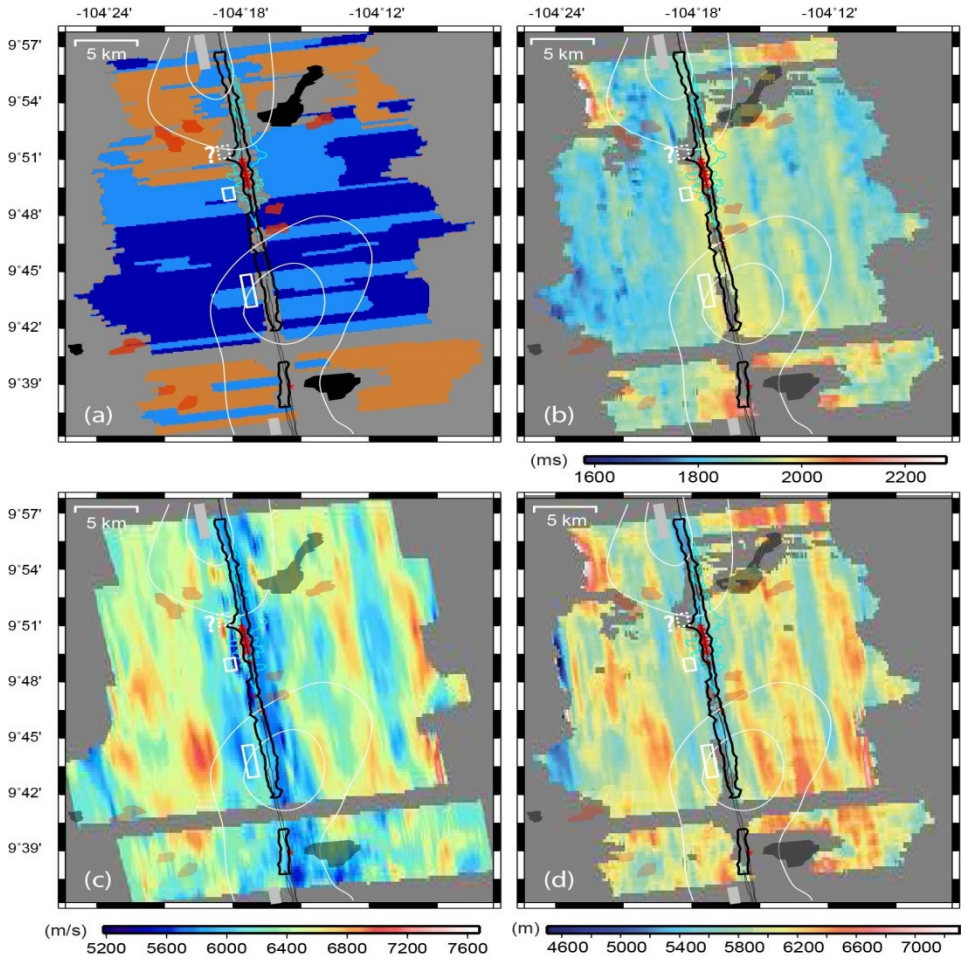

Figure 3.10 Moho transition zone reflection character (a), crustal TWTT (b), average crustal velocity (c) and crustal thickness (d) from this work, and their relationship with magmatic segmentation, hydrothermal activity and MLVZs. Third-order segment boundaries are shown with filled gray rectangles, fourth-order segment boundaries are shown with unfilled white rectangles, and the disputed third-order segment boundary is shown with the dashed white rectangle. Location of MLVZs shown with white contours is from *Toomey et al.* [2007]. Color scale is the same as Figure 3.7 for MTZ character. Source of other information same as in Figure 3.1.

In order to see whether these long wavelength average crustal velocity variations across the axis (Figure 3.5d) follow that of the seafloor bathymetry, the residual bathymetry, and the residual interval velocity were computed and overlaid (Figure 3.11c, f). Smoothing of

the seafloor and the average velocity maps were done using a Gaussian filter of 10 km length (Figure 3.11b, e). The residual seafloor bathymetry on the Cocos plate includes two axis-parallel zones of negative residual values in the order of ~100 m. These coincide roughly with the negative residual interval velocity contours suggesting that the long wavelength average crustal velocity variations across the axis, and the off-axis LVZ are an artifact of 3D PreSTM introduced by abrupt changes in seafloor depth.

3.5.3 Average Crustal Thickness

The average thickness of the crust in the study area (5920±320 m) on each of the plates (Cocos 5970±300 m and Pacific 5850±300 m) and on each individual section (Figures 3.8d, 3.10d and Table 3.4) agrees within the error bounds, suggesting a uniform crustal production in at least the last 180 Ka. Individual crustal thickness measurements, excluding outliers, vary beyond the estimated error limits with the thinnest (5030±300 m) and thickest (7200±300 m) crust giving a crustal thickness range of 2.17 km. This value is ~25% more than the crustal thickness variation (1.75 km) reported in chapter 2. It is about the same as the crustal thickness variation (2.3 km) estimated from the MCS study of *Barth and Mutter* [1996] for the second-order ridge segment between 9°15'N and 9°50'N, and it is about 20% more than the maximum crustal thickness range of 1.8 km for the latter latitude range estimated from the wide angle OBS study of *Canales et al.* [2003]. Combined, these studies show that the crust produced at second- and third-order segments of a fast spreading center is not of uniform thickness and the suggested 2D pattern of mantle upwelling at fast spreading centers [e.g., *Lin and Phipps Morgan*, 1992] is too simplistic. However, these crustal thickness variations are significantly less than the crustal thickness variations (~4 km) found along an individual segment of a slow

spreading center [e.g., *Canales et al.,* 2000] suggesting that a 3D pattern of mantle upwelling at fast spreading centers similar to slow spreading centers is improbable. An alternate hypothesis of 3D mantle upwelling with ductile deformation of the hot, lower crust, which smooths out initial differences in crustal thickness seems to apply to fast spreading centers [*Bell and Buck*, 1992].

The average crustal thickness in the study area (5920±320 m) obtained from the results of detailed MVA and 3D MCS reflection imaging in this work is about 3% larger than the average crustal thickness of 5.75 km estimated for our study area by *Barth and Mutter* [1996]. For the area between 9°42'N to 9°57'N, the average crustal thickness (5884±320 m), is ~2.4% larger than the same provided in chapter 2 (5740±320 m), and ~4% larger than crustal thickness of *Barth and Mutter* [1996] for this area. Despite the difference in thickness, the three results agree within the error limits.

In contrast to Chapter 2, crustal thickness can be determined for some areas below the AML and OAMLs (Figure 3.10d) forming an area of ~25 km^2 . However, crustal thickness has not yet been provided for some areas below the AML and OAMLs (Figure 3.8a, 3.10d) where the Moho reflection was not imaged (Figure 3.8a, 3.10b). Based on the discussion in section 3.5.1, it is likely that the Moho is formed at zero age and applying more advanced imaging techniques (e.g., Prestsck depth migratin) to this dartaset could provide the crustal thickness for the areas below the AML where Moho has not been imaged. Below the OAMLs, melt ascending from the uppermost mantle to the upper crust could have overprinted the MTZ.

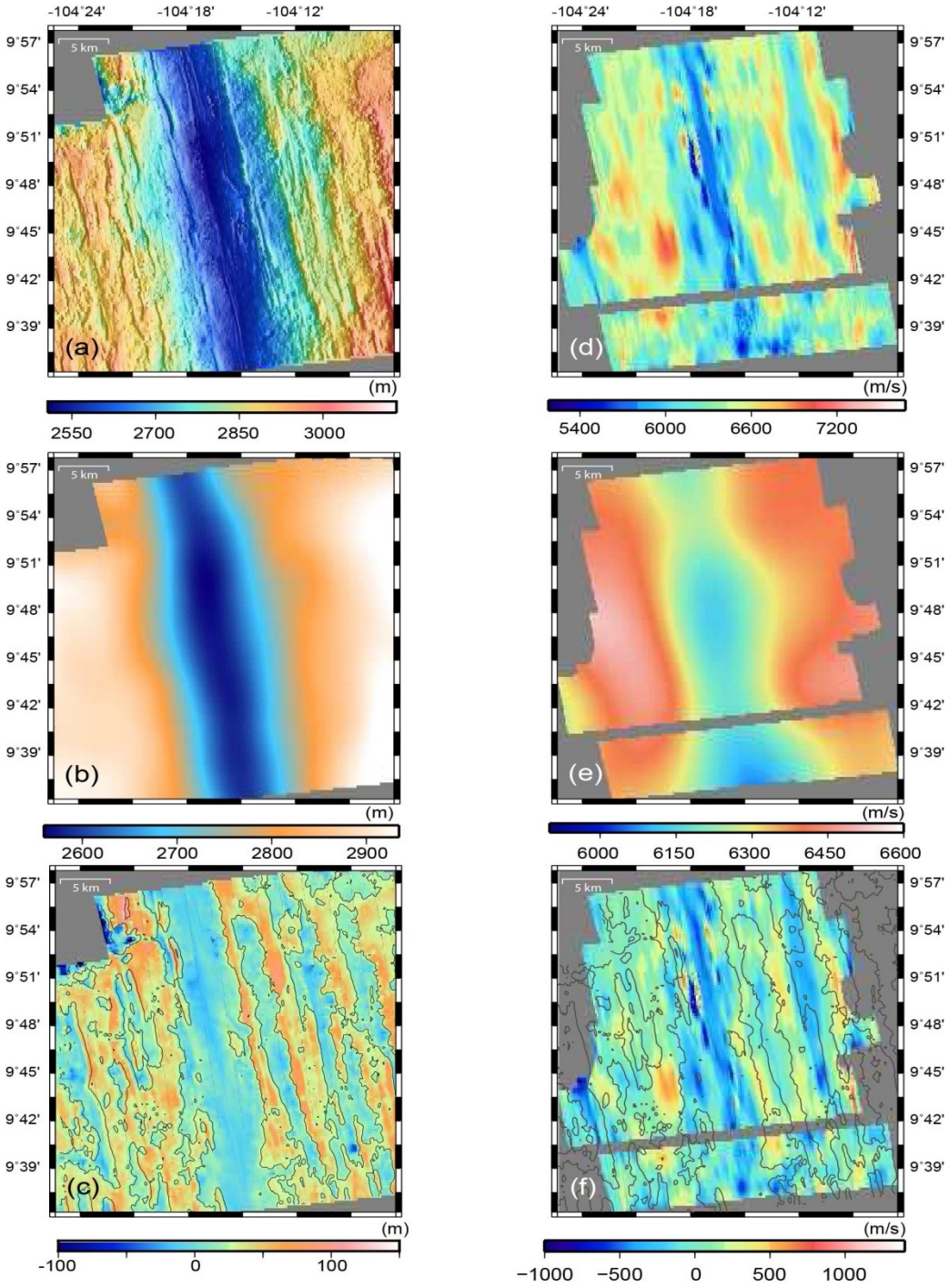

Figure 3.11 Residual interval velocity and seafloor depth in the study area: the seafloor depth in the study area before (a) and after smoothing using a 10-km-wide Gaussian filter (b), and their difference (c). The interval velocity at Moho level before (d) and after smoothing using a 20-km-wide Gaussian filter (e), and their difference (f) with the residual bathymetry contours of (c) overlaid.

3.5.4 Comparing the MCS-derived Crustal Thicknesses

The crustal thickness provided in Chapter 2 was computed by converting the crustal TWTT to depth using the 3D interval velocity volume determined by OBS velocity profiles. This crustal thickness is referred to as the poststack-derived crustal thickness. In this chapter the crustal thickness was computed by depth converting the crustal TWTT using the average velocity derived from MVA method. This crustal thickness is referred to as PreSTM-derived crustal thickness. Shown in Figure 3.12, is the difference between the poststack- and PreSTM-derived crustal thicknesses. The average crustal thickness difference is -165 m, with the minimum and maximum of ~-1000 m, and ~1000 m respectively. For most of the area between 9°42'N to 9°57'N, the poststack-derived crustal thickness is thinner than the PreSTM-derived crustal thickness. The poststack- and prestack-derived crustal thicknesses show marked differences along the ridge axis, at ~10 km of axis on the Cocos plate, and in an isolated area at ~5 km from the ridge axis on the Pacific plate (Figure 3.12c). What is the source of these crustal thickness differences?

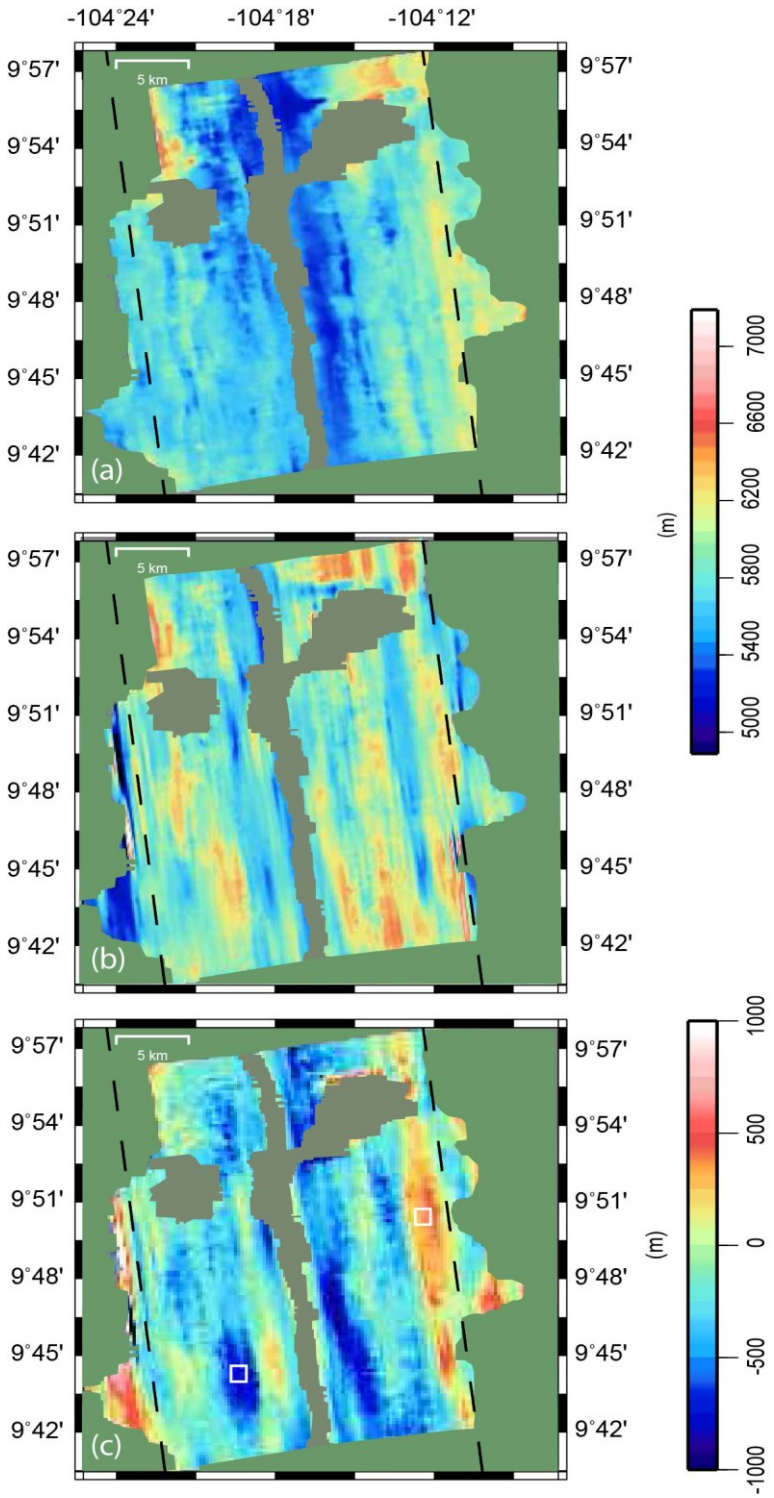

Figure 3.12 Comparing the crustal thickness computed from poststack migration (Chapter 2) and prestack migration. The computed crustal thickness of Chapter 2 from 9°42'N to 9°57'N (a), the same from this chapter (b), and their difference (c). The dashed lines show the OBS velocity profiles of *Canales et al.* [2003].

The difference between the crustal TWTT used for computing poststack- and PreSTM-derived crustal thickness is negligible (average value of 24 ms). This suggests that the velocity volumes used for depth conversion are the main source of difference between the poststack- and PreSTM-derived crustal thicknesses.

In order to see how the velocity models used for computing the poststack- and PreSTM-derived crustal thicknesses differ, two sample velocity functions were extracted from the interval velocity volumes used for computing these crustal thicknesses that are shown in Figure 3.13. The locations of these velocity functions are shown in Figure 3.12 with the white squares.

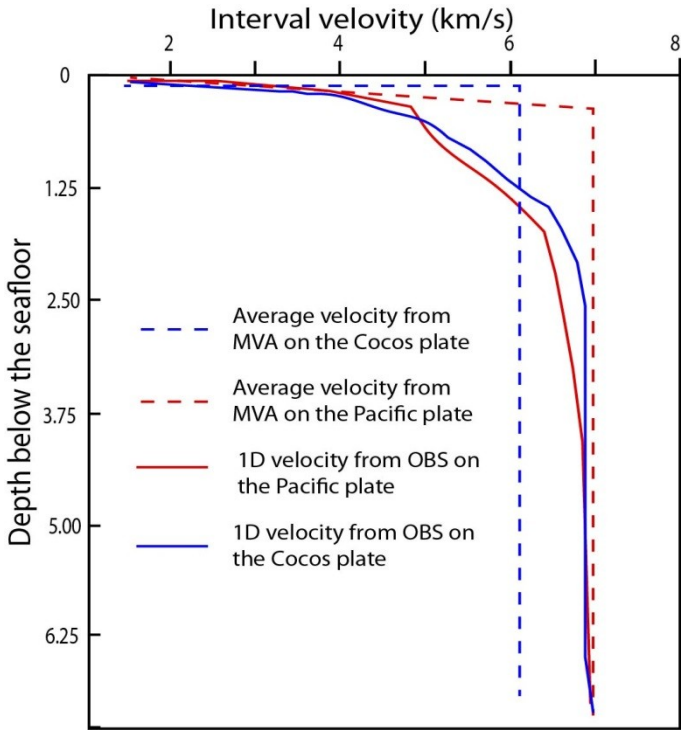

Figure 3.13 Sample 1D velocity function extracted from the 3D velocity volumes used for converting crustal TWTT to depth. The blue and red velocity functions are from the Cocos and Pacific plate, respectively with locations shown in Figure 3.12 with white squares. The velocity functions with constant velocity are from the 3D velocity volume computed from MVA, and the velocity functions that show variations with depth are from the 3D velocity volume built from OBS velocity profiles of *Canales et al.* [2003].

The 1D velocity function on the Pacific plate (solid red line in Figure 3.13), where the poststack-derived crustal thickness is thinner than the PreSTM-derived crustal thickness (Figure 3.12) includes a ~3-km-thick region where the velocity is ~7 km/s. At this location, the average velocity from MVA is ~7 km/s (dashed red line in Figure 3.13) for the entire crust.

The 1D velocity functions on the Cocos plate (solid blue line in Figure 3.13), where the poststack-derived crustal thickness is thicker than the PreSTM-derived crustal thickness includes a ~500-m-thick high-gradient region that is underlain by a ~1.3-km-thick layer with velocity of ~6.5 km/s. The average velocity used for computing the PreSTM-derived crustal thickness at this location (dashed blue line in Figure 3.13) is ~6 km/s for the entire crust and as a result the PreSTM-derived crustal thickness is thicker than poststack-derived crustal thickness at this location.

Given that the 1D velocity functions from wide-angle OBS study are much more geologically reasonable than the average velocities obtained from MVA method, in-situ crustal thickness differences between the prestack- and poststack-derived crustal thicknesses were expected. However, the average velocity measurements from the two methods agree within the error bounds. The average velocity of the crust in the study area (6320±170), and for each plate (Cocos 6300±160 and Pacific 6320±160) agrees within the error bounds with the average P-wave velocity of *Canales et al.* [2003] for the Cocos (~6200±200 m/s) and Pacific (~6350±200 m/s) plates for the upper 6 km of the crust in the study area. The average velocity for the 9°42'N to 9°57'N is 6330±170 which is ~1% smaller than the average velocity of 6395±200 m/s computed from OBS velocity profiles in Chapter2.

3.5.5 Comparison between OBS- And MCS-derived Crustal Thickness Measurements

The average crustal thickness of 6.8 km for the study area based on the wide-angle OBS results of *Canales et al.* [2003] is larger than those based on the MCS reflection data presented in this chapter. Several possible explanations are considered for these differences. First, the two datasets do not extend to the same crustal age. The 3D MCS area extends to 150 Ka old crust and the wide-angle OBS study is constrained by axis-parallel lines located on older, 300 Ka crust. Second, the wide-angle PmP arrivals come from rays turning within the MTZ and the thickness computed from these arrivals may correspond to the base of the MTZ. On the other hand, the Moho reflections observed in MCS reflection data represent the top of the MTZ. To investigate this, the OBS-derived crustal thicknesses along the best-constrained OBS velocity profiles of *Canales et al.* [2003] with the poststack- and PreSTM-derived crustal thicknesses are compared. The location of these OBS velocity profiles are shown in Figure 3.12 with dashed lines and the result of comparisons are shown in Figures 3.14 and 3.15. These figures show that the OBS-derived crustal thickness is larger than the crustal thickness measurements from reflection imaging. In Figure 3.14, the Moho is impulsive from 9°42'N to ~9°48'N (this is shown with the color shadings) and the MTZ is thin. In this latitude range, the OBS- and poststack-derived crustal thicknesses should be identical because the same OBS velocity values were used for depth converting the crustal TWTT in poststack-derived crustal thickness measurements. However, the difference between the OBS- and poststack-derived crustal thicknesses varies by ~750-1000 m on the Pacific plate, and between ~50-650 m on the Cocos plate (Figure 3.14c, f). On the Cocos plate (from 9°49'N to 9°57'N), the difference between OBS- and poststack-derived crustal

thicknesses becomes more stable and changes between ~150 m to ~350 m (Figure 3.14f), which is within the error bounds. These comparisons show that in the areas where MTZ is thick and picking the Moho TWTT is associated with higher uncertainty, the difference between MCS- and OBS-derived crustal thicknesses agrees within the error bounds. The uncertainty associated with identifying the onset of energy on the PmP arrivals in wide-angle OBS data could bias the estimated crustal thickness. These secondary arrivals could be masked by the coda of first arrivals, and it is possible that the PmP picks in the wide-angle OBS study are late with respect to the onset of the PmP phases, resulting in an overestimation of crustal thickness [*Canales et al.,* 2003]. From 9°42'N to 9°48'N on the Cocos and Pacific plate, the MTZ is thin and the uncertainty in picking the Moho TWTT is minimum (Figure 3.7a, 3.14c, f). In this area, the largest difference between the OBS- and poststack-derived crustal thicknesses is observed. This could be related to overestimation of the crustal thickness in the wide-angle OBS study because of the uncertainty in PmP picks.

The difference between the OBS- and PreSTM-derived crustal thicknesses is stable from 9°48'N to 9°57'N (Figure 3.15f). This stability in the difference between crustal thickness measurements could be caused by a reduction of 500 m/s in the average velocity of the crust due to the effect of approaching the Clipperton fracture zone. This may suggest that a combination of uncertainty in picking the PmP phases in wide-angle OBS data and the along-strike changes in the OBS velocity may explain the difference between the MCS- and OBS-derived crustal thicknesses in Figure 3.14 and 3.15.

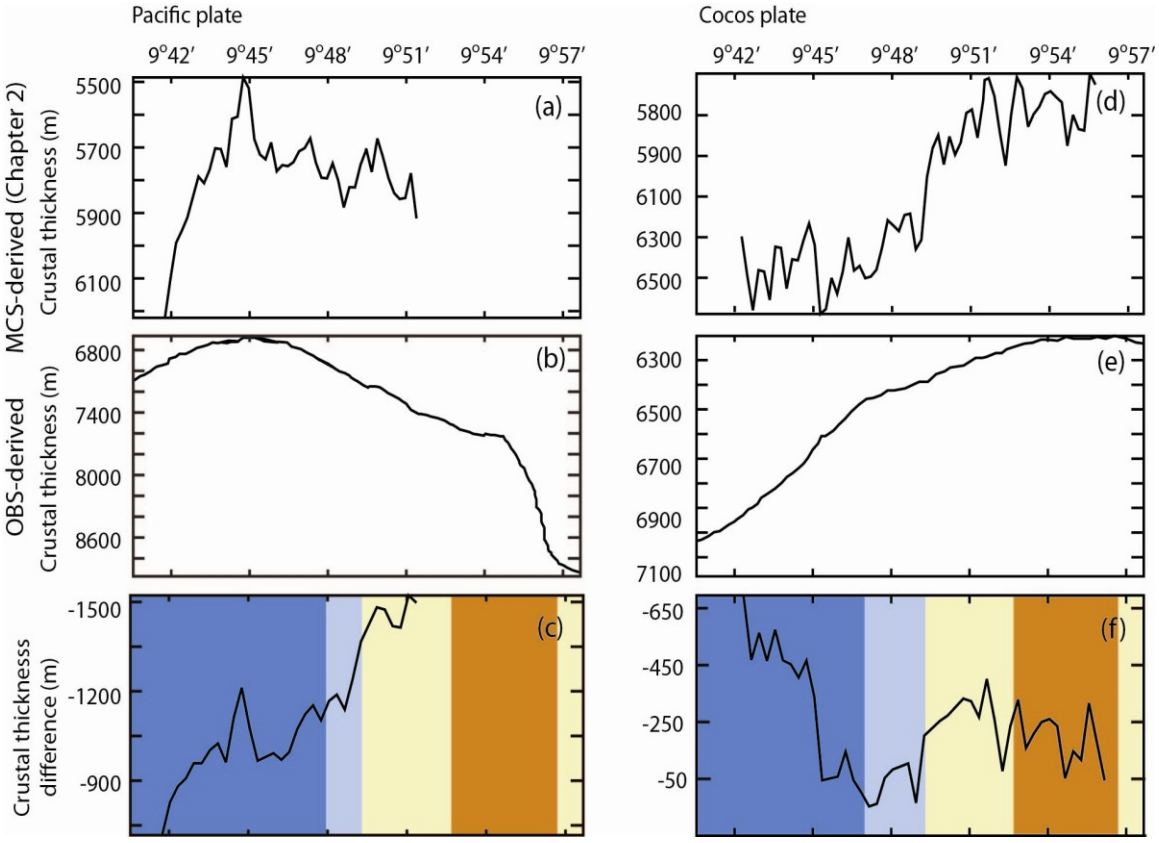

Figure 3.14 Comparing OBS- and MCS-derived crustal thicknesses. The MCS-derived crustal thickness from Chapter 2 along the OBS profile of *Canales et al.* [2003] on the Pacific plate (a), the OBS-derived crustal thickness along the OBS profiles of *Canales et al.* [2003] on the Pacific plate (b), and their difference (c). The MCS-derived crustal thickness from Chapter 2 along the OBS profiles of *Canales et al.* [2003] on the Cocos plate (d), the OBS-derived crustal thickness along the OBS profiles of *Canales et al.* [2003] on the Cocos plate (e), and their difference (f). The background color shows the type of Moho. Color coding is the same as Figure 3.7. The yellow color shows the transition from thin MTZ to thick MTZ.

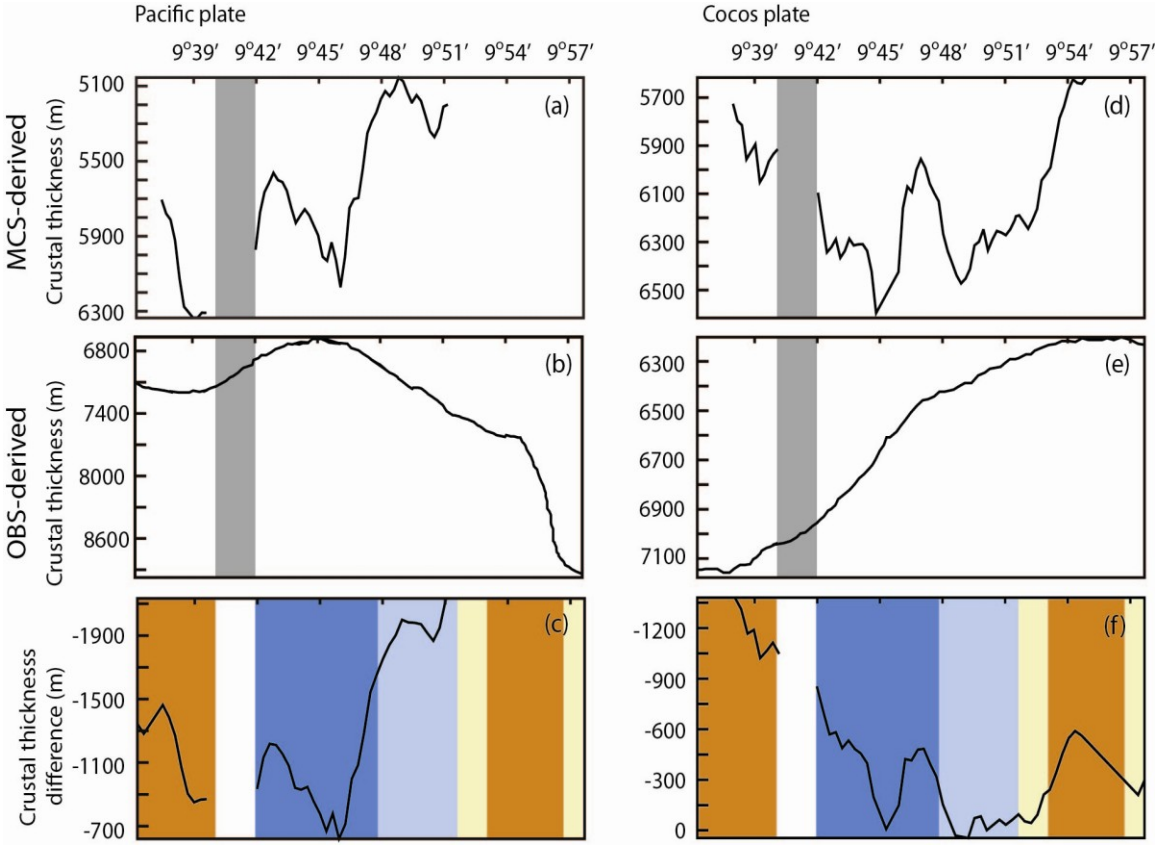

Figure 3.15 Comparing OBS- and MCS-derived crustal thicknesses. The MCS-derived crustal thickness from Chapter 3 along the OBS profile of *Canales et al.* [2003] on the Pacific plate (a), The OBS-derived crustal thickness along the OBS profiles of *Canales et al.* [2003] on the Pacific plate (b), and their difference (c). The MCS-derived crustal thickness from Chapter 3 along the OBS profile of *Canales et al.* [2003] on the Cocos plate (d), the OBS-derived crustal thickness along the OBS profiles of *Canales et al.* [2003] on the Cocos plate (e), and their difference (f). The background color show the type of Moho. Color coding is the same as Figure 3.7. The yellow color shows the transition from thin MTZ to thick MTZ. No data were collected for the white area in (c) and (f).

3.5.6 Crustal Thickness and Type of Moho Variations: Implications for Ridge Segmentation

The Moho transition zone character and the crustal thickness combined can provide complementary view on the ridge segmentation at fast-spreading ridges [*Aghaei et al.*, 2013, submitted]. The results from the latter study suggest that third-order ridge discontinuities are associated with major changes in the MTZ character and/or crustal

thickness while the MTZ character and crustal thickness do not show much variability at fourth-order ridge discontinuities. The relation between small-scale third- and fourth-order ridge discontinuities with crustal thickness and MTZ character is re-evaluated in light of the computed crustal thickness and mapped MTZ character for the area between 9°37'5'N to 9°57'N.

There are three third-order discontinuities centred at about 9º37'N, 9º51.5'N, and 9º57'N in the study area [*White et al.,* 2006; *Carbotte et al.,* 2013; *Aghaei et al.,* submitted]. Except the third-order discontinuity at 9°51.5'N, the other two discontinuities are not disputed. These undisputed discontinuities occur at the southern and northern ends of the study area where the most distinctive OAMLs are imaged, low-effusion rate volcanism is inferred [*White et al.,* 2002], low-temperature hydrothermal venting is observed, and the AML and the ridge axis are relatively deep (Figure 3.16a). The MTZ character and the crustal thickness show significant variations withon the undisputed third-order segment boundaries. The crust thickens sharply from 9°56'N to 9°57'N, and the MTZ thins. At the southern third-order segment boundary, both the near-axis crustal thickness and MTZ thicken. At the fourth-order segment boundaries centred at 9°49'N and 9°45'N, the MTZ is thin and the crustal thickness shows small changes. The lack of variation in MTZ character combined with small changes in crustal thickness at these fourth-order discontinuities may suggest that third-order ridge segments are not independent magmatic units. The results from crustal thickness and MTZ character seem to support the *Macdonald et al.* [1988] suggestion that third-order ridge segmentation in magma supply is related to the process of mantle melt extraction, whereas the smallest-scale fourth-order segmentation is driven by mid-crustal magma systems.

Given that the fourth-order segment boundaries in the study area are associated with minor changes in both MTZ and crustal thickness, the occurance of such a boundary at 9°53'N as suggested by *White et al.* [2006] is unlikely. The combined MTZ character and crustal thickness support the presence of the third-order segment boundary of *White et al.* [2002] at 9°51.5'N, since it falls in a region of major changes in both MTZ and crustal thickness (Figure 3.16).

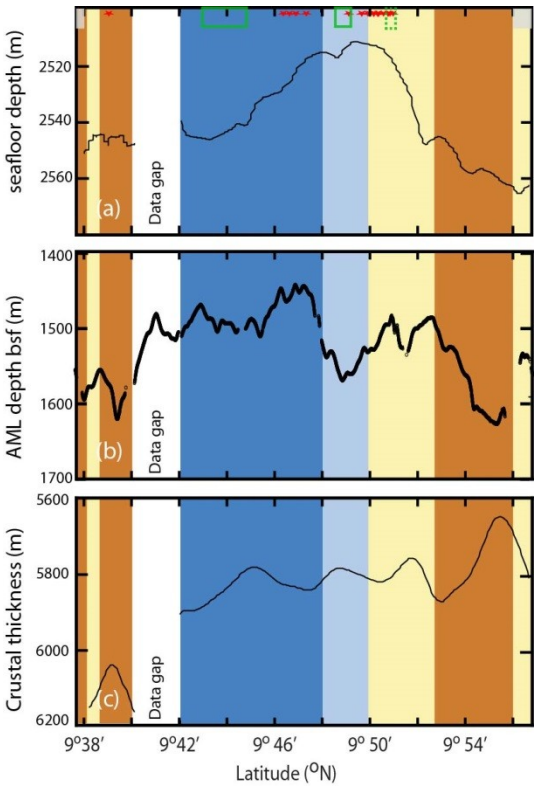

Figure 3.16 Relationship between the MTZ character (see Figure 3.7 for color shading) and: (a) axial seafloor depth; (b) AML depth bsf; (c) MCS-derived crustal thickness. The MCS crustal thickness in (f) is average crustal thickness for the area near the ridge axis (±0.5 to 3.0 km or crust ~10-55 Ka old). Third-order segment boundaries are shown with filled gray rectangles; fourth-order segment boundaries are shown with open green rectangles; debated third-order segment boundaries are shown with dashed green rectangles. Locations of discontinuities are from *Haymon et al.* [1991], *White et al.* [2002; 2006], *Carbotte et al.* [2013], and *Aghaei et al.* [2013, submitted]. The red stars show location of high-tempratre hyrothernal vents *from Haymon et al.* [1991]. The yellow color shows the transition from thin MTZ to thick MTZ.

3.6 Conclusions

The result of applying the state-of-the-art 3D PreSTM for the first time to the most high-resolution, multi-source and multi-streamer 3D MCS data thus far collected for any MOR environment has yielded the most detailed information to date on the MTZ character, crustal thickness, and average crustal velocity along the EPR between 9°37.5'N to 9°57'N, excluding a 3.3-km-wide gap between 9°40'N to 9°42'N. The MTZ was imaged, and the crustal thickness was computed for ~94% of the study area, with 37% impulsive, 35% shingled, and 28% diffusive reflection characteristics. Examination of 728 km^2 of the produced 3D reflection cube, and the average 3D velocity model provides new insight into the (1) age of Moho formation, (2) crustal thickness, (3) average crustal velocity, (4) ridge segmentation, and (5) style of crustal accretion across this section of the EPR.

(1) The average crustal velocity for the study area of 5920±320 m is ~3% larger than the average crustal thickness of 5.75 km estimated for the study area by an earlier 2D MCS study [*Barth and Mutter*,1996]. The average crustal thickness for the area between 9°42'N to 9°57'N (5882±320 m) is ~2.5 % larger than the same computed from poststack migration in Chapter 2. The average crustal thickness of 5920±320 m is significantly less than the OBS-derived average crustal thickness of ~6.8 km for the study area. The best agreement between the MCS- and OBS-derived crustal thickness estimates is observed where the MTZ is thick and picking Moho has high uncertainty. This suggests that the uncertainty associated with picking the PmP arrivals in wide-angle OBS studies could have introduced a bias in crustal thickness estimates. This may explain the ~1 km difference in the average crustal thickness between reflection and wide-angle OBS studies in the study area. The average crustal thickness computed in this work varies little

from Pacific to Cocos plate, as well as between the investigated sections of the study area suggesting a uniform crustal production in the last 180 Ka. However, the individual crustal thickness can vary by as much as 2.7 km. This crustal thickness variation is significant for the portion of the fast spreading ridge studied in this work showing that the sheet-like pattern of mantle upwelling is too simplistic for fast spreading centers.

(2) Moho reflection events are imaged for the first time at a limited number of locations below the AML away from any major discontinuities. The upper crust at the areas where Moho is imaged seems to have a significantly lower P-wave attenuation factor compared to areas where Moho is invisible below the AML. This may suggest that the absence of Moho reflections below the AML is likely due to seismic energy attenuation in the upper crust. This indicates that the oceanic Moho forms contemporaneously with the oceanic crust.

(3) The average crustal velocity is 6320±170 m/s. The axial LVZ is ~6 km wide with an average velocity of ~6 km/s. The average velocity for the 9°42'N to 9°57'N is 6330±170, which agrees with the average velocity of 6395±200 m/s computed from OBS velocity profiles for the same area within the error bounds.

(4) The two undisputed third-order discontinuities identified from high-resolution bathymetric maps of the EPR, geochemical investigations, tomographic images, and reflection images of the AML, are associated with major changes in MTZ character and near-axis crustal thickness. This suggests that the third-order segmentation is governed by melt extraction processes within the uppermost mantle.

CHAPTER 4 AVO CHARACTERIZATION OF THE TWO LARGE MID-CRUSTAL OAMLS AT THE EPR FROM 9º37.5'N TO 9º54'N

4.1. Introduction

On-axis magmatim and crustal accretion at intermediate-to-fast spreading mid-ocean ridges (MORs) are believed to occur in a narrow (~3 km) axial zone [e.g., *Herron et al*., 1978; *Detrick et al.,* 1987]. This accretion zone is characterized by a thin (<~200 m), elongated mid-crustal magma body known as the axial magma lens (AML) that sits atop of a ~5-10-km-wide low-velocity zone (LVZ) that extends to the base of the crust and uppermost mantle [e.g., *Vera et al.,* 1990; *Hussenoeder et al.,* 1996; *Dunn et al.,* 2000]. However, there is a growing body of evidence consistent with off-axis magmatism and therefore continuation of crustal accretion away from this narrow axial zone [e.g., *Goldstein et al.,* 1994; *Sims et al.,* 2003; *Crawford and Webb*, 2002; *Durant and Toomey,* 2009*; Canales et al.,* 2012*, Han et al.,* 2013, submitted]. *Durant and Toomey* [2009] attributed the observed P-wave diffractions, seismic attenuation, and the P-to-S wave converted phases about 20 km east of the East Pacific Rise (EPR) axis at 9°20'N to the presence of a melt lens about 2 km beneath the seafloor that is underlain by low-velocity, high attenuation crust. The results from seafloor compliance measurements at the EPR showed low-velocity partial melt zones 10 km east of the ridge axis at 9°48'N, and Moho-level melt sills about 2.5 km east of the ridge axis at 9°03'N [*Crawford and Webb*, 2002]. On the EPR ridge flanks, the results from petrological studies showed anomalously young basalts up to ~4 km from the ridge axis [e.g. *Goldstein et al.,* 1994; *Sims et al.,* 2003].

The strongest seismic evidence for off-axis magmatism has come from the results of a recent high resolution 3D multichannel seismic (MCS) reflection survey conducted between 9°37.5'N and 9°57'N on the EPR that has resulted in clear images of a network of upper- to mid-crust reflectors ~4-10 km away from the ridge axis [*Mutter et al.,* 2009; *Canales et al.,* 2012; *Aghaei et al.,* 2013, submitted, *Chapter3*]. These off-axis seismic reflectors were interpreted as melt lenses based on the reversed polarity of these reflection events relative to the seafloor and the Moho. Additional support for this interpretation came from ocean bottom seismometer (OBS) recordings that showed strong attenuation of the seismic waves propagating through the crust beneath the imaged reverse polarity reflection events [*Canales et al.,* 2012]. The melt content of these off-axis magma lenses (OAMLs) has not yet been determined, and it is not known if the mid-crustal AMLs and OAMLs are connected or not. Understanding the melt content of the imaged OAMLs can shed light on the dynamics of off-axis magmatism, a subject of current debate.

The physical properties of the mid-crustal axial magma body, including its melt content and composition, have been detailed using different methods. One-dimensional waveform inversion and 2D partial-offset stacking of the P-to-S converted waves reflecting off the AML are examples of such methods [e.g., *Singh et al.,* 1998; *Canales et al.,* 2006]. The 1D waveform inversion provides a quantitative measure of the in-situ melt content of the AML, and 2D partial-offset stacking has been used for qualitative estimates of along-axis variations in melt content of the AML. More recently, the applicability of the AVO crossplotting technique [*Castagna et al.,* 1998] for determining spatial variations in melt content of the AML was shown by *Marjanović* [2013].

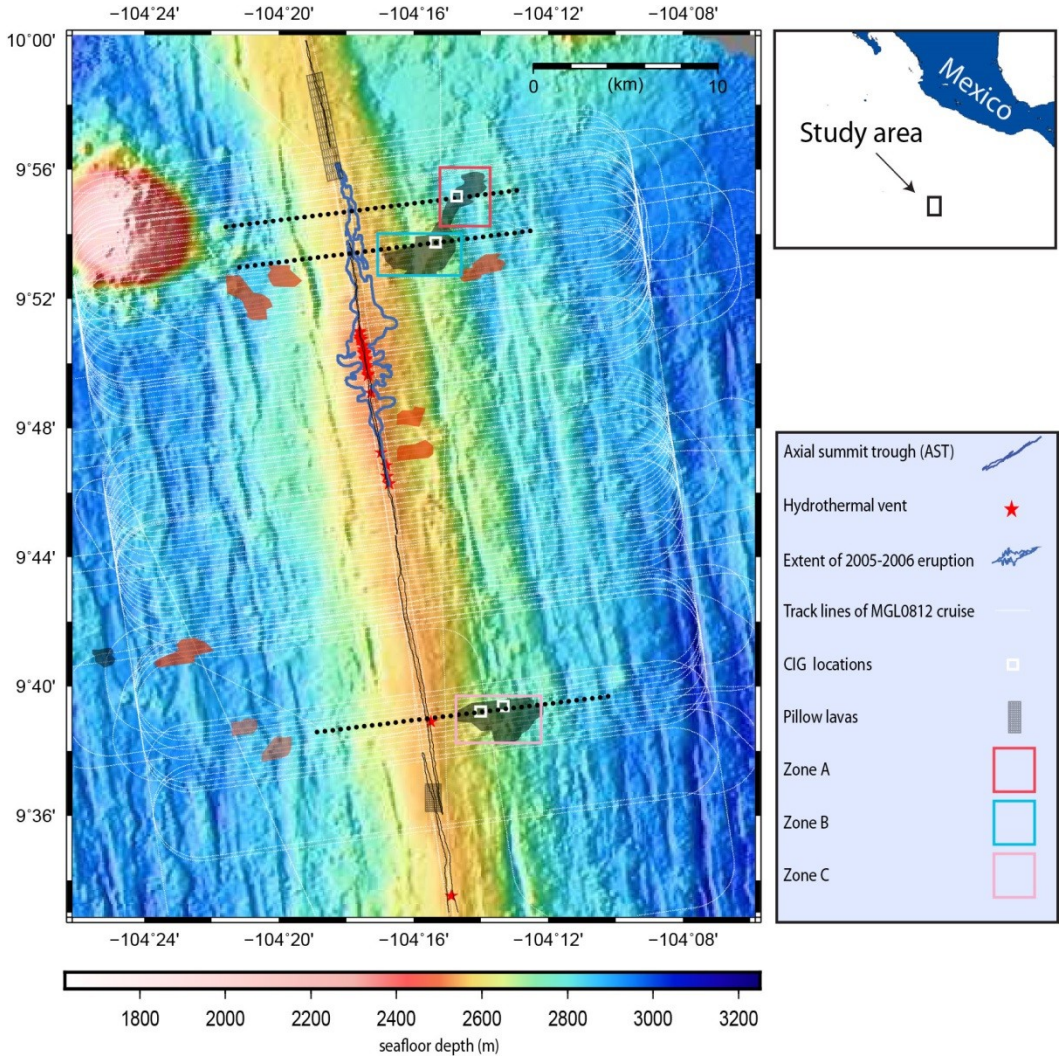

Figure 4.1 Ship track for cruise MGL0812 shown with thin white lines superimposed over the EPR bathymetry (color background) between 9°35'N and 10°N latitude. Four white squares show the location of the CIGs shown in Figures 4.2, 4.3 and 4.5. Dotted black lines show the surface trace of in-lines shown in Figures 4.2, 4.3, and 4.4 from the 3D migrated stack presented in Chapter 3. Lower- and upper-crust OAML locations are shown with red and black filled polygons, respectively. Locations and extent of pillow lavas are from *White et al.* [2002]. Hydrothermal vent locations are from *Haymon et al.* [1991] and the Marine Geoscience Data System. Axial summit trough (AST) is as interpreted by *Soule et al.* [2007]. Extent of 2005-2006 eruption is from *Soule et al.* [2009]. From north to south, the red, blue, and pink rectangles outline zones A, B, and C that are subject to this study.

In this chapter, partial-offset P-wave stacks and the Amplitude Variations with Offset (AVO) crossplotting technique have been used for assessing the melt distribution of upper-crust OAMLs in zones A, B, and C shown in Figure 4.1. The partial-offset P-wave

stacks provide a qualitative melt assessment, and the AVO crossplotting technique has been used to estimate the melt distribution of the OAMLs quantitatively. The results from comparing the AVO pattern of reflected signal from a single interface on synthetic common midpoint (CMP) gathers is very similar to the AVO pattern of the reflected signal from a ~40-m-thin layer [*Marjanović*, 2013]. The synthetic CMPs were computed using the modeled source wavelet of *R/V Langseth*. Since the thickness of AML in the study area is ~40 m [*Xu*, 2012], the single-interface approach for AVO analysis is used in this chapter. The velocity structure of the crust between the seafloor and the OAMLs, and between the upper- and lower-crust OAMLs has been determined where possible.

4.2. Data and Study Area

The first multi-source and multi-streamer 3D MCS data (MGL0812) covering a ridge magmatic-hydrothermal system were collected in the summer of 2008 along a 37-km-long section of the fast-spreading EPR between 9°37.5'N and 9°57'N [*Mutter et al.,* 2009] (Figure 4.1). The survey extends on both ridge flanks out to ~10 km away from the ridge axis, or to ~180 Ka-old crust as the spreading rate (11 cm/yr full rate) was stable during the last ~0.73 Ma [*Carbotte and Macdonald,* 1992]. The investigated portion of the EPR has been the subject of numerous geologic, geomorphic, geophysical, geochemical, and hydrothermal surveys and probably is the most investigated section of the global MOR system.

The axial zone of the EPR in this area is the most densely and the most frequently sampled portion of any MOR [e.g*., Perfit and Chadwick*, 1998; *Smith et al.,* 2001; *Goss et al.,* 2010]. In addition to the axial zone, the lavas erupted off axis are sampled at a limited number of locations [e.g., *Sims et al.,* 2003]. The off-axis lavas sampled to ~4 km

to either side of the crust from 9°48'N to 9°52'N at the EPR have U-series model ages that appear to be younger than those predicted by steady state spreading rate models [*Sims et al.,* 2003]. Anomalously young ages for most samples collected ~4 km away from the axial summit trough (AST) at 9°31'N at the EPR have been determined by means of ^{238}U-^{230}Th and ^{235}U-^{231}Pa dating techniques [*Goldstein et al.,* 1992; 1994]. These results suggest that a significant portion of the lavas were erupted some 4 km away from the axial zone.

A bright and almost continuous reflection originating from the mid-crustal AML and interpreted to mark the top of an axial magma chamber (AMC) characterized by a LVZ has been identified in the study area by earlier 2D MCS experiments [e.g., *Herron et al.,* 1980; *Detrick et al.,* 1987; *Harding et al.,* 1993; *Kent et al.,* 1993] and is clearly imaged with the 3D MCS data [*Mutter et al.,* 2009; *Canales et al*., 2012; *Aghaei et al.,* 2013, submitted] used in this study. This bright reflection is visible along the axis and lies at an average depth of 1.6 km bsf [*Carbotte et al.,* 2013]. The width of the AML reflector varies from ~0.5 to ~2.0 km in the study area [*Carton et al.,* 2010; *Aghaei et al.,* 2013, submitted]. The thickness of the mid-crustal AML has also been constrained by applying 1D waveform inversion. These results show that the AML is ~30 m thick at 9°40'N [*Collier and Singh,* 1997].

Intra-crustal OAMLs of variable shape and surface area have also been identified within the study area (Figure 4.1) [*Canales et al.,* 2012; *Aghaei et al.,* 2013, submitted, *Chapter 3*] using the same 3D MCS data analyzed in this work. The most prominent upper-crust OAMLs are observed to the east of the ridge axis on the Cocos plate [*Canales et al.,* 2012; *Aghaei et al.,* submitted] (Figure 4.1). The upper-crust OAMLs centred at ~9°38 on

the Cocos plate are imaged at an average TWTT of ~0.75 s below seafloor (bsf) and extend ~1.2 km to ~5.9 km distance from the ridge axis (Figure 4.1). Deeper reflection events at an average TWTT of ~1.3 s bsf are found below these OAMLs at ~2.5 km to ~5.0 km from the ridge axis. Two lower-crust OAMLs with an average TWTT of ~1.4 s bsf are found ~8 and ~10 km west of the ridge axis between ~9°37.5'N and 9°39'N (Figure 4.1). The upper-crust OAMLs to the east of the ridge axis between ~9°52'N and 9°56'N are observed 0.7-0.8 s TWTT bsf with the shallower ones closer to the ridge axis. A deeper OAML at ~9°52.5'N is present at ~7.5 km east of the ridge axis at ~1.35 s TWTT bsf. These OAMLs were reported by *Canales et al.* [2012]. The OAMLs to the west of the ridge axis between ~ 9°52'N and 9°53'N are lower-crust OAMLs centred ~5 km and ~3.5 km from the ridge axis at 1.22-1.75 s TWTT bsf, respectively. Two lower-crust OAMLs are found at ~9°48'N centered ~1.5 km from the ridge axis at 1.8 s TWTT bsf. The lower-crust OAML centred at ~10 km from the ridge axis at ~9°41'N on the Pacific plate appears at 1.64 s TWTT bsf.

Most recently, quantitative and qualitative constraints on the melt content of the AML were obtained by using high-resolution swath 3D MCS data collected from the Siqueiros to the Clipperton transforms [*Xu*, 2012; *Marjanović,* 2013]. *Marjanović* [2013] provided results on relative spatial variations in melt content of the magma lens along this first-order ridge segment by testing, for the first time, the applicability of the crossplotting AVO analysis technique [*Castagna et al.,* 1998] to MCS data collected over a ridge environment. From 2D partial-offset stacking of a subset of the swath 3D MCS data from 9°30'N to 10°N, *Xu* [2012] found four prominent 2-4-km-long melt-rich AML zones spaced 5-10 km from each other. Melt-poor sections with 12-20% of melt occupy 75% of

the 60-km-long portion of the EPR (9°30'N to 10°N) and melt-rich sections with 95-100% melt are present along 25% of its length.

4.3. Data Preparation for AVO Analysis

The dataset used in Chapters 2 and 3 has also been used for AVO analysis in this chapter. The data processing sequence applied for the AVO analysis was focused on preserving the relative amplitudes of the seismic data while retaining the broadest possible signal band. Since AVO equations are derived for a horizontally stratified earth, carrying out AVO analysis on common image gathers (CIGs) rather than on common midpoint (CMP) gathers is suggested [*Yilmaz,* 2001]. Based on these considerations, the chosen prestack data processing for AVO analysis included 1D bandpass filtering, 2D filtering using the LIFT approach [*Choo et al.,* 2004], offset-dependent spherical divergence correction, surface-consistent amplitude balancing and trace editing. The LIFT method was simplified so as not to include a signal-add-back step. These steps are detailed in Appendix A. After prestack data preparation, 3D Kirchhoff PreSTM was applied to the data. The migration aperture for running the 3D PreSTM was 2.5 km in the in-line and cross-line directions. During the Kirchhoff summation, the amplitudes were multiplied by true amplitude weights using the procedure of *Peles et al.* [2001] to recover the true reflection amplitudes. The resultant PreSTM gathers or CIGs were analyzed by applying LIFT to remove the noise masking OAMLs and Moho reflection events. The LIFT method is a robust amplitude-preserving approach and its application for noise removal is recommended when the target of processing is rock property estimation [*Choo et al.,* 2004].

For LIFT, the CIGs were first divided into low-frequency (0–8-15 Hz) and high-frequency (15-22–200-220 Hz) bands. A residual mid-frequency (8-15–15-22 Hz) range was obtained by subtracting the low and high frequency components from the full spectrum. An FX filter was applied to the low frequency band followed by a median filter applied to data in all frequency bands. All the individual frequency bands are summed at the end to give the processed CIGs. Details on the LIFT processing step can be found in Appendix B. The LIFTed CIGs were used for AVO analysis. The range of angle of incidence used for AVO analysis was limited to 30° because the Shuey approximation [*Shuey,* 1989] to the Zeoppritz equations used in this study is only valid for angles of incidence less than 30°. The angles of incidence were computed using the 3D velocity model developed in Chapter3. The AVO analysis was done for the upper-crustal OAMLs because the P-waves reflecting of the top of these reflection events exhibit high S/N ratio, which is not the case for deeper OAMLs. These high S/N ratio areas are shown in Figure 4.1 as zones (A), (B), and (C).

One of the potential problems during AVO analysis is the presence of non-flat CIGs that are a result of errors in the velocity moveout correction. This problem is handled during migration velocity analysis (MVA) in which the optimum migration velocity for each reflection event is found by flattening the reflection event along the offset axis of the CIGs. Flattening of CIGs during MVA is shown for sample CIGs in Figures 4.2, 4.3. and 4.4 from zones (A), (B), and (C), respectively. The location of these CIGs and their corresponding in-lines and cross-lines are shown in Figure 4.1. The background theory for MVA was explained in Chapter 3, and more details can be found in Appendix B.

In-line 2224 across zone (A) and a sample CIG ~6.5 km east of the ridge axis along this in-line are shown in Figure 4.2. The upper-crust OAML on this CIG is flattened (Figure 4.2b) by finding the optimum residual moveout (RMO) velocity that flattens the OAML reflection on this CIG (Figure 4.2e, f). By finding the RMO value, the average velocity between the seafloor and the upper-crust OAML at this point (~5500 m/s) is determined. In Figure 4.3, in-line 2128 across zone (B) and a sample CIG along this in-line ~4.8 km east of the ridge axis are shown. The flattened upper-crust OAML is shown in Figure 4.3b. Flattening by finding the optimum RMO value is shown in Figure 4.3e, f. The average velocity between the seafloor and upper-crust OAML at this point is ~5200 m/s. In Figure 4.4, in-line 1429 and two sample CIGs from zone C along this in-line located ~4 km and ~5.2 km east of the ridge axis are shown. The flattened upper-crust OAMLs are shown in Figure 4.4b, e. On the CIG closer to the ridge axis, upper- and lower-crust OAMLs are observed that can be used to determine the velocity between these features by finding the RMO value for both of these events (Figure 4.5a-f).

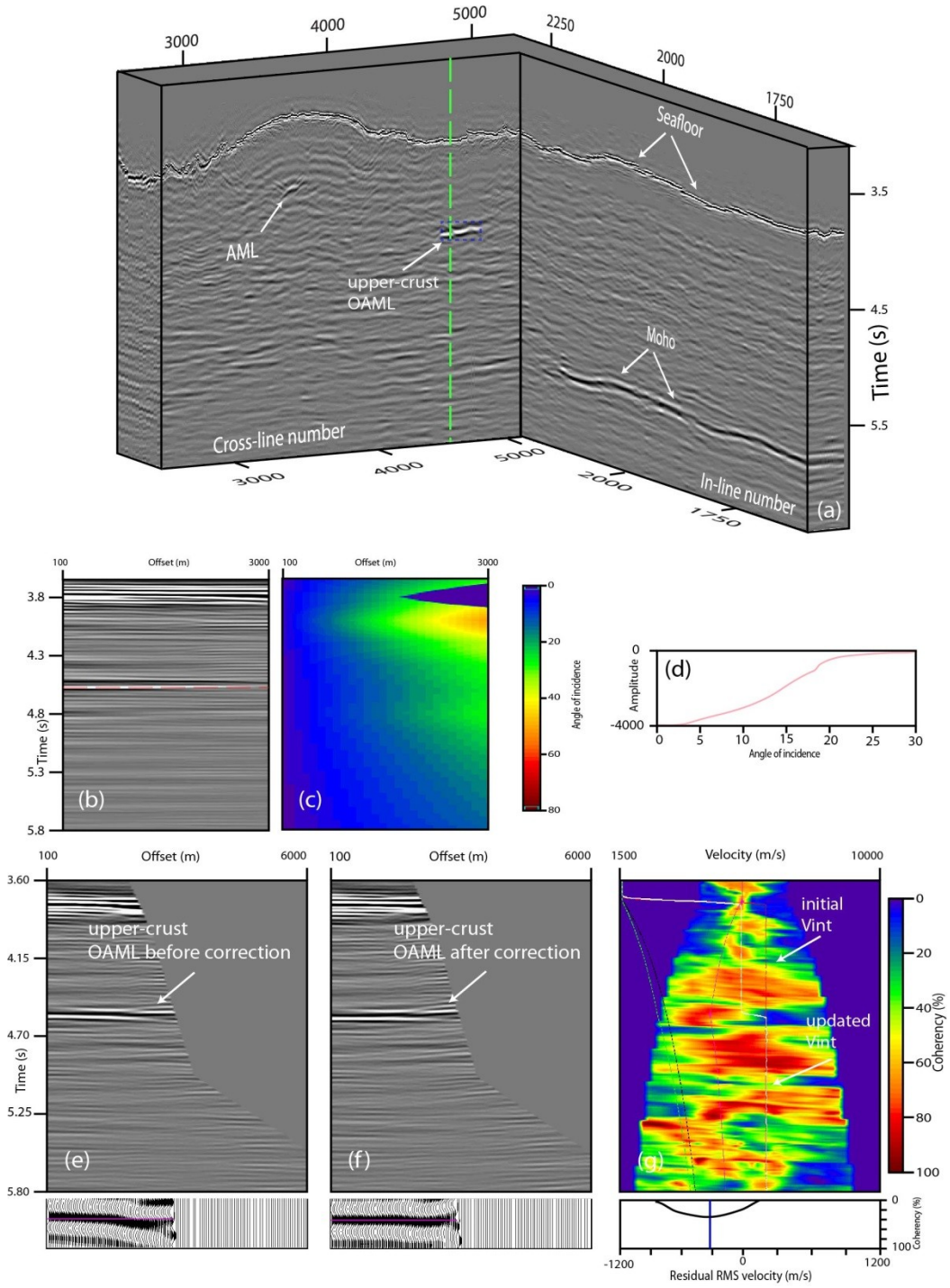

Figure 4.2 An in-line from zone (A) and a sample CIG on this in-line used for performing AVO analysis. a) In-line 2224 where the AML, upper-crust OAML, and Moho reflections are shown with white arrows. The green dashed line shows location of the CIG shown in (b) and (e). The dashed yellow rectangle shows the AVO analysis window in this zone. (b) and (c) are the CIG at cross-line 4552 and its corresponding angle of incidence, respectively. The maximum offset is limited to 3 km. (d) The amplitude variation with angle of incidence of the upper-crust OAML marked with dashed red line in (b). The same CIG of (b) with full offset before (e) and after (f)

flattening the OAML reflection by decreasing the RMS velocity by ~300 m/s. g) Velocity spectrum of (e) where the updated interval velocity is shown with white solid line and the updated RMS velocity is shown with green dashed line. The small boxes below (e) and (f) show the zoomed OAML reflection before and after updating the initial velocity, respectively. After decreasing the RMS velocity by ~300 m/s, the OAML event flattens. The small box below (g) shows the coherency of the picked event. The surface location of this CIG is shown in Figure 4.1 in Zone A.

4.4. AVO Analysis

Two semi-infinite isotropic homogenous elastic half spaces that are in contact at an interface are considered. Elastic parameters of V_{p1}, V_{s1} , and ρ_1 for the first (overlaying) medium, and V_{p2}, V_{s2} , and ρ_2 for the second (underlying) medium are assumed. For an incident plane wave in the upper layer, the reflection and transmission coefficients as a function of angle of incidence and six independent elastic parameters, three on each side of the reflecting interface, are described by the Zeoppritz equations [*Aki and Richards*, 1980]. The Zeoppritz equations were simplified by *Aki and Richards* [1980] for analysis of P-wave reflections assuming small changes in elastic parameters along the interface. For an angle of incidence smaller than 30°, *Shuey* [1985] showed that the P-wave reflection coefficient $R(\theta)$ can be approximated by

$$R\ \theta\ = A + BSin^2(\theta) \tag{4-1}$$

In this equation, (θ) is the angle of incidence, (A) is the AVO intercept, and (B) is the AVO gradient. This equation, known as Shuey's two-term equation is detailed in Appendix C. The AVO intercept (A) is the acoustic term and is a measure of the normal incidence amplitude, while the AVO gradient (B) is related to the average Poisson's ratio of the upper layer and lower layer [*Castagna and Swan,* 1997] and is a function of S-wave velocity.

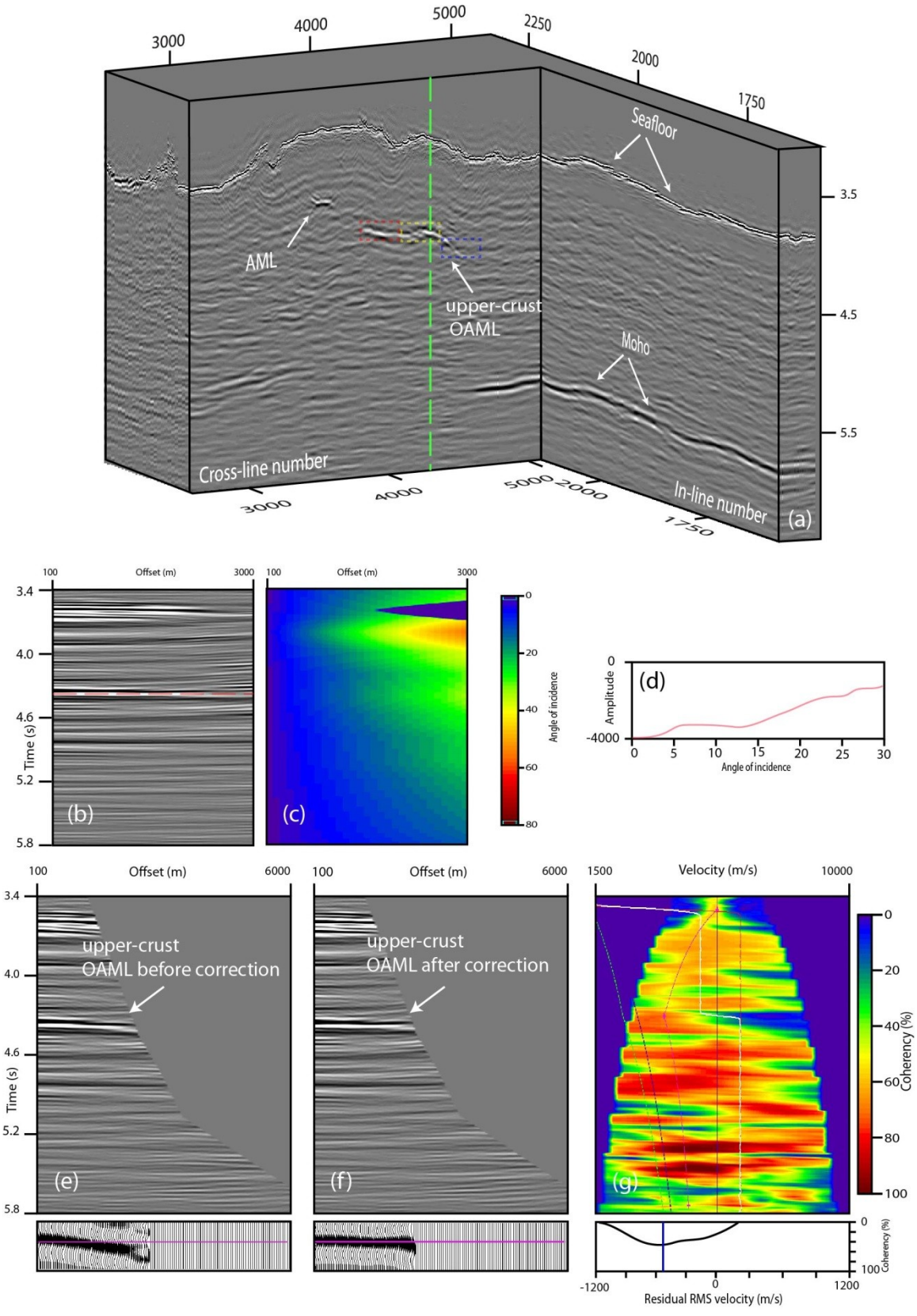
3000
4000
5000
2250
2000
1750
Seafloor
AML
upper-crust
OAML
Moho
3.5
4.5
5.5
Cross-line number
In-line number
(a)
Offset (m)
Time (s)
(b)
(c)
Angle of incidence
Amplitude
(d)
Angle of incidence
upper-crust
OAML before correction
upper-crust
OAML after correction
(e)
(f)
Velocity (m/s)
(g)
Coherency (%)
Residual RMS velocity (m/s)

Figure 4.3 An in-line from zone B and a sample CIG used for performing AVO analysis. a) In-line 2128 where the AML, upper-crust OAML, and Moho reflections are shown with white arrows. The green dashed line shows the location of the CIG shown in (b) and (e). The dashed blue, red and yellow rectangles show the AVO analysis windows. (b) and (c) are the CIG at cross-line 4288 and its corresponding angle of incidence, respectively. The maximum offset is limited to 3 km. d) The amplitude variation with angle of incidence of the event marked with red dashed line in (b). Common image gather at cross-line 4288 before (e) and after (f) flattening the OAML reflection by reducing the RMS velocity by ~500 m/s . g) Velocity spectrum of (e) where the updated interval velocity is shown in white solid line, the updated RMS velocity is shown with dashed green line, and the initial velocity is shown with solid red line. The small boxes below (e) and (f) show the zoomed OAML before and after picking, respectively. After decreasing the RMS velocity by ~500 m/s, the OAML event flattens.

Melt has a profound effect on the S-wave velocity of crustal rocks [*Anderson and Spetzler*, 1970; *Mavko*, 1980; *Carlson*, 2001] and it changes the AVO pattern of the P-wave reflected off a crustal melt lens (Figure 4.6). Shown in Figure 4.6 are the AVO pattern of the reflected P-wave from the top of a partially melted lenses (with Vp=3.0 km/s, Vs=2.0 km/s, and ρ=2700 kg/m^3) and the AVO pattern of reflected P-wave from the top of a fully melted lens (with Vp=2.9 km/s, Vs=0, and ρ=2700 kg/m^3) [*Murase and McBriney*, 1987]. For the background gabbro Vp=7.0 km/s, Vs=3.75 km/s, and ρ=2700 kg/m^3 [*Iturrino et al.,* 1991]. These theoretical results show that the decrease in amplitude with increasing angle of incidence of the reflected P-wave off a partial melt lens varies significantly as a function of melt content which suggest that the AVO analysis can provide some insight on the melt content of OAMLs.

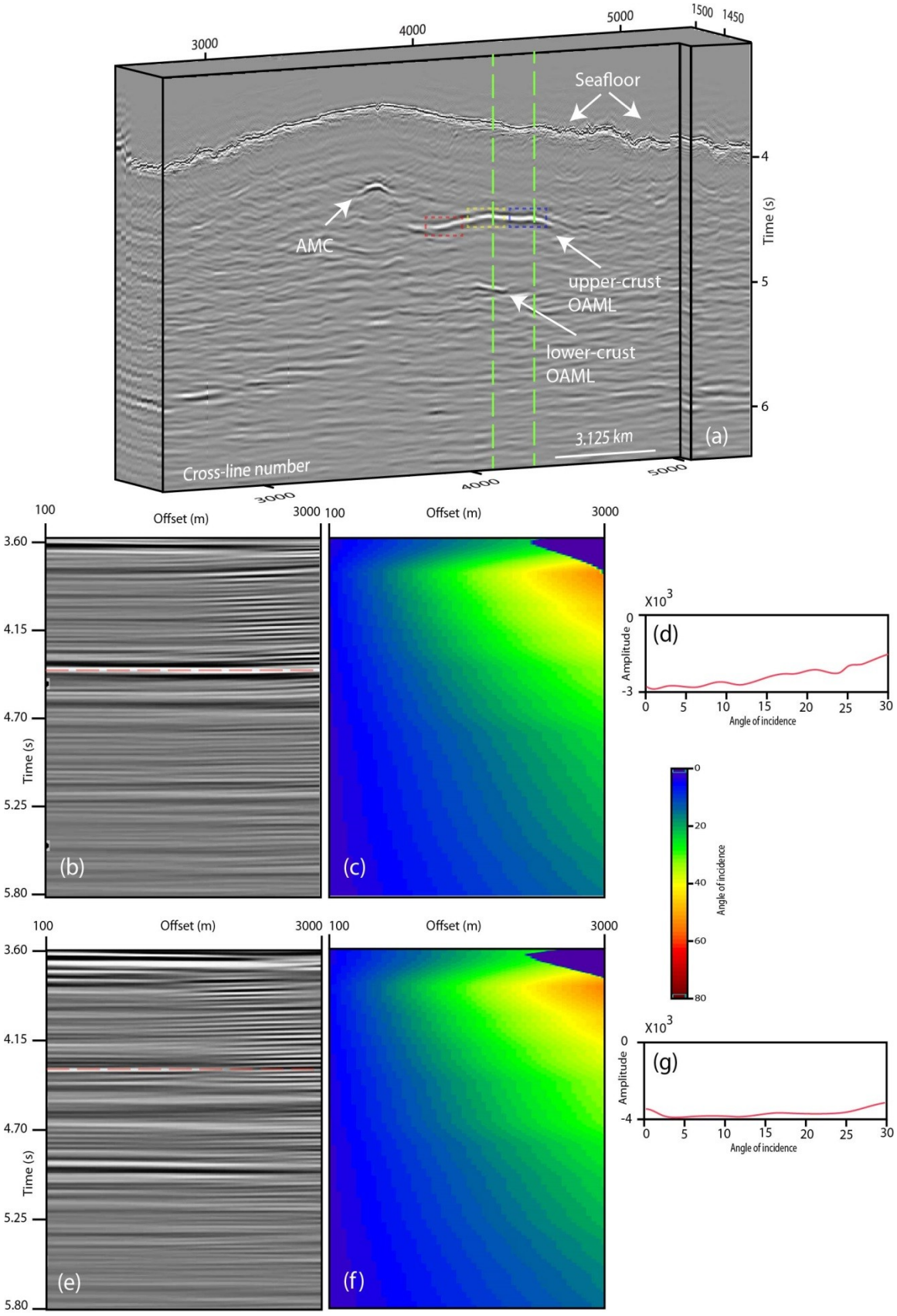
3000
4000
5000
1500
1450
Seafloor
AMC
upper-crust OAML
lower-crust OAML
3.125 km
(a)
Cross-line number
Time (s)
4
5
6
100
Offset (m)
3000
3.60
4.15
4.70
5.25
5.80
(b)
(c)
(d)
X10^3
Amplitude
Angle of incidence
(e)
(f)
(g)
0
20
40
60
80

Figure 4.4 An in-line from zone C and two CIGs used for performing AVO analysis. a) In-line 1429 where the AML, OAMLs, and Moho reflections are shown with white arrows. The dashed green line shows the locations of the two CIGs shown in (b) and (e). The dashed blue, red and yellow rectangles show the AVO analysis windows. (b) Common image gather at cross-line 4355 and its corresponding angle of incidence (c). (d) The amplitude variations with angle of incidence of the reflection event marked with dashed red line in (b). (e) Common image gather at cross-line 4163 and its corresponding angle of incidence (f). (g) The amplitude variations with angle of incidence of the reflection event marked with dashed red line in (e). The locations of these CIGs are shown in Figure 4.1 with the white squares in zone C.

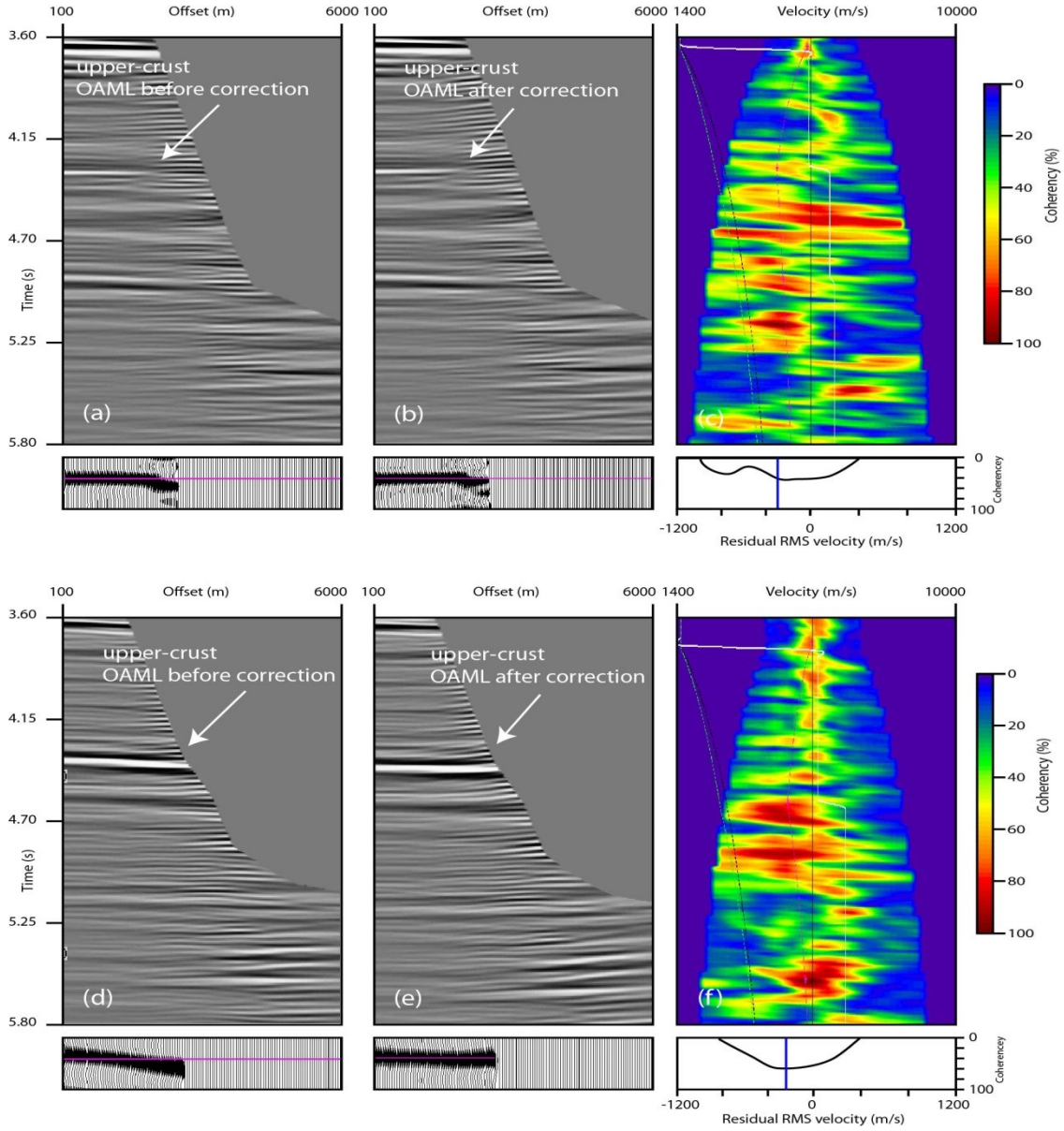

Figure 4.5 The two sample CIGs of Figure 4.4 and their corresponding velocity spectra used for performing MVA. a) Common reflection point 4163 where the OAML event is under corrected

because of too high initial velocity. b) Common image gather of (a) after flattening the OAML event by decreasing the RMS velocity. c) Velocity spectrum of (a) where the updated interval velocity is shown in white and the updated RMS velocity is shown in green dashed line. The small boxes below (a) and (b) show the zoomed OAML before and after picking, respectively. After decreasing the RMS velocity by ~370 m/s, the OAML event flattens. The small box below (c) shows the coherency of the picked event. d) Common image gather 4355 where the OAML event is under corrected because of too high initial velocity. e) Common image gather of (d) after flattening the OAML event by decreasing the RMS velocity. f) Velocity spectrum of (d) where the updated interval velocity is shown in white and the updated RMS velocity is shown in green dashed line. The small boxes below (d) and (e) show the zoomed OAML before and after picking, respectively. After decreasing the RMS velocity by ~370 m/s, the OAML event flattens. The small box below (f) shows the coherency of the picked event.

Two complementary AVO analysis methods are used in this chapter: P-wave partial stacking and the AVO crossplotting method. In the partial P-wave stacking method, limited angle stacks are created to perform AVO analysis. The results from this method are qualitative rather than quantitative but are commonly used and insightful. With defining background trends for different melt percentages using the Hashin-Shtrikman bounds [*Hashin and Shtrikman*, 1963], the results from the AVO crossplotting technique are interpreted quantitatively, as explained in more detail in Section 4.4.2. The two complementary methods of P-wave partial stacking and AVO crossplotting technique were used together to assess the melt content of the upper-crust OAMLs of zones A, B and C shown in Figure 4.1.

4.4.1 P-wave Partial-offset Stacking

Partial stacks provide a robust and quick way of evaluating AVO responses, and identifying anomalous regions along a given horizon [e.g., *Bacon et al.,* 2003]. In this method, sub-stack volumes are produced and they are inspected visually. Partial stacks are normalized by the number of contributions to each sample, therefore the final amplitude of partial stacks is a normalized amplitude. Identifying the range of angle of

incidence for creating partial stacks that best shows the AVO character is important. From Figure 4.6, it seems that the best range of angle of incidence that can be used for creating a near-normal stack is 0° to 20°, while for mid-angle stack, this range of values is 20° to 30°.

The signal envelope computed for the near-normal and mid-angle stack volumes corresponding to the upper-crust OAMLs of zones A, B. and C (Figure 4.1) are depicted in Figure 4.7. In this figure, the signal envelopes of the near-normal stacks (created from an angle of incidence of 0° to 20°) and mid-angle stacks (created from angle of incidence 20° to 30°) are shown on a sample in-line and cross-line from each zone. The signal envelope , which is a seismic attribute showing seismic energy [*Taner et al*., 1979], is significantly reduced in the mid-angle stacks. This pattern of the seismic energy decrease with offset was theoretically predicted for the reflected P-wave from the top of a melt lens (Figure 4.6). However, it is not yet clear if the observed patterns of signal envelope in Figure 4.7 are indications for the presence of melt in zones A, B, and C or not. The results of AVO crossplotting technique obtained from seismic amplitudes are interpreted in the framework derived from Hashin-Shtrikman bounds [*Hashin and Shtrikman*, 1963] to investigate if zones A, B, and C are melt-rich or they are void of melt.

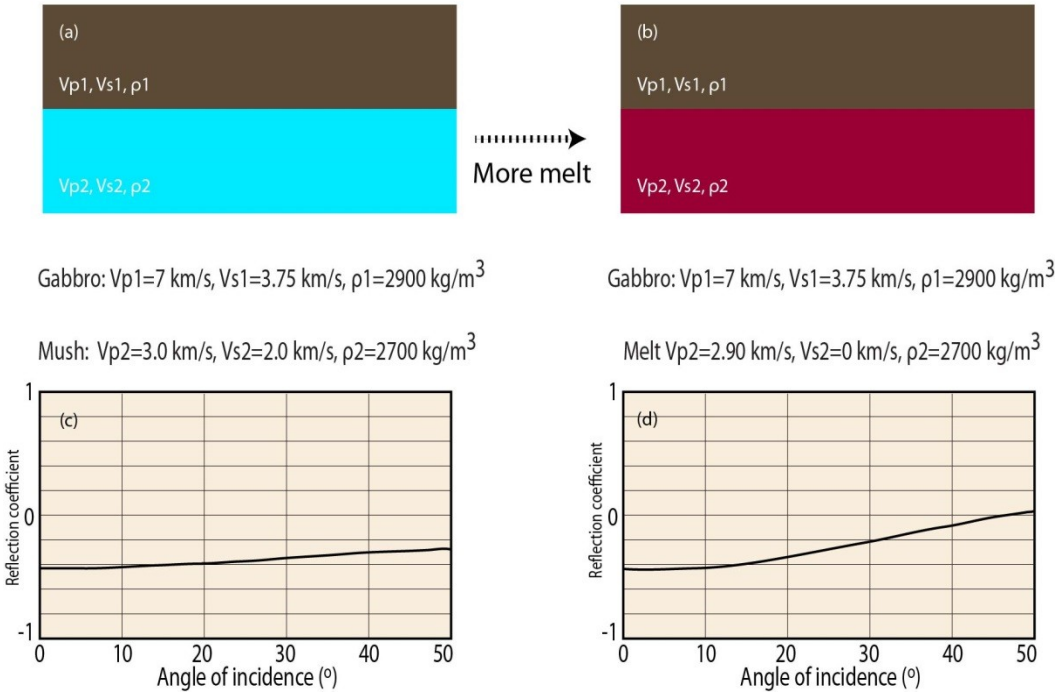

Figure 4.6 Two OAML cases of mush and melt occurring in a crustal gabbro background with the theoretically computed reflection coefficient. a) In the first model, it is assumed mush (Vs=2.0 km/s) is within the OAML. b) In the second model, it is assumed that pure melt (Vs=0) fills the OAML. c) The theoretically computed reflection coefficient of reflected P-wave from gabbro/mush interface for angle of incidence 0° to 50°. d) The theoretically computed reflection coefficient of reflected P-wave from gabbro/melt interface for angle of incidence 0° to 50°. The angle of incidence range of 0° to 20°, and 20° to 30° can be used for creating partial stacks and showing qualitatively the amplitude decrease with angle of incidence/offset.

4.4.2 AVO Crossploting

For crossploting, the AVO intercept (A) and AVO gradient (B) need to be calculated first. This calculation is done using CIGs with the reflected event of interest flattened. To provide a framework for interpretation of the computed AVO attributes, the background trends in the A-B plane are then computed. The intercept (A) and the gradient (B) in the Shuey approximation are calculated via a least-square seismic inversion for each sample in a CIG over a selected portion of a 3D seismic volume using equation 4-1. *Castagna et al.* [1998] have shown that crossploting the AVO intercept (A) and the AVO gradient (B) facilitates AVO interpretation.

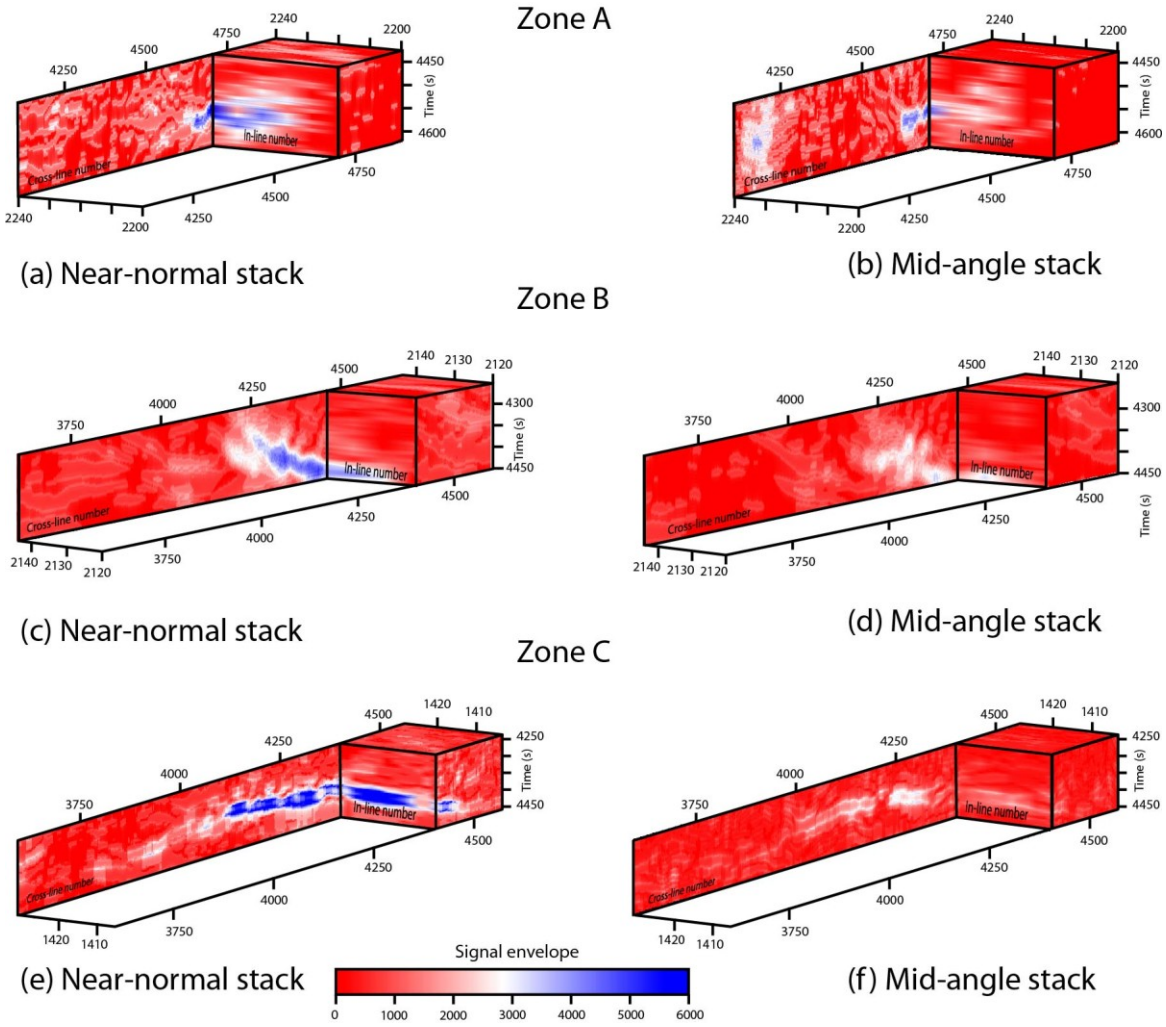

Figure 4.7 Signal envelope computed from the near-normal stack (angle of incidence 0° to 20°) and mid-angle stack (20° to 30°) for the three zones shown in Figure 4.1. a) Signal envelope for the near-normal stack of zone A. (b) Signal envelope for the mid-angle stack of zone A. c) Signal envelope for the near-normal stack of zone B. d) Signal envelope for the mid-angle stack of zone B. e) Signal envelope for the near-normal stack of zone C. (f) Signal envelope for the mid-angle stack of zone C. These figures show that the seismic energy of the mid-angle stack section is significantly less than near-normal stack. This pattern of the amplitude decrease with offset was predicted for the reflected P-wave from the top of a gabbro/mush or gabbro/melt lens in Figure 4.5.

In this framework of AVO interpretation, each (A, B) pair maps into a point in the A-B plane based on their AVO behavior. Depending on the location of the (A,B) pairs in the A-B plane, they are classified as AVO classes I, II, III, or IV. The AVO classes I, II and

III that were originally defined for gas sands by *Rutherford and Willimas* [1989] and later extended to class IV by *Castagna and Smith* [1994] are shown in Table 4.1. In the A-B plane, where A is along the x-axis and B is along the y-axis, class I represents high-impedance sands, class II represents near-zero impedance contrast sands or dim spots, and class III represents low-impedance sands or bright spots. AVO class IV occurs if the S-wave velocity of the lower layer is lower than that of the overlaying formation. In the latter case, the amplitude of the reflected event decreases with offset.

Table 4.1 A summary of the AVO classes [*Castagna and Swan,* 1997]. AVO class IV applies to Figure 4.6 and is the focus of this study. The A vs. B plots in Figure 4.8c, or Figure 4.9 show the quadrants.

AVO Class	Relative impedance	Quadrant	Intercept (A) sign	Gradient (B) sign	Amplitude vs. offset
I	Higher than overlaying unit	IV	+	-	Decreases
II	About the same as the overlaying unit	II, III, or IV	+ or -	-	Increases or decrease
III	Lower than overlaying unit	III	-	-	Increases
IV	Lower than overlaying unit	II	-	+	Decreases

For brine-saturated clastic rocks interbedded with shale, there is a well-defined relationship between the AVO intercept (A) and the AVO gradient (B) known as the "background" trend in the AVO crossplot plane [*Castagna and Swan,* 1997]. This relationship was developed based on the work of *Gardner et al.* [1974] who showed that there is an approximately linear relationship between P-wave velocity and density. *Castagna et al.* [1985] later demonstrated that there is a similar (linear) relationship between P- and S-wave velocities in brine-saturated sandstone and shale. In a given time

window, deviations from this background trend are indicative of hydrocarbons or unusual lithologies.

Assuming that the density contrast between two layers is negligible, it was shown by *Foster et al.* [1997; 2010] that the relation between the AVO intercept (A) and gradient (B) can be simplified to:

$$B = (1 - 8\ \frac{V_s}{V_p}^{2})A \tag{4-2}$$

In this equation, V_p and V_s are the average P-wave and S-wave velocities of the two media ($\frac{V_{p1}+V_{p2}}{2}$ and $\frac{V_{s1}+V_{s2}}{2}$). This equation implies that lines of constant $\frac{V_p}{V_s}$ pass through the origin. Furthermore, the slope of the predicted background trend depends only on the background $\frac{V_p}{V_s}$ ratio. As $\frac{V_p}{V_s}$ increases, the slope of the background trend becomes more positive, or the trend rotates counterclockwise for the AVO intercepts (A) plotted along the x-axis [*Castagna et al.,* 1998].

Based on the above discussion of the AVO crossplotting technique, it is inferred that various constant ratios of V_p over V_s can be used to define the background trends.

The relation between elastic parameters as a function of melt percentage is not known and extracting a background trend in the intercept-gradient plane is not straightforward for this reason. To calculate this background trend for different percentages of melt in the EPR environment, I used the *Hashin-Shtrikman* [1963] bounds to constrain the upper and lower velocity limits for a constant fractions of melt (

Figure **4.8**). Following *Xu* [2012], I considered the maximum bound to correspond to an end-member model of unconnected melt inclusions in a solid host, where Vp=6.2 km/s,

Vs = 3.0 km/s, and ρ = 2800 kg/m^3, and the minimum bound to represent the opposite end-member model of unconnected crystals in a molten host, where Vp = 2.9 km/s, Vs = 0 km/s, and ρ = 2700 kg/m^3 , for a pure melt.

Figure 4.8a shows the P- and S-wave velocities computed for different melt percentages following the *Hashin-Shtrikman* [1963] relation for the physical properties of a two-phase material. I assumed gabbro with elastic parameters of Vp=7.0 km/s, Vs=3.75 km/s, and ρ=2900 kg/m^3 [*Iturrino et al.,* 1991] for the background medium.

Figure **4.8**b shows the ratio of the average P-wave velocity (V_p) to the average of S-wave velocities (V_s) of the upper and lower layer computed from the upper Hashin-Shtrikman bounds. It is clear that ($\frac{V_p}{V_s}$) is significantly affected by melt percentage. To define the background trend for a range of melt percentages, I averaged the $\frac{V_p}{V_s}$ ratio for melt percentages of 0 to 100% for percentage intervals of 20%. This average $\frac{V_p}{V_s}$ in equation 4-2 resulted in the five background trends shown in Figure 4.8c.

4.5. Results

4.5.1 P-wave Partial Stacking Results

The result of computing signal envelope s of the near-normal stack and mid-angle stack volumes of zones (A) to (C) are shown in Figure 4.7. Among the three zones, the largest difference between the signal envelope of near-normal stack and mid-angle stack volumes is found in Zone C (Figure 4.7e, f).

Figure 4.7e shows that the signal envelope on the near-normal stack is large along in-line 1429, and all the cross-lines from 4000, to 4500. For these same in-line and range of

cross-lines, the signal envelope is significantly reduced on the mid-angle stack volume (Figure 4.7f).

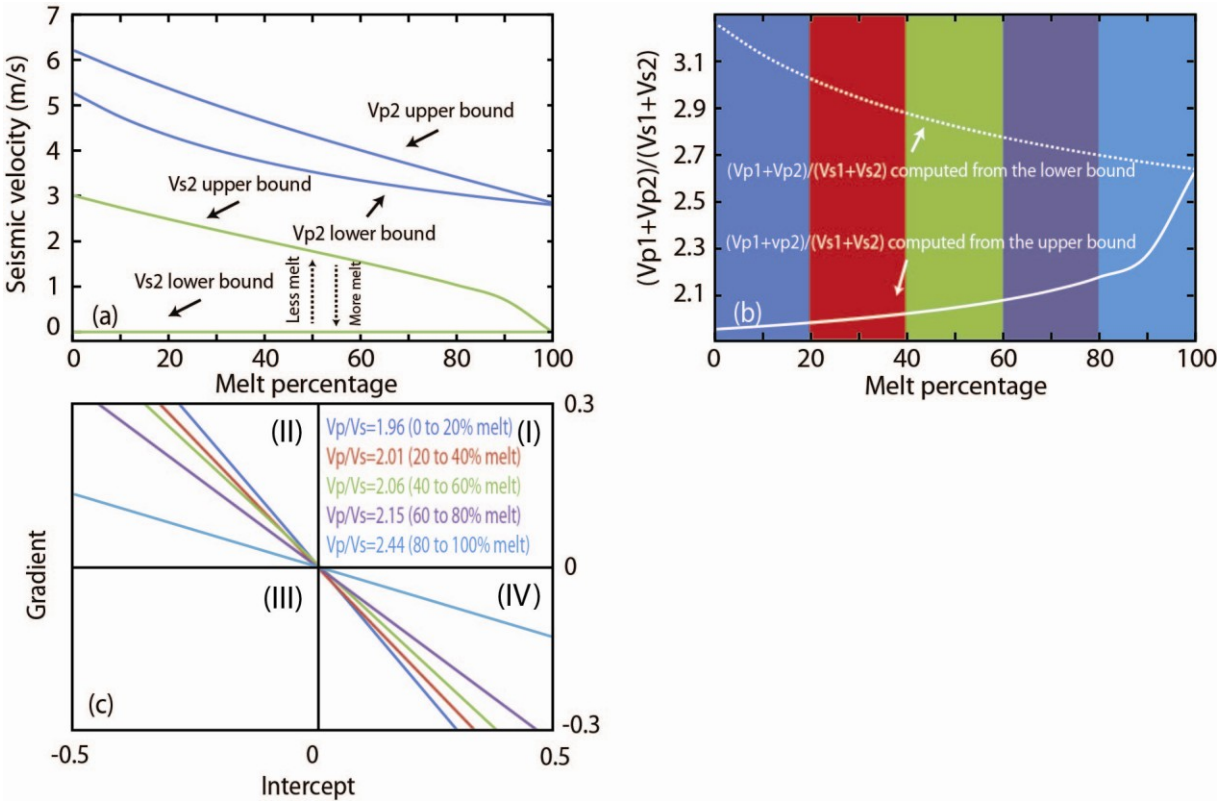

Figure 4.8 A framework for estimating melt percentage and interpreting AVO crossplot results using the Hashin-Shtrikman bounds. a) Computed P- and S-wave velocities from the assumed lower and upper bounds on elastic properties for melt and crystals. The upper bounds are shown in blue and the lower bounds are shown in green. b) Assuming that the background medium is gabbro, the Vp/Vs ratio is computed from the lower bound (dashed white line) and the upper bound (solid white line). This parameter is detailed in the text. c) The average Vp/Vs for the melt percentages shown in the background of (b) is computed from the upper bound curve of (b) and the background trend is computed for each melt percentage. The average Vp/Vs was not computed from the lower bound because the computed background trends will fall in quadrants I and III which is at odds with the amplitude decrease with offset predicted in Figure 4.5 and AVO pattern IV (Table 4.1).

The signal envelope of the near-normal stack volume of zone B (Figure 4.7c) for in-line 2144, and cross-lines 4150 to 4250 is larger than the signal envelope of the mid-angle stack volume for the same in-line and range of cross-lines (Figure 4.7d). The signal

envelope values of the mid-angle stack volume of zone A are smaller than the values for the near-normal stack in this zone (Figure 4.7a, b).

4.5.2 The AVO Crossplotting Results

The purpose of AVO crossplotting in this study is to estimate melt percentage qualitatively for the upper-crust OAMLs shown in Figure 4.1. In the areas selected for AVO crossplotting, the S/N ratio of the OAML reflections on the CIGs is high (Figures 4.2, 4.3 and 4.4). For zones (B) and (C), the AVO crossplotting has been done for three separate windows to examine melt percentage variation along the OAMLs. The OAML in zone (A) is not as large as the OAMLs in zones (B) and (C) and the crossplotting was performed in one time window where the S/N ratio is comparable to the S/N ratio of zones (B) and (C). The analysis windows in zones (B) and (C) extend for 1250 m in the cross-line, 900 m in the in-line direction, and 100 ms in the vertical direction. The analysis window of zone (A) is the same as zones (B) and (C) except that it is 600 m wide in the in-line direction. These analysis windows are shown in Figures 4.2, 4.3, and 4.4 with dashed blue rectangle (time window 1), yellow rectangle (time window 2) and red rectangle (time window 3).

The results of AVO crossplotting for the time windows 1, 2, 3 of Figures 4.2, 4.3, and 4.4 are shown in Figure 4.9. The crossplotted values occur dominantly in quadrants II and IV which corresponds to AVO class IV, in which the amplitude decreases with offset (Table 4.1). Values occur in in quadrant II and IV because for each positive-negative amplitude pair, two (A,B) pairs are computed; one (A,B) pair is computed from the positive amplitude that is plotted in quadrant IV, and the other pair is computed from the negative amplitude that occur in quadrant II. If the positive and negative amplitudes have

the same absolute values, the crossplotted values will be symmetrical with respect to the origin.

To facilitate melt percentage estimation in each analysis window and interpret the results, the background trends calculated in

Figure 4.8c are projected to the A-B plane. The calculated background trends show a counterclockwise rotation from melt-poor magma lenses toward melt-rich magma lenses. The best-fitting A vs. B linear trends are calculated for the crossplotted data and shown with solid black line in Figure 4.9. The $\frac{V_p}{V_s}$ was calculated from the slope of the best-fitted trend line using equation 4-2. The $\frac{V_p}{V_s}$ values change from the minimum value of 1.37 in zone A to the maximum value of 1.94 in analysis window 1 of zone (C). In zone (C), this value is 1.52 in analysis window 3, and 1.90 in analysis window 2. In zone B, the $\frac{V_p}{V_s}$ is lower than zone (C) for all the analysis windows and it is 1.70 for analysis window 1, 1.87 for analysis window 2, and 1.56 for the analysis window 3. The $\frac{V_p}{V_s}$ ratios in zone (C) for analysis window1 (1.94) and analysis window2 (1.90) are similar and they are different from the computed value for analysis window 3 (1.52) which is at the edge of the OAML. A similar value of $\frac{V_p}{V_s}$ ratio for analysis window 3 (1.56) is found in zone (B). The $\frac{V_p}{V_s}$ ratio for the only analysis window of zone A is 1.37.

4.5.3 Velocity Measurements Results

The average velocities between the seafloor and the upper-crust OAMLs, between the seafloor and the lower-crust OAMLs, and between the upper- and the lower-crust

OAMLs were measured using the CIGs (Figures 4.2e-f, 4.3e-f, 4.5a-f). The results of these velocity measurements are summarized in Table 4.2. On the CIGs with strong and continuous OAMLs, the Moho reflection was not strong enough for measuring the velocity between the OAMLs and the Moho.

The average velocity between the seafloor and the lower-crust OAMLs on the northern Pacific plate (9°51'-52'N) (5950 m/s) is higher than the same velocity (5840 m/s) for the northern Cocos plate (9°52'-52'N) (Figure 4.1). For the southern Pacific plate (9°37.5'-39'N), however, the average velocity between the seafloor and the lower-crust OAMLs is low (5700 m/s). In this same latitude range on the Cocos plate, the average velocity between the seafloor and the lower-crust OAMLs is ~5800 m/s. The velocity between the upper- and lower-crust OAMLs at zone C (Figures 4.4, 4.5a-c) is ~6100 m/s.

4.6. Discussion

The results from AVO crossplotting show that the OAMLs are either void of melt or they contain <20% melt. This may suggest that the OAMLs are remnants of past off-axis melt lenses which melt has dissipated because of either off-axis eruptions, or feeding the AML. These possibilities for melt drainage, and the source of melt reservoir for the OAMLs are discussed.

4.6.1 Melt Content of Upper-crust OAMLs

The results of AVO crossplotting for melt content estimation are shown in Figure 4.9. The intercept-gradient pairs occur between the vertical axis (A=0) and the 0-20% background trend that indicates a high crystalline component for the OAMLs. This is consistent with the results of AVO crossplotting of *Marjanović* [2013] for the AML

where the distribution of intercept-gradient pairs shows a counterclockwise rotation towards melt-rich background trends of Figure 4.9.

The correlation factor of the best-fitting trend (the solid black line) does not exceed 0.5 in any of the zones. The low value for the correlation factors is because the analysis windows were chosen to include a flat portion of the OAMLs, and exclude noise. As a result, these time windows suitable for performing AVO crossplotting were small (900m in the in-line direction and 1250 m in the cross-line direction). The fitted linear trend in the AVO crossplotting study of *Marjanović,* [2013] for the AML has a better correlation factor. This is due to large analysis windows (>~8 km along the axis), and relatively flat AML and seafloor along the axis. However, the best-fitting trends are only important in that they can be used for computing the $\frac{V_p}{V_s}$ ratios. Thus, the low value of correlation factor does not change the conclusion reached here that OAMLs are melt-poor with <20% of melt. Because of technical problems, it was not possible to output the data points of Figure 4.9 and fit a least-square trend with higher correlation factor.

Strong P-to-S wave converted phases have been observed at regions along the axis of the EPR where the AML contains a high percentage of melt. The converted phases are strongest on the mid-offset range, and are hardly seen near-offset. In addition, the stacking velocity of these events is lower than the stacking velocity for the AML [e.g., *Xu*, 2012]. No such converted phases have been observed in zones A, B, and C which may further indicate that the upper-crust OAMLs are melt-poor. The reflections observed in zone C below the upper-crust OAMLs (Figure 4.4a) are not converted phases because

a) these events extend to zero offset on the CIGs (Figure 4.5a), b) their RMS velocity is higher than the RMS velocity of the upper-crust OAMLs (Figure 4.5a, b).

The low melt percentage of the upper-crust OAMLs may not be surprising because the estimated melt content for the 60-km-long section of the AML from 9°30'N to 10°N at the EPR shows that >75% of this section is melt-poor with an average melt content of ~16% [*Xu*, 2012].

Two possibilities are considered for the low melt percentage of the upper-crust OAMLs, a) the upper-crust OAMLs are drained because of off-axis eruptions, or b) the amount of available melt for off-axis magmatism is reduced because they are feeding the on-axis magmatic systems. Volcanic edifices have been observed above the OAMLs in zone C [*Han et al.,* 2013, submitted]. However, the total volume of these volcanic edifices is ~5.3% of the total extrusive volume, and ~0.3% of the total crustal volume in this area. This may show that off-axis eruption above the OAMLs is not significant. However, in situ seafloor observation is required to confirm this conclusion since small volcanic edifices does not necessarily imply low-volume eruptions. Although there are no currently known bathymetric or morphologic evidence that indicates off-axis eruption from the OAMLs in zones A and B (between 9°52'N and 9°57'N), anomalously young lavas have been found from studies of basalt samples collected across the EPR from 9°48 to 9°52'N that may indicate off-axis eruptions within ~4 km of the spreading centre [*Sims et al.,* 2003]. Some investigators, however, suggest that the sampled off-axis young lavas originate within the AST and have been transported several kilometers off-axis via surficial and/or subsurface channels [e.g., *Haymon et al.,* 1993; *Waters et al.,* 2010]. Within zones A and B, no samples have been collected near or above the OAMLs yet and

the hypothesis of upper-crust OAML drainage because of off-axis eruption for these zones remains to be examined by future sampling of lavas above the OAMLs.

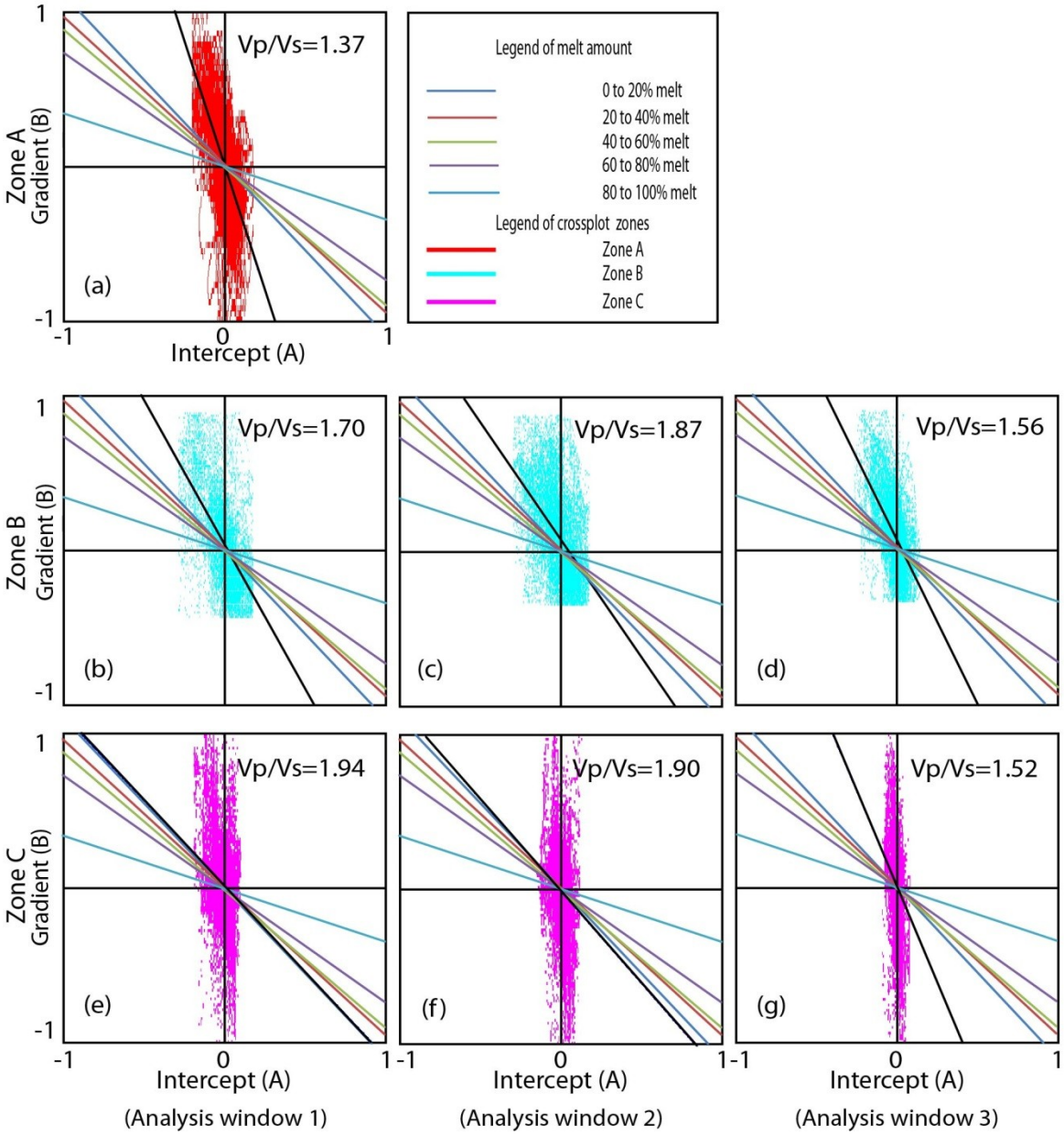

Figure 4.9 The result of crossplotting intercept and gradient. Intercept is calculated from the angle of incidence range of 0° to 20° and gradient is calculated from the angle of incidence range of 20° to 30° of the CIGs. (a) shows the result of crossplotting for the analysis window in zone A shown in Figure 4.2a with dashed blue rectangle. The best linear fit is shown with solid black line. (b) to (d) show the result of crossplotting for the analysis windows shown with dashed blue, yellow and red rectangles in Figure 4.3a, respectively. The best linear fit is shown with solid black line. (e) to (f) show the result of crossplotting for the analysis windows shown in Figure 4.4a shown with

dashed blue, yellow and red rectangles, respectively. The best linear fit is shown with the solid black line.

Table 4.2 Average velocity between the seafloor and the OAMLs.

Feature	Latitude range	Velocity Range (m/s)	Average velocity (m/s)	Standarad deviation
Upper-crust OAML (Cocos)	9˚37.5-39'N	4515-6037	5300	370
Upper-crust OAML (Cocos)	9˚52-56'N	5638-6653	5860	190
Lower-crust OAML (Cocos)	9˚52-53'N	5609-6324	5840	130
Lower-crust OAML (Pacific)	9˚51-52'N	5732-6582	5950	210
Lower-crust OAML (Pacific)	9˚37.5-39'N	5485-5918	5700	100

The second possibility for melt-poor upper-crust OAMLs is that the melt in upper-crust OAMLs could have migrated toward the on-axis magmatic systems [*Canales et al.,* 2012]. There are some indications of connectivity between the AML and the upper-crust OAMLs (Figure 4.4a). Upward migration of the melt from upper-crust OAMLs toward the AML is likely considering the buoyancy of melt in the crust [*Han et al.,* 2013; submitted, Figure 4.4a]. This shows that the OAMLs, unlike the AML, are sporadic events which contribution in formation of the lower crust is a few percent (~3%) [*Han et al.,* 2013; submitted].

4.6.2 Melt Source of the Upper-crust OAMLs

Below the upper-crust OAMLs on the northern Cocos plate (~9°53-56'N) (Figure 4.1), a thick MTZ indicates the presence of a large volume of melt in the uppermost mantle [*Nedimović et al.,* 2005; *Chapter 3*] and attenuation of the seismic waves propagating below these upper-crust OAMLs shows elevated temperatures in the lower crust [*Canales et al.,* 2012]. The availability of a large volume of melt in the uppermost mantle and local thermal heterogeneity in the crust might have facilitated vertical melt migration from the

uppermost mantle to the upper-crust. That the MTZ is overprinted below the upper-crust OAMLs in this area could be because of melt delivery from the uppermost mantle to the upper-crust in this zone. However, no upper-crust OAMLs were imaged on the northern Pacific plate (9°50'-56'N) (Figure 4.1) below which a large volume of uppermost mantle melt reservoir is also expected to exist [*Chapter 3*]. For this area, the seismograms recorded by the ocean-bottom seismometer (OBS) on the Pacific plate show no sign of attenuation [*Canales et al.,* 2012], suggesting that the lower crust is not thermally heterogeneous in this area. This may suggest that the presence of a melt reservoir is not sufficient to from the upper-crust OAMLs and local thermal heterogeneity is required to facilitate melt migration from the uppermost mantle to the upper crust.

Although there are no seismic attenuation data available for the crust below the OAMLs imaged in the southern Cocos plate (9°37.5'-39'N) (Figure 1.4), the average velocity between the seafloor and lower-crust OAMLs is similar to that in the same interval for the northern Cocos plate (~9°53-56'N) (Table 1.4), a large volume of melt in the uppermost mantle is inferred based on the presence of a thick MTZ in this area [*Chapter 3*] and the MTZ is overprinted below the upper-crust OAMLs in this zone as it is in the northern Cocos plate [*Chapter 3*]. These may indicate an elevated temperature in the lower crust and vertical melt migration from the uppermost mantle to the upper crust in zone C.

The low melt percentage of the OAMLs is consistent with results from numerical modeling which indicate that the majority of the melt extracted from the mantle is focused toward the spreading center along the permeability barriers developed at the base of the lithosphere [e.g., *Hebert and Montesi,* 2010].

The upper-crust OAMLs may reflect local melt anomalies in the shallow mantle. The presence of such melt anomalies have been predicted from recent thermochemical modeling of *Katz and Weatherly* [2012] for melt extraction at MORs. These models suggest that magmatic segregation at a chemically heterogeneous mantle result in melt pooling and crystallization at the base of the crust. These melt pools may supply magma to the OAMLs through high-porosity, high-permeability channels or dikes.

4.7. Conclusion

From advanced analysis of the first multi-source, multi-streamer 3D MCS data over a MOR environment, clear images of a number of upper- and lower-crust magma lenses on the flanks of the fast-spreading EPR between 9°37.5'N to 9°57'N were provided. The melt content of these OAMLs was determined for the first time using an AVO crossplotting technique. The results of AVO crossplotting for the upper-crust OAMLs from ~9°37.5'N to ~9°39'N, and from ~9°52'N to ~9°55'N show that these magma bodies contain <20% melt. The drainage of these upper-crust OAMLs could be caused by melt migration from upper-crust OAMLs upward to the AML.

Although the melt content of the OAMLs is low, their geophysical signature in the lower crust and Moho are significant. The MTZ below the OAMLs is overprinted probably because of melt migration from the upper mantle to the upper crust, and the seismic attenuation data indicate elevated temperature in the lower crust beneath the upper-crust OAMLs [*Canales et al.*, 2012; *Aghaei et al.,* 2013, submitted].

The availability of a large volume of melt in the uppermost mantle along with local thermal heterogeneity in the lower crust are required for formation of relatively large

upper-crust OAMLs. Below the upper-crust OAML centred at ~9°39'N, a number of bright reflections were identified that were interpreted as deeper magma lenses. The velocity between the upper-crust OAML and these lower-crust OAMLs is not low. This may show that the area between upper- and lower-crust OAMLs is devoid of melt.

The low melt percentage of the OAMLs estimated in this study indicates that the OAMLs contribute very little to formation of the lower crust. This is consistent with the results from a recent study that shows the total volume of the crust produced by the OAMLs is ~3% [*Han et al.,* 2013, submitted]. This may suggest that the OAMLs, unlike the AML, are sporadic events.

CHAPTER 5 CONCLUSIONS AND FUTURE WORK

5.1 Conclusions

I applied standard poststack migration and prestack time migration (PreSTM) to the first high-resolution multi-source and multi-streamer 3D multichannel seismic (MCS) dataset collected over a mid-ocean ridge (MOR). The data were collected across the northern East Pacific Rise (EPR) from 9°37.5'N and 9°57'N. The 3D PreSTM was applied for the first time to a 3D MCS MOR dataset. The results have yielded the most detailed maps of the Moho transition zone (MTZ) reflection character, crustal thickness, and average crustal velocity to date. These results are provided at a scale, resolution and geometric accuracy comparable to available maps of seafloor morphology, and volcanic and hydrothermal activity. This made it possible to achieve the main objectives of my thesis, which are to investigate the relationship between the crustal thickness/Moho character and ridge segmentation, style of crustal accretion, and off- and on-axis magmatism. The off-axis magma lenses (OAMLs) were also examined using the P-wave partial stack and amplitude variations with offset (AVO) crossplotting technique. The obtained results represent the first ever constraints on the OAML melt content.

The subarea from 9°42'N to 9°57'N was first investigated using standard 3D poststack migration [*Aghaei et al.*, 2013, submitted]. The MTZ reflections were imaged and crustal thickness determined within ~87% of the study area. Impulsive MTZ reflections, marked by single phase and continuous events, cover over 41% of the total area. Shingled MTZ reflections, also defined as single-phase events though segmented by vertical offsets into sections ≤2 km long, are found across 29% of the study area. Diffusive MTZ reflections, identified by multiphase arrivals, are distributed over 17% of the survey area.

The standard 3D poststack migration work was followed by application of Kirchhoff 3D PreSTM to all of the 880 km^2 of the area covered between 9°37.5'N and 9°57'N, which excluded the region from 9°40'N to 9°42'N where no data were collected. With this more advanced imaging method, the MTZ reflections were imaged within ~92% of the study area, with ~66% of the total characterized by impulsive reflections interpreted to represent a thin MTZ (10s of meters thick) and 26% characterized by diffusive reflections interpreted to represent a thick MTZ (100s of m to a few km thick). The impulsive MTZ reflection arrival area, as with the migrated stack result, is further subdivided into continuous sections (>2 km long) covering ~35% of the total area, and shingled sections covering ~31% of the total area. The MTZ is dominantly diffusive at the southern (9°37.5'N-9°40'N) and northern (9°51'N-9°57'N) ends of the study area, and it is impulsive in the central region from 9°42'N to ~9°51'N.

Analysis of the produced 3D reflection cubes gives new insight into (1) average crustal velocity, (2) crustal thickness, (3) age of Moho formation, (4) ridge segmentation, and (5) style of crustal accretion [*Chapters 2 and 3*]. Analysis of the AVO results provides constraints on the OAML melt content and their contribution to crustal formation [*Chapter 4*].

5.1.1 Average Crustal Velocity

The MCS derived average crustal velocity for 9°37.5'N to 9°57'N, excluding 9°40'N to 9°42'N, is 6320±170 m/s. The average crustal velocity for the area between 9°42'N and 9°57'N is 6330±170, which agrees within the error bounds with the average crustal velocity of 6395±200 m/s computed by *Canales et al.* [2003] from ocean-bottom seismometer (OBS) velocity profiles for the same area.

5.1.2 Crustal Thickness

(1) The average crustal thickness from the results of PreSTM of 5920±320 m for 9°37.5'N to 9°57'N, excluding a 3.3-km-wide area (9°40'N to 9°42'N), is ~3% larger than the average crustal thickness of 5.75 km estimated for the study area by an earlier 2D MCS study [*Barth and Mutter*,1996]. For the area between 9°42'N and 9°57'N, the PreSTM average crustal thickness (5884±320 m) is ~2.4% larger than the same obtained from the results of poststack migration (5740±320 m), and ~4% larger than crustal thickness of *Barth and Mutter* [1996] (5500 m) for this area. Despite the difference in thickness, the three results agree within the error limits.

(2) The average crustal thickness computed in this work varies little from Pacific to Cocos plate, as well as between the investigated sections of the study area suggesting uniform crustal production in the last 180 Ka. However, the individual crustal thickness measurements can vary by as much as 2.7 km between 9°37.5'N and 9°57'N, excluding the area from 9°40'N to 9°42'N. The crustal thickness variation is 1.75 km for the area between 9°42'N and 9°57'N. These crustal thickness variations are significant for the portion of the fast spreading ridge studied in this work showing that the sheet-like pattern of mantle upwelling hypothesis for the fast-spreading centers is overly simplistic.

(3) The PreSTM derived average crustal thickness of 5920±320 m is significantly less than the crustal thickness of ~6.8 km derived for the study area from wide-angle seismic refraction studies [*Canales et al.,* 2003]. The MCS and wide-angle crustal thickness estimates are especially different (~0.6-1 km) where the MTZ is thin. This may suggest that the uncertainty associated with picking the PmP arrivals on OBS records, which often show a ringing signature, could have introduced a bias in crustal thickness estimates

in wide-angle refraction studies [*Canales et al.,* 2003]. Alternatively, the interpreted thin MTZ may not be so thin but may rather consist of a major change in structures and therefore velocity at the location of the imaged Moho reflection, with a very gradual increase in velocity below that does not result in any observable later arriving reflections.

5.1.3 Age of Moho Formation

Moho reflections are imaged for the first time at a limited number of locations below the axial magma lens (AML) away from any ridge discontinuities. For the areas where Moho reflections are not imaged below the AML, the upper crust is characterized by a high P-wave attenuation factor and the AML has a high melt content [*Xu*, 2012]. Moreover, the AML is also generally wider in these areas. This may indicate that the oceanic Moho in general forms contemporaneously with the oceanic crust but that it is not imaged in all areas below the AML because even the advanced PreSTM cannot fully handle the imaging challenges related to large lateral velocity variations around melt lenses and strong seismic energy attenuation throughout the crust.

5.1.4 Ridge Segmentation

Key observations pertaining to ridge segmentation that emerge from the analysis of the MTZ character and near-axis crustal thickness are: (a) The undisputed third-order ridge discontinuities at 9˚56-58'N and 9°36'N-9°38'N, evident in the seafloor morphology of the axial zone, geochemical investigations, tomographic inversions, and MCS reflection imaging of the AML appear to be associated with a change in the MTZ character and crustal thickness; (b) These changes occur over an area 3-4 km long indicating that third-order discontinuities are not point locations, in agreement with other recent ridge segmentation studies; (c) The undisputed fourth-order ridge discontinuity at 9°49'N

appear to show no correlation with variations in the MTZ character and/or crustal thickness. In general, this suggests that the third-order segmentation is governed by melt distribution within the uppermost mantle while the fourth-order ridge segmentation arises from mid- to upper-crustal processes. In this light, the controversial third- and fourth-order segment discontinuities along the investigated section of the northern EPR were reinterpreted. The debated third- or fourth-order ridge segment boundary at 9˚44.8'N is assigned a fourth-order status. The ridge segment boundary with contested location at 9˚51.5'N or 9˚53'N that was previously interpreted as a fourth-order discontinuity is assigned a third-order discontinuity status centered at 9˚51-51.5'N.

5.1.5 Style of Crustal Accretion

The style of crustal accretion varies in the study area. This is inferred: (a) based on the main results of the extensive 3D reflection imaging provided in this work, such as maps of MTZ character and crustal thickness; (b) in the context of existing knowledge gathered from detailed mapping of ophiolite structures and controlled source seismic studies; (c) from the results of thermal modeling of oceanic crustal accretion. The MTZ character maps suggest more efficient mantle melt delivery to the AML within the central part of the study area (9°42'N to 9°49.5'N) compared to the southern (9°37.5'N to 9°39'N) and northern (9°49.5'N to 9°57'N) sections of the study area. This is consistent with the greater off-axis magmatism observed in the southern and northern ends of the study area. The lower crust more closely follows the multiple magma body model of lower crust accretion in the southern and northern sections of the study area but it seems to be accreted mainly from the AML (gabbro-glacier model of lower crust accretion) in the central section of the study area. The near-axis crust (±0.5-3 km from the ridge axis)

thickens by ~400 m from north to south showing that mantle melt supply enhances towards the south.

5.1.6 Melt Content of the OAMLs

The investigated OAMLs contain very little (<20%) melt suggesting that their contribution to the lower-crust formation is small. This is consistent with *Han et al.* [2013, submitted] study showing that the OAMLs contribute ~3% to the overall crustal formation. The small percentage of melt in OAMLs perhaps indicates that most of melt at fast-spreading ridges is focused toward the ridge axis and that the OAMLs are sporadic events. The OAMLs investigated in this work could also be at the end of their life span or are now mostly drained because of either recent off-axis eruptions or their melt migrating to the AML. However, even though the melt content of the investigated OAMLs is not significant, the crust beneath them seems to be thermally altered and the MTZ overprinted suggesting recent vertical ascent of melt from the upper mantle to mid crust.

5.2 Future work

The next steps in understanding the dynamics of crustal accretion at MORs and ridge segmentation could focus on:

(1) *The linkage between crystallization depths and MTZ character.* The study of major element and volatile concentration in olivine-hosted melt inclusion at 9°50'N where the MTZ is transitional, thin on the Cocos plate and thick on the Pacific plate, shows that >50% of the whole crust crystallizes from melts accumulating within the AML, whereas >25% of crustal crystallization takes place from melt lenses located in the lower crust [*Wanless and Shaw*, 2012]. In other words the AML contributes to formation of ~33% of

the lower crust. Further melt-inclusion studies, for example within areas of thin MTZ (e.g., 9°45'N) and thick MTZ (e.g., 9°53'N), are needed to better determine the linkage between the MTZ character and the crystallization depth.

(2) *Reinterpretation of the gravity anomalies in the study area.* Focused mantle upwelling and melt migration has been suggested to explain the source of the bull's-eye-shaped pattern of mantle Bouguer anomaly (MBA) at 9°50'N. For calculating the MBA, a constant crustal thickness of 6 km was assumed by *Wang et al.* [1996]. The detailed crustal thickness maps presented in this thesis show that assuming a constant crustal thickness of 6 km for the study area is too simplistic. These crustal thickness maps are essential for re-calculating the MBA for the study area and explaining the source of the bull's-eye-shaped pattern of the MBA.

(3) *Inferring the source of asymmetry between Pacific and Cocos plates in the study area.* The source of a marked asymmetric seafloor depth, residual gravity, and rate of subsidence between the Cocos and Pacific plates at the EPR between 12°N to 16°N was attributed to the presence of a warmer mantle beneath the Cocos plate which implies a smaller elastic thickness for the lithosphere [*Cormier et al.*, 2011]. The MTZ character and reflection strength, layer 2A thickness, volcanic deposition, and seafloor depth are asymmetric with respect to the ridge axis in the study area [*Sohn et al.,* 2004; *Escartin et al*., 2007; *Aghaei et al.,* 2013, submitted] but the average crustal thickness is not. In addition, the largest OAMLs in the study area are found on the Cocos plate, and a zone of elevated temperature in the lower crust is inferred for the Cocos plate [*Canales et al.*, 2012]. The source of this asymmetry is not known. Detailed grids of bathymetric, gravity,

and magnetic data can be compiled and used to explain the source of the observed asymmetry.

(4) *The linkage between seismic attenuation of the crust and the MTZ reflection character.* The P-wave seismic attenuation of the upper crust at ~9°43'N is five times greater than the same at ~9°49'N [*Xu*, 2012]. The Moho reflections were imaged below the AML at 9°49'N, whereas Moho was not identified below the AML at 9°43'N. This suggests that attenuation of the seismic energy in the upper crust could be one of the main reasons for the lack of imaged Moho reflections below the AML. Additional investigations into seismic attenuation of the upper crust for other areas where Moho is not imaged below the AML or OAML are needed.

(5) *Temporal changes in the physical property of the magmatic system.* The results provided in this thesis can provide a baseline image against which changes in the physical properties of the magmatic system over the coming decade can be assessed. Future repeat 3D seismic reflection studies, known as time-lapse or 4D seismic imaging, can track changes in subsurface magma distribution and provide invaluable information on the dynamics of crustal accretion at MORs.

(6) *Seismic tomography and prestack depth migration to constrain the age of Moho formation.* The first clear images of Moho below the AML away from any major ridge discontinuities were presented in Chapter 3. However, Moho reflection is still absent below the AML and OAMLs for much of the study area and this could be due to imaging problems. Testing this hypothesis requires applying tomography to detail velocities in the upper crust, where they vary the most, followed by prestack depth migration (PreSDM)

because this imaging method takes into account large lateral velocity changes occurring in the areas of magma accumulation and where the seafloor is rugged. An accurate velocity model of the crust is crucial for a successful PreSDM. Velocity of the uppermost oceanic crust (Layer 2A) can be constrained by 1D traveltime tomography of downward continued shot gathers. Velocity structure of layer 2B can be computed in a joint 2D inversion that uses both downward continued and standard shot gathers [*Newman et al.,* 2010]. This can then be used for input to waveform tomography of the same data. The average interval velocity model calculated from MVA in Chapter 3 can be used for constraining velocity structure of layer 3. Applying PreSDM to the areas where Moho is absent could provide a more robust answer to the question of Moho formation age. In addition, the difference between PreSDM and PreSTM results could be evaluated and the feasibility of applying PreSDM to the data from the ridge environment could be tested.

(7) *Examining the 3D PreSTM volume for new structural information about the oceanic Moho and the MTZ.* Questions that could be readily addressed regarding the structure of oceanic Moho and MTZ based on the provided Moho characteristics maps in this dissertation include: 1) Does the shingling display consistent dip and onlap patterns in the map area? 2) Does it dip toward the ridge or away from it and if so, does the dip direction flip across the ridge axis? 3) Do the shingles only appear on E-W lines, which would suggest they strike N-S. 4) Does the shingling change or disappear with age, suggesting that it is obliterated by shear and strain in the mantle, perhaps the same shearing that causes mantle anisotropy? It is noticeable in Figure 2.6 that shingling is more common close to the ridge, while impulsive MTZ is more common away from the ridge. 5) Do the

dips of the shingling radiate inward or outward, suggesting bowl or dome structures consistent with the cumulate layering in magma chambers or with upwelling structures?

REFERENCES

Aghaei, O., M.R. Nedimović, H. Carton, J.P. Canales, S.M. Carbotte, J.C. Mutter (2013), Crustal thickness and Moho character of the fast-spreading East Pacific Rise from 9˚42'N to 9˚57'N from poststack-migrated 3D MCS data, submitted to *Geochem. Geophys. Geosyst*.

Aki, K. I., and P. G. Richards (1980), Quantitative seismology, *W. H. Freeman and Co.*

Anderson, D. L., and H. Spetzler (1970), Partial melting and the low-velocity zone, *Phys. Earth. Planet. Int.*, 4(1), 62-64, doi:10.1016/0031-9201(70)90030-0.

Bacon, M., R. Simm, and T. Redshaw (2003), 3-D Seismic Interpretation, Cambridge Univ. Press, Cambridge, U. K.

Barth, G. A., and J. C. Mutter (1996), Variability in oceanic crustal thickness and structure: Multichannel seismic reflection results from the northern East Pacific Rise*, J. Geophys. Res.*, 101, 17951–17975, doi: 10.1029/96JB00814.

Batiza, R., and Y. Niu (1992), Petrology and magma chamber processes at the East Pacific Rise -9˚30'N, *J. Geophys. Res.,* 97, 6779–6797.

Benn, K., A. Nicolas, and I. Reuber (1988), Mantle-crust transition zone and origin of wehrlitic magmas: evidence from the Oman ophiolite, *Tectonophysics,* 151, 75-85.

Biondi, B (2006). 3D seismic imaging, Society of Exploration Geophysicists.

Boudier, F., A. Nicolas, and B. Ildefonse (1996), Magma chambers in the Oman ophiolite: Fed from the top and the bottom, *Earth Planet. Sc. Lett*., 144, 239–250.

Brocher, T. A., J. A. Karson, and J. A. Collins (1985), Seismic stratigraphy of the oceanic Moho based on ophiolite models: *Geology*, 13, 62–65.

Buck, R. W., and W. Sue (1989), Focused mantle upwelling below mid-ocean ridges du to feedback between viscosity and melting. *Geophys. Res. Lett.*, 16(7), 641-644.

Calvert, J, A (1995), Seismic evidence for a magma chamber beneath the slow-spreading Mid-Atlantic Ridge. *Nature,* 377, 410-414.

Canales, J. P., R. S. Detrick, D. R. Toomey, and W. S. D. Wilcock (2003), Segment scale variations in the crustal structure of 150-300 kyr old fast-spreading oceanic crust (East Pacific Rise, 8°15'N–10°5'N) from wide-angle seismic refraction profiles, *Geophys. J. Int., 152*(3), 766–794, doi:10.1046/j.1365-246X.2003.01885.x.

Canales, J. P., S. C. Singh, R.S. Detrick, S. M. Carbotte, A.J. Harding, G. M. Kent, J. B. Diebold, J. Babcock, and M. R. Nedimović (2006), Seismic evidence for variations in axial magma chamber properties along the southern Juan de Fuca Ridge, *Earth Planet. Sc. Lett.*, 246, 353-366.

Canales, J. P., M. R. Nedimović, G. M. Kent, S. M. Carbotte, and R. S. Detrick (2009), Seismic reflection images of a near-axis melt sill within the lower crust at the Juan de Fuca ridge, *Nature*, 460, 89–93, doi:10.1038/nature08095.

Canales, J. P., H. Carton, S. M. Carbotte, J. C. Mutter, M. R. Nedimović, M. Xu, O. Aghaei, M. Marjanović, and K. Newman (2012), Network of off-axis melt bodies at the East Pacific Rise. *Nat. Geosci*., 5, 279–283, http://dx.doi.org/10.1038/ NGEO1377.

Cann, J. R (1974), A model for oceanic crustal structure developed. *Geophysical Journal of Research Astronomy Society*, 39, 169-187.

Chen, Y. J., and J. Phipps Morgan, (1996), The effects of spreading rate, the magma budget, and the geometry of magma emplacement on the axial heat flux at mid-ocean

Carbotte, S., and K. Macdonald (1992), East Pacific Rise 8°–10°30'N: Evolution of ridge segments and discontinuities from SeaMARC II and three-dimensional magnetic studies, *J. Geophys. Res.,* 97, 6959–6982, doi: 10.1029/91JB03065.

Carbotte, S. M., Ponce-Correa, G., & Solomon, A. (2000). Evaluation of morphological indicators of magma supply and segmentation from a seismic reflection study of the EPR 15°30'-17°N. *J. Geophys. Res.,* 105, 2737-2759.

Carbotte, S. M., M. Marjanović, H. Carton, J.C. Mutter, J.P. Canales, M.R. Nedimović, S. Han, and M.R. Perfit (2013), Fine-scale segmentation of the crustal magma reservior beneath the East Pacific Rise, *Nat. Geosci., in press*.

Carlson, R. L. (2001), in *Handbook of Elastic Properties, Liquids, and Gases*, eds Levy, M., Bass, H. and Stern, R., 377–461, Academic Press, New York.

Carton, H. D., S. M. Carbotte, J. C. Mutter, J. P. Canales, M. R. Nedimović, O. Aghaei, M. Marjanović, and K. R. Newman (2010), Three-dimensional seismic reflection images of axial melt lens and seismic layer 2A between 9°42'N and 9°57'N on the East Pacific Rise, Abstract OS21C-1514, *Presented at 2010 Fall Meeting, AGU*, San Francisco, California.

Castagna, J. P., and S. W. Smith (1994), Comparison of AVO indicators: A modeling study, *Geophysics*, 59, 1849-1855.

Castagna, J. P., and H. W. Swan, (1997), Principles of AVO crossplotting, *The leading Edge,* Society of Exploration Geophysicists, 17, 337-342.

Castagna, J. P., H. W. Swan, and D. J. Foster (1998), Framework for AVO gradient and intercept interpretation, *Geophysics,* 63 (3), 948-956.

Chen, Y. J., and J. Phipps Morgan (1996), The effects of spreading rate, the magma budget, and the geometry of magma emplacement on the axial heat flux at mid-ocean ridges, *J. Geophys. Res*, 101, 11475–11482.

Choo, J., J. Downton, and J. Dewar (2004), Lift: a new and practical approach to noise and multiple attenuation, *First Break*, 22, 39–44.

Christeson, G. L., G. M. Purdy, and G. J. Fryer (1992), Structure of young upper crust at the East Pacific Rise near $9^0$30'N, *Geophys. Res. Lett*., 19, 1045–1048.

Christensen, N. I., and M. H. Salisbury (1975), Structure and constitution of the lower oceanic crust. *Review of Geophysics and Space Physics*, 1357-1386.

Christeson, G. L., G. M. Purdy, and G. J. Fryer (1992), Structure of young upper crust at the East Pacific Rise near 9°30'N, *Geophys. Res. Lett.*, 19, 1045–1048.

Collier, J. S., and S. C. Singh (1997), Detailed structure of the top of the melt body beneath the East Pacific Rise at 9°40'N from waveform inversion of seismic reflection data., *J. Geophys. Re.,* 102(B9), 20287-20304.

Detrick, R. S., J. C. Mutter, P. Buhl, and I. I. Kim (1990), No evidence from multichannel reflection data for a crustal magma chamber in the *MARK* area on the Mid-Atlantic Ridge, *Nature,* 347, 61-64.

Collins, J. A., T. M. Brocher, and J. A. Karson (1986), Two-dimensional seismic reflection modeling of the inferred crust-mantle transition in the Bay of Islands Ophiolite, *J. Geophys. Res.,* 91, 12520–12538.

Cormier, M.H., K.D. Gans, D. S. Wilson (2011), Gravity lineaments of the Cocos Plate: Evidence for a thermal contraction crack origin, *Geochem. Geophys. Geosyst*., Q07007, 12, 7, doi:10.1029/2011GC003573.

Crawford, W. C., and S. C. Webb (2002), Variations in the distribution of magma in the lower crust and at the Moho beneath the East Pacific Rise at 9°–10°N, *Earth Planet. Sci. Lett*., 203, 117–130, doi:10.1016/S0012-821X(02)00831-2.

Detrick, R. S., P. Buhl, E. Vera, J. Mutter, J. Orcutt, J. Madsen, and T. Brocher (1987), Multi-channel seismic imaging of a crustal magma chamber along the East Pacific Rise, *Nature, 326*, 35–41.

Dunn, R. A., and D. R Toomey (1997), Seismological evidence for three-dimensional melt migration beneath the East Pacific Rise, *Nature* 388, 259–262.

Dunn, R. A., D.R. Toomey, and S.C. Solomon (2000), Three-dimensional seismic structure and physical properties of the crust and shallow mantle beneath the East Pacific Rise at 9°30′N, *J. Geophys. Res.*, 105, p. 23,537–23,555, doi: 10.1029/2000JB900210

Durant, D. T. and D. R. Toomey (2009). Evidence and implications of crustal magmatism on the flanks of the East Pacific Rise. *Earth Planet. Sc. Lett.*, 287, 130-136.

Durant, D. T. (2011), Effects of the off-axis melt supply at fast-spreading mid-ocean ridges: a study of the 9˚-10˚N region of the East Pacific Rise, Ph.D. thesis, Dep. of Geol. Sciences., Univ. of Oregon, Eugene, Oregon, USA.

Escartín, J., A. Soule, D. J. Fornari, M. A. Tivey, H. Schouten, and M. R. Perfit (2007), Interplay between faults and lava flows in construction of the upper oceanic crust: The East Pacific Rise crest 9°25–9°58 N, *Geochem. Geophys. Geosyst.,* 8, Q06005, doi:10.1029/2006GC001399.

Gardner, G.H.F, L. W. Gardner, and A. R. Gregory (1974), Formation velocity and density-the diagnostic basics for stratigraphic traps, *Geophysics,* 39, 770–780.

Goldstein, S. J., M. R. Perfit, R. Batiza, D. J. Fornari, and M. T. Murrell (1994), Off-axis volcanism at the East Pacific Rise detected by uranium-series dating of basalts. *Nature,* 367, 157-159.

Forsyth, D. W (1992), Geophysical constraints on mantle flow and melt migration beneath mid-ocean ridges, in *Mantle Flow and Melt Generation at Mid-ocean Ridges*, *Geophys. Monogr. Ser*.,71, pp. 1–65, edited by Phipps Morgan, J., et al., AGU, Washington, DC.

Foster, D.J., S.W. Smith, S. Dey-Sarkar, and H.W. Swan (1997), A Closer Look at Hydrocarbon Indicators, 63rd Ann. Internat. Mtg., Soc. Expl. Geophys., Expanded Abstracts, 731-733.

Foster, D.J., R. G. Keys, and F. D. Lane (2010), Interpretation of AVO anomalies, *Geophysics*, 75(5), 75A3-75A13.

Goss, A. R., M. R. Perfit, W. I. Ridley, K. H. Rubin, G. D. Kamenov, S. A. Soule, A. T. Fundis, and D. J. Fornari (2010), Geochemistry of lavas from the 2005–2006 eruption at the East Pacific Rise, 9°46'N-9°56'N: Implications for ridge crest plumbing and decadal changes in magma chamber compositions, *Geochem. Geophys. Geosyst*., 11, Q05T09, doi:10.1029/2009GC002977.

Han, S., H. D. Carton, S. M. Carbotte, J. C. Mutter, J. Canales, and M. R. Nedimović (2011), 3D Seismic Reflection Images of an off-axis melt lens and its associated upper crust around 9° 39'N, East Pacific Rise. Abstract OS22A-02 *presented at 2011 Fall Meeting, AGU*, San Francisco, Calif., 5-9 Dec.

Han, S., S. M. Carbotte, H. Carton, J. C. Mutter, O. Aghaei, M. R. Nedimović, J.P. Canales (2013), Architecture of Off-Axis Magma Bodies at EPR 9˚37-40'N and Implication for Oceanic Crustal Accretion, submitted to *Earth Planet. Sc. Lett.*

Harding, A. H., J. A. Orcutt, M. E. Kappus, E. E.Vera, J. C. Mutter, P. Buhl, R. S. Detrick, and T. M. Brocher (1989), Structure of young oceanic crust at 13°N on the East Pacific Rise from expanding spread profiles., *J Geophys. Res.*, 94 (B9), 12163-12196.

Harding, A. J., G. M. Kent, and J. A. Orcutt (1993), A multichannel seismic investigation of upper crustal structure at 9˚N on the East Pacific Rise: Implications for crustal accretion, *J. Geophys. Res*., 98, 13925–13944.

Hashin, Z., and S. Shtrikman (1963), A variational approach to the theory of the elastic behaviour of multiphase materials, *Journal of the Mechanics and Physics of Solids*, *11*(2), 127-140, doi:10.1016/0022-5096(63)90060-7.

Herron, T. J., Ludwig, W. J., Stoffa, P. L., Kan, T. K., & Buhl, P. (1978). Structure of the East Pacific Rise from multichannel seismic reflection data. *J. Geophys. Res.*, 83, 798-804.

Hussenoeder, S. A., J. A. Collins, G. M. Kent, R. S. Detrick, and the TERA Group. (1996), Seismic analysis of the axial magma chamber reflector along the southern East Pacific Rise from conventional reflection profiling. *J. Geophys. Res.*, 101, 22,087-22,105.

Haymon, R. M., D. J. Fornari, M. H. Edwards, S. M. Carbotte, D. Wright, and K. C. Macdonald (1991), Hydrothermal vent distribution along the East Pacific Rise crest (9°9'–54'N) and its relationship to magmatic and tectonic processes on fast spreading mid-ocean ridges, *Earth Planet. Sc. Lett., 104*, 513–534, doi:10.1016/0012-821X(91)90226-8.

Haymon, R. M., D. J. Fornari, K. L. Von Damm, M. D. Lilley, M. R. Perfit, J. M. Edmond, W. C. Shanks, III, R. A. Lutz, J. M. Grebmeier, S. Carbotte, D. Wright, E. McLaughlin, M. Smith, N. Beedle, and E. Olson (1993), Volcanic eruption of the mid-ocean ridge along the East Pacific Rise crest at 9°45'–52'N: Direct submersible observations of seafloor phenomena associated with an eruption event in April, 1991, *Earth Planet. Sc. Lett., 119*, 85–101, doi:10.1016/0012-821X(93) 90008-W.

Haymon, R. M., and S. M. White (2004), Fine-scale segmentation of volcanic/hydrothermal systems along fast-spreading ridge crests, *Earth Planet. Sc. Lett., 226*, 367–382, doi:10.1016/j.epsl.2004.08.002.

Henstock, T. J., A. W. Woods, and R. S. White (1993), The accretion of oceanic crust by episodic sill intrusion, *J. Geophys. Res*., 98, 4143–4161.

Herron, T. J., P. L. Stoffa, and P. Buhl (1980), Magma chamber and mantle reflections - East Pacific Rise, *Geophys. Res. Lett*., 7, 989–992.

Jousselin, D., and A. Nicolas (2000), The Moho transition zone in the Oman ophiolite-relation with wehrlites in the crust and dunites in the mantle. *Mar. Geophys. Res.,* 21, 229-2241.

Iturrino, G. J., N. I, Christensen, S. Kirby, M. H. Salisbury (1991), Seismic velocities and elastic properties of oceanic gabbroic rocks from hole 735B, *Proceedings of the Ocean drilling program*, 118.

Kampfmann, W., and H. Berckhemer (1985), High temperature experiments on the elastic and anelastic behaviour of magmatic rocks, *Phys. Earth. Planet. Int*., 40(3), 223-247, doi:10.1016/0031-9201(85)90132-3.

Katz, R. F. & Weatherley, S. M. (2012). Consequences of mantle heterogeneity for melt extraction at mid-ocean ridges. *Earth Planet. Sc. Lett.*, 335-336, 226-237.

Kennett, B. L. N., and J. A. Orcutt (1976), A comparison of travel time inversions for marine refraction profiles. *J. Geophys. Res.*, 81, 4061-4070.

Karson, J. A., J. A. Collins, and J. F. Casey (1984), Geologic and seismic velocity structure of the crust/mantle transition in the Bay of Islands ophiolite complex, *J. Geophys. Res*., 89, 6126–6138, doi:10.1029/JB089iB07p06126.

Kent, G. M., A. J. Harding, and J. A. Orcutt (1993), Distribution of magma beneath the East Pacific Rise between the Clipperton transform and the 9˚17'N deval from forward modeling of common depth point data, *J. Geophys. Res*., 98, 13,945–13,969.

Kent, G. M., A. J. Harding, J. A. Orcutt, R. S. Detrick, J. C. Mutter, and P. Buhl (1994), Uniform accretion of oceanic crust south of the Garrett transform at 14˚15'S on the East Pacific Rise, *J. Geophys. Res.*, 99 , 9097-9116,doi:10.1029/93JB02872.

Kent, G. M., S. C. Singh, A. J. Harding, M. C. Sinha, J. A. Orcutt, P. J. Barton, R. S. White, S. Bazin, R. W. Hobbs, C. H. Tong, and J. W. Pye (2000), Evidence from three-dimensional seismic reflectivity images for enhanced melt supply beneath mid-ocean ridge discontinuities, *Nature*, 406, 614-618.

Kelemen, P. B., K. Koga, and N. Shimizu (1997), Geochemistry of gabbro sills in the crust-mantle transition zone of the Oman ophiolite: Implications for the origin of the oceanic lower crust, *Earth Planet. Sc. Lett*., 146, 475–488.

Kelemen P. B., and E. Aharonov (1998), Periodic formation of magma fractures and generation of layered gabbros in the lower crust beneath oceanic spreading ridges, in *Faulting and Magmatism at Mid-Ocean Ridges, Geophys. Monogr. Ser*., vol. 106, edited by W.R Buck et al., pp 267–289. AGU, Washington, D.C.

Kong, L. S. L., S. C. Solomon, and G. M. Purdy (1992), Microearthquake characteristics of a Mid-Ocean Ridge along-axis high. *J. Geophys. Res.*, 97(B2), 1659-1678.

Langmuir, C. H., J. F. Bender, and R. Batiza (1986), Petrological and tectonic segmentation of the East Pacific Rise, 5˚30'N– 14˚30'N, *Nature*, 322, 422–429.

Lin, J., G. M. Purdy, H. Schouten, J. C. Sempere., and C Zervas, C. (1990). Evidence from gravity data for focused magmatic accretion along the Mid-Atlantic Ridge. *Nature*, 344, 627-32.

Louden, K.E., R. S. White, C. G. Potts, and D. W. Forsyth, (1986), Structure and seismotectonics of the Vema Fracture Zone, Atlantic Ocean. *Journal of the Geological Society of London*, 143, 795-806.

Macdonald, K. C., J. C. Sempere, and P. J. Fox (1984), East Pacific Rise from Siqueiros to Orozco fracture zones: Along strike continuity of axial neovolcanic zone and structure and evolution of overlapping spreading centers, *J. Geophys. Res*., 89, 6049–6069.

Macdonald, K. C., P. J. Fox, L. J. Perram, M. F. Eisen, R. M. Haymon, S. P. Miller, S. M. Carbotte, M.H. Cormier, and A. N. Shor (1988), A new view of the mid-ocean ridge from the behavior of ridge axis discontinuities, *Nature,* 335, 217–225, doi:10.1038/335217a0.

Macdonald, K. C., P. J. Fox, S. P. Miller, S. M. Carbotte, M. H. Edwards, M. F. Eisen, D. J. Fornari, L. J. Perram, R. Pockalny, R. M. Haymon, D. S. Scheirer, S. Tighe, C. Weiland, D. Wilson (1992), The East Pacific Rise and its flanks 8°–18°N: History of segmentation, propagation and spreading direction based on SeaMARC II and SeaBeam studies, *Mar. Geophys. Res*., 14, 299–344.

Macdonald, K. C (1998), Periodic formation of magma fractures and generation of layered gabbros in the lower crust beneath oceanic spreading ridges, in *Faulting and Magmatism at Mid-Ocean Ridges, Geophys. Monogr. Ser*., vol. 106, edited by W.R Buck et al., pp 27–58. AGU, Washington, D.C.

Maclennan, J., T. Hulme, and S. C. Singh (2004), Thermal models of oceanic crustal accretion: linking geophysical, geological and petrological observations, *Geochem. Geophys. Geosyst.* 5, Q02F25, doi:10.1029/2003GC000605.

Marjanović, M (2013), Signatures of present and past melt distribution at fast and intermediate spreading centers, Ph.D. thesis, Dep. of Marine Geol. and Geophys., Lamont-Doherty Earth Observatory, Columbia University, Palisades, New York, USA.

Mavko, G. M. (1980), Velocity and attenuation in partially molten rocks, *J. Geophys. Res*., 85(B10), 5173-5189.

Morris, E., and R. S. Detrick (1991), Three-dimensional analysis of gravity anomalies in the Mark Area, Mid-Atlantlc Ridge 23°N. *J. Geophys. Res.,* 96(B3), 4355-4366.

Morton, J. L., and N. Sleep (1985), Seismic reflections from a Lau Basin magma chamber, in Geology and Offshore Resources of Pacific Island Arcs-Tonga Region, *Earth Sciences Series*, 2, edited by D. W. Scholl, and T. L. Vallier, Circum-Pacific Council for Energy and Mineral Resources 441453, Houston,Texas.

Murase, T., and A. R. McBirney (1973), Properties of some common igneous rocks and their melts at high temperatures, *Geol. Soc. Am. Bull*., 84, 3563-3592.

Mutter, J. C., S. M. Carbotte, M. R. Nedimović, J. P. Canales, and H. Carton (2009), Seismic imaging in three dimensions on the East Pacific Rise. *Eos. Trans. AGU,* 90, 374–375, http://dx.doi.org/10.1029/2009EO420002.

Nedimović, M. R., S. M. Carbotte, A. J. Harding, R. S. Detrick, J. P. Canales, J. B. Diebold, G. M. Kent, M. Tischer, and J. M. Babcock (2005), Frozen magma lenses below the oceanic crust, *Nature*, 436, 1149–1152, doi:10.1038/nature03944.

Nedimović, M. R., S. M. Carbotte, J. B. Diebold, A. J. Harding, J. P. Canales, and G. M. Kent (2008), Upper crustal evolution along the Juan de Fuca Ridge flanks. *Geochem. Geophys. Geosyst.,* 9, Q09006, http:// dx.doi.org/10.1029/2008GC002085.

Newman, K., M. Nedimović, M. Delescluse, W. Menke, J. P. Canales, S. Carbotte, H. Carton, J. Mutter (2010), East Pacific Rise axial structure from a joint tomographic inversion of traveltimes picked on downward continued and standard shot gathers collected by 3D MCS surveying, *EGU*, 2-7 May, Vienna, Abstract No. 2010EGUGA. 1213383N.

Nicolas, A. and F. Boudier (1995), Mapping oceanic ridge segments in Oman ophiolites, *J. Geophys. Res.,* 100, 6179–6197.

Nicolas, A., F. Boudier, and B. Ildefonse (1996), Variable crustal thickness in the Oman Ophiolite: Implication for oceanic crust, *J. Geophys. Res*., 101, 17941–17950.

Orcutt, J., N. Kennett, L. Dorman, and W. Prothero (1975), A low-velocity zone underlying a fast-spreading ridge crest, *Nature*, 256, 475–476.

Peles, O., D. Kosloff, Z. Koren, and M. Tygel (2001), A practical approach to true amplitude migration, *Journal of seismic exploration*, 10,183-203.

Phipps Morgan, J., and Y. Chen (1993), The genesis of oceanic crust, magma injection, hydrothermal circulation and crustal flow, *J. Geophys. Res*., 98, 6283–6297.

Pratt, R. G., and Worthington, M. H. (1990), Inverse theory applied to multi-source cross-hole tomography. Part I: Acoustic wave-equation method, *Geophys. Prospect.*, 38, 287-310.

Purdy, G. M., and R. S. Detrick (1986), Crustal structure of the Mid-Atlantic Ridge at 23°N from seismic refraction studies. *J. Geophys. Res.*, 91, 3739-3762.

Quick, J. E., and R. P. Delinger (1993), Ductile deformation and the origin of layered gabbro in ophiolites, *J. Geophys. Res*., 98, 14015-14027.

Rabinowicz, M., A. Nicolas, and J. Vigneresse (1984), A rolling mill effect in the asthenosphere beneath oceanic spreading centers, *Earth Planet. Sc. Lett*., 67, 97–108, doi:10.1016/0012-821X(84)90042-6.

Raitt, R.W (1956), Seismic-refraction studies of the Pacific Ocean Basin, *Bull. Geol. Soc. Am.*, 67, 1623–1640.

Reuber, I., P. Nehlig, and T. Juteau (1991), Axial segmentation at a fossil oceanic spreading centre in the Haylayn block (Semail nappe, Oman): Off-axis mantle diapir and advancing ridge tip, *J. Geodyn*., 13, 253–278.

Riddihough, R. P (1984), Recent movements of the Juan de Fuca plate. *J. of Geophys. Res.*, 89, 6980-6994.

Rohr, K., B. Mildreit, and C. J. Yorath (1988), Asymmetric deep crustal structure across the Juan de Fuca Ridge, *Geology*, 16, 533-537.

Rutherford, S. R. and R. H. Williams (1989), Amplitude-versus-offset variations in gas sands, *Geophysics*, 54, 680-688.

Scheirer, D. S., and K. C. Macdonald (1993), Variation in cross-sectional area of the axial ridge along the East Pacific Rise: Evidence for the magmatic budget of a fast-spreading center, *J. Geophys. Res.*, 98, 7871–7885, doi:10.1029/ 93JB00015.

Schouten, H., and C. Denham (1995), Virtual ocean crust, *Eos Trans. AGU*, 76, Spring meet. Suppl., 84.

Shen, Y., Forsyth, D. W., Scheirer, D. S., & Macdonald, K. C. (1993). Two forms of volcanism: Implications for mantle flow and off-axis crustal production on the west flank of the Southern East Pacific Rise, *J. Geophys. Res.*, 98, 17,875-17,889.

Shuey, R. T (1985). A simplification of the Zeoppritz equations, *Geophysics,* 50, 609-614.

Singh, S. C., A. J. Harding, G. M. Kent, M. C. Sinha, V. Combier, S. Bazin, C. H. Tong, J. W. Pye, P. J., Barton, R.W. Hobbs, R. S. White, and J. A. Orcutt (2006), Seismic reflection images of the Moho underlying melt sills at the East Pacific Rise, *Nature,* 442, 287–290.

Sinton, J. M., S. M. Smaglik, J. J. Mahoney, and K. C. Macdonald (1991), Magmatic processes at superfast spreading mid-ocean ridges: glass compositional variations along the East Pacific Rise 13°-23°S, *J. Geophys. Res*. 96, 6133–6155.

Sinton, J. M., and R. S. Detrick (1992), Mid-ocean ridge magma chambers, *J. Geophys. Res.*, 97, 197-216.

Smith, M. C., M. R. Perfit, D. J. Fornari, W. I. Ridley, M. E. Edwards, G. Kurras, and K. L. Von Damm (2001), Magmatic processes and segmentation at a fast spreading mid-ocean ridge: Detailed investigation of an axial discontinuity on the East Pacific Rise crest at 9°37'N, *Geochem. Geophys. Geosyst., 2*, 1040, doi:10.1029/2000GC000134.

Sohn, R. A., S. C. Webb, and J. A. Hildebrand (2004), Fine-scale seismic structure of the shallow volcanic crust on the East Pacific Rise at 9o50'N, *J. Geophys. Res.,* 109, B12104, doi:10.1029/2004JB003152.

Soule, S. A., D. J. Fornari, M. R. Perfit, and K. Rubin (2007), New insights into mid-ocean ridge volcanic processes from the 2005–2006 eruption of the East Pacific Rise, 9°46'N– 9°56'N, *Geology, 35*, 1079–1082, doi:10.1130/G23924A.1.

Soule, S. A., J. Escartín, and D. J. Fornari (2009), A record of eruption and intrusion at a fast spreading ridge axis: Axial summit trough of the East Pacific Rise 9-10°N. *Geochem. Geophys. Geosyst.* 10, Q10T07.

Stoffa, P. L., P. Buhl, T. J. Herron, J. K. Kan, and W. J. Ludwig (1980), Mantle reflections from beneath the crestal zone of the East Pacific Rise from multi-channel seismic data, *Mar. Geol*., 35, 83–97.

Stork, C (1992), Reflection tomography in the postmigrated domain, *Geophysics*, 57(5), 680-692.

Tian, T., S. D. Wilcock, D. R. Toomey, and R. S. Detrick (2000), Seismic heterogeneity in the upper crust near the 1991 eruption site on the East Pacific Rise, 9˚50'N, *Geophys. Res. Lett*., 27, 2369–2372, doi:10.1029/1999GL011191.

Tolstoy, M., J. P. Cowen, E. T. Baker, D. J. Fornari, K. H. Rubin, T. M. Shank, F. Waldhauser, D. R. Bohnenstiehl, D. W. Forsyth, R. C. Holmes, B. Love, M. R. Perfit, R. T. Weekly, S. A. Soule, B. Glazer (2006), A sea-floor spreading event captured by seismometers, *Science*, 314, 1920–1922, doi:10.1126/ science.1133950.

Toomey, D. R., G. M. Purdy, S. C. Solomon, and W. S. D. Wilcock (1990), The three-dimensional seismic velocity structure of the East Pacific Rise near latitude 9!300N, *Nature,* 347, 639–645, doi:10.1038/347639a0.

Toomey, D.R., W.S.D Wilcock, R.S. Detrick, and R. A. Dunn (1998), Mapping melt and matrix flow in the uppermost mantle: preliminary results from undershooting the EPR, *Eos Trans. AGU*, 79, Fall Meet. Suppl., F805.

Toomey, D. R., Jousselin, D., Dunn, R. A., Wilcock, W. S. D. and Detrick, R. S, (2007), Skew of mantle upwelling beneath the East Pacific Rise governs segmentation. *Nature* 446, 409–414.

Toomey, D. R., and E. E. E Hooft (2008), Mantle upwelling, magmatic differentiation, and the meaning of axial depth at fast-spreading ridges, *Geology,* 36 (9), 679–682.

Vera, E. E., J. C. Mutter, P. Buhl, J. A. Orcutt, A. J. Harding, M. E. Kappus, R. S. Detrick, and T. M. Brocher (1990), The structure of 0- to 0.2-m.y.-old oceanic crust at 9°N on the East Pacific Rise from expanded spread profiles, *J. Geophys. Res., 95*, 15529–15556.

Wang, X., Cochran, J.R. & Barth, G.A., 1996. Gravity anomalies, crustal thickness, and the pattern of mantle flow at the fast spreading East Pacific Rise, 9°–10°N: evidence for three-dimensional upwelling, *J. geophys. Res*., 101, 17 927–17 940.

Wanless, V. D., and A. M. Shaw (2012), Lower crustal crystallization and melt evolution at mid-ocean ridges, *Nat. Geosci*., 5, 651–655, doi:10.1038/ngeo1552.

White, S. M., R. M. Haymon, D. J. Fornari, M. R. Perfit, and K. C. Macdonald (2002), Correlation between volcanic and tectonic segmentation of fast-spreading ridges: Evidence from volcanic structures and lava flow morphology on the East Pacific Rise at 9˚–10˚N, *J. Geophys. Res.,* 107, 2173, doi: 10.1029/2001JB000571.

White, S. M., R. M. Haymon, and S. Carbotte (2006), A new view of ridge segmentation and near-axis volcanism at the East Pacific Rise, 8˚–12˚N, from EM300 multibeam bathymetry, *Geochem. Geophys. Geosyst*., 7, Q12O05, doi:10.1029/2006GC001407.

White, R. S., D. McKenzie, and R. K. O'Nions (1992), Oceanic crustal thickness from seismic measurements and rare earth element inversions. *J. Geophys. Res.,* 97, 19683-19715.

Xu, M., (2012), Advanced geophysical studies of accretion of oceanic lithosphere in Mid-Ocean Ridges characterized by contrasting tectono-magmatic settings, Ph.D thesis, Dep. of Marine Geol. and Geophys., Woods Hole Institute of Oceanography, Massachusetts, USA.

Yilmaz, Ö. (2001), Seismic Data Analysis, *Society of Exploration Geophysicists*, Tulsa, Oklahama, USA.

APPENDIX A THREE-DIMENSIONAL (3D) SEISMIC DATA ACQUISITION AND PROCESSING

The first 3D multi-source/streamer/channel seismic reflection experiment (MGL0812) over a magmatic-hydrothermal system was conducted in summer 2008 across the EPR at 9˚50'N [*Mutter et al.,* 2009]. The primary 3D survey grid spans the ridge axis between 9˚42'N and 9˚57'N and a smaller grid ~3.3 km to the south extends from ~9˚37.5'N to 9˚40'N. Two narrow swaths of data were acquired south of this area at 9˚35'N and 9˚30'N (Figure A.1).

In this appendix, I introduce data acquisition parameters for the MGL0812 survey, explain 3D geometry definition for processing the data, and detail prestack and poststack processing of the collected 3D MCS data. The objectives of the data processing are to optimally image all reflections with particular emphasis on the AML, OAML, and Moho reflection events. Reflection signal form the top of the AML and from Moho are shown on CMP supergathers formed after applying prestack processing to the data (Figure A.2). Locations of these supergathers are shown in Figure A.1.

I defined four distinctive 3D survey grids for data processing that is detailed in section A.2. The first gird encompasses the data from 9˚42'N and 9˚57'N. The second 3D grid includes the data from ~9˚37.5'N to 9˚40'N. Two other small grids are defined for the two swaths of data located to the south at 9˚35'N and 9˚30'N.

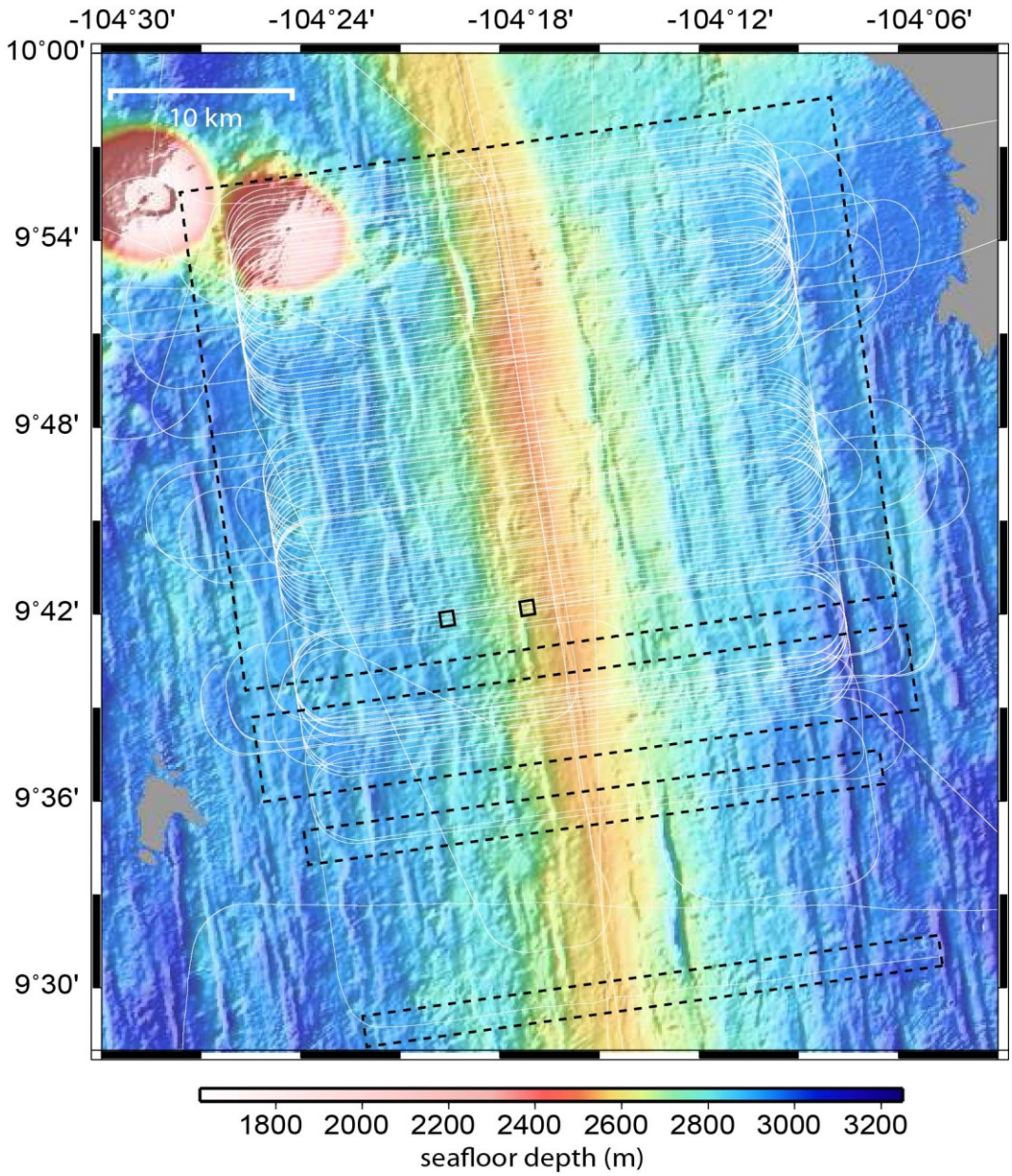

Figure A.1 Ship track for cruise MGL0812 (thin white lines) superimposed over the EPR multibeam bathymetry between 9˚28'N and 10˚N collected during the cruise. Dashed boxes outline the extent of the area used for configuring 3D geometry. Black squares show centers of the CMP supergathers from Figure A.2.

The focus of this study are the large northern box between 9˚42'N and 9˚57'N and the second largest box between 9˚37.5'N to 9˚40'N. After geometry configuration, prestack processing was applied to the data. For testing processing flows, I modeled a synthetic

shot gather and combined it with pure ambient noise recorded during the field survey. Preserving the reflection seismic signal while increasing the signal-to-noise (S/N) ratio was the main criterion for choosing prestack processing parameters. Poststack processing includes 3D poststack Kirchhoff time migration, time-variant scaling and time-variant filtering. Data were also prestack Kirchhoff time migrated. This process is detailed in Appendix B.

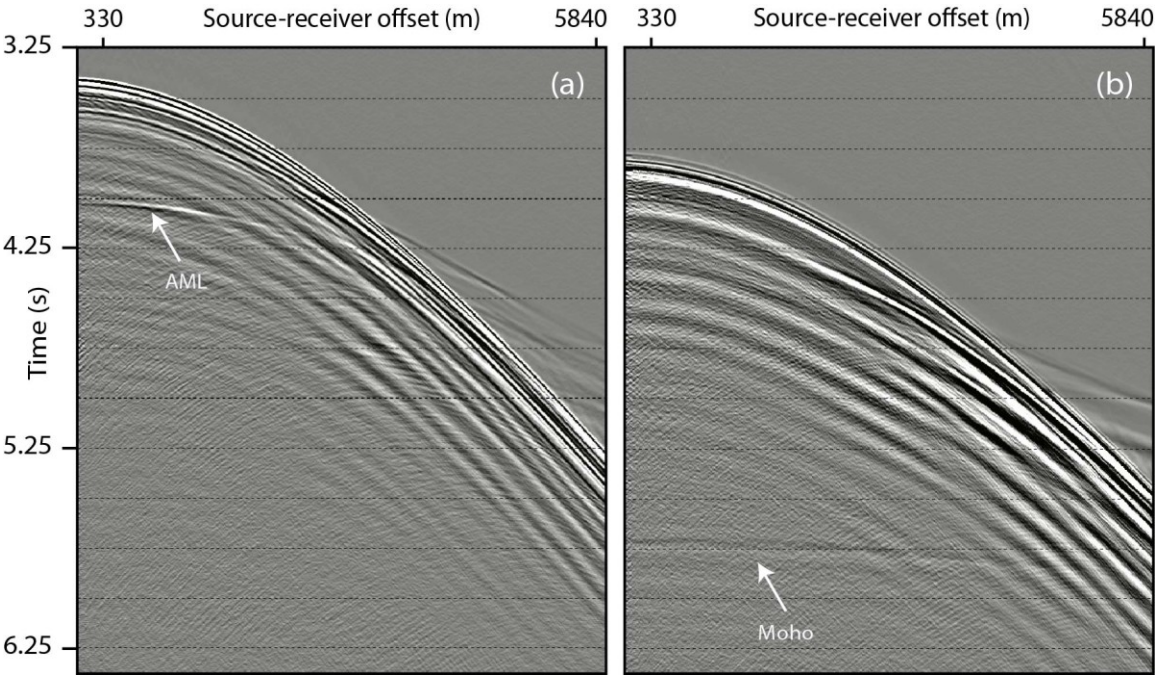

Figure A.2 CMP supergathers showing: a) AMC reflection formed by combining CMPs from 15 in-lines (in-lines 1612 to 1625) and 51 cross-lines (cross-line 3450 to 3500); b) Moho reflection formed by combing CMPs from 31 in-lines (in-lines 1570-1600) and 201 cross-lines (cross-lines 2200 to 2400). Location of these CMP supergathers is shown in Figure A.1.

A.1 3D MCS Data Acquisition

To collect the 3D multichannel seismic (MCS) data, four 6-km-long hydrophone cables or streamers, each consisting of 468 groups of hydrophones with group spacing of 12.5 m, were towed at a depth of 10 m. Separation between streamers was 150 m so that the

total separation between outermost streamers was 450 m (Figure A.3a). Recording time was 10240 ms and sample rate was 2 ms. Two seismic sources, each comprised of two linear arrays of nine airguns with a total volume of 3300 in^3 were towed at a depth of 7.5 m. The modeled source signature and its amplitude spectrum are shown in Figure A.3b. The two sources were fired in an alternating (flip-flop) mode every 37.5 m resulting in eight CMP profiles per sail line separated by 37.5 m. After completing a sail line, a large turning radius of ~5000 m is required for running into a new sail line. To minimize the number of turns, two racetrack loops are filled at the same time (Figure A.4). Sail lines were 300 m apart, and 24 km long with 4 km on each side for run-in and run-out that provided 16 km of nominal full-fold coverage of 40 across the ridge axis. The 3D MCS data acquisition parameters are summarized in Table A.1 and the geodetic information in Table A.2.

The four streamers and two air gun sources were navigated with a combination of Global Positioning System (GPS) located on each tailbuoy and on each gun string, 32 acoustic transponders, and 80 streamer compasses located every 300 m along each hydrophone cable. The acoustic transponders were located on each gun string, two on the streamer head, two placed mid streamer, and two on the tail of the streamer, and one at each tailbouy. This navigation system resulted in shot and receivers position accuracy of <1 m and <3 m, respectively. The streamer compasses used for controlling depth of each streamer have accuracy better than 1 m.

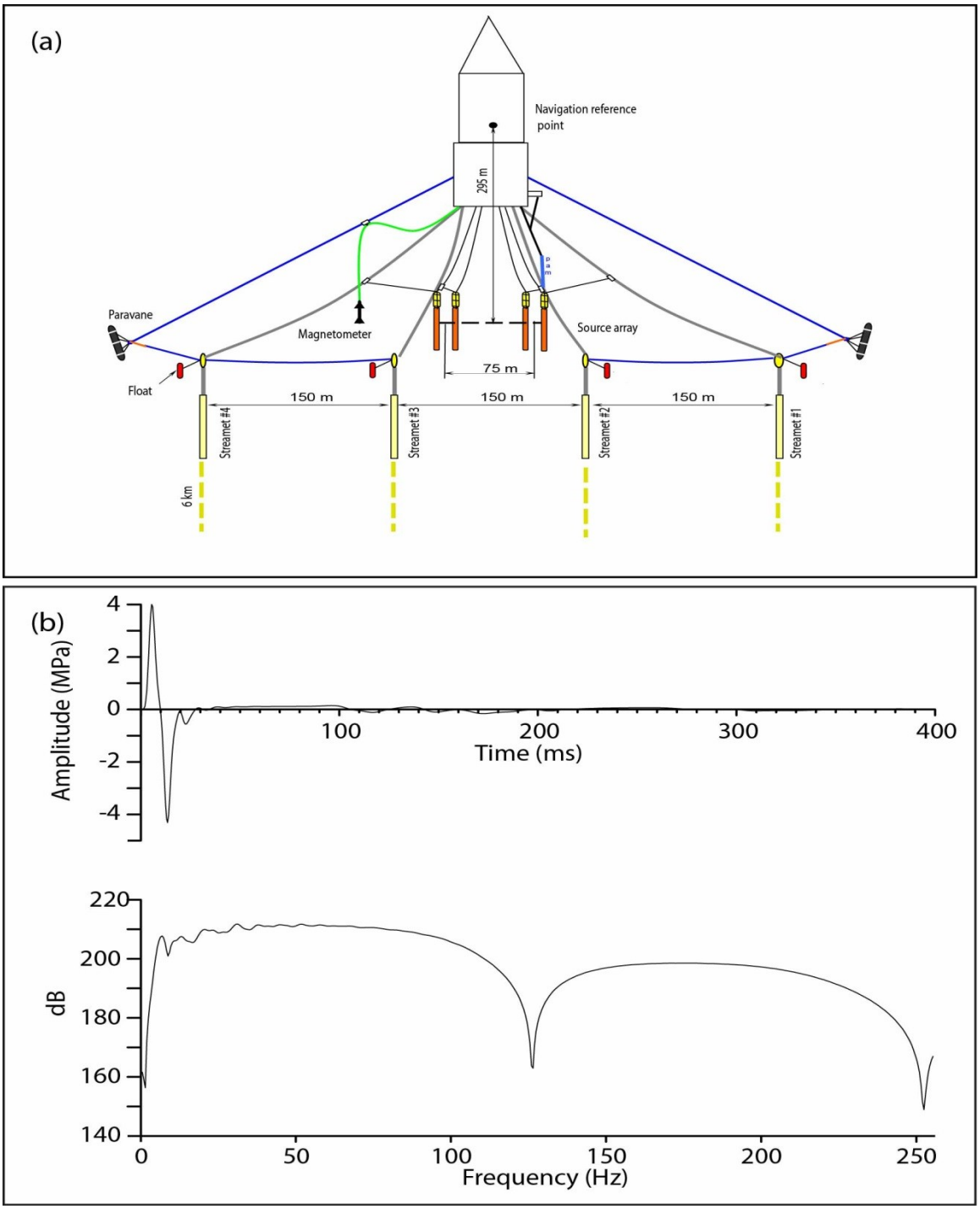

Figure A.3 Tow configuration of the MGL0812 survey (a) and modeled source signature (b). Streamers are separated 150 m and the nominal near offset (distance between the centers of sources to the nearest channel) is 200 m. The compass birds, distributed along the streamer every 300 m, are used to control streamer depth and collect compass data used to model the shape of the streamer and compute receiver locations. The two energy sources each have two string arrays. Each array is composed of 10 guns, one of which is a spare gun. Without the spare gun, volume of each source array is 3300 in3. (b) Modeled source signature for two strings at 6 m depth.

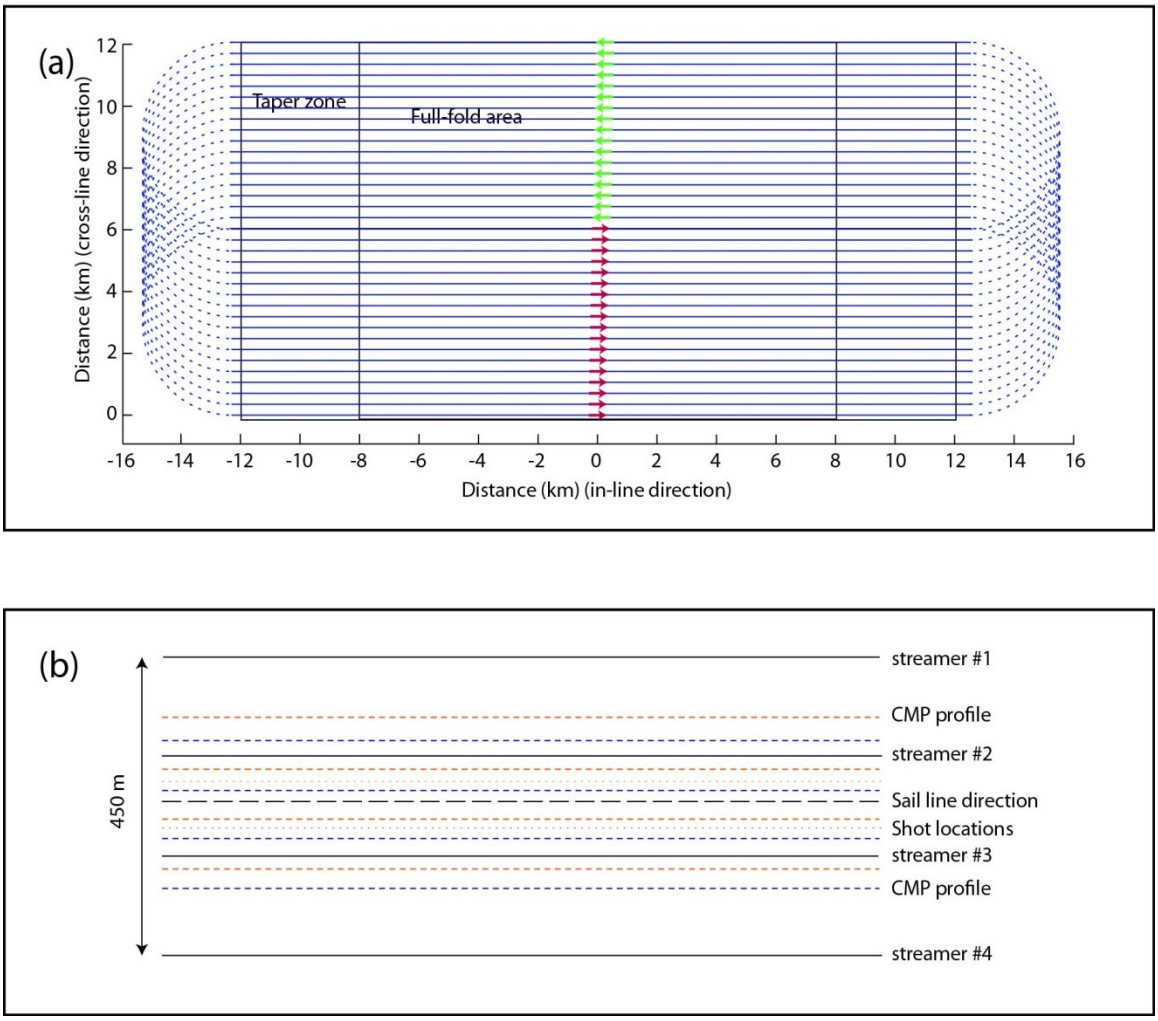

Figure A.4 Schematic racetrack of MGL0812 3D survey [*Mutter et al.,* 2009] (a) and schematic CMP profiles of a sail line (b). (a) The solid lines show the location of sail lines separated by 300 m and dashed lines show the turns. To achieve full-fold coverage width of 16 km, the length of each sail line was extended by about 4 km at both ends. Two complete racetracks and two incomplete racetracks were recorded during the MGL0812 survey. (b) Eight CMP lines are recorded per each sail line traverse.

Table A.1 Summary of 3D MCS data acquisition parameters for the EPR3D project.

Major navigation components	Seismic Navigation System	C-Nav primary
	Survey datum	WGS84
	Navigation reference point (NRP) to Antennae	4.87 m
	NRP to source	295 m
	Antenna to Source	299.87 m
	Compass birds	Yes
	Tail buoy Positioning	Yes
Receiver configuration	Minimum offset	200 m (nominal)
	Total number of channels	1872
	Number of streamers	4
	Number of channels	468
	Channel interval	12.5 m
	Streamer length	6000 m
	Streamer separation	150 m
	Near-channel number	468
	Streamer depth	10 m
Source configuration	Number of source arrays	2 (each with two strings)
	Alternate Shooting	Yes
	Source pressure	2000 psi nominal
	Number of air guns	20 (10 guns per string)
	Source depth	7.5 m
	Shot control	Distance
	Shot Interval	37.5 m
Recording	Sample interval	2 ms
	Recording length	10.240 sec
	Format	SEGD

Table A.2 Geodetic information for the survey.

Grid	Universal Transverse Mercator (UTM)
Projection Type	Universal Transverse Mercator (UTM), Northern Hemisphere
Projection Zone	13
Longitude at Origin (Central Meridian)	105 W
Height unit	Meters
Angle units	Degree
Grid Units	Meters
Geoid	WGS84

The geometry of the survey yields nominal full-fold of 40 traces per CMP bin that is 37.5 m wide and 6.25 m long in cross-ridge-axis and along-ridge-axis direction, respectively. Nevertheless, fold distribution deviated from the nominal value due to streamer feathering, survey gaps caused by marine life, and technical shutdowns (Figure A.5). The average feathering was ±5˚ requiring minimal infill. Gaps in the survey due to marine life and technical shutdown were closed with reshoot lines. For more details on data acquisition and the operational experience of this 3D seismic data acquisition project, please refer to *Mutter et al.* [2009].

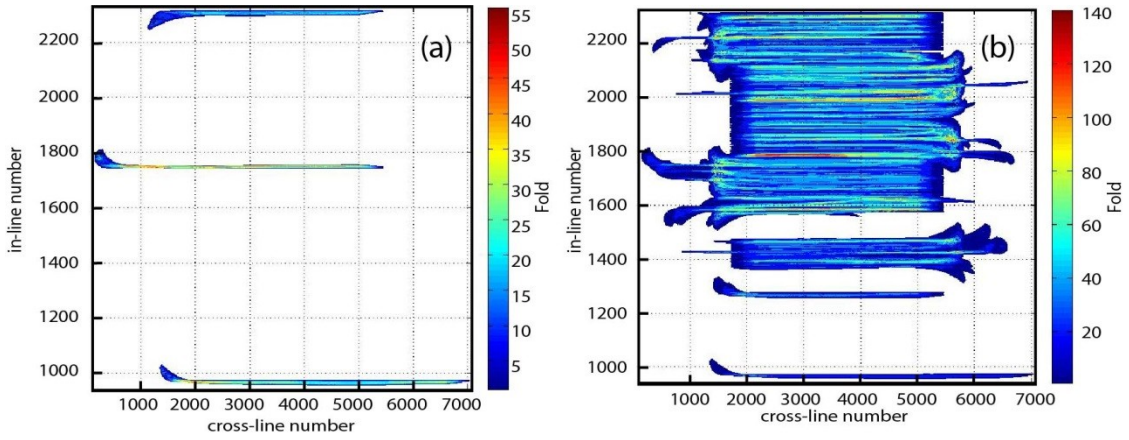

Figure A.5 EPR3D fold map and survey boundary for geometry definition. a) Fold map distribution of sail line 972P (defining the survey boundary to the east and south), 1784P (defining the survey boundary to the west) and 2316P (defining the northern limit of the survey) that are used to setup the 3D project boundaries for geometry definition. b) Fold map of each individual sail line. The gaps in (b) is because of technical problems during data acquisition.

This area consists of 94 primary (collected along the designed survey grid), 11 infill lines (collected in-between primaries due to high streamer feathering), and 10 reshoot sail lines (recollected along the planned grid due to data gaps associated either with technical problems or with marine mammal sightings).

The smaller area between 9˚37.5'N to 9˚40'N covers ~100 km^2 and consists of 14 sail lines that are separated from the larger 3D area by 3.3 km. A pair of lines were also acquired south of this area at 9˚35'N and a single line just south of 9˚30'N (Figure A.1). The 3D project consists of 111 sail lines with a total length of 3781.95 km of sail line data. Each of the sail lines forms eight CMP profiles and therefore the CMP line acquisition is 30255.6 km. The full dataset consists of 99,888 shots, 186,998,336 sources-receive pairs or data traces, and a 957,890,520,320 data samples.

A.2 Geometry Definition

Survey geometry is defined by providing the origin of the survey, length and width of the survey and orientation of the survey. These parameters in addition to a nominal bin size define a regular and rectangular grid of bins where coordinate of the center of each bin are specified. The positive x and y axes point towards east and north, respectively. The orientation of the 3D survey measured counterclockwise with reference to positive x-axis is 8°, or the azimuth of in-lines is 82º N. The nominal bin size is 37.5 m in the y direction and 6.25 m in the x direction. After defining the survey grid, data traces with x and y coordinates stored in trace headers are assigned to formed nominal bins.

Because there were four distinct data collection areas during this survey, all aligned along the ridge axis, I first defined a global grid, and then divided it into four distinctive 3D survey grids (Figure A.1). The main motivation for defining separate 3D survey grids are the large gaps in data between the survey areas shown in Figure A.1. Separate 3D surveys have the advantage of avoiding empty bins during velocity model building and 3D migration. The formed global 3D grid is defined so as to include all the across-axis sail

lines from sail line 0972P in the southmost grid to sail line 2316P in the northmost grid with a margin of 300 m in every direction (Figure A.1). To set up the global geometry and define the global grid boundaries, the sail lines that extend to the southernmost, northernmost, easternmost and westernmost point are chosen. Navigation information for these sail lines is summarized in Table A.3 The sail line numbering starts with the first sail line number 952 (this numbering is from the field experiment) with increment of 8. The number attributed to the first in-line in the global 3D survey grid is also chosen to be 952 so that each in-line coincides with the sail line that has the same number. This is possible because the increment of sail line numbering is also 8 and there are 8 CMP in-lines associated with each sail line. The first cross-line (the line orthogonal to the shooting direction) was chosen to be 101 on the larger, global grid. The parameters for the EPR3D global grid are given in

Table A.4.

Individual grids were extracted for four areas from south to north as subsets of the global grid (Figure A.1):

Grid 1: This grid forms the first grid (the southmost grid) and includes sail line 0972P.

Grid 2: This is the second grid from the south and includes two sail lines of 1268P and 1276P.

Grid 3: This grid is the third grids and includes fourteen sail lines.

Grid 4: This is the largest grid (the northmost grid) and includes ninety two sail lines.

Table A.3 Sail lines defining the northern, southern, eastern and western boundaries of the global grid dimension.

Sail line	**Boundary limit definition**	**Shot point range**
0972P	S and E limits	897-1800
1748P	W limit	681-1539
2316P	N limit	861-1539

Table A.4 Global grid parameters used to define 3D geometry for EPR3D data analysis.

Parameter	**Value**
Number of in-lines	1383
Number of cross-lines	6982
Distance between in-lines	37.5 m
Distance between cross-lines	6.25 m
X-coordinate origin in UTM	562089.67 m
Y-coordinate origin in UTM	1045621.17 m
Angle of survey with respect to the east direction	8 °
First in-line label	944
First cross-line label	101

Table A.5 Parameters defining origin and orientation of grid for each survey.

Parameter	**Survey 1**	**Survey 2**	**Survey 3**	**Survey 4**
Number of in-lines	96	102	245	831
Number of cross-lines	5783	5820	5820	6888
Distance between in-lines	37.5 m	37.5 m	37.5 m	37.5 m
Distance between cross-lines	6.25 m	6.25 m	6.25 m	6.25 m
X-coordinate origin in UTM for the SW corner	569510.49 m	568290.42 m	564571.29 m	559208.79 m
Y-coordinate origin in UTM for the SW corner	1046664.10 m	1057815.32 m	1059489.01 m	1066119.72 m
Azimuth of sail lines	82°N	82°N	82°N	82°N
First in-line label	944	1243	1301	1496
First cross-line label	1300	1355	803	101

A.3 Data Processing

After assigning data traces to the specified bin locations, the processing steps in Figure A.6 were applied to the data. I started processing the data by testing 1D bandpass filters. The results of these tests, which are detailed in Section A.3.1 show that resampling the data to 4 ms is not an option and that a trapezoid bandpass filter with corner frequencies of 1-6-200-220 Hz is appropriate for this dataset.

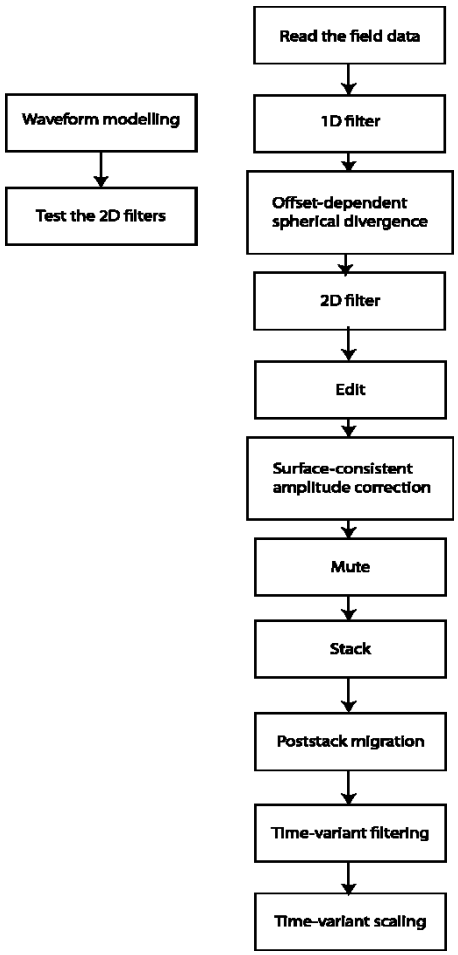

Figure A.6. Flowchart of the processing applied to data in Chapter 2.

Applying spherical divergence to compensate for geometrical spreading is detailed in Section A.3.2. In this section I show that applying offset-independent spherical divergence overcorrects the data at offsets greater than 2 km, which is not the case with the offset-dependent spherical divergence correction. 2D filtering to remove low-frequency cable noise is explained in Section A.3.3 together with the tests that were applied to a synthetic shot gather computed for the purpose of this test. Applying a simplified version of LIFT algorithm [*Choo et al.,* 2004] that does not include the signal-add-back step removes noise efficiently and prevents zeroing traces that were flagged as "bad" in a semi-automated data editing approach. Surface-consistent deconvolution to improve the temporal resolution and supress peg-leg multiples is summarized in Section A.3.4. Surface-consistent amplitude correction to balance abnormally high/low shot and channel amplitudes with an example from sail line 1572P is detailed in Section A.3.5. After de-noising and amplitude normalization, AML and Moho reflections can be identified on CMP supergathers (Figure A.2). However, a consistent and systematic moveout velocity analysis is not possible because Moho reflection is not continuous enough and is not present at some locations. Therefore, three velocity volumes were produced by hanging the available 1D and 2D velocity functions from the seafloor. CMP bin gathers were NMO corrected using these velocity volumes, stretched far offset arrivals were muted and the gathers were summed to form the 3D stack volumes. The stack volume produced using the ESP1 velocity function provided the best overall image of all structures. Velocity analysis and stacking are summarized in Section A.3.6.

Poststack processing (Section A.3.7) includes seafloor multiple mute to reduce migration noise and 3D Kirchhoff poststack time migration followed by time-variant scaling and

time-variant filtering. Migration aperture size is chosen to be 3.5 × 3.5 km for imaging AML and Moho

A.3.1 Bandpass Filtering

A trapezoid zero-phase bandpass filter with corner frequencies of 1-6-200-220 Hz was applied to the field data (Figure A.7). Zero-phase bandpass filtering resulted in a significantly better result than minimum-phase filtering. After applying minimum-phase bandpass filter, a significant portion of the low-frequency noise was still persistent on the shot gathers. Applying a zero-phase bandpass was acceptable because the signal bandwidth was sufficiently broad that the filter did not change the phase of the reflection arrivals. To decide if resampling the data to 4 ms and therefore limiting the frequency band to 125 Hz is an option, the raw shot gather shown in Figure A.7a is filtered with a series of 40-Hz-wide bandpass filters (Figure A.8). The filtered data show that the reflection and diffraction signal is also present from 125 to over 200 Hz and, hence, useful in the imaging process.

A.3.2 Geometric Spreading Correction

Shot energy spreads on a spherical wavefront and decays as the wavefront propagates through the earth. Assuming that the seismic velocity is constant, the wavefront area increases proportionally to r^2, where r is the propagated distance. Therefore, the wave amplitude scales inversely with the distance the wave travels (1/r). To compensate for this effect and recover amplitude decay as a function of offset and traveltime, spherical divergence correction is applied to seismic data.

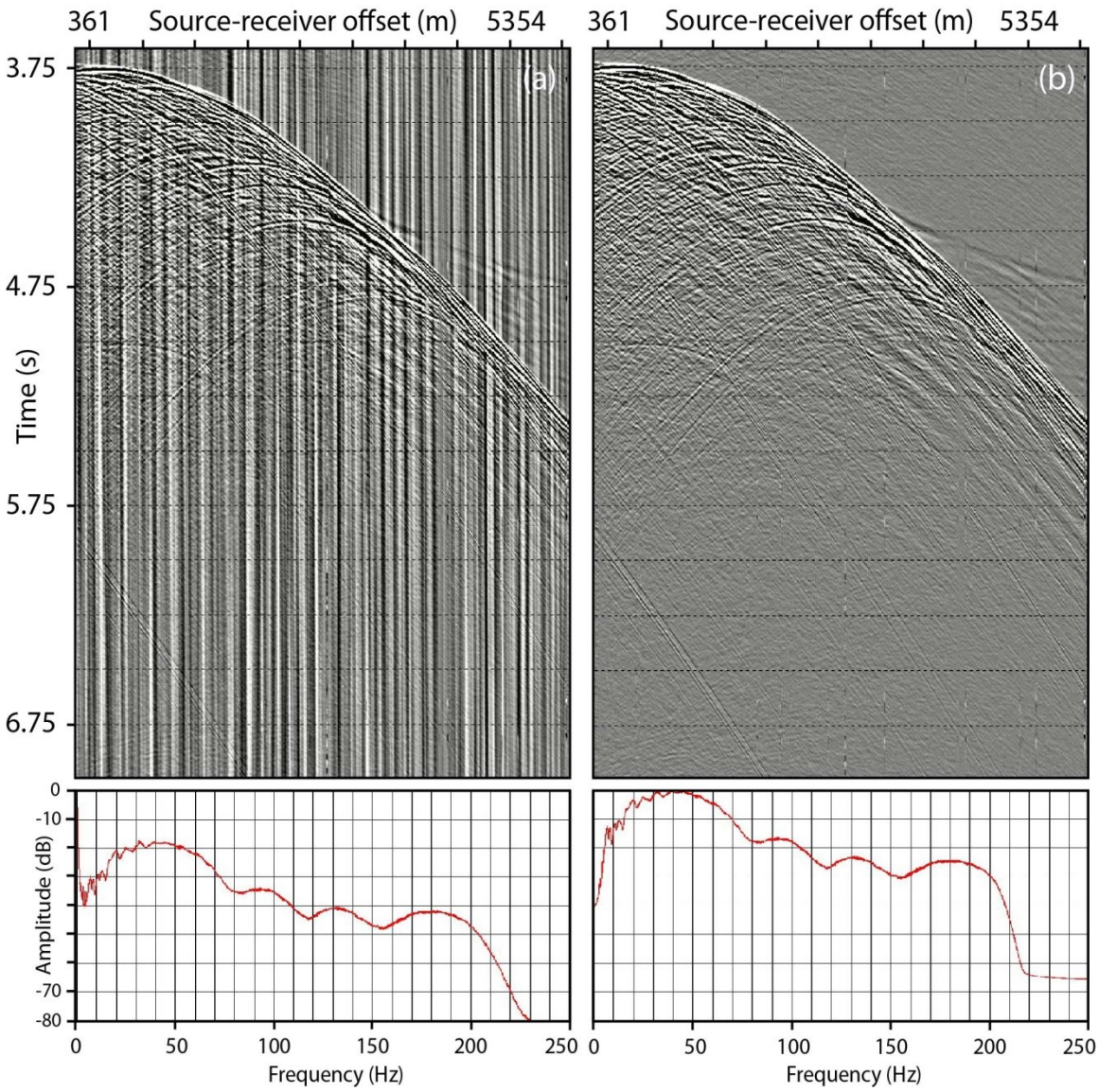

Figure A.7 Trapezoid bandpass filtering. Shot gather 1074, sail line 1972P, cable 2 (a) before applying and (b) after applying a trapezoid zero-phase bandpass filter with corner frequencies of 1-6-200-220 Hz. Corresponding amplitude spectrums are shown below the shot gather.

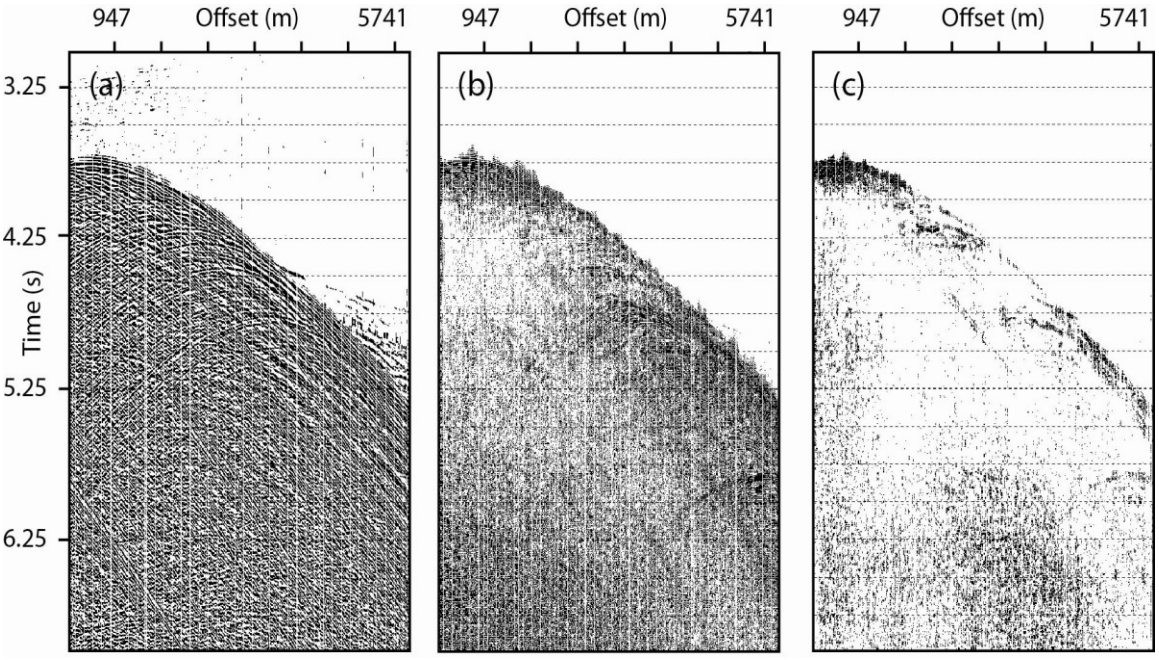

Figure A.8 Application of 40-Hz-wide trapezoid bandpass filters to Figure A.7b. Results of filtering with corner frequencies of a) 1-6-46-66 Hz b) 80-86-126-146 Hz and c) 160-166-206-226 Hz. Panel (c) shows that the data in this frequency range, at least at shallow depth, is not noise and can be used in data processing. Therefore, resampling the data to 4 ms and in this way limiting the frequency content to 125 Hz is not a constructive option.

For a layered earth model, amplitude decay for zero-offset data g(0) is expressed as follows [*Newman,* 1973]:

$$g\ 0\ = \frac{\mathrm{T}\ 0\ \mathrm{V}^2}{\mathrm{V}_0} \tag{A-1}$$

where $T(0)$ is the normal-incidence two-way traveltime (TWTT), $V^2 = \ \frac{\mathrm{n}}{\mathrm{i}=1}\frac{\mathrm{t_i V_i^2}}{\mathrm{t}}$ is the root-mean square (RMS) velocity, and V_0 is velocity of the first layer.

Ursin and Dahl [1989] have shown that the geometrical spreading varies greatly with offset and this effect needs to be considered when estimating offset variation of the reflection coefficient. *Ursin* [1990] presents the formulae for the offset-dependant spherical divergence correction. It contains the second and third term of the Taylor

expansion for geometrical spreading and provides a more precise correction for the EPR3D data collected using the 6-km-long streamers. ESP1 velocity function of *Vera et al.* [1990] hung from the seafloor was used for calculating geometric spreading correction factors (Figure A.9). The result of applying offset-dependant and offset-independent spherical divergence correction to a synthetic shot gather show that applying offset-independent correction overcorrects traces at mid-offset range (Figure A.10). The result of applying offset-dependant spherical divergence correction to data is depicted in Figure A.11.

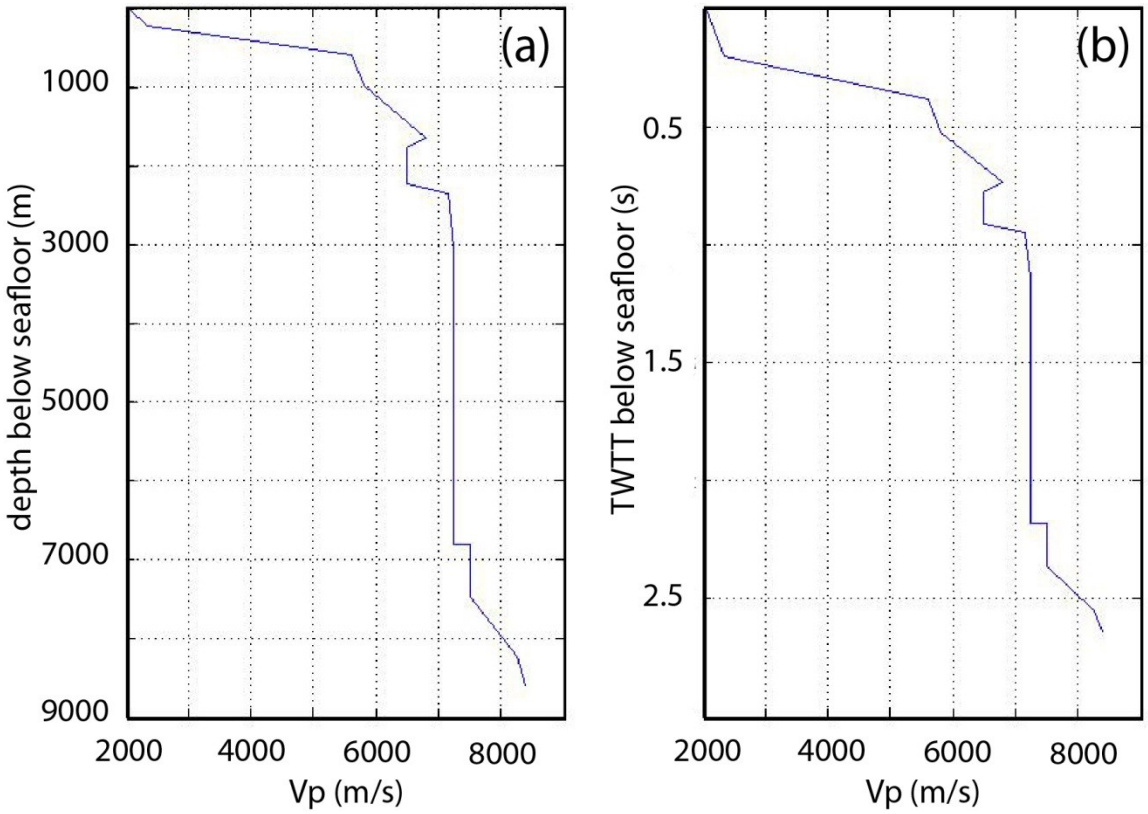

Figure A.9 Compressional velocity function of Vera et al. [1990] (ESP1) as a function of a) depth and b) TWTT.

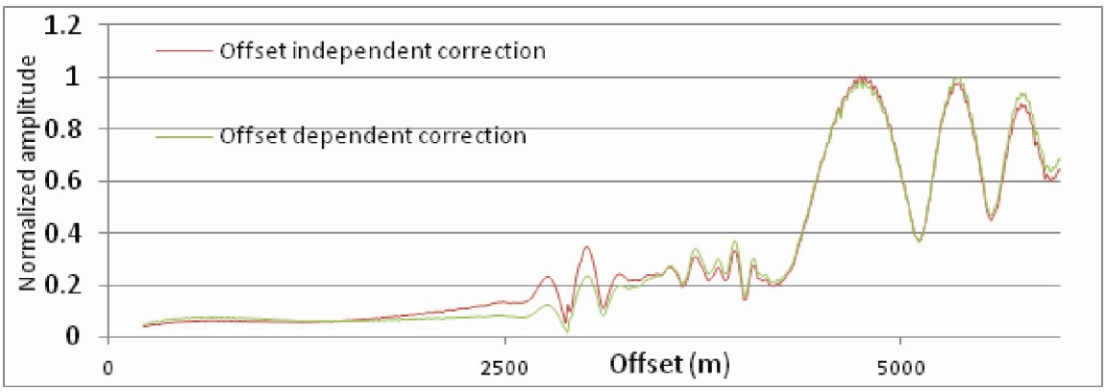

Figure A.10 Amplitude variations with offset of seafloor reflection for a synthetic shot gather after geometric spreading correction. Applying offset-independent geometrical spreading correction results in overcorrection of amplitudes at mid-offset.

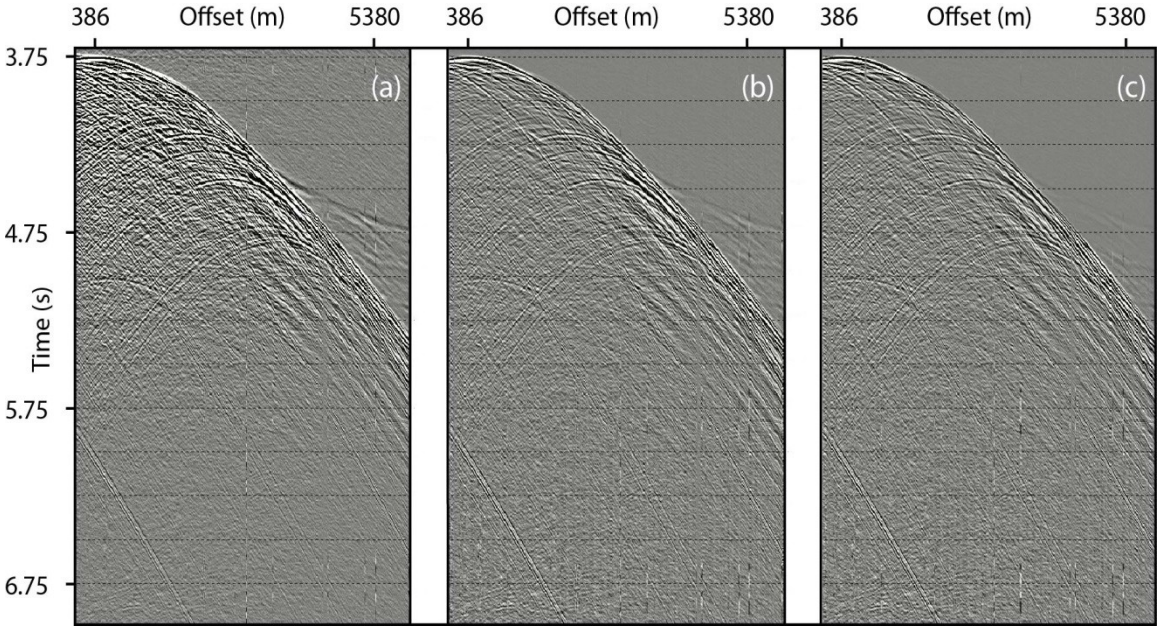

Figure A.11 Application of geometric spreading correction. Shot gather 1074, sail line 1972P, cable 2 after applying a) bandpass filter, b) bandpass filter and offset-independent spherical divergence correction, c) bandpass filter and offset-dependent spherical divergence correction. Application of offset-independent spherical divergence correction overcorrects the data.

A.3.3 Testing 1D and 2D Filters on EPR 3D Seismic Data

To evaluate the effectiveness of available filters on removing ambient and streamer noise from the EPR 3D seismic data, a shot gather was modeled in frequency domain using *Pratt's* [1990] P-wave full waveform acoustic modeling code. The simulated shot gather models major P-wave reflection events of the EPR3D MCS survey including AML and

Moho reflections. Pure ambient and streamer noise recorded during data acquisition was added to the modeled shot gather to produce a synthetic gather that was then used for testing of available 2D filters.

A.3.3.1 Modeling in Frequency Domain

Modeling in frequency domain requires a velocity profile and a source function, which includes the wavelet type, amplitude spectrum, and number of frequencies. A further requirement includes choosing an appropriate damping factor (τ) to avoid time domain wraparound or aliasing. To simulate AML and Moho reflections, a hybrid velocity model was constructed (Figure A.12). I used ESP5 velocity function of *Vera et al.* [1990] to constrain velocity variation with depth from seafloor to AML. This model comprises a water layer, uppermost crustal velocity structure (layers 2A and 2B), a large velocity gradient immediately above AML, and an AML that is located ~1.7 km below the seafloor. For the lower crustal gabbro section I used a gradient velocity layer and a velocity step increase that marks the Moho boundary. A minimum phase Keuper wavelet with a bandwidth from 0 to 50 Hz was used as the source function (Figure A.13), although for some tests the Keuper wavelet bandwidth was from 0 to 30 Hz.

As aliasing is a known problem in techniques that synthesize seismograms in the frequency domain [*Mallick and Frazer*, 1987], it is important to suppress the late arrivals to avoid wraparounds. This is vital for evaluation of 2D filters as the least possible modeling noise should be present in the data.

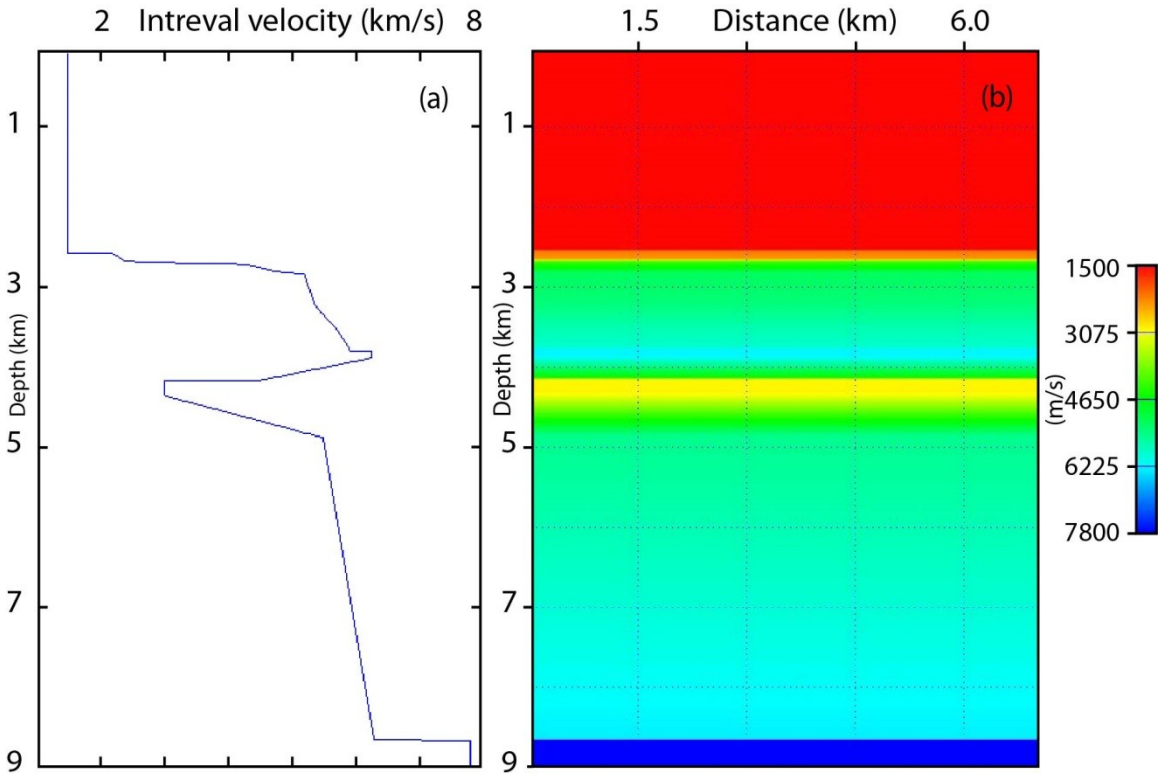

Figure A.12 Hybrid velocity profile used for modeling a synthetic shot gather. a) ESP5 velocity function of *Vera et al.* [1990] was used for the velocity variation with depth from the seafloor to AML, velocity gradient layer for the lower crustal gabbros, and a step function was used in the velocities to simulate Moho boundary. b) Velocity profile for modeling created based on velocity function in (a).

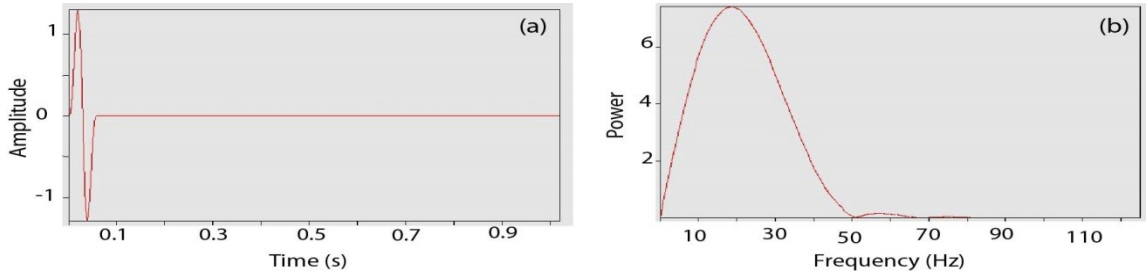

Figure A.13 Source function used for modeling: a) Minimum phase Keuper wavelet with a bandwidth of 0 to 50 Hz; b) frequency spectrum of this wavelet.

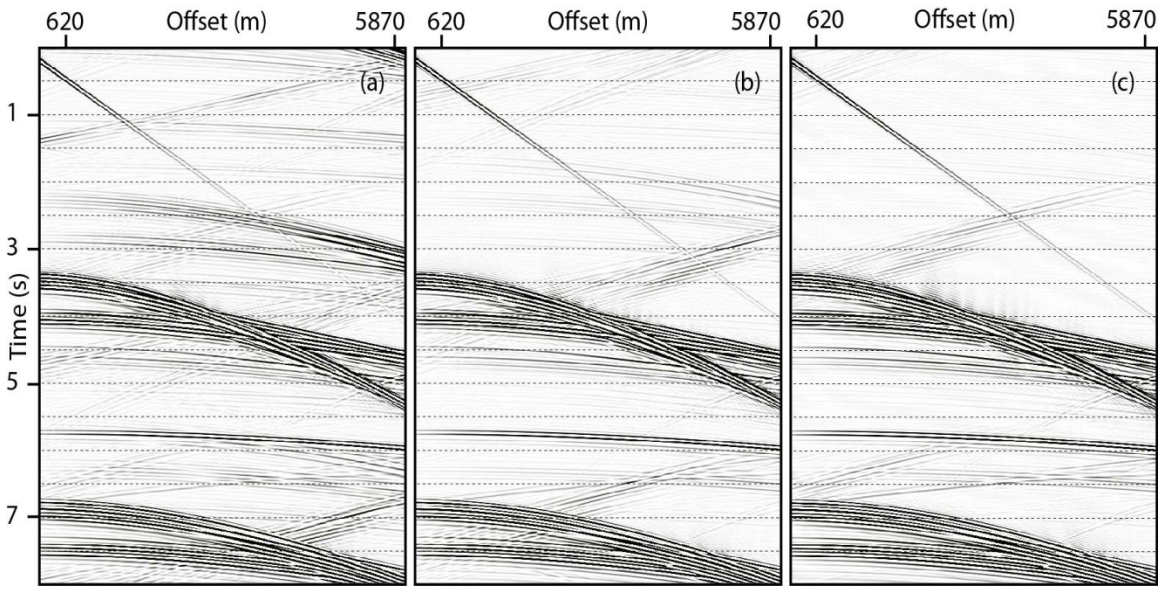

Figure A.14 Testing the effect of the number of modeled frequencies on suppressing wraparound noise: a) 240, b) 360 and c) 480 modeling frequencies. All three synthetic shot gathers shown were produced using a source with frequency bandwidth from 0 to 30 Hz; τ factor was kept constant at 6 s. This test indicates that increasing the number of modeling frequencies suppresses wraparounds. Note that the data amplitudes in the plots were strongly boosted to show the modeling noise, which has resulted in oversaturation of reflections and multiples.

A number of modeling frequencies and attenuation factors ($1/\tau$) were tested to choose their best combination for suppressing the wraparounds. The testing results show that increasing the attenuation factor (this is equal to decreasing τ value in the code) and increasing the number of frequencies for modeling generally reduce wraparound (Figure A.14 and Figure A.15). The final parameters for forward modeling are shown in Table A.6, and the corresponding shot gather is shown in Figure A.16. The modeling grid cell size is 7.5×7.5 m. This allows for finite difference modeling of a wavefield with frequencies of up to 50 Hz.

Shot gather of Figure A.16 with and without cable and ambient noise is shown in Figure A.17. Amplitude scaling factor used to multiply the synthetic data before combining them with noise was calculated by dividing the RMS amplitude of the pure noise gather with

the RMS amplitude of the modeled shot gather. This resulted in a one to one S/N ratio. It is simple to increase the S/N ratio of the combined gather by increasing the scaling factor used to multiply the synthetic data. However, as the combined gather will be used for testing the performance of 2D filters, a lower S/N ratio of this gather compared to field data is preferred.

Signal-to-noise ratio of the modeled shot gather with noise and a recorded shot gather are compared in Figure A.17. As modeling in frequency domain was done using frequency bands of 0 to 30 and 0 to 50 Hz, the recorded shot gather was lowpass filtered with 30 Hz and 50 Hz selected as tapering frequencies. Near trace of the synthetic and field gathers are compared in Figure A.18.

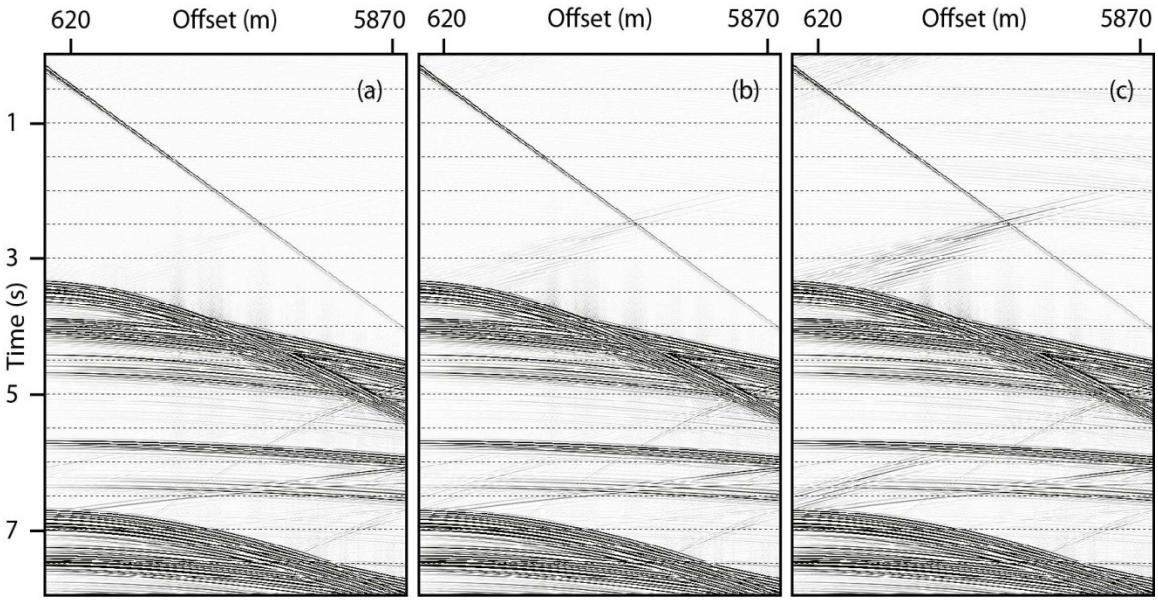

Figure A.15 Testing the effect of attenuation factor τ on suppressing wraparound effect: $\tau = 2.2$ (a), 4.2 (b), and 6.2 (c). Source frequency bandwidth for modeling was 0-50 Hz. The low τ value suppresses wraparounds more effectively.

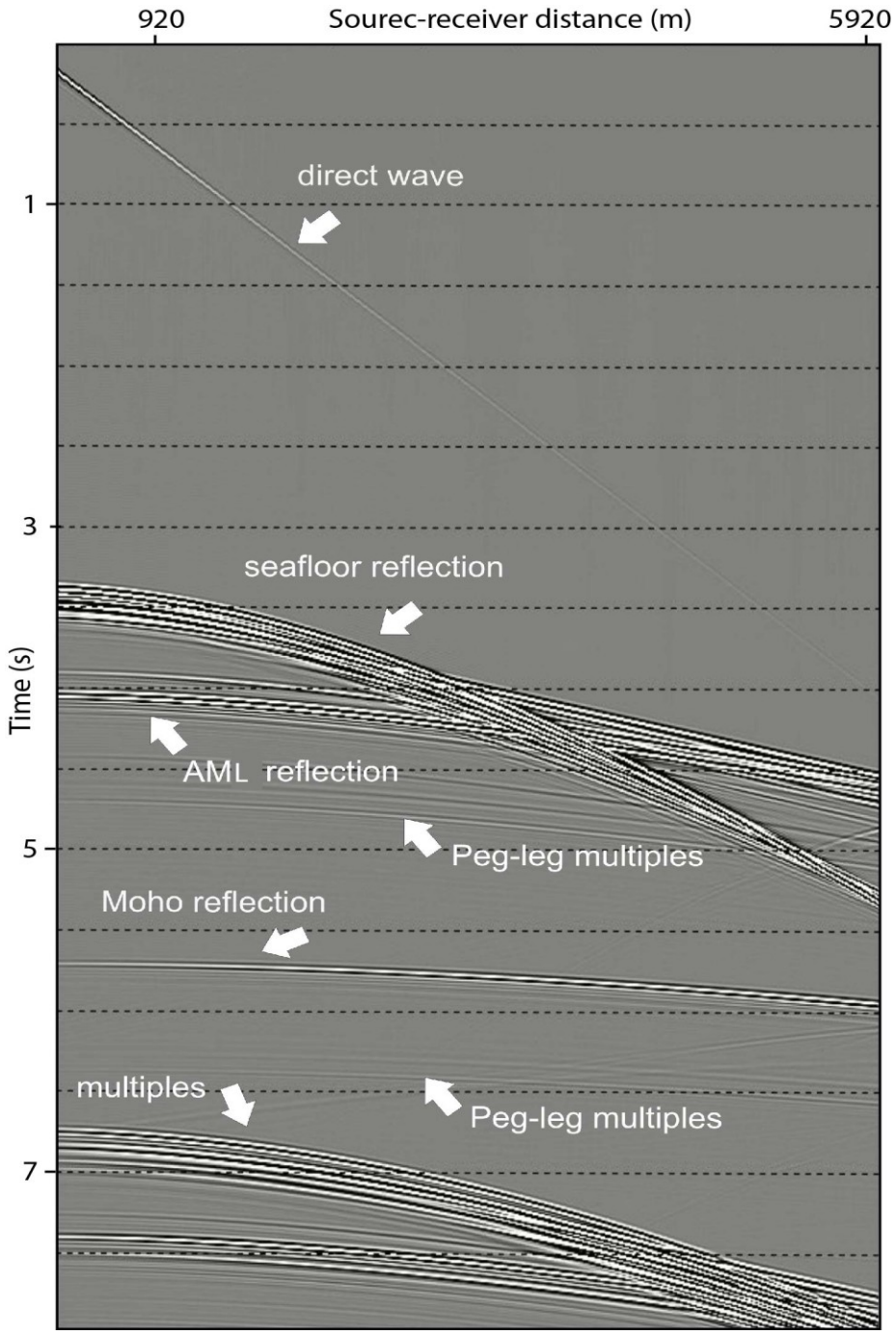

Figure A.16 Modeled shot gather using parameters from Table A.6. Keuper wavelet with a bandwidth from 0 to 50 Hz was used as the source function to produce this shot gather. The seafloor, AML and Moho reflection events are identified.

Table A.6 Final selected parameters for forward modeling of the synthetic shot gather in frequency domain.

Source frequency bandwidth (Hz)	0-50
Spatial sampling (m)	7.5
Number of frequencies	800
Attenuation factor (tau)	2.2
Grid size	935×1200
Number of channels	468
Group interval (m)	12.5

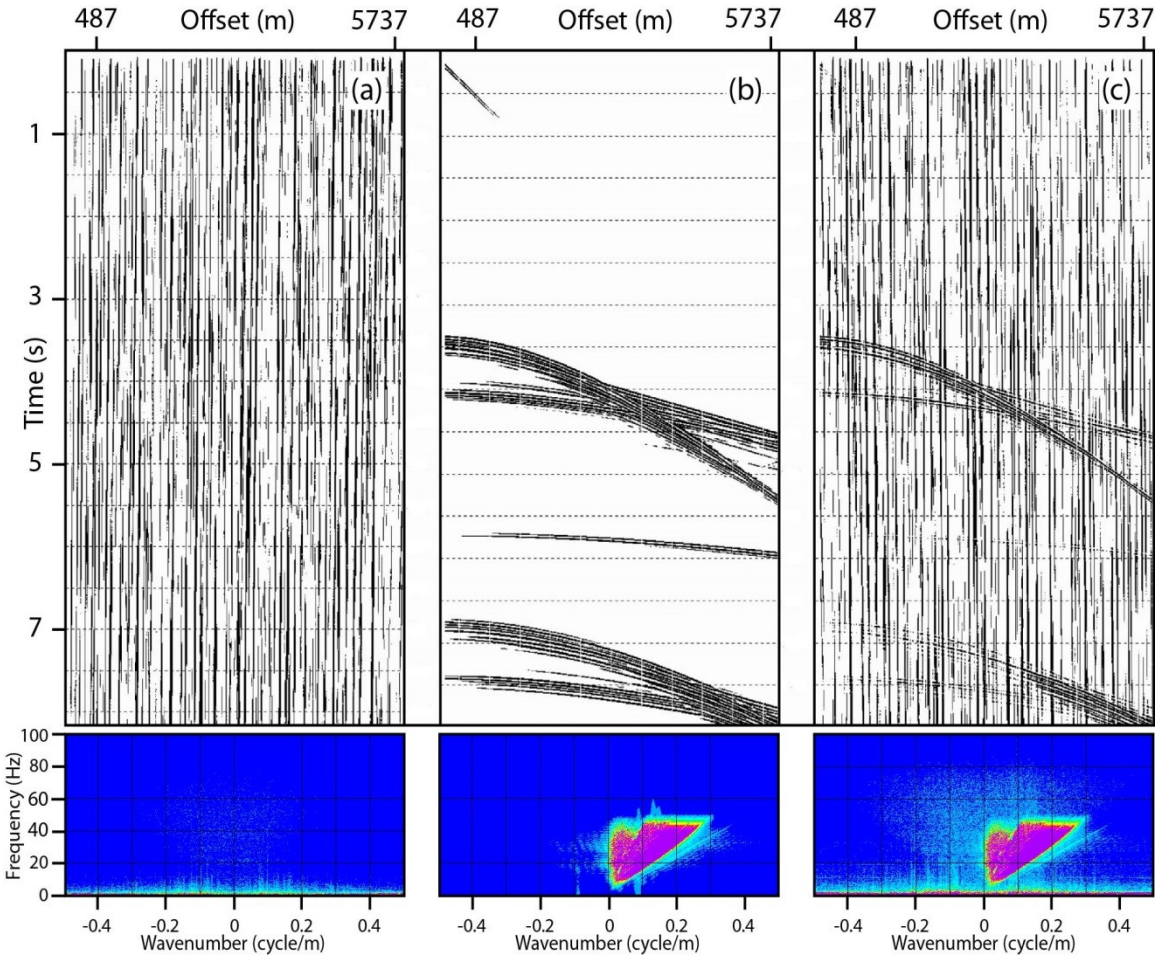

Figure A.17 Ambient and streamer noise (a) recorded by streamer 2 on shot 44 during acquisition of line Axis1 combined with the synthetic shot gather of Figure A.15(b) to produce a shot gather (c) that is used for evaluating available 2D filtering routines. Bottom figures show FK spectrum of (a), (b) and (c). For display purpose, maximum frequency is limited to 100 Hz. Note that the dominant ambient and streamer noise is in the 1-15 Hz frequency range.

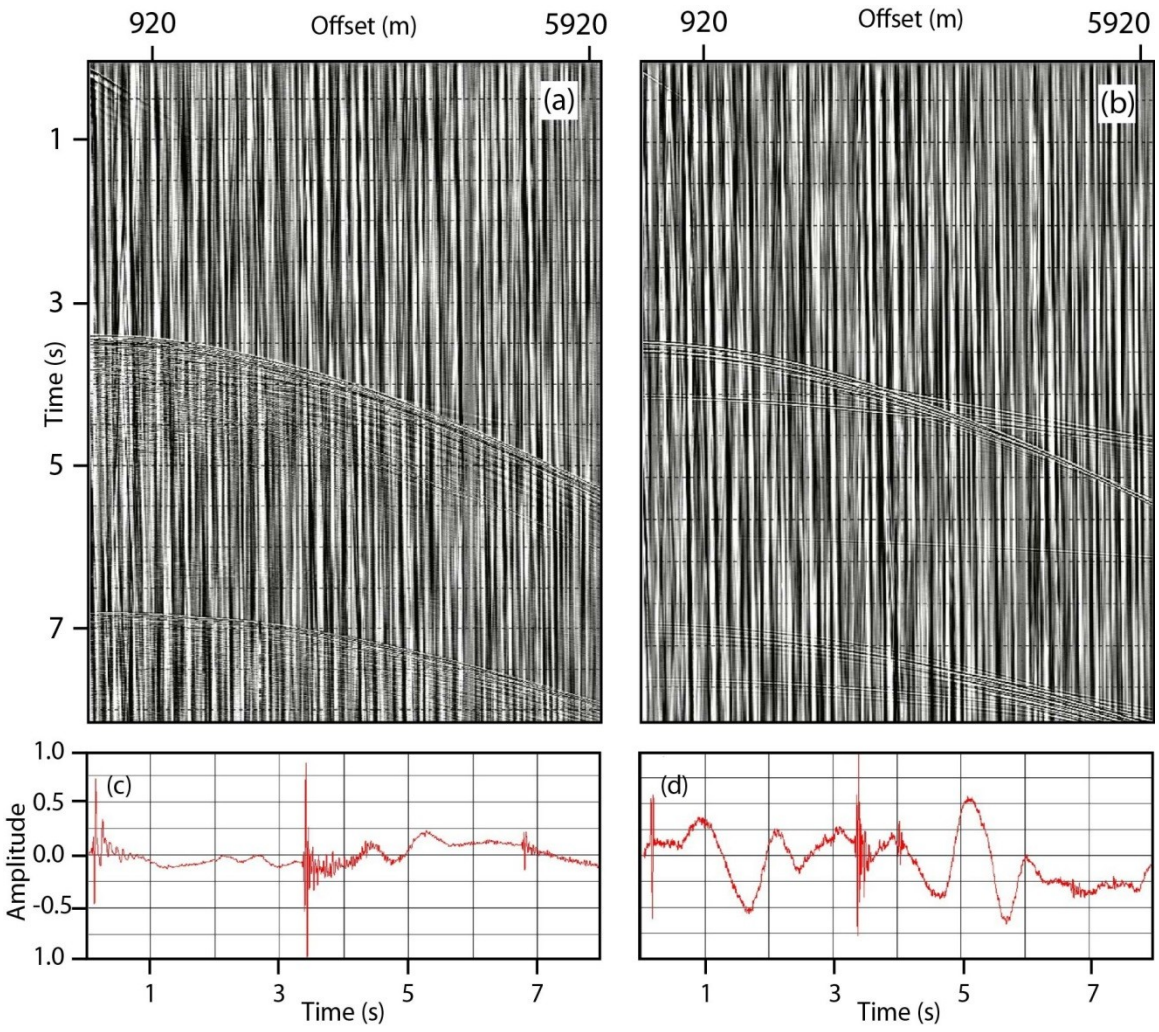

Figure A.18 Comparison between modeled shot gather combined with noise and a field shot gather. a) Field recorded shot gather 44 of sail line AXIS1, streamer 2. b) Modeled shot gather combined with noise. c) Near trace of (a). d) Near trace of (b) showing that scaling factor with the method explained in text is appropriate for filtering purpose as long as S/N ratio of the modeled shot gather is lower than the signal to noise ratio of field data.

A.3.3.2 Testing 2D filters: Comparison of FK, FX and LIFT module

The LIFT methodology [*Choo et al.,* 2004] for removing noise is compared to the FK and FX 2D filters using the synthetic data (see Table A.6 for modeling parameters) with added field ambient and streamer noise. The result of applying FK, FX and LIFT filters to this synthetic shot gather is depicted in Figure A.19. Comparison of the filtered gathers and the pure signal synthetic gather shows that all of these filters remove the background

noise successfully. FX filter is only applied to the frequency range dominated by noise, which for cable tow noise is from 0 to ~15 Hz with the noise amplitude rapidly decaying at frequencies above ~8 Hz.

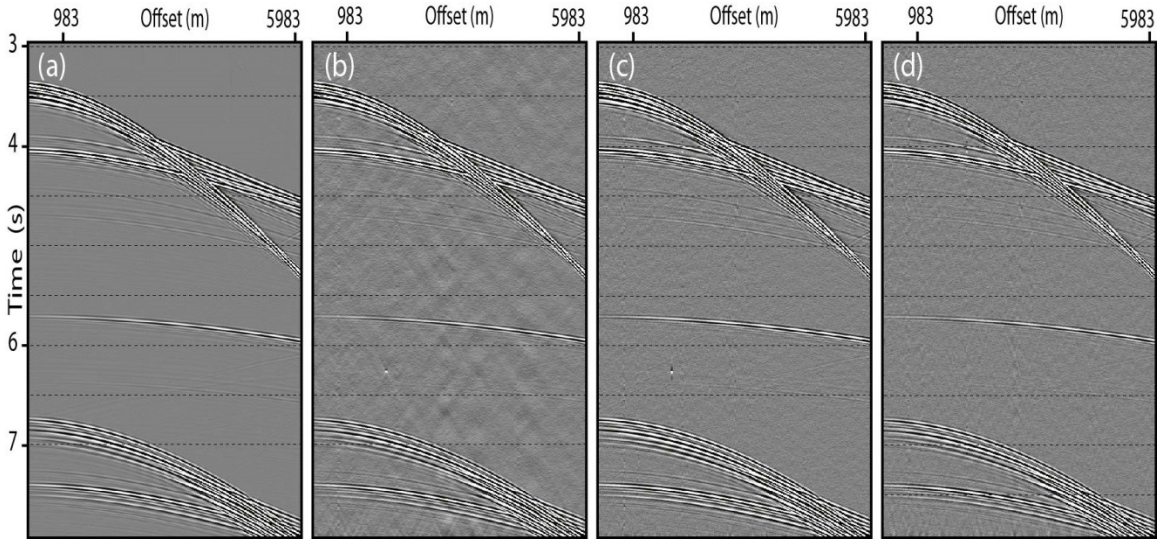

Figure A.19 Comparison of the results of applying FK, FX and LIFT filters to the synthetic shot gather with added streamer noise. a) Modeled shot gather without noise. b) FK filter with frequency - wavenumber values for the polygon of: -500 km^{-1}/0 Hz; -500 km^{-1}/40 Hz; -20 km^{-1}/2 Hz; 20 km^{-1}/2 Hz; 500 km^{-1}/40 Hz; 500 km^{-1}/0 Hz applied to data in Figure A.17c. c) FX filter with frequency range 0-8 Hz applied to data in Figure A.17c. d) LIFT algorithm applied to Figure A.17c data. The FK filter frequency-wavenumber values for the polygon used in LIFT are: -500 km^{-1}/0 Hz; -500 km^{-1}/15 Hz; -20 km^{-1}/2 Hz; 20 km^{-1}/2 Hz; 500 km^{-1}/15 Hz; 500 km^{-1}/0 Hz.

Figure A.19c shows FX filter applied to 0-8 Hz frequency range. If a broader frequency range is selected for filtering (e.g., 0-10 Hz), which is needed for complete removal of cable tow noise, part of the reflection signal is removed as well (Figure A.20). Therefore, FK and LIFT filters are compared from here on as applying the FX filter is not the optimal filtering option.

The coherent noise introduced to data after applying FK filter (Figure A.19b), which makes FK filtering appear as even less effective than FX filtering, is removed after a trapezoid bandpass filter is applied to the data (Figure A.21). The FK spectrum of LIFT

and FK filters (Figure A.21) are identical after applying trapezoid bandpass filtering indicating that both FK and LIFT filter can be used provided that data are mildly bandpass filtered (1-6-200-220 Hz).

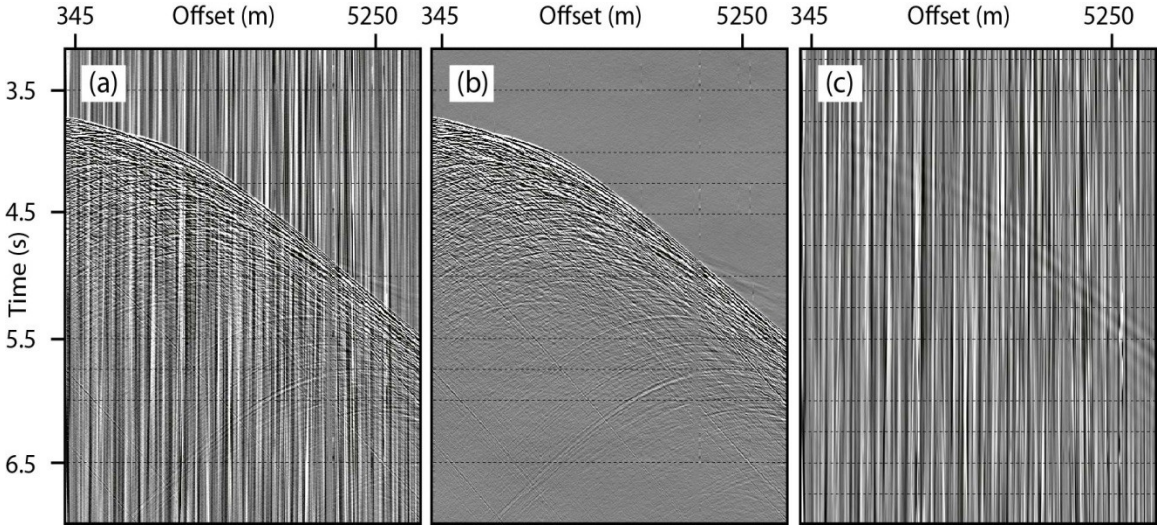

Figure A.20 Applying FX filter to field data. Sail line 972P, shot 990, streamer 2 before (a) and after (b) applying FX filter (0-10 Hz). c) Difference between (a) and (b). Part of the seafloor reflection is removed after applying FX filter.

This is not surprising considering that the LIFT approach is based on subdividing the data into frequency bands and, sometimes, offset bands and then applying a series of filters to the subdivided data including the FK filter for the lowest frequency subgroup of the data.

In the LIFT approach, the data are decomposed into noise and signal components by applying user-defined bandpass filters in the first step. The noise component includes the dominant type of noise that needs to be suppressed by LIFT. Examining the data shows that the dominant noise in EPR3D is in the frequency range of 1 to 15 Hz (Figure A.17). Therefore for LIFT the data were subdivided into low-frequency (0-15-20 Hz) and high-frequency (20-25-200-220 Hz) bands. The mid-frequency range of 15-20-20-25 Hz is formed by subtracting the full spectrum from the combination of low and high frequency

components. It would be ideal to separate the data into 0 to 15 Hz and >15 Hz, but separating the data by sharp cutoff frequencies results in ringing.

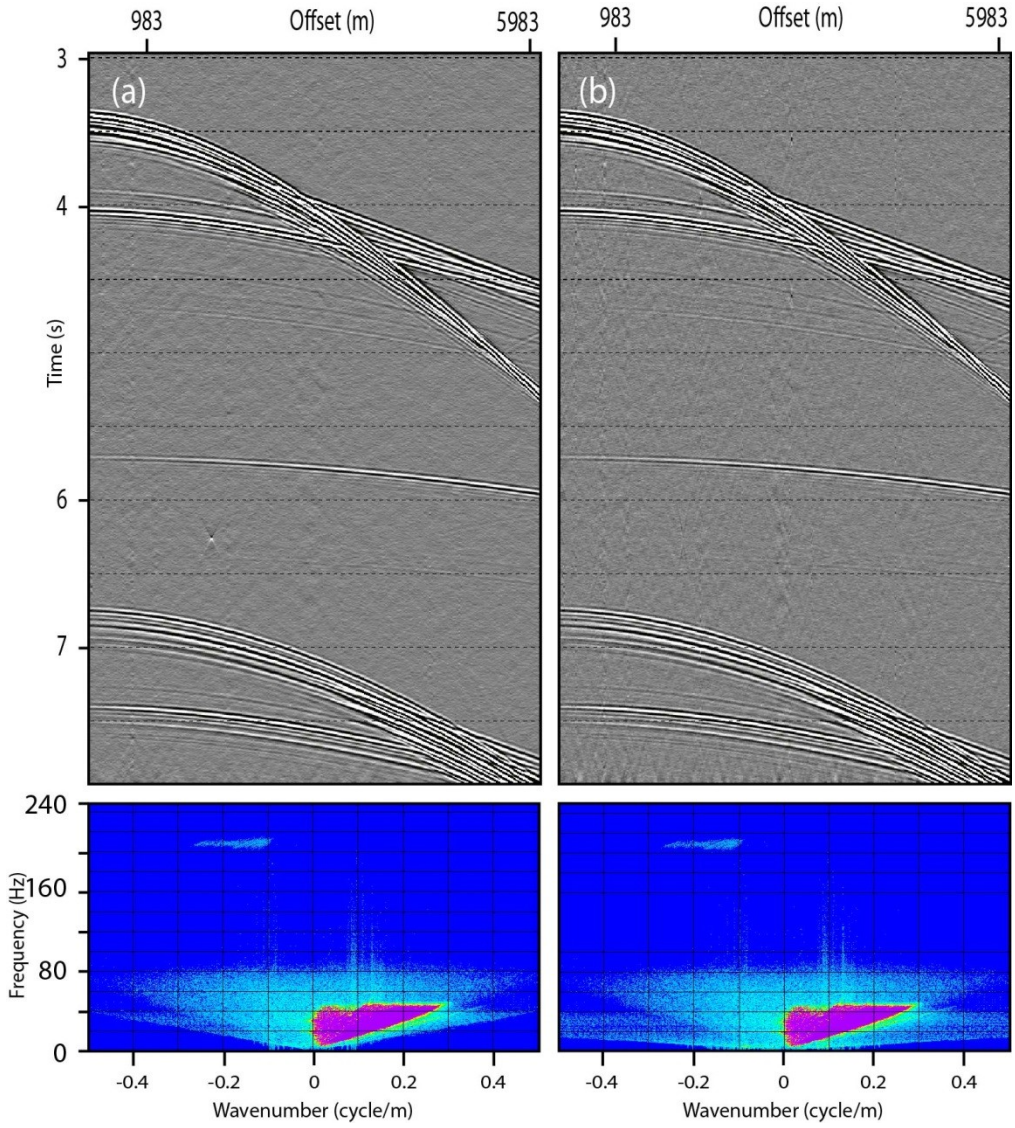

Figure A.21 Comparison of the FK and LIFT filtering results after applying a bandpass filter. a) Shot gather from Figure A.19b after applying a trapezoidal bandpass filter (1-6-200-220 Hz). b) Shot gather of Figure A.19d after applying bandpass filter (1-6-200-220 Hz).

Applying FK and LIFT filters on field data rather than on synthetic data has a complication associated with it. We consider shot 990 of streamer 2 in sail line 972P and FK spectrum of this shot (Figure A.22). Presence of spikes on the traces causes noise

smearing to the surrounding traces after applying FK and LIFT filters (Figure A.23). Applying bandpass filtering before applying 2D filters reduces noise leakage but does not prevent it. To overcome the noise leakage problem, we decided to test applying and removing automatic gain control (AGC) before and after the 2D filtering respectively. The results show that noise leakage problem is greatly reduced when using this simple procedure (Figure A.24). Comparing the result of applying LIFT and FK shows there are some disadvantages in applying FK filter compared to LIFT approach. After applying LIFT the spikes present in data are significantly suppressed (Figure A.24) whereas these spikes are still present after applying FK in the low frequency band component. For suppressing spikes in the mid- and high-frequency bands, a time gate is provided and the median RMS amplitude value is calculated in the corresponding gate for the user-defined number of neighbouring traces. The designed time gate should be proportional to the spike length. The median value is compared to the amplitude of the trace in the time gate. If the trace amplitude exceeds threshold amplitude, it is scaled down. Removal of random spikes as part of the LIFT approach for the mid- and high-frequency bands, as well restricting application of the FK filter only to the lower frequency band precondition data better for further analysis than the simple application of the FK filter to the full frequency band. Because residual spikes in data produce migration artefacts and deteriorate the seismic reflection image, LIFT approach is desirable.

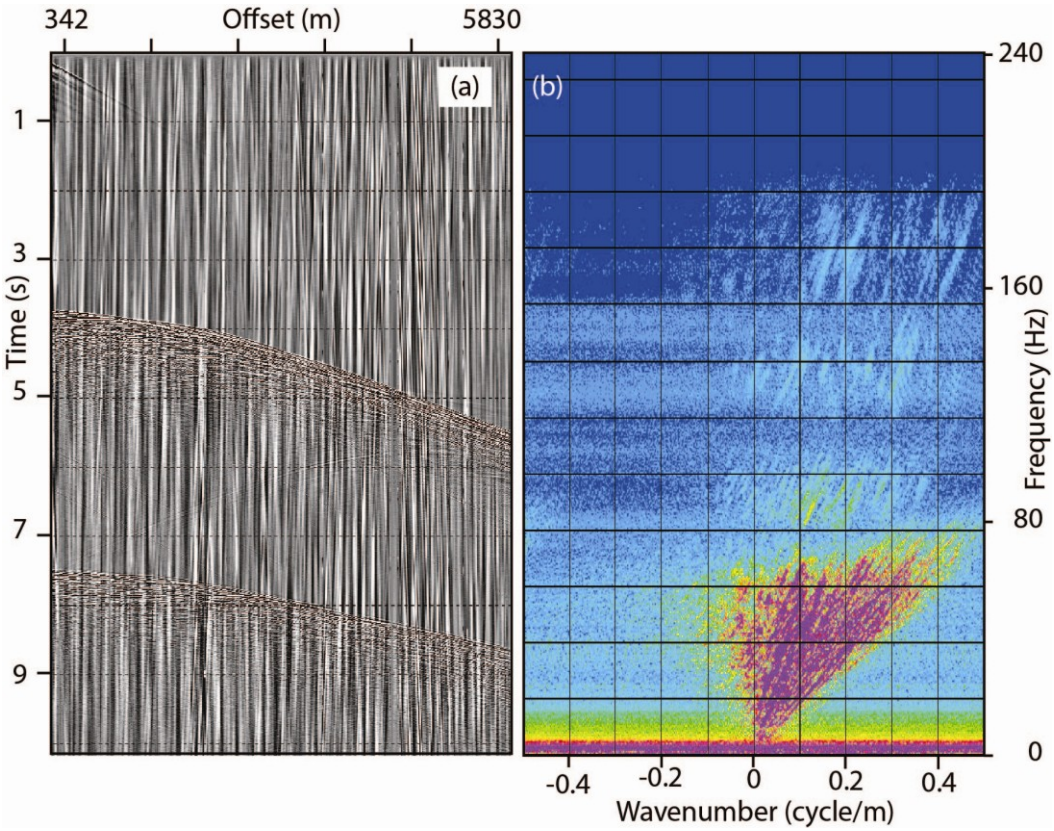

Figure A.22 Shot gather 990, sail line 972P, streamer 2 from the EPR 3D survey in (a) t-x and (b) F-K domain.

When turning onto a sail line or turning after completing a sail line, the level of streamer and ambient noise is significantly increased (Figure A.25). Our tests indicate that noise removal using LIFT for these shots is not as efficient as for shots within the straight segments of the sail lines (see Figure A.22a and Figure A.24b). The reason for this is the lower S/N ratio. If the S/N is too poor, LIFT approach will not give any benefit [*Dewar et al.,* 2003]. To increase the S/N ratio for these shots, traces for which noise level is above a threshold value are flagged in a semi-automatic approach. The noise in the flagged traces is suppressed by applying frequency spectrum balancing. In this 1D filter, the seismic trace is decomposed into signal and noise components by applying a user-defined frequency band. The noise component is subtracted from the original input trace and their

envelopes are calculated by computing amplitude of the corresponding complex trace [*Taner et al.,* 1979]. The envelope of the noise component is compared to the envelope of signal component and the traveltime ranges where the noise component exceeds the signal component are scaled down. Both components of scaled noise and signal are then summed to give the final result.

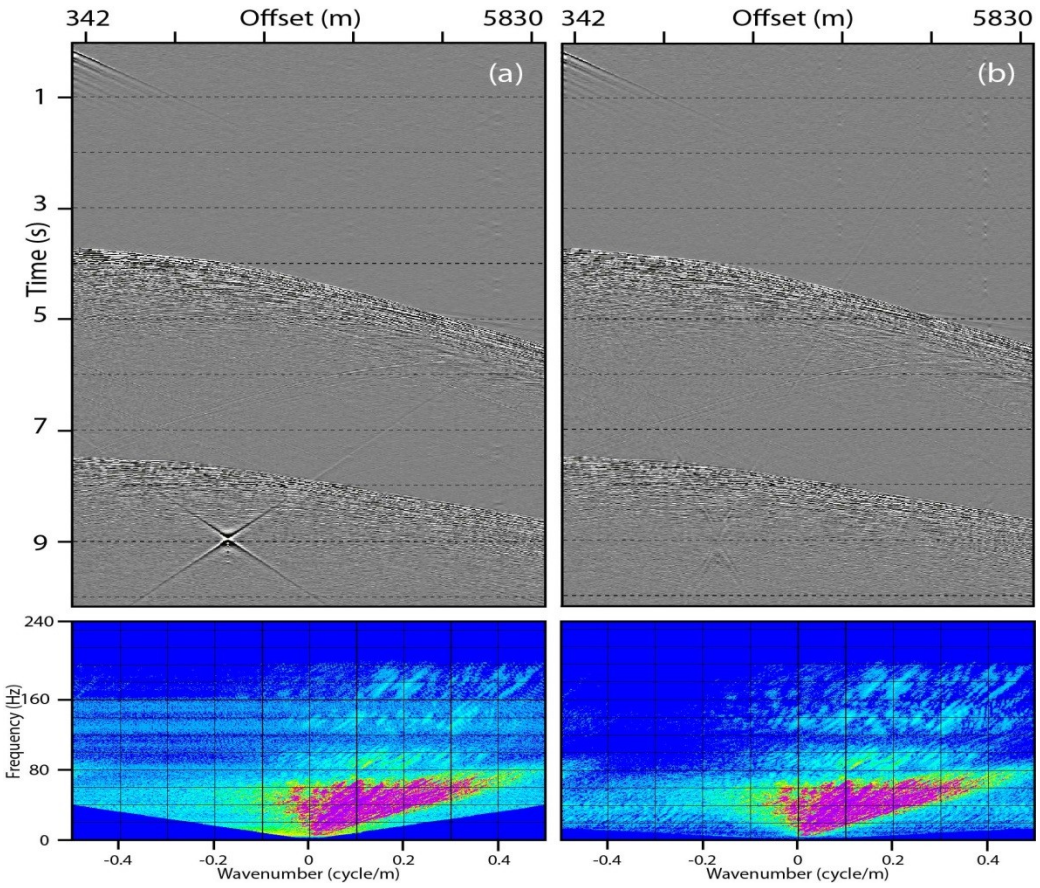

Figure A.23 Noise smearing after FK and LIFT filtering. Noise leakage after FK (-500/0, -500/40, -20/2, 20/2, 500/40, 500/0 km-1/Hz) filtering (a) is greater than after LIFT filtering (b).

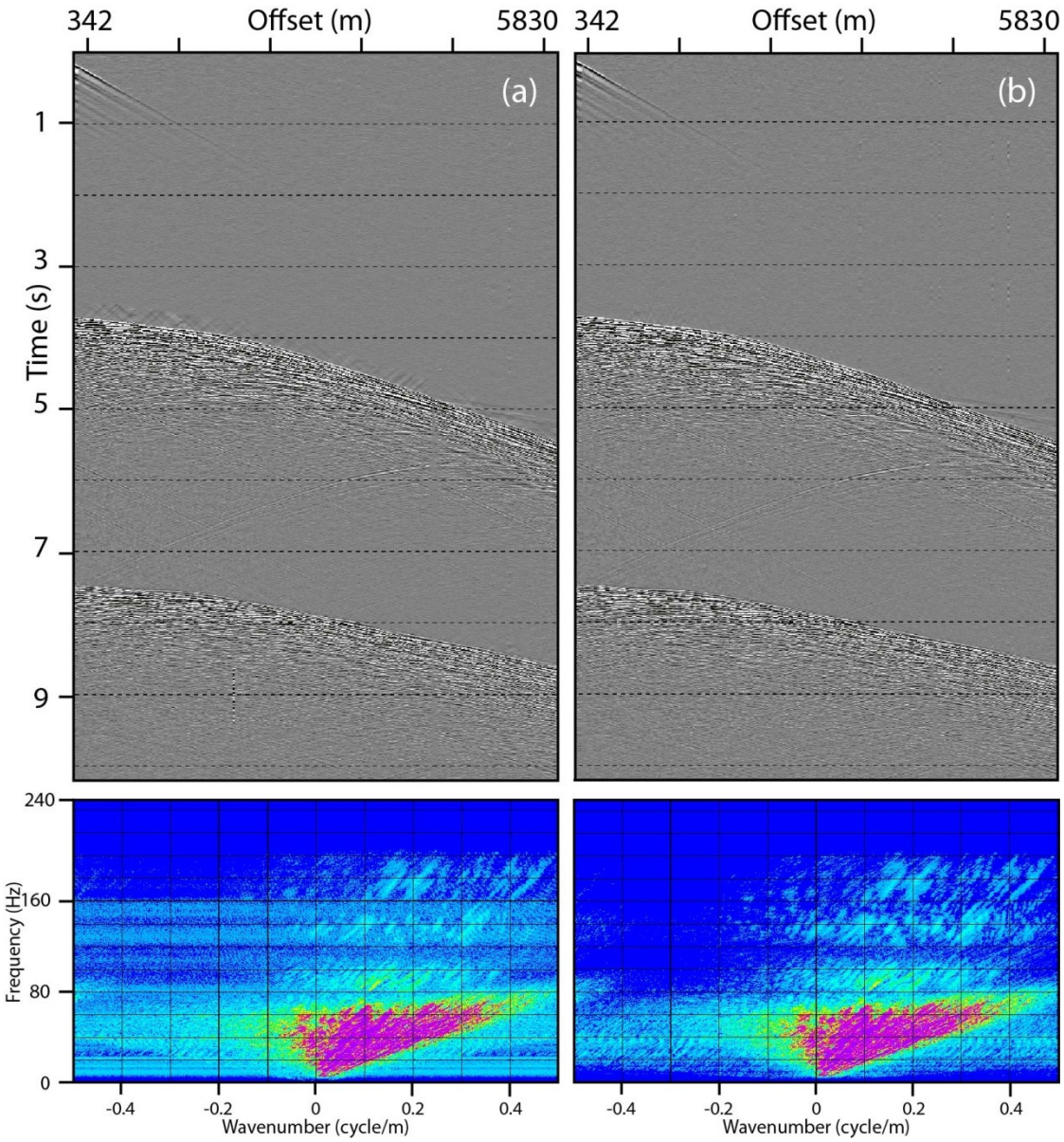

Figure A.24 Effects of combining application and removal of AGC with 2D filtering. a) Shot gather from Figure A.23a after applying and removing AGC before and after FK filtering, respectively. b) Shot gather from Figure A.23b after applying and removing AGC before and after FK filtering used in LIFT, respectively. Shot gathers were bandpass filtered before applying AGC.

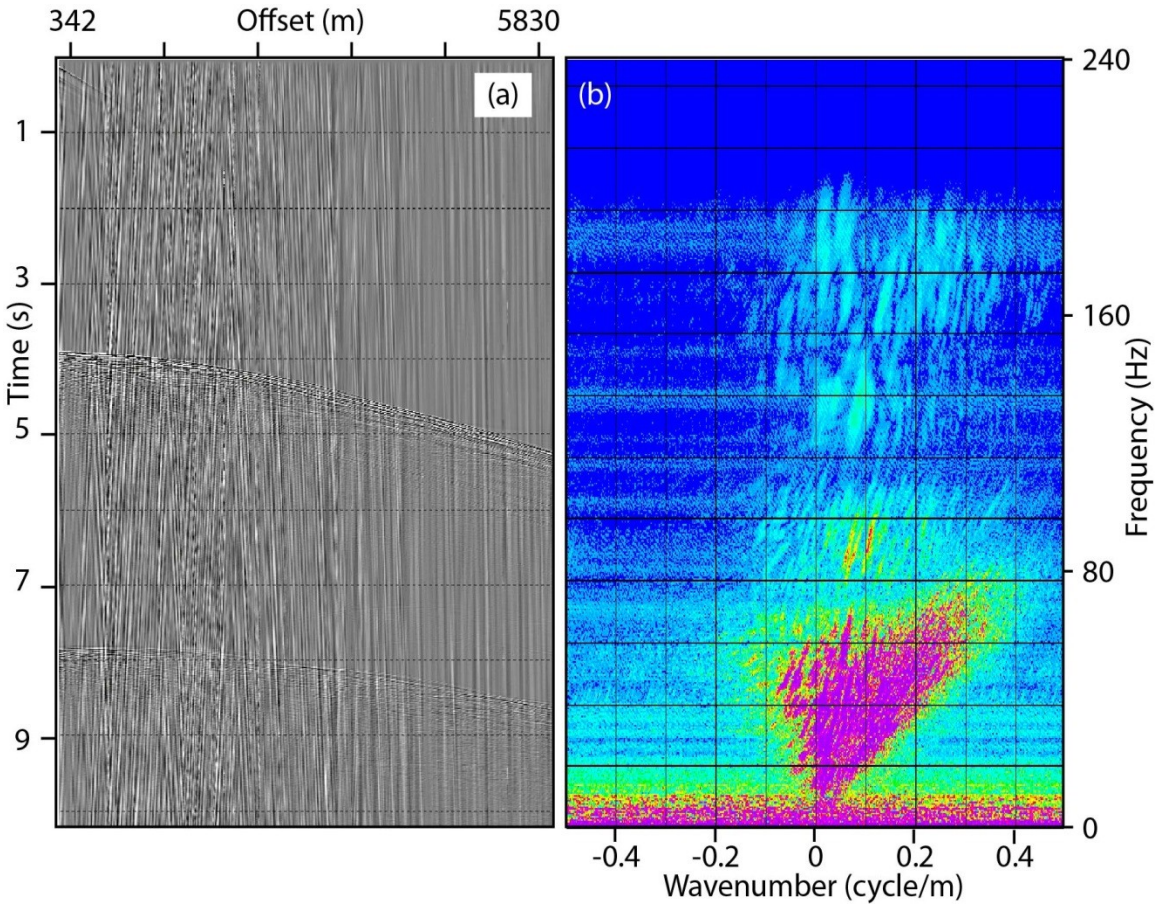

Figure A.25 Shot 899 of sail line 972P, steamer 2. The shots recorded while turning onto a sail line have a higher level of streamer and ambient noise.

Frequency-wavenumber values of the FK filter applied to low-frequency band of data during LIFT are -500/0, -500/15,-150/15, -20/2, 20/2, 150/15, 500/15, 500/0 km^{-1}/Hz. The median value is compared to the amplitude of the trace in the time gate. If the trace amplitude exceeds threshold amplitude, it is scaled down. Figure A.26 and Figure A.27 show frequency decomposition and LIFT application, respectively. Summary of the 1D and 2D filtering applied to EPR3D data is as follows:

- Trapezoid zero phase bandpass filtering with corner frequencies of 1-6-200-220 Hz applied to the entire data set;

- Frequency spectrum balancing of noisy traces with the threshold frequency of 12 Hz;

- FK filtering (-500/0, -500/15,-150/15, -20/2, 20/2, 150/15, 500/15, 500/0,-500/0 km^{-1}/Hz) of the low frequency band (1 to 15 Hz) of the data within the LIFT method;

- Median filtering with the parameters in Table A.7 to all frequency ranges within LIFT method.

Table A.7 Median filter parameters for different frequency ranges

Frequency range	Amplitude calculation method for finding median value	Number of traces for median calculation	Time gate size (ms)
0–15–20 Hz	RMS	51	100
15–20-20–25 Hz	RMS	51	100
20–25–200–220 Hz	RMS	51	200

The result of applying LIFT to shot 899 (Figure A.25) with the parameters detailed in Table A.7 is shown in Figure A.28. This figure shows that applying LIFT increases the S/N ration significantly and it prevents zeroing the traces that were flagged as bad traces before applying LIFT. For this reason, it is suggested to edit the data after 2D filtering (Figure A.6).

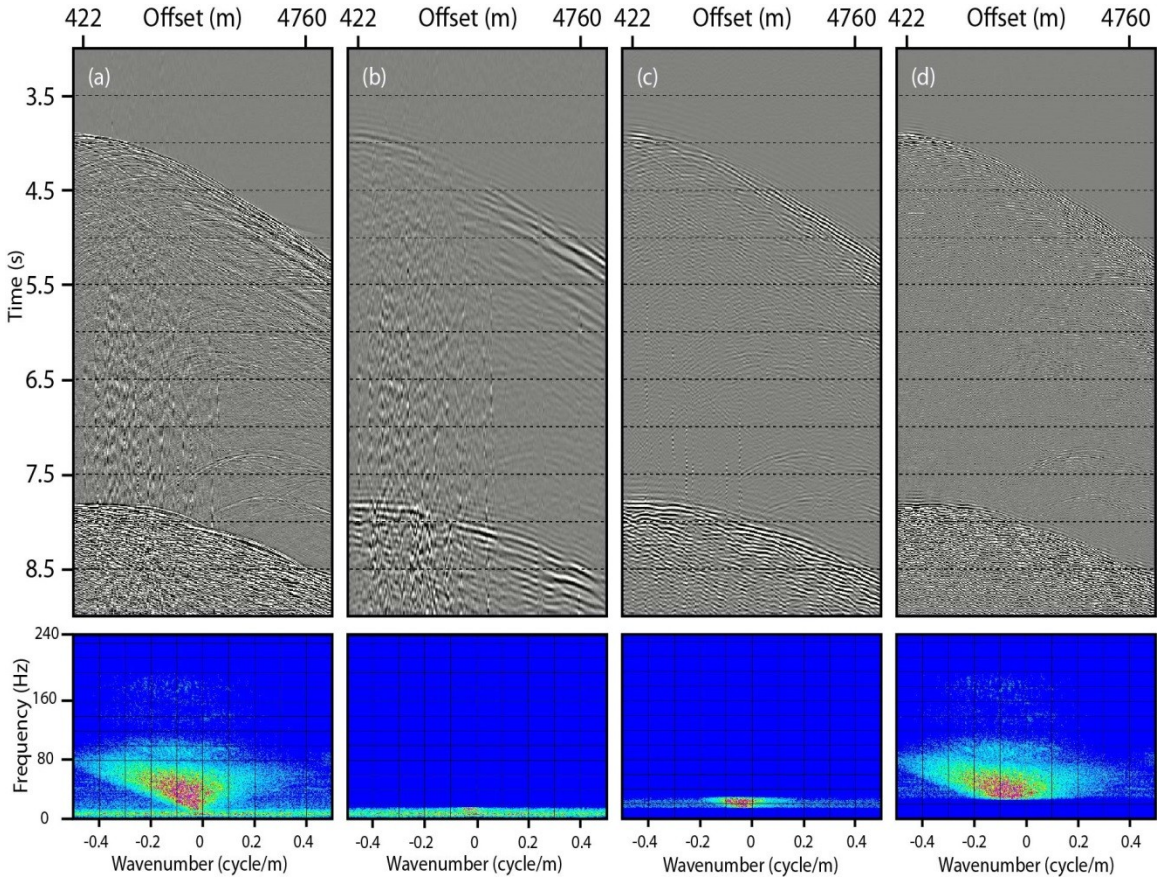

Figure A.26 Decomposing data into three frequency bands. (a) Sail line 972P, shot 899, cable 2 after trapezoid bandpass filter and frequency spectrum balancing. Decomposing (a) into frequency ranges of (b) 0-15-20 Hz, (c) 15-20-20-25 Hz and (d) 20-25-200-220 Hz. Bottom figures are FK spectrum of (a), (b), (c) and (d).

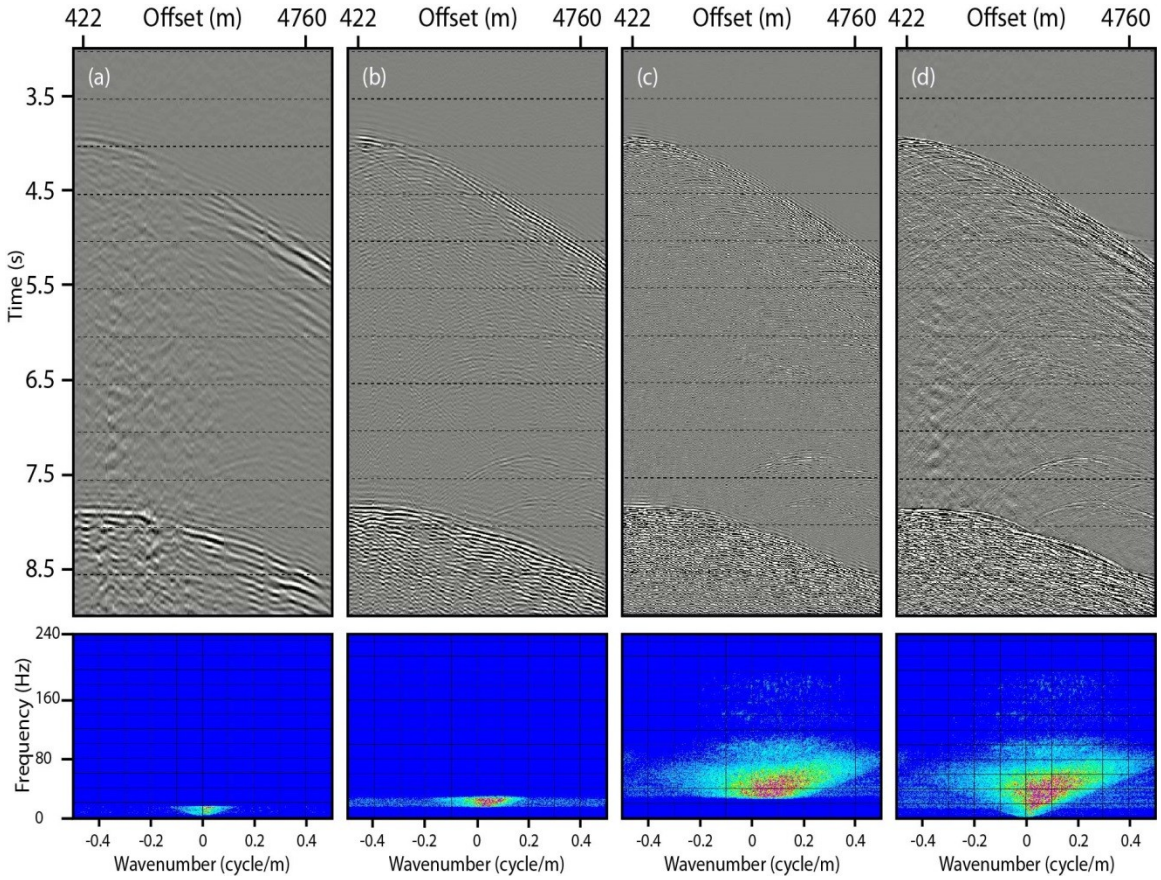

Figure A.27 Steps of the LIFT approach. a) FK filtering with corner values of -500/0, -500/15,-150/15, -20/2, 20/2, 150/15, 500/15, 500/0,-500/0 km^{-1}/Hz applied to data from Figure A.26b followed by the median filter of Table A.7. (b) Median filtering with the parameters from Table A.7 applied to data from Figure A.26c. (c) Median filtering with the parameters from Table A.7 applied to data from Figure A.26d. (d) summation of a, b and c.

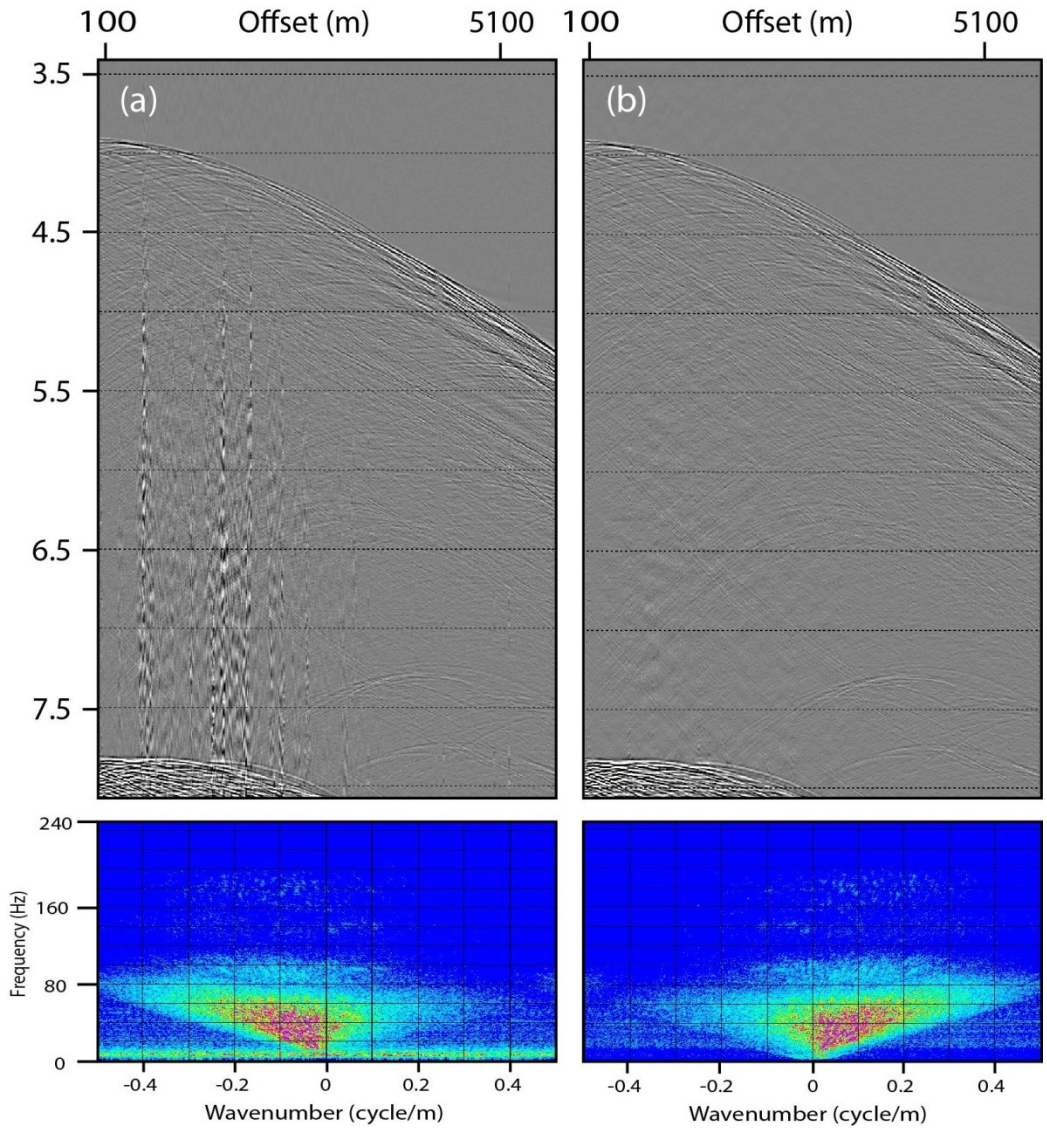

Figure A.28 LIFT filtering. a) Shot 899 of sail line 972P, streamer 2 after a) bandpass filter and spherical divergence correction and b) applying LIFT to (a).

A.3.4 Surface-consistent Amplitude Balancing

The advantage of surface-consistent amplitude balancing is its ability to separate different signal amplitude contributions to the estimated amplitude spectrum of the data [*Cary and Lorentz*, 1993]. Balancing amplitudes in this way is an appropriate and needed step in data preparation for AVO analysis. For the EPR3D data set, the surface-consistent amplitude balancing was carried out by decomposing the data into shot, channel and

CMP components. The shot and channel components collect the near surface effects on the reflected amplitude and are removed, which in this case are source signature and receiver impulse response. The CMP component collects the geology effect and is preserved, which is the effect of smooth subsurface reflectivity variation on the recorded wavelet [*Cary and Lorentz,* 1993].

The source and channel components are removed by multiplying each trace with the following scale factor:

$$s = e^{-a} \qquad \text{(A-2)}$$

where (s) is the scale factor and (a) is the computed contribution from shot and channel components. The shot and channel components are computed from decomposing the seismic amplitude to three components by calculating the log RMS values for each trace and solving a surface-consistency model for shot, channel and CMP.

As an example, RMS amplitude of data traces computed from the seafloor to 150 ms above the first seafloor multiple of sail line 1572P, cable2 before and after applying surface-consistent balancing is shown in Figure A.29. Amplitude of channels with extremely low values (channel number 136 for example), is boosted after balancing. The energy of the shot gathers with larger shot numbers particularly shot numbers 1250 to 1300 is increased after applying surface-consistent balancing (Figure A.29c). The CMP component of surface-consistent balancing for the EPR3D is shown in Figure A.30. The CMP component is not applied as it is considered to contain geology.

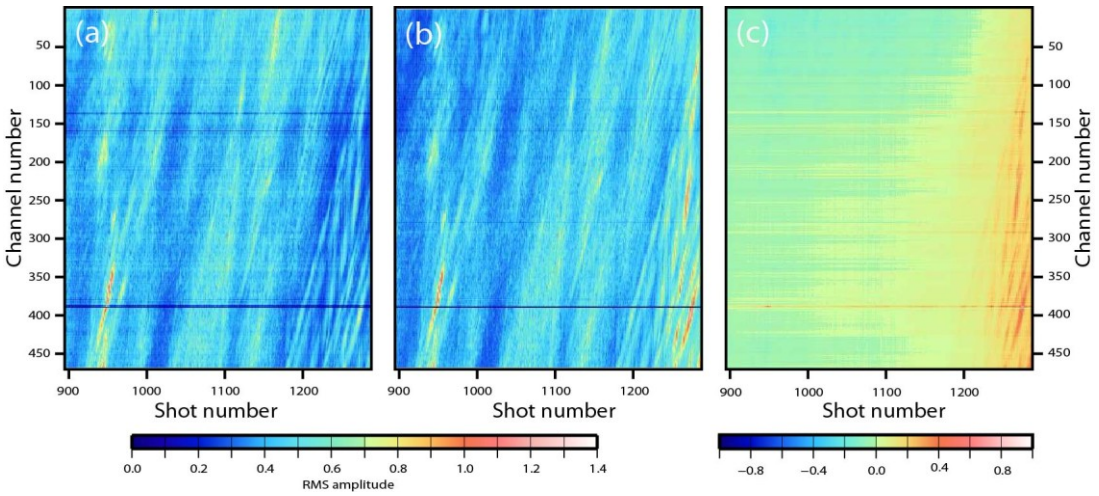

Figure A.29 RMS amplitude of inline 1572P, cable2 a) before applying surface-consistent balancing, b) after applying surface-consistent balancing, and c) the difference between (a) and (b).

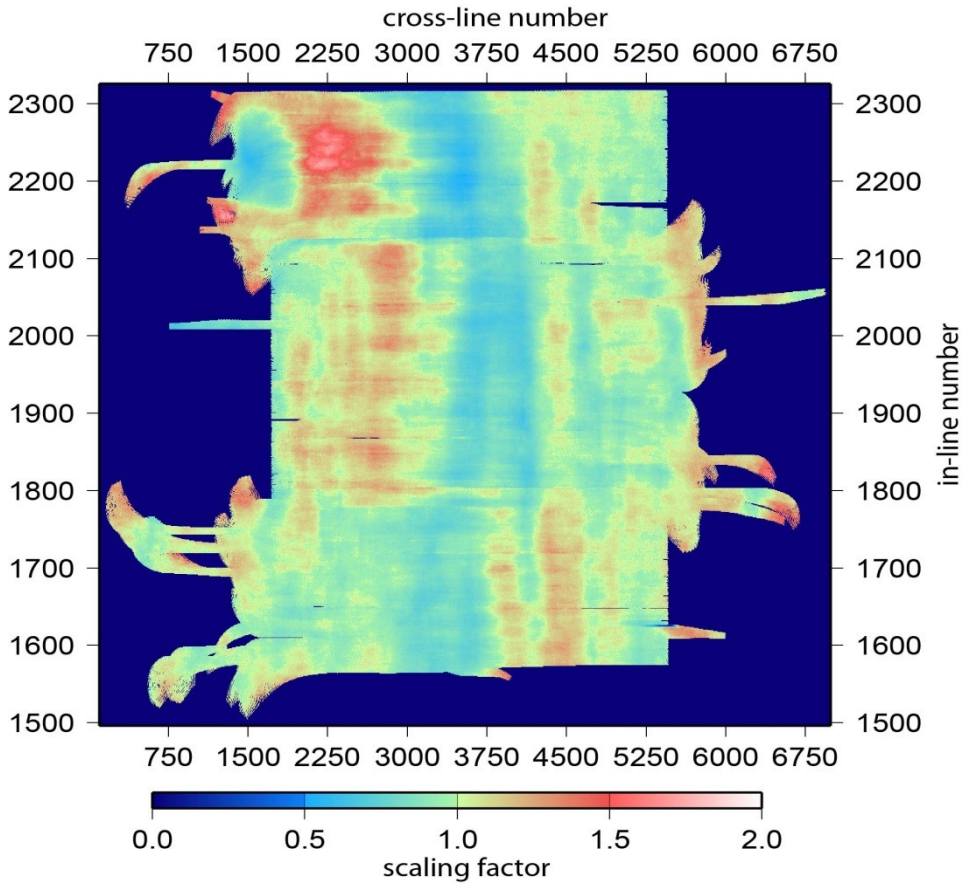

Figure A.30 CMP model of surface consistent amplitude balancing that collects reflectivity information.

A.3.5 Surface-consistent Deconvolution

To improve temporal resolution and suppress peg-leg multiples the whole suite of available deconvolution algorithms was tested. Unfortunately, while the surface-consistent deconvolution provided the best results, the deconvolution process overall was not successful at improving the EPR3D data. Spiking and predictive surface-consistent deconvolution were tested using a combination of operator lengths (80 to 320 ms with 20 ms increment) and prediction gaps (0 to 36 ms with 8 ms increment) but all applied processes resulted in part of the reflection, refraction and diffraction signal removed from the data. Therefore, we did not apply deconvolution to the data.

A.3.6 Velocity Analysis and Stacking

As it was pointed out earlier, a systematic and consistent NMO velocity analysis is not possible because the Moho reflection is not strong enough and continuous enough on CMP supergathers. Therefore, a few 3D velocity models were developed for stacking the data by hanging existing 1D velocity functions from the seafloor. These velocity models are the ESP5 function [*Vera et al.,* 1990] determined from axial data, ESP1 function [*Vera et al.,* 1990] determined using data collected ~10 km off the axis, and the cross-axis OBS velocity profile at 9˚50'N [*Canales et al.,* 2012]. Normal moveout is applied to the CMP bin gathers followed by manual muting of the stretched events in a 150×300 m grid. Three stack volumes were produced by summing these gathers. The stack volume produced using the ESP1 function provides the best overall image of the structures of interest including the AML.

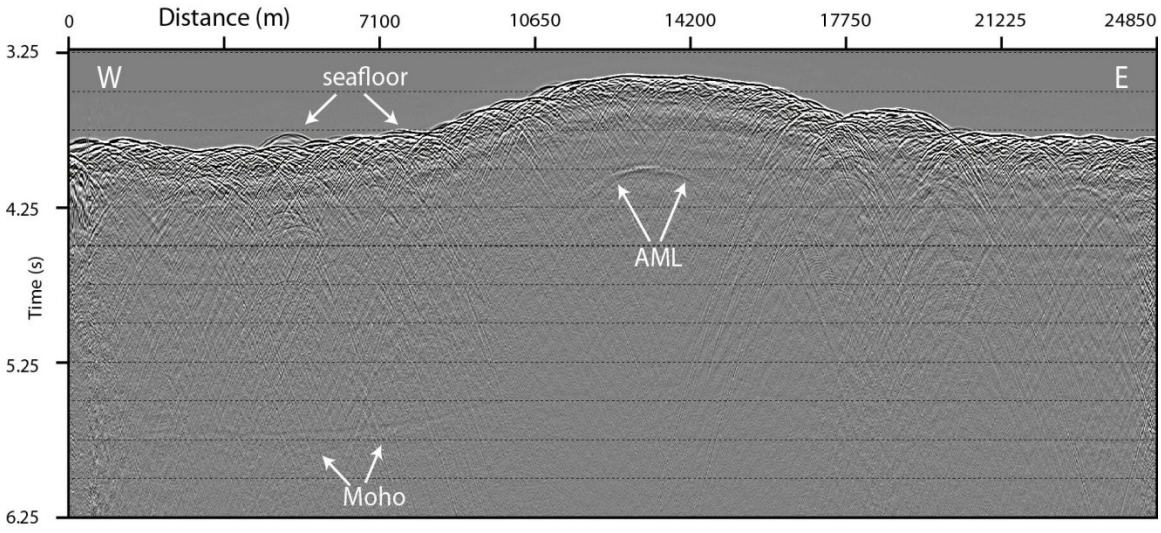

Figure A.31 Stack section of in-line 1640. AML and Moho reflections are marked with white arrows.

The AML reflection event is present on all the in-line stack sections at about 4100 ms TWTT. On the stack section, the Moho reflection appears at about 2 s below seafloor but it is not visible on all stack sections. Figure A.31 shows stack section of in-line 1640 as an example where AML and Moho are marked.

A.3.7 Poststack migration

Kirchhoff integral method can accommodate irregular data geometry and can be used to image subsurface structure of any dip [*Ratcliff et al.,* 1992]. Another important computational advantage of Kirchhoff method is its efficiency, as it can run only on a subset of the whole 3D cube (target-oriented migration). For target-oriented migrations, the computational cost of Kirchhoff method is reduced in proportion to the reduction in image size. In contrast, the computational cost of target-oriented migration by wavefield-

continuation methods is seldom substantially lower than the cost of full-volume migration [*Biondi,* 2007].

The possibility of performing target-oriented migration is particularly advantageous for migration velocity analysis (MVA), when migration is applied iteratively to improve the accuracy of the velocity model. Therefore, I choose to apply Kirchhoff migration to EPR3D data. Earlier versions of 3D Kirchhoff migration consisted of two sets of 2D migration in orthogonal directions [*Gibson et al.,* 1983] but the migration used here is based on a full 3D algorithm, i.e. the full input dataset limited only by the chosen aperture is used in the migration process. As spatial aliasing affects all kinds of migrations and migration aperture is an important factor in practical implementation of Kirchhoff migration, I discuss these parameters here.

The dominant structural dip in the study area is along the cross-axis direction (Figure 2.4). The Moho can dip as much as 10° in the first 6 km from the ridge axis but is relatively flat from 6 to ~10 km distance away from the ridge axis. The AML and OAMLs reflections mostly have dips from 0 to ~10°, with a limited number of locations where these events have dips of up to 20°. Spatial sampling is very fine (6.25 m) in the cross-axis direction. The maximum unaliased frequency for the Moho reflection is ~350 Hz and, therefore, spatial aliasing is far from being a problem in this direction for imaging the Moho reflection (Figure A.32). Aliasing is also not a problem for imaging the AML and OAML reflections. Even for the areas where these events have a dip of ~20° the maximum unaliased frequency is ~180 Hz.

Trace interpolation could be considered in the along-axis direction, as the spatial sampling is relatively coarse (37.5 m) in this direction. But there are no dipping events in

this direction (Figures 3.6, 3.9) and, therefore, no spatial aliasing producing artefacts (Figure A.32). However, Kirchhoff migration is affected by another type of aliasing called operator aliasing that can degrade the seismic image quality at all dips [*Lumley et al.,* 1994]. To overcome this problem, local triangular anti-aliasing filter is used in 3D Kirchhoff migration [*Lumley et al*., 1994].

The next important parameter in practical implementation of Kirchhoff migration that has a direct effect on the cost of migration is migration aperture width. *Yilmaz* [1987] shows that both the excessively large and excessively small migration apertures result in poor seismic images. *Sun* [1998] suggests a minimum migration aperture that is twice the Fresnel zone for both poststack and prestack migration. The Fresnel zone variation with the half source-receiver offset is shown in Figure A.33 [*Sun and Bancroft*, 2001]. At zero offset, twice the Fresnel zone at Moho is ~2430 m suggesting that the minimum migration aperture for poststack migration is ~2430 m. The aperture size for poststack migration is selected to be 3500 m, larger than the minimum size of twice the Fresnel zone as additional improvement in quality of the imaged Moho reflection was observed by increasing the aperture size.

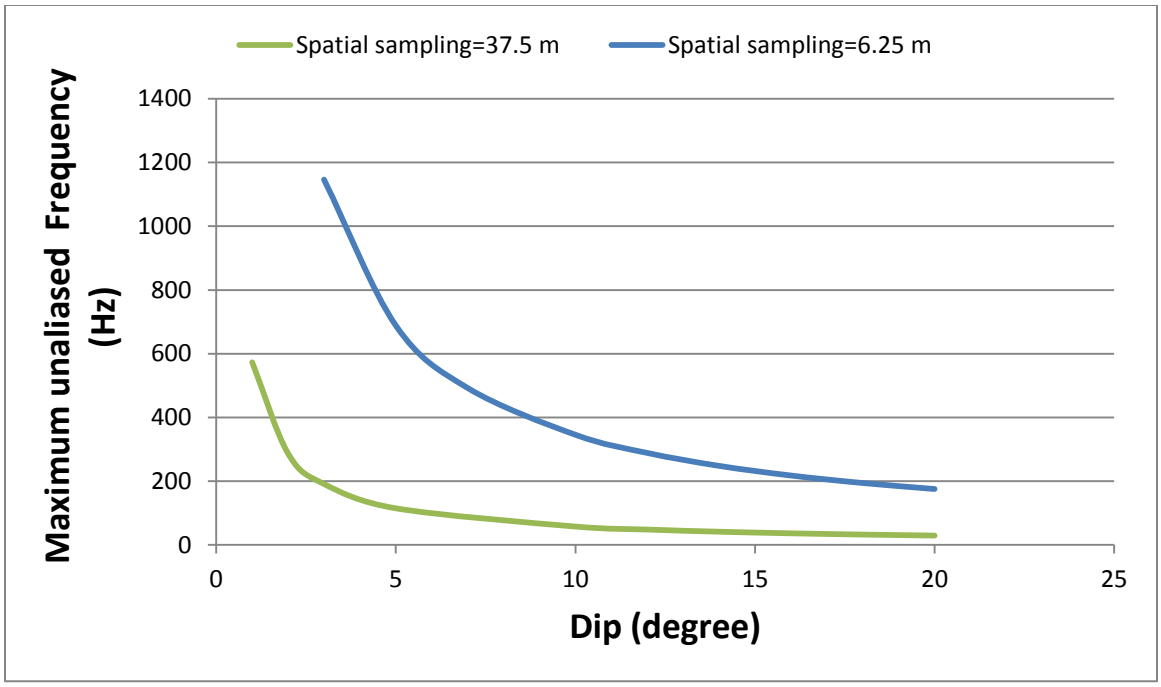

Figure A.32 Maximum unaliased frequency for different dips along the in-line (blue) and cross-line (green) directions [*Yilmaz,* 1987]. As the dominant dip is along the in-line direction and spatial sampling is sufficiently fine in this direction, spatial aliasing is not a problem.

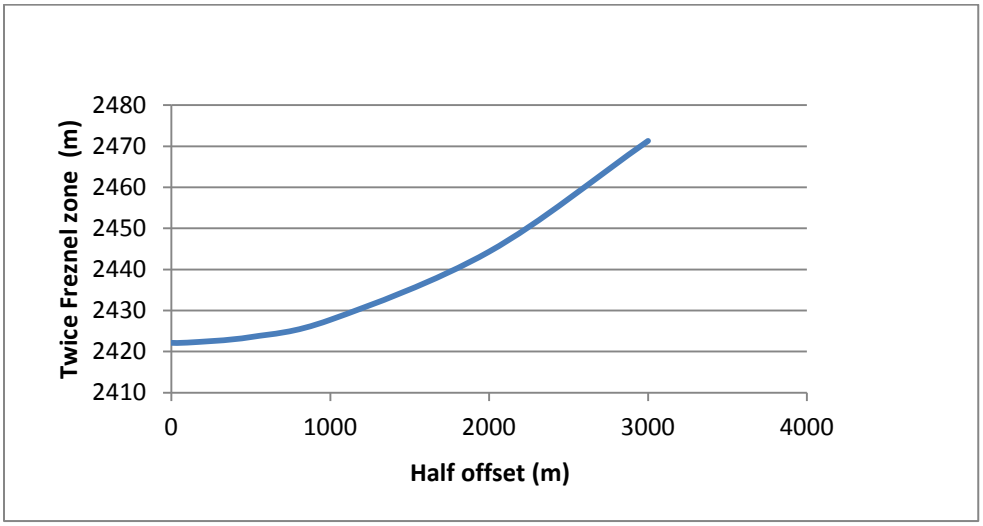

Figure A.33 Fresnel zone variation with the source-receiver half-offset for migrating Moho reflection. The maximum half-offset is the source-receiver distance that contributes to the diffraction summation in Kirchhoff prestack migration. Poststack migration is migration of the zero-offset section. The Fresnel zone is ~1210 m for Moho at zero offset. Assuming that twice the Fresnel zone is the minimum migration aperture, this figure shows that the minimum migration aperture for imaging Moho using poststack Kirchhoff migration is ~2420 m.

I applied trace amplitude balancing to the migrated stack volume to boost amplitudes of weak areas relative to strong seafloor amplitude. A sliding time gate, 250 ms long at the seafloor and 150 ms long at greater traveltimes, was chosen to calculate the inverse of the average absolute amplitude of each gate that was then used to multiply the data sample found at the middle of the gate. The computed scalars are small for seafloor where the average amplitude is high and large for areas with weak amplitude. After trace amplitude balancing, I applied time variant trapezoid bandpass filter to the data.

References

Cary, P. W., and G. A. Lorentz (1993), Four-component surface-consistent deconvolution, *Geophysics*, 58, 383-392.

Choo, J., J. Downton, J. and Dewar (2004). Lift: a new and practical approach to noise and multiple attenuation, *First break*, 22:39-44.

Gibson, B., K. Larner, and S. Levin (1983), Efficient 3D migration in two steps, *Geophys. Prosp.,* 31, 1-33.

Mallick, S., and N. L. Frazer (1987), Practical aspects of reflectivity modeling, *Geophysics*, 52:1355-1364.

Newman, P (1973). Divergence effects in a layered earth, *Geophysics*, 38, 481-488.

Pratt, R. G., and M. H. Worthington (1990), Inverse theory applied to multi-source cross-hole tomography. Part I: Acoustic wave-equation method, *Geophys. Prosp*., 38, 287-310.

Ratcliff, D.W., S.H. Gray, and N.D., Jr. Whitmore (1992), Seismic imaging of salt structures in The Gulf of Mexico, *The Leading Edge*, 11(4), 15–31.

Sun, J (1998). On the limited aperture migration in two dimensions, *Geophysics*, 63: 984-994.

Ursin, B (1990), Offset-dependent geometrical spreading in a layered medium, *Geophysics,* 55, 492-496.

Ursin. B., and T. Dahl (1989), Seismic reflection amplitudes, Presented at the 5lst Ann. Mtg., Eur. Assn. Expl. Geophys.

Vera, E. E., J. C. Mutter, P. Buhl, J. A. Orcutt, A. J. Harding, M. E. Kappus, R. S. Detrick, and T. M. Brocher (1990), The structure of 0- to 0.2-m.y.-old oceanic crust at 9°N on the East Pacific Rise from expanded spread profiles, *J. Geophys. Res.,* 95, 15529–15556.

Yilmaz, O (1987), Seismic data processing. Tulsa: SEG Press.

APPENDIX B THREE-DIMENSIONAL KIRCHHOFF PRESTM

This appendix explains basic kinematics of the 3D PreSTM and MVA, and the processes applied to CIGs for producing the prestack migrated volumes in Chapter 3. The main objectives of applying 3D PreSTM are optimal imaging of the AML, OAML and Moho reflection events, and measuring the average velocity of the crust in the study area as outlined in Chapter 3. The migration algorithm used for this purpose is 3D Kirchhoff migration. The processing steps for data preparation before applying 3D PreSTM to the data were detailed in Appendix A, and the initial velocity used for running the first pass of 3D PreSTM was shown in Figure 3.2.

For running 3D Kirchhoff migration, *Geodepth* software was used. There are two options for running 3D Kirchhoff migration with this software with two different results: a) direct output of final migrated images; b) direct output of CIGs, which can be summed to obtain the result in (a). The second option also facilitates flattening of reflection events in CIGs through MVA, processing of the CIGs, and application of mute before stacking the processed CIGs. The second option usually leads to significantly improved migrated images.

B.1 Basics of Kirchhoff Migration

Kirchhoff migration is a migration algorithm based on diffraction summation [*Schneider*, 1978]. In practice, the integral form of *Schneider* [1978] is approximated with a finite sum expressed in equation (B-1) [*Biondi,* 2007]

$$I(\alpha) \approx \quad_{i\in\varphi} W_i(\alpha_i, m_i, h_i) D[t = t_D \;\; \alpha_i, m_i, h_i \;\;] m_i, h_i, \tag{B-1}$$

where the image point $I\ \alpha$ (see Figure B.1), defined in 3D space $\alpha = x_\alpha, y_\alpha, z_\alpha$, is equal to the summation of the data values $D(t)$ evaluated at t and weighted by a scale factor W_i. (m) and (h) are midpoint and offset vectors, respectively (Figure B.1), and the subscript (i) shows the number of data traces in migration aperture (φ).

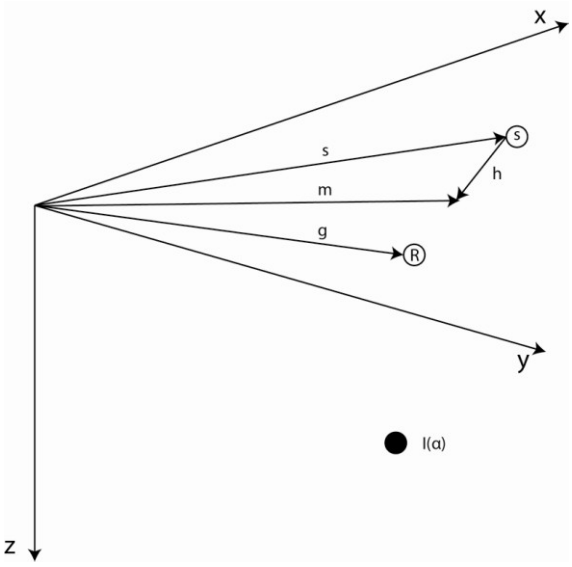

Figure B.1 The geometric relationships used in equation (B-1). The source (s) and receiver vectors (g) are used to define the midpoint (m) and offset (h) vectors. The midpoint vector (m) is $\frac{s+g}{2}$, and offset vector (h) is $\frac{s-g}{2}$, and the image point is $\boldsymbol{I(\alpha)}$.

The summation in (B-1) is limited to the migration aperture centered at the image point. The time shift D(t) is the total time between the source location to the image point (t_s) and from the image point to the receiver (t_r) (Figure B.2), defined by the Double Root Square (DRS) equation [*Claerbout*, 1985] of

$$t_i = \sqrt{\frac{t_0^2}{4} + \frac{(x-h)^2}{V^2}} + \sqrt{\frac{t_0^2}{4} + \frac{(x+h)^2}{V^2}}, \qquad \text{(B-2)}$$

in which x is the surface location of the midpoint, and h is the half offset between shot and receiver, t_0 is the vertical twtt between subsurface and surface location of the scattepoint, and V is the constant velocity to the scattepoint location.

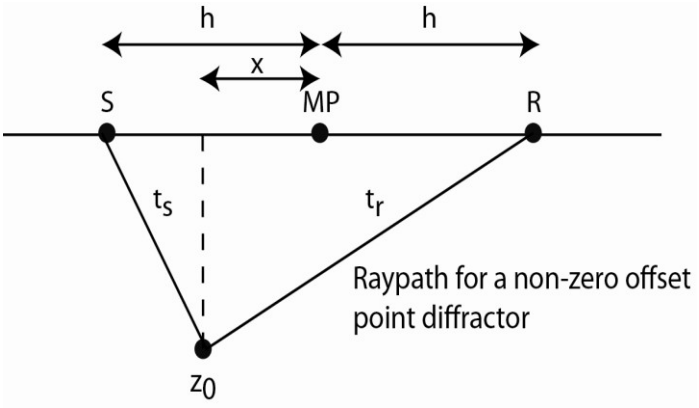

Figure B.2 Geometry of the straight raypath for calculating the traveltime of a scattepoint in Kirchhoff PreSTM. The scatterpoint in the subsurface (Z_0) is located at x=0, and the source (S) and the receiver (R) are located h-x and at h+x, respectively. The midpoint (MP) is located at x, and the scatterpoint is at x=0. The traveltime between the scatterpoint and the source location is t_s and the traveltime between the scatterpoint and the receiver location is t_r. Modified from *Bancroft* [1998].

In 3D, these traveltimes define summation surfaces that are the basis of Kirchhoff migration. The summation surfaces can be interpreted as being diffraction surfaces for scatterpoints in the subsurface [*Biondi,* 2007] (Figure B.3).

The migration aperture therefore has a cone-like shape in 3D PreSTM (Figure B.4). The input midpoints that contribute to a single image point are limited to a circular area centered on the surface location of the image point. The migration aperture size increases with depth which makes imaging of deep targets computationally time-consuming.

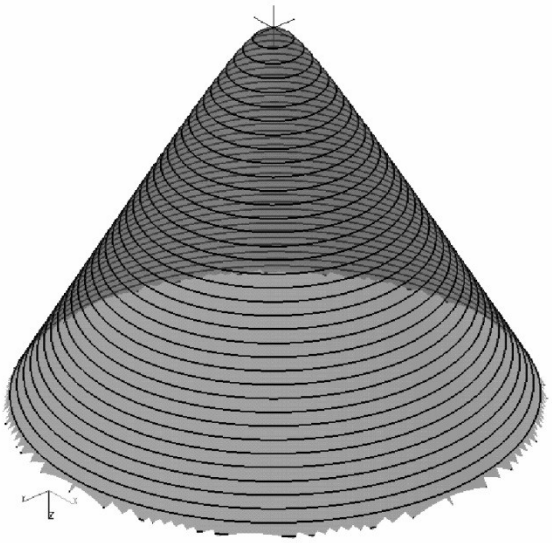

Figure B.3 A zero-offset summation surface in 3D produced from DRS equation. The vertical axis is the time axis, and horizontal axes are the midpoint axes. Equal traveltimes are shown with circular contours. The image point is shown with the cross at the apex of the summation surface. From *Biondi* [2007].

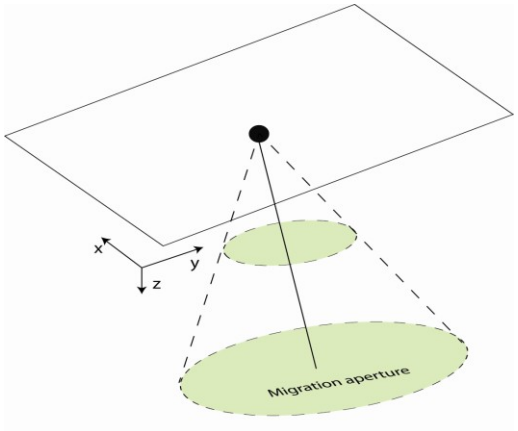

Figure B.4 Schematic illustration of the migration aperture for Kirchhoff prestack migration. The migration aperture is wider for deep targets.

It was shown by *Sun and Bancroft* [2001] that the minimum migration aperture should be at least twice of the Fresnel zone for preserving the true reflection amplitude and producing satisfactory images (Figure B.5).

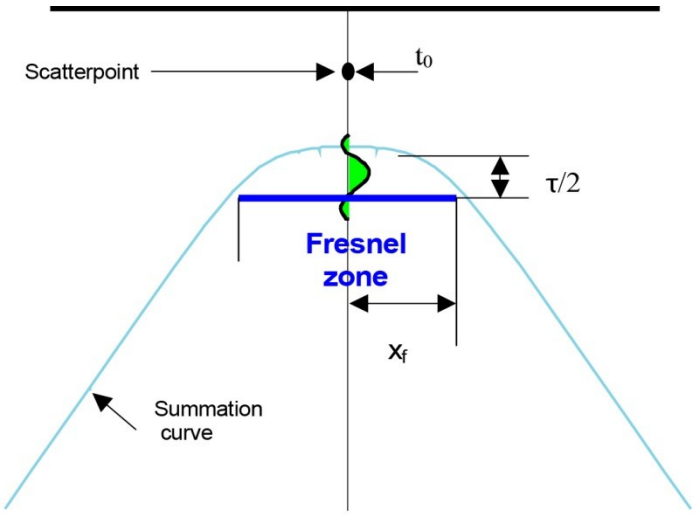

Figure B.5 Fresnel zone and summation hyperbola for a common-offset section. The dark blue solid line shows the Fresnel zone, and the light blue curve shows the summation hyperbola. From *Sun and Bancroft* [2001].

Sun and Bancroft [2001] also have shown that the Fresnel zone radius is offset dependent and increases with source-receiver distance

$$x_f = \frac{\sqrt{\tau V_{RMS}^2 \sqrt{\frac{4h^2}{V_{RMS}^2} + t_0^2}}}{4 - \frac{h^2}{4h^2 + V_{RMS}^2}}, \tag{B-3}$$

where h is half source-receiver offset, $t_0$is vertical twtt, $V_{RMS}$is RMS velocity at the scatter point, and τ is dominant period of the seismic wavelet (see Figure B.1). For Moho reflection, the Fresnel zone variation with offset is shown in Figure B.6. Assuming a Moho level target in our data (t_0 of 5.5 s, dominant frequency of 15 Hz and RMS velocity of 4000 m/s), the Fresnel zone is 1235 m for half-offset 3000 m. Therefore, based on *Sun and Bancroft* [2001]'s argument, the minimum migration aperture of 2450 m is needed for our data set to preserve Moho reflection amplitudes and focus seismic

energy. Our chosen migration aperture for the final pass of 3D PreSTM was 2500 m in the in-line and cross-line directions. The result of 3D PreSTM with a larger aperture of 3500 m did not lead to improved images.

In the Kirchhoff summation used in this work, the input samples are multiplied by amplitude weights of W_i which enable the recovery of the reflection amplitude of subsurface horizons. The weights for 3D migration are calculated by the same procedure used in *Peles et al.* [2001].

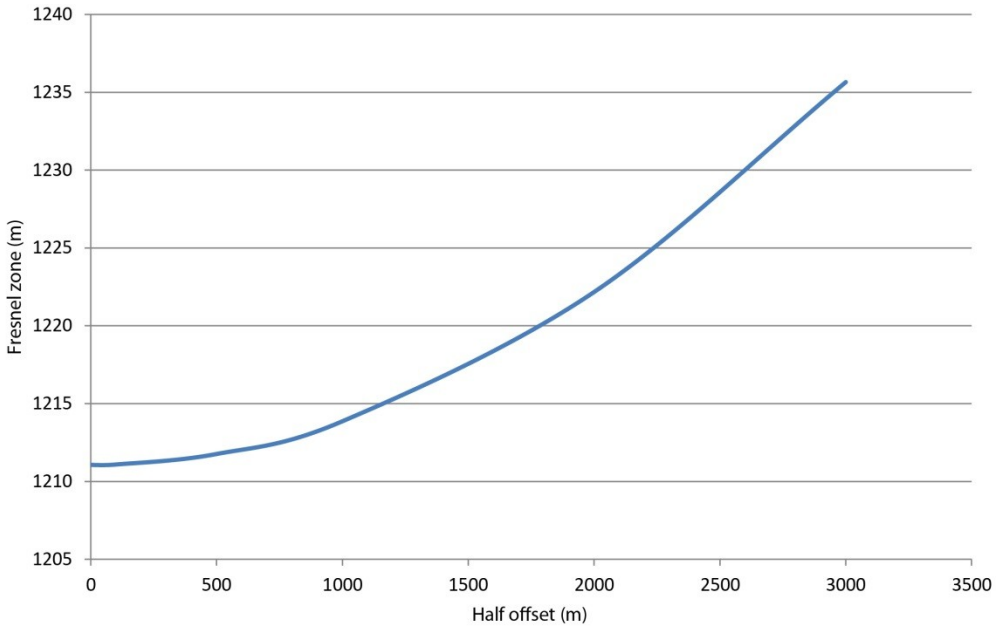

Figure B.6 Fresnel zone radius variation with half source-receiver offset at Moho. The source-receiver offset is shown in Figure B.1 for a scatterpoint.

If the velocity changes gradually in the horizontal direction, the constant velocity in equation B.2 is replaced with the RMS velocity function. In this case, the migration is called time migration. Estimating the RMS velocity through time migration by evaluating the CIGs is possible as a result of the average velocity (V_{RMS}) entering directly in expressions of the corresponding summation surfaces. This is an advantage over prestack

depth migration because there is no such direct relation between the computed traveltime in depth migration through dynamic raytracing and interval velocity, and as a result estimating the interval velocity is a complex inverse problem.

Another difference between time migration and depth migration is that the imaging and time-to-depth conversion are independent tasks in time migration. This is an advantage of time migration over depth migration because the velocity models for focusing the data (average velocity) are easier to estimate than velocity models for accurate time-to-depth conversion (interval velocity). In depth migration, both imaging and time-to-depth conversion depends on the accuracy of the interval velocity. If the estimates of interval velocity are inaccurate, the produced images are deteriorated and the reflectors are mispositionned [*Biondi,* 2007].

B.2 Migration Velocity Analysis

The summation of the diffraction hyperbola in Kirchhoff prestack migration can be done in two steps. In the first step, all the data points with the same offset are summed together, and the second step involves summing across offsets (Figure B.7). This two-step workflow is advantageous because it allows for velocity analysis. If the velocity used in migration is correct, the common-offset planes will be correctly migrated, and the resultant CIGs are flat (Figure B.7). However, if the velocity is wrong, the CIGs are not flat. By flattening the CIGs through MVA, the initial velocity is updated and the 3D PreSTM is performed with the updated velocity.

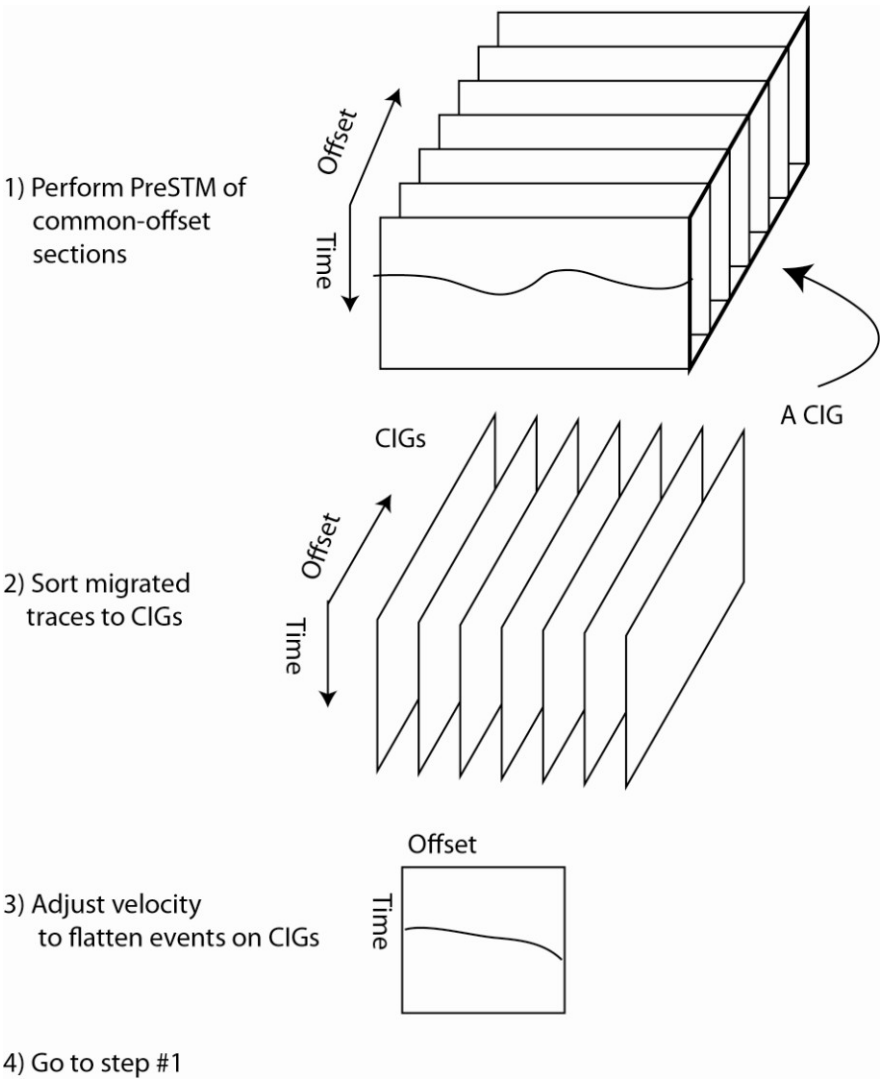

Figure B.7 . Illustration of velocity analysis in the postmigrated domain. If the velocity used for migration were correct, each migrated section of step 1 would be identical, and the CIGs of step 2 would be flat. When an incorrect velocity field is used, the events on CIGs are not flat. Migration velocity analysis in step 3 flattens the events on CIGs. Modified from *Stork* [1992].

B.3 Processing Steps Applied to CIGs

For attenuating the linear noise that masks the Moho reflection in CIGs, I used the LIFT method. The main idea of LIFT in the first step is to separate noise from signal very roughly and then add back signal from the noise, as detailed in *Choo et al.* [2004]. After separating most of the signal from the noise with residual signal, I extracted this residual

signal from what was considered mostly noise and added that back to the signal that was very effective for improving the S/N ratio without introducing filter noise, which is the key problem without LIFT.

For applying LIFT, I first decomposed the CIGs into three frequency bands. These frequency bands are low-frequency (0-8-15 Hz), mid-frequency (8-15-15-22 Hz) and high-frequency (15-22-200-220 Hz). Ideally, the data should be divided into two frequency bands of 0-8 Hz, and >8 Hz because the dominant noise is within the frequency range 0 to ~8 Hz. But sharp cutoff frequencies result in ringing and for this reason the cutoff frequencies are provided by corner frequencies in the trapezoid bandpass filter. In separating the data into frequency bands by bandpass filtering, the mid-frequency band is extracted by subtracting the combination of low- and high-frequency bands from the full spectrum.

The data decomposition in to three frequency bands is shown in the third row of Figure B.8. The CIG (A) is decomposed into low-frequency (BL) and high-frequency (DH) by applying a bandpass filter. The mid-frequency (CM) is the result of subtracting (A) from the combination of (BL) and (DH). An FX filter followed by a median filter is applied to the low-frequency component (BL) in Figure B.8. The result of applying these filters to the low-frequency component is the low-frequency signal (BLS). The result of subtracting the low-frequency component (BL) from the low-frequency signal (BLS) includes some residual signal and mainly noise. This residual low-frequency signal is separated from what is considered mainly noise (BL-BLS) in Figure B.8 by applying an FX filter and a median filter which results is added back to BL that is the low-frequency signal. This summation forms the LIFTed low-frequency component. The same

procedure is applied to the CM and DH, the mid- and high-frequency component of the CIG (Figure B.8). The summation of the LIFTed low- mid- and high-frequency component builds the LIFTed CIG. An example of a LIFTed CIG is shown in Figure B.9h. The CIG without any filter applied is shown in Figure B.9a, the low- mid- and high-frequency components (as shown in Figure B.8) are Figure B.9b, Figure B.9c, and Figure B.9d, respectively. The LIFTed low- mid- and high-frequency are Figure B.9e, Figure B.9f, and Figure B.9g, respectively. The LIFTed gather is Figure B.9h that is the summation of Figure B.9e, Figure B.9f, and Figure B.9g.

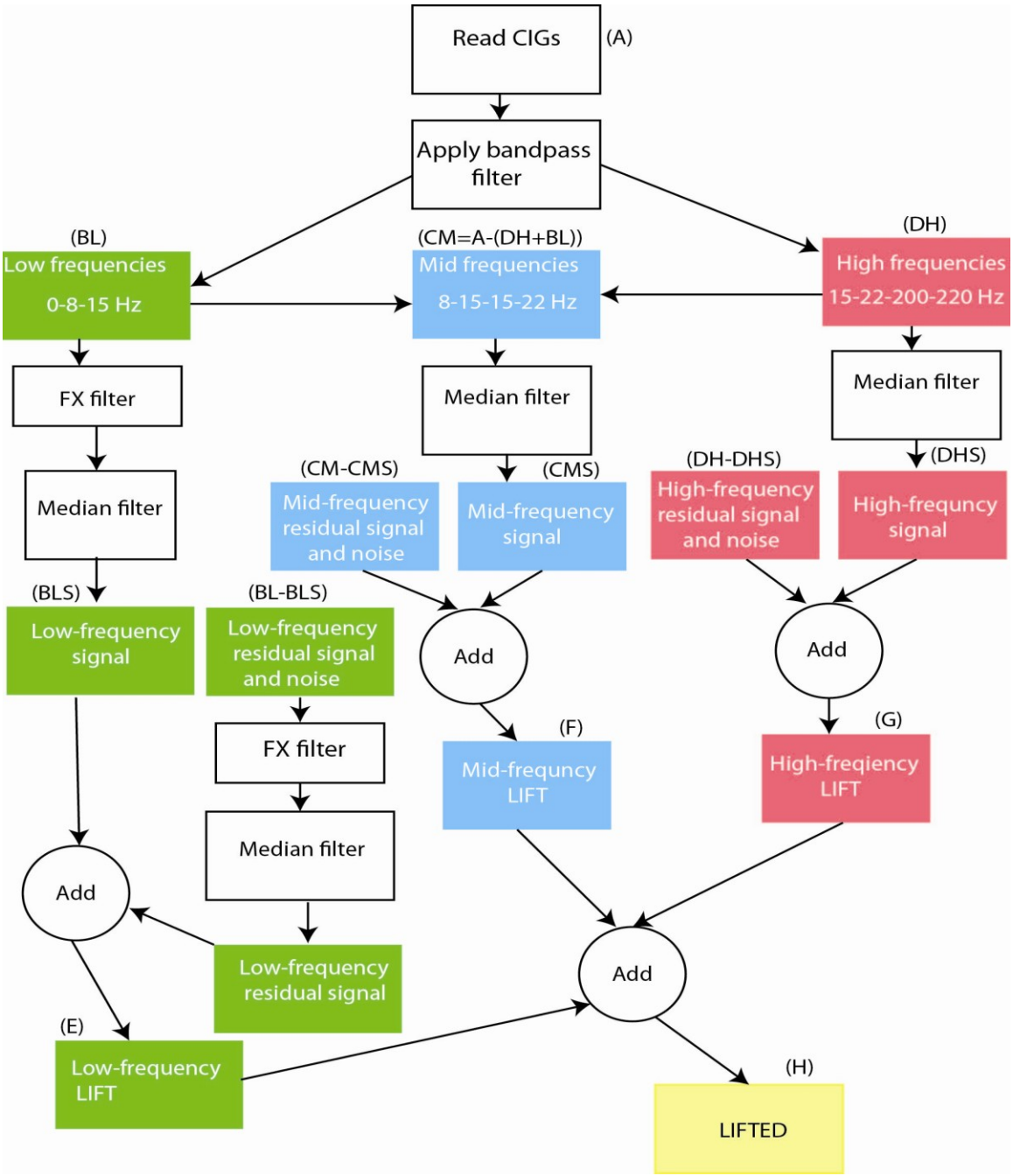

Figure B.8 The LIFT processing flow applied to CIGs. (A) is decomposed into frequency bands of (BL) 0-8-15 Hz, (CM) 8-15-15-22 Hz, and (DH) 15-22-200-220 Hz. Median filter and FX filters are applied to (BL) and the residual low-frequency noise (BL-BLS). The result of applying FX and median filter to the residual low-frequency noise is added back to BLS to get the low-frequency LIFT (E). For producing the mid-frequency signal (CMS), median filter is applied to (CM). Residual mid-frequency signal is the result of applying median filter to (CM-CMS) that is added back to CMS to get the mid-frequency LIFT (F). The same procedure is applied to high-frequency band (DH) to achieve the high-frequency LIFT (G). The final LIFT (H) is summation of (E), (F), and (G).

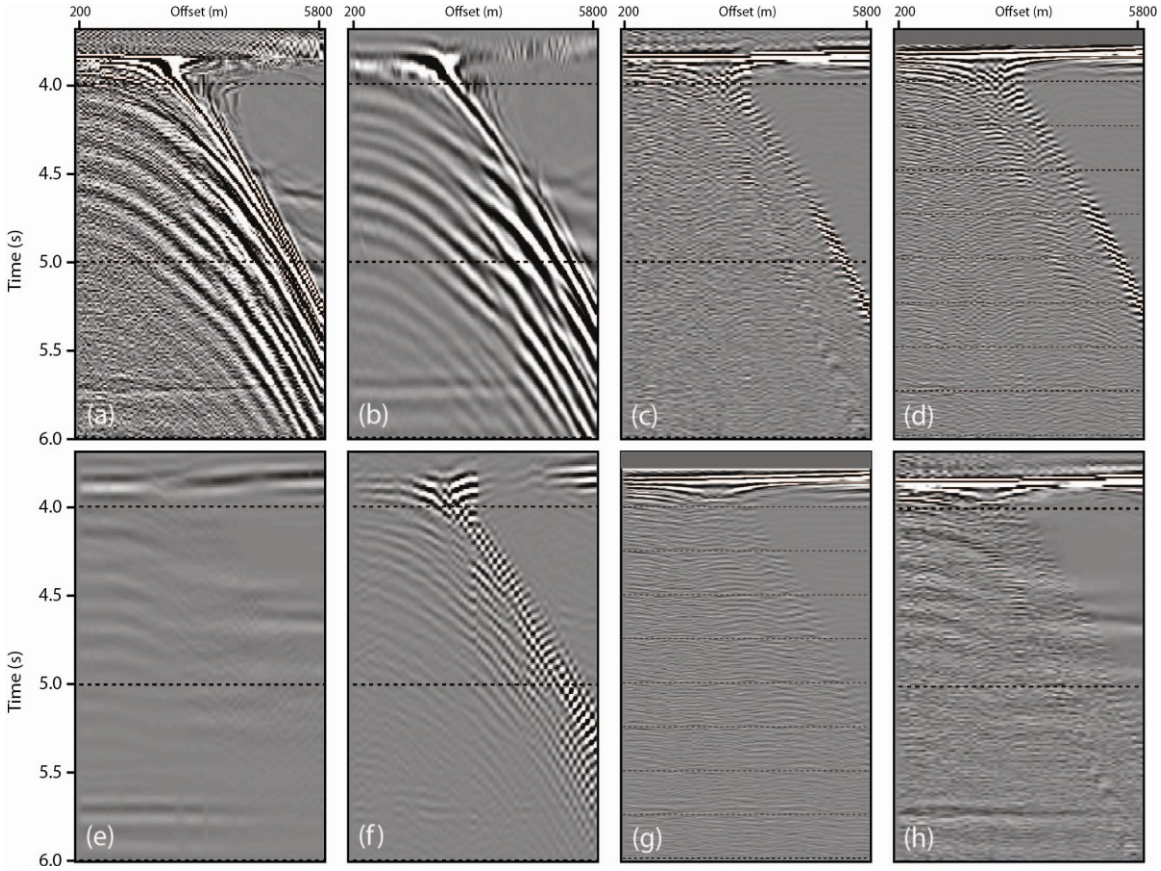

Figure B.9 Application of LIFT (B-H) to a sample CIG gather from in-line 1672 and cross-line 2224 (a). Decomposition of (a) into low-frequency band (0-8-15 Hz) (b), mid-frequency band (8-15-15-22 Hz) (c), and high-frequency band (15-22-200-220 Hz) (d) components. The low-frequency component after applying median filter, FX filter and adding back signal (e), the mid-frequency component after applying median filter and adding back signal (f), and the high-frequency component after applying median filer and adding back signal (g). (h) is the summation of (e) to (g).

References

Biondi, B (2006), 3D seismic imaging, Society of Exploration Geophysicists.

Bancroft, J.C (2001), A Practical Understanding of Pre- and Poststack Migrations, Society of Exploration Geophysicists.

Choo, J., J. Downton, and J. Dewar (2004), Lift: a new and practical approach to noise and multiple attenuation. *First Break*, 22, 39–44.

Claerbout, J.F (1985), Imaging the Earth's Interior, Blackwell Scientific Publications.

Peles, O., D. Kosloff, Z. Koren, and M. Tygel (2001), A practical approach to true amplitude migration, *Journal of seismic exploration*, 10,183-203.

Schneider, W. A (1978), Integral formulation for migration in two-dimensions and three-dimensions, *Geophysics*, 43(1), 49–76.

Stork, C (1992), Reflection tomography in the postmigrated domain, *Geophysics*, 57(5), 680-692.

Sun, S. and J. C. Bancroft (2001), How much does the migration aperture actually contribute to the migration result?, SEG Int'l Exposition and Annual Meeting, San Antonio, Texas, September 9-14.

APPENDIX C OVERVIEW OF THE AVO THEORY

The Zeoppritz's equations describe the exact plane wave amplitude of a reflected P-wave as a function of angle of incidence, but these equations are complicated to derive petrophysical parameters, and as a result different approximations to the Zeoppritz's equations were suggested for practical applications. The first approximation was suggested by *Bortfield* [1961] that was further simplified by *Aki and Richards* [1980]. In *Aki and Richard* [1980] approximation, the amplitude of the reflected P-wave as a function of angle of incidence for the configuration shown in Figure C.1 is expressed by

$$\boldsymbol{R\ \theta\ \approx A\frac{\Delta V_p}{V_P}+B\frac{\Delta\rho}{\rho}+C\frac{\Delta V_s}{V_s}} \quad \text{(C-1)}$$

where : $A = 1 + tan^2(\theta)$, $B = 1/2(1 - (2\rho V_s)^2)$, $C = -(2\rho V_s)^2$, $\Delta\rho = \rho_2 - \rho_1$, $\Delta V_s = V_{s2} - V_{s1}$, $\Delta V_p = V_{p2} - V_{p1}$, $\theta = (\theta_1 + \theta_2)/2$, $V_p = (V_{p1} + V_{p2})/2$, $V_s = (V_{s1} + V_{s2})/2$, $\rho=(\rho2+\rho1)/2$.

Another form of the *Aki and Richards* [1980] approximation was provided by *Shuey* [1985]. This equation relates the amplitude of the reflected P-wave to density, P-wave velocity, and S-wave velocity across the interface shown in Figure C.1

$$R\ \theta_1\ \approx A+B\sin^2\theta_1+C(\tan^2\theta_1-\sin^2\theta_1) \quad \text{(C-2)}$$

where: $A = \frac{1}{2}\ \frac{\Delta V_p}{V_p}+\frac{\Delta\rho}{\rho}$, $B = \frac{1}{2}\frac{\Delta V_p}{V_p}-2\frac{{V_s}^2}{{V_p}^2}(2\frac{\Delta V_s}{V_s}+\frac{\Delta\rho}{\rho})$, $C = \frac{1}{2}\frac{\Delta V_p}{V_p}$, $\Delta\rho = \rho_2 - \rho_1$, $\Delta V_s = V_{s2} - V_{s1}$, $\Delta V_p = V_{p2} - V_{p1}$, $V_p = (V_{p1} + V_{p2})/2$, $V_s = (V_{s1} + V_{s2})/2$, $\rho=(\rho2+\rho1)/2$.

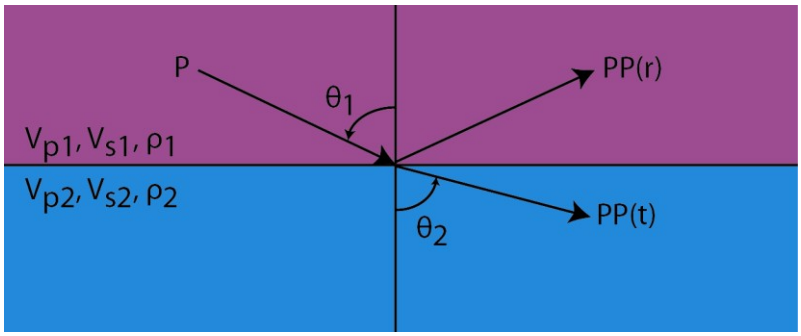

Figure C.1 Reflection and transmission for an incident P-wave at an interface between two elastic half spaces. The angle of incident for the P-wave (P) is θ_1 and the angle of transmission for the transmitted P-wave (PP) is θ_2. V_{P1}, V_{s1}, and ρ_1 are P-wave velocity, S-wave velocity and density of the upper layer, respectively. The lower layer has P-wave velocity V_{p2}, S-wave velocity V_{s1}, and density ρ_2.

In equation C-2, known as the Shuey's three-term equation, the first term is the normal incidence reflection coefficient, the second term is dominant at intermediate angles ($0°<\theta<30°$), and the third term is dominant as the critical angle is approached. The third-term is negligible at intermediate angles of incidence leading to a two-term approximation

$$R\ \theta_1 \approx A+B\sin^2\theta_1 \qquad \text{(C-3)}$$

Equation (C-3) is known as Shuey's two-term AVO equation that has greatly simplified AVO analysis. The first term (A) is the zero-offset reflectivity controlled by the contrast in acoustic impedance. The second term (B) depends mainly on the $\frac{V_p}{V_s}$ ratio or the Poisson's ratio.

Foster at al. [2010] showed that there is a linear relationship between A and B in the form

$$B = \ 1-8\gamma^2\ A-4\gamma\Delta\gamma+(4\gamma^2-1)\frac{\Delta\rho}{2\rho} \qquad \text{(C-4)}$$

where $\gamma = \frac{V_s}{V_p}$, and $\Delta\gamma = \frac{\Delta V_s}{V_s} - \frac{\Delta V_p}{V_p}$, $\Delta\rho = \rho_2 - \rho_1$, $\Delta V_s = V_{s2} - V_{s1}$, $\Delta V_p = V_{p2} - V_{p1}$,

$V_p = (V_{p1} + V_{p2})/2$, $V_s = (V_{s1} + V_{s2})/2$, $\rho=(\rho 2+\rho 1)/2$.

Assuming that the density contrast is negligible along an interface, equation C-4 can be further simplified to

$$B = \ 1 - 8\gamma^2 \ A - 4\gamma\Delta\gamma \qquad \text{(C-5)}$$

Equation C-5 shows that crossplotting A vs. B results in a group of lines parallel to $B = \ 1 - 8\gamma^2 \ A$ that is known as the fluid line [*Foster et al.,* 2010].

References

Aki, K., and P.G. Richards (1980), Quantitative Seismology, *W.H. Freeman and Co.*

Bortfeld, R (1961), Approximation to the reflection and transmission coefficients of plane longitudinal and transverse waves. *Geophy. Prosp.*, 9, 485-502.

Shuey, R. T (1985). A simplification of the Zoeppritz equations, *Geophysics*, 50, 609-614.

Foster, D.J., R.G. Keys, and F. D. Lane (2010), Interpretation of AVO anomalies, *Geophysics*, 75(5), 75A3–75A13.